Hollow Core Fibre-Based Gas Discharge Laser Systems and Deuterium Loading of Photonic Crystal Fibres

Bateman, Samuel

Award date:
2015

Awarding institution:
University of Bath

Hollow Core Fibre-Based Gas Discharge Laser Systems and Deuterium Loading of Photonic Crystal Fibres

submitted by

Samuel Alec Bateman

for the degree of Doctor of Philosophy

of the

University of Bath

Department of Physics

October 2014

for
Mum & Dad

Contents

Acknowledgements

I'd like to thank:

Tim and Pete for always being available to offer help, thoughts and advice.

Jim for his help in the drawing tower, and always being willing to provide input on all things Supercontinuum.

Gareth for putting up with my streams of photonics questions.

Steve and Alan for their endless hours spent helping me in the drawing tower.

Fei and Walter for providing the negative curvature fibres for my work, and always being available to answer my questions concerning them.

Fianium for the use of their laser.

Laura for proof reading these chapters and spotting errors and typos.

All the other members of the CPPM, who have made working there such an enjoyable experience.

Finally, I'd like to thank William for his endless thoughts and advice, for reading this Thesis, and his unfailing support for me over the course of my PhD.

Overview

This Thesis will cover work carried out at the University of Bath between October 2010 and October 2014, primarily covering two topics of research. The first is an investigation into the effectiveness of a new technique for loading a supercontinuum photonic crystal fibre with deuterium gas. The second concerns recent steps taken towards the development of a fibre-based gas discharge laser using noble gases. This work is broken down further into two separate investigations, an RF excitation approach and a DC excitation approach.

Chapter 1 briefly outlines the historical development of optical fibres, from basic concepts up to photonic crystal fibres and the most recent negative curvature fibres. Some different types of fibre and the process of fabrication are described.

Chapter 2 begins by describing the guidance mechanisms harnessed in optical fibres and photonic crystal fibres, from the simplistic ray model to a more accurate description of modes and birefringence. Bandgap guidance and the ARROW model is then discussed in the context of the latest fibres that employ this form of guidance, which is relevant for the research presented in Chapters 7 and 8. The Chapter then describes the nature of dispersion in the fibre, and how the microstructure can be altered to engineer the dispersive behaviour. The relevant loss mechanisms present over the silica transparency window are then outlined, and finally the behaviour of gain is discussed, with a focus on gas discharge lasers, which are the subject of Chapters 7 and 8.

Chapter 3 describes the role of nonlinearity in photonic crystal fibres, starting with the source of nonlinear behaviour and the variations between optical fibres and bulk nonlinear crystals. Specific nonlinear processes are described, such as Four Wave Mixing and Raman generation, before finally discussing the combination of nonlinear effects that take place in broad supercontinuum generation, which is relevant to research

described in Chapter 5.

Chapter 4 provides the background theory behind the research on photo-darkening described in Chapter 5. The source of and causes of certain defect formation in silica is discussed, followed by the most recent treatment techniques used to prevent or mitigate the damage from defects in silica.

Chapter 5 contains the results of the research investigation carried out to assess the effectiveness of a new technique for loading deuterium into a supercontinuum generating photonic crystal fibres. Two structurally identical fibres are fabricated, one annealed with deuterium and one remaining untreated. Both are exposed to high intensity, defect forming radiation, intended to photo-darken the fibre and introduce defects to the glass. A third fibre set, taken from the untreated fibre, is then loaded with deuterium using the new technique, and exposed in the same manner and compared to the first two. The resulting attenuation across the silica spectral window is measured and the effectiveness of the new loading method is evaluated.

Chapter 6 describes the theory and operating mechanisms behind gas discharge lasers, which is the subject of Chapters 7 and 8. Some of the basic concepts behind gas discharges are covered, including the types of collision in a discharge, the Debye length and the electron temperature, before outlining the different driving regimes of RF and DC excitation. Finally, the specific lasing mechanisms of helium neon and helium xenon are described, with a focus on certain mid-IR emission lines which are the subject of the subsequent work.

Chapter 7 concerns the research into RF excited fibre gas discharges, describing the motivation behind the work, the equipment and novel negative curvature fibre used to carry it out, and the steps taken in understanding the nature of the gas discharges initiated. Several spectra of the light emitted from different gas discharges is presented, and a basic gain measurement is carried out for lines between 3 μm and 3.5 μm.

Chapter 8 contains the results of further research into fibre-based gas discharge lasers, this time using a DC excitation method. The differences between this and the prior chapter is discussed, the approach is outlined and the equipment used is described. Spectral data for different lengths of discharge is presented, and measurements of the gain are analysed and discussed. Repeatability is assessed and the necessary further steps to be taken towards a full laser are outlined.

Chapter 1

Background to Optical Fibres

1.1 Introduction

Optical fibres, specifically photonic crystal fibres, act as the fundamental technology behind the research presented in this thesis. Therefore these early chapters describe the nature and underlying theory of this technology, and provide an understanding of how it is used in the investigations carried out in later chapters.

This first chapter will discuss the background behind modern optical fibres, starting with a brief overview of the history of the development of optical fibres, covering early glass waveguides before moving on to step index fibres and then the more recent development of photonic crystal fibres. The technology is then brought up to the present with a description of hollow core photonic crystal fibres and negative curvature fibres, and their potential use in modern gas laser technologies is noted.

This is followed by an overview of the types and typical structures found in photonic crystal fibres, with the conventional methods of measuring and quantifying the dimensions of the fibre microstructure stated. Finally, the process followed when fabricating photonic crystal fibres is described. This method is relevant to the research presented in Chapter 5, where experiments are carried out on two fibres fabricated in this way.

1.2 A Brief History of the Development of Optical Fibres

The underlying principle behind optical fibres, the ability of a structure to act as a waveguide for light, was first demonstrated in the 1840s [1], using a stream of water falling from a hole in a container to a basin below to guide light. John Tyndall later explored and defined this effect in 1870 [2], calling it *Total Internal Reflection* (TIR). The guidance of light in thin strands of various materials was explored over the subsequent decades, with several early 20th century technologies relying on this ability to manipulate light. The efficiency of this technology was improved with the addition of a low refractive index cladding layer around a high index core, and in the 1950s the first glass optical fibres were introduced.

These early step-index fibres suffered from very high loss, often up to 1000 $\mathrm{dBkm^{-1}}$, making them unsuitable for use in long distance data transmission. However, researchers Charles Kao and George Hockham at the company Standard Telephones and Cables theorised in their 1966 paper that the high loss in optical fibres was not due to an insurmountable physical limit such as scattering, and could in fact be reduced to below 20 $\mathrm{dBkm^{-1}}$ by increasing the purity of the guidance material [3]. The researchers also suggested that an ideal candidate as a material for low loss optical fibres was fused silica, SiO_2, due to its inherent purity. This realisation revolutionised the field of fibre optics and telecommunications, later earning Charles Kao the Nobel Prize for Physics in 2009 [4]. By 1969 the loss limit for fibre optics had been reduced to approximately 4 $\mathrm{dBkm^{-1}}$ [5], and by 1988 the first transatlantic fibre optics cable was laid, making fibre based telecommunications a reality.

Achieving low losses in the transmission of optical fibres was not only beneficial for telecommunications, but also made it possible for fibres to be used as amplifiers with their own inherent gain, which then ultimately led to new fibre-based laser systems. By that time step-index and graded-index fibres consisted of a silica glass core doped with small amounts of other elements. That doped core was surrounded with a cladding jacket, either undoped or, occasionally, doped so as to lower the refractive index of the cladding layer. This resulted in the required guidance behaviour, arising from the customised index difference between the core and cladding. If the core dopant included a laser-active element, such as ytterbium or neodymium, then in addition to the modification of the refractive index the fibre could act as a gain medium. This concept was quickly realised in bulk glass, as early as 1961 [6], and applied to optical fibres shortly afterwards to develop the first fibre lasers [7]. However, the technology

was not harnessed into commercial devices until the 1980s.

Optical fibres made entirely from pure silica were first demonstrated in 1974 by a group at Bell Labs [8]. However, these fibres did not contain a periodic cladding structure, and it was not until the mid-1990s, when a group at the University of Southampton, led by Philip St. J. Russell, developed the first silica optical fibre with a periodic cladding structure [9]. The guidance of this fibre was achieved through a hexagonal photonic crystal cladding microstructure, made up of air-filled holes around a solid glass core, and was named *Photonic Crystal Fibre* (PCF) by the group. This new type of optical fibre allowed for a broader range of customisation, such as greater confinement of the propagating light and more precise control of the dispersive properties, and made the harnessing of significant nonlinear processes possible, without the need for a dopant.

As with Charles Kao in his 1966 paper, this began a new revolution and renewed interest in optical fibre technology, and saw the quick development of a wide range of new fibre devices based on this concept. Only a few years after the first publication, a *Hollow-Core Photonic Crystal Fibre* (HCPCF) was demonstrated by the same group [10], harnessing photonic bandgaps as the method of confining light in an air-filled core, which is itself surrounded by an air-filled photonic crystal cladding. This resulted in new gas sensing technologies, fibre lasers and a variety of nonlinear devices [11, 12, 13, 14].

More recently, a new family of PCFs have been developed by several research groups [15, 16, 17, 18, 19]. These hollow-core fibres consist of a structure with a negative curvature at the core boundary, and do not require complex cladding structures made up of many rings to achieve effective light confinement. This new class of PCF harnesses a form of guidance known as *Negative Curvature Fibres* (NCF). These fibres allow for the guidance of light at wavelengths beyond 2 μm, where silica is highly absorbing, and so present an opportunity for the development of entirely new technologies that harness the advantages of optical fibre technology in the mid-infra-red. The hollow-core aspect of NCF fibres make them ideal candidates for the development of new gas lasers, operating on length scales and at wavelengths which were previously not accessible. The availability of these fibres is the core motivation behind the gas laser work presented in Chapters 7 and 8.

1.3 The Types and Structure of Photonic Crystal Fibres

As mentioned earlier in Section 1.2, a solid-core photonic crystal fibre contains a microstructure of air holes in its cladding, usually arranged into a hexagonal array. A solid defect acts as the core, usually located in the centre of the cladding microstructure, as shown in Figure 1.1.

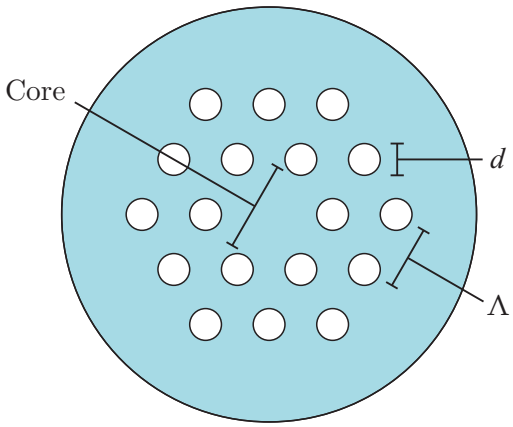

Figure 1.1: A typical solid core PCF structure, with the hole size d, the pitch Λ, and the core labelled.

The dimensions of this structure are conventionally quantified using several standard measurements, each of which is labelled in Figure 1.1. The pitch, Λ, is the distance from the centre of one cladding hole to the centre of an adjacent cladding hole, while the diameter of the holes is represented by the symbol d.

By altering the dimensions of the cladding microstructure, the guidance behaviour of the fibre can be customised. For instance, increasing the proportion of air in the cladding by increasing $^{d}/_{\Lambda}$ results in the effective index being lowered to any level desired above that of air (a refractive index of 1). Changing the number of cladding rings, or adding multiple cladding layers with different d and Λ values also allows for PCF guidance customisation. This is discussed in greater detail later in this Chapter.

A whole range of different microstructures can be used to build fibres with extremely flexible capabilities. Some examples of PCF microstructures are shown in Figure 1.2, the top three images showing a conventional solid core PCF, a hollow core photonic bandgap fibre, and an all-solid bandgap fibre. The bottom three images all show a "ring" fibre, where the cladding is made up of a series of air rings. The final fibre is

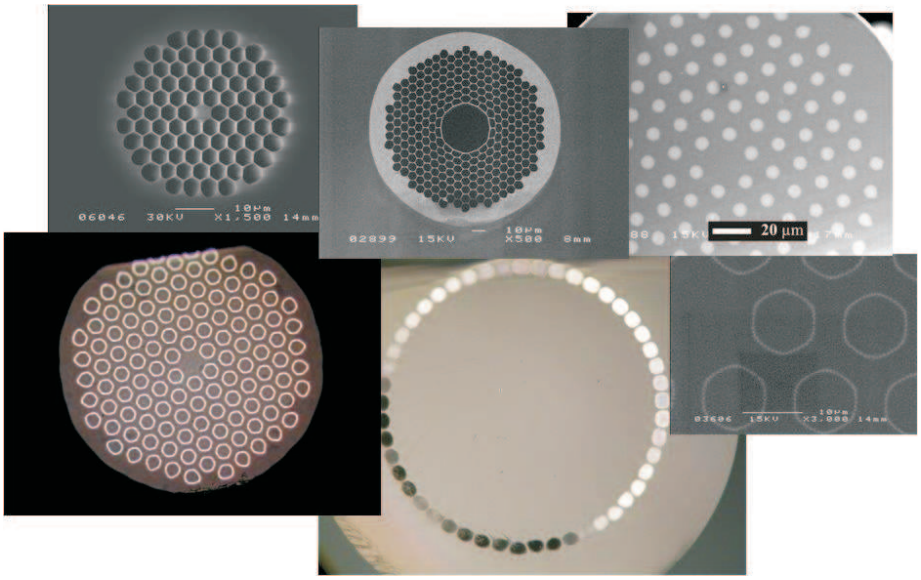

Figure 1.2: Some different examples of PCF microstructures fabricated at the University of Bath. Clockwise from the top left: a solid core photonic crystal fibre, a hollow core photonic bandgap fibre, an all-solid photonic bandgap fibre, a close shot of a photonic bandgap fibre with a cladding array formed of rings, an individual cane used to fabricate the ring fibre, and a full image of the ring fibre.

shown on the left, with an individual cane for one ring shown in the middle, and a closer shot of the cladding structure on the right.

The way that the microstructure allows the PCF to guide light in its core is described further in Chapter 2.

1.4 The Fabrication of Photonic Crystal Fibres

Fabricating photonic crystal fibre is carried out using the "stack and draw" technique [20]; where a macroscopic structure is built from capillaries, slid inside a large tube, and that tube is then fed vertically through a furnace, where the heat softens the glass. This allows it to be drawn under tension, causing it to thin down to a diameter on the scale of around 100 μm. The structure inside the tube is preserved as the tube thins, through the application of pressure within the holes making up the internal structure. This prevents surface tension from causing the holes to collapse as the tube thins, and so the holes are maintained inside the final photonic crystal fibre, in the

form of a microstructure.

The critical piece of equipment used in drawing fibre is the fibre drawing tower. This structure allows silica glass rods of around 1 m in length to be clamped at the top and fed vertically downwards into a filament furnace, which can reach temperatures of up to 2300 K, at a given "feed rate". The furnace acts to soften the glass as it passes through, so that a set of belt trackers below can grip and pull the glass downwards as it passes from the furnace at a "draw rate" which is higher than the feed rate of the rod above. This process acts to draw the glass down into a longer, thinner structure, and serves as the basic mechanism in each stage of fibre drawing. Since the draw rate, feed rate, and furnace temperature are all customisable, the diameter of the glass after drawing is controllable, and can be monitored using a laser measurement device at the furnace output.

The initial stage of fibre fabrication is to draw capillaries for the stack which will eventually be the fibre microstructure. Most often, these are tubes made from a pure form of silica glass, chosen because their ratio of inner to outer diameters closely matches the desired ratio of hole size d to pitch Λ in the final fibre. The tubes, typically having an outer diameter of the order of 10 mm, are fed into the furnace and drawn down to capillaries of the order of 1 mm or 2 mm. The capillaries are then placed onto a *stacking rig* in a hexagonal configuration, as shown in the first step of Figure 1.3, forming the "stack" about 2 cm to 3 cm in height. In a standard solid-core PCF, the central position serves as the core, and so a solid rod of silica glass replaces the capillary in that position.

The stack is then slid inside a larger tube, chosen to have an inner diameter that closely fits the dimensions of the stack. To prevent the outer capillaries of the hexagonal stack from falling into the empty spaces inside the circular tube, a series of solid "packing rods" are used to fill the gaps. The six capillaries at the corners of the stack can be removed to minimise the number of packing rods required, as shown in Figure 1.3. The jacketed stack is then fed through the furnace and drawn down to a series of 1 m long canes, usually 3 mm to 5 mm in diameter. To preserve the microstructure of the stack, the gaps between the capillaries, sometimes referred to as the "interstitial holes", are evacuated, causing almost all of them to collapse during the draw down to canes.

The final drawing stage to fibre again involves jacketing one of the 1 m long canes, which is then prepared so that pressure can be applied directly to the inside of the holes in the microstructure through a fitted brass cap. The application of pressure

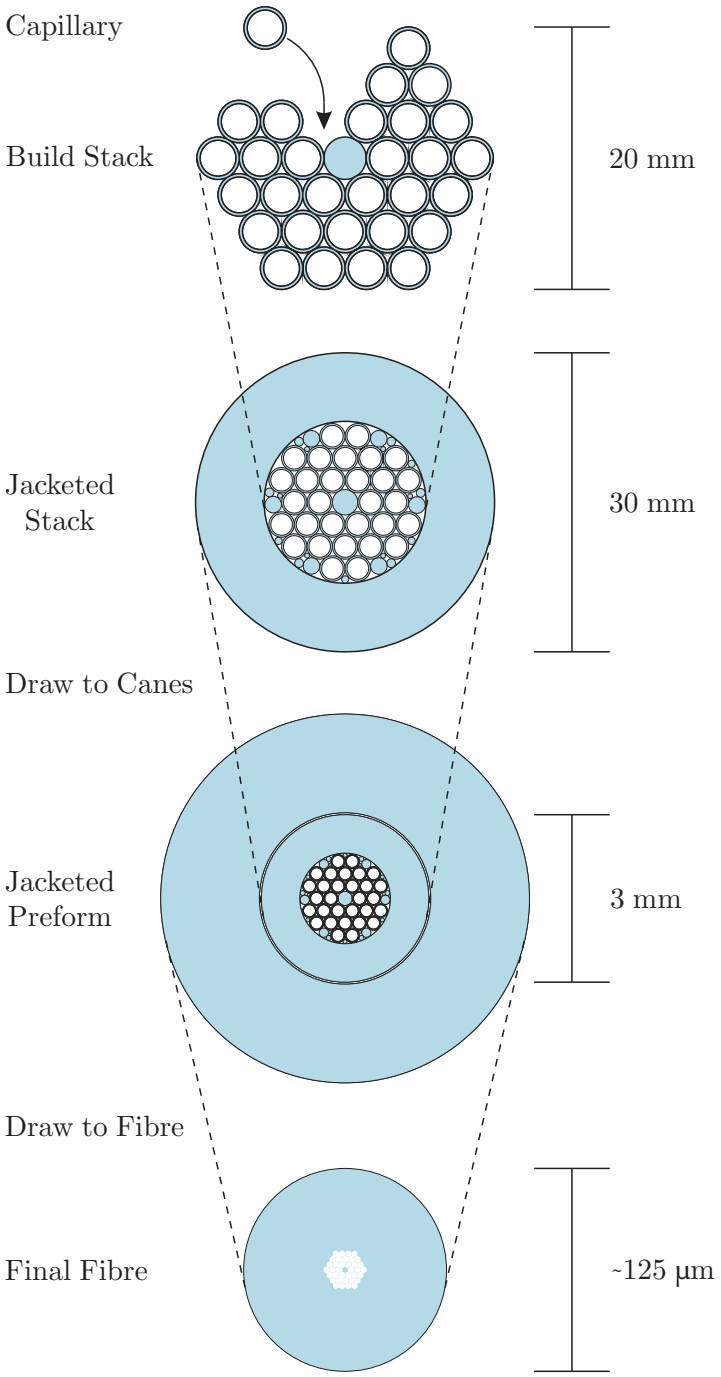

Figure 1.3: The steps taken during the fabrication process of a typical solid core PCF. The stacked structure is preserved through every stage of the fabrication, forming a microstructure in the final fibre.

during this final stage allows for the fine-tuning of the dimensions of the final fibre microstructure by inflating or deflating the holes. The change can then be monitored during the draw through the fibre outer diameter using the laser measurement device at the output of the furnace.

Finally, after the fibre is drawn out of the furnace it is passed through a polymer coating machine, where an even layer of liquid polymer is applied to the outside of the fibre and cured by a UV lamp. This coats the fibre in a layer of flexible polymer chains, which acts to protect the glass of the fibre, prevents damage and breakages from exposure to the air, and allows the fibre to be more flexible by exhibiting a low Young's Modulus value. It is then wound on to a spool for storage or for use in the lab.

1.4.1 Fabricating Birefringent and Polarisation-Maintaining Fibres

Birefringent and polarisation-maintaining PCF, as described later in Section 2.4.1, are conventionally also fabricated using the stack and draw method. Most simply, they can be defined as fibres with deliberate structural defects along one axis across the core, which work to maintain the polarisation of linearly polarised light which is aligned to that axis [21]. Some examples of birefringent PCF are shown later in Figure 2.3.

The defects in the microstructure which give rise to the birefringent behaviour are either built into the stack at the beginning of the fabrication process, or introduced to a uniform structure through the application of differential pressures during the fibre draw stage.

In the first case, the defect is added by placing a few capillaries with larger or smaller internal hole diameters at strategic points either side of the core. This defect from the different hole sizes can then be preserved with each draw phase, so that it is still present in the final fibre. However, this means the same pressure is applied across all of the holes in each draw phase, which can result in unpredictable degrees of inflation for the defect holes as a result of the balance of surface tension across the whole structure. This slight difference from the expected hole sizes can be problematic in fibres where the size of the desired structure is very specific, such as in four wave mixing fibres (discussed later in Section 3.4).

An alternative fabrication technique for birefringent fibres is to apply differential pressures to an initially uniform stack, causing two holes either side of the core to over or

under-inflate, forming the defects at the final draw phase to fibre [22]. The application of different pressures to different parts of the preform carries the advantage of greater flexibility and precision in the resulting fibre, but is harder to achieve practically.

Chapter 2

Guidance Mechanisms and Dispersive Behaviour in Optical Fibres and PCF

2.1 Introduction

This Chapter aims to describe the guidance behaviour in optical fibres and PCF, starting with a simplistic ray model approach to understand light propagation along fibres, followed by a more realistic treatment using guided modes and the propagation constant. Birefringence in optical fibres is then described, and how it is practically used in polarisation-maintaining fibres.

Guidance in solid core fibres is then contrasted with bandgap guidance, described using the ARROW model, before applying this to the more recent sub-class of negative curvature fibres. This type of fibre is directly relevant to research presented in Chapters 7 and 8.

The dispersive behaviour of light in optical fibres is then explored, with the different contributions and their mechanisms described, before outlining how this can be harnessed in PCF to customise the dispersion profile of the fibre.

This is followed by a description of the various loss mechanisms acting in optical fibres,

including the different wavelength dependences and relative strengths of those mechanisms. The effect of fibre bending on the losses and the equivalent loss mechanisms in hollow core fibres are also explained.

Finally, the behaviour of gain is discussed in the context of gas discharge lasers, focussing on the mechanisms resulting in small-signal gain and gain saturation. This is directly relevant to research discussed in Chapters 7, and 8.

These topics form an understanding of the basic behaviour of propagating light observed in the fibres used in Chapters 5, 7, and 8.

2.2 Optical Fibres and The Ray Model

As mentioned in Section 1.2, conventional step-index optical fibres are usually made up of a core doped with small amounts of an additional element, such as germanium dioxide (or a rare earth metal for some applications), surrounded by an undoped or differently-doped silica cladding [23]. This creates either a gradual or immediate change in the refractive index across the radius of the fibre. Figure 2.1 shows a simple refractive index profile for a conventional step-index fibre.

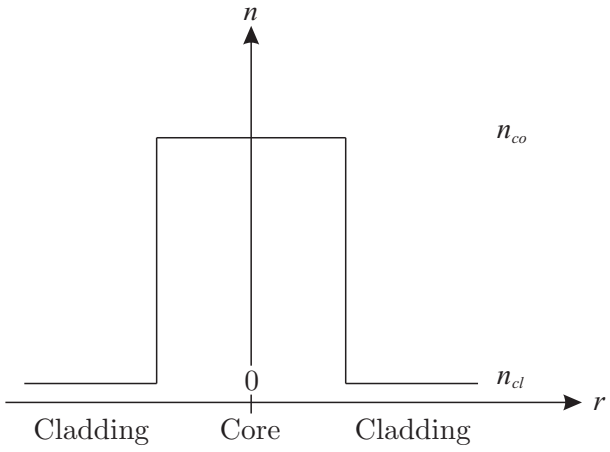

Figure 2.1: Refractive index profile of a step-index fibre, with the refractive index n, radial distance from the centre of the fibre r, and the core and cladding indices n_{co} and n_{cl}.

This "top hat" shape of profile, with a clearly defined core-cladding boundary, is also found in PCF, where the air-filled microstructure lowers the refractive index of the

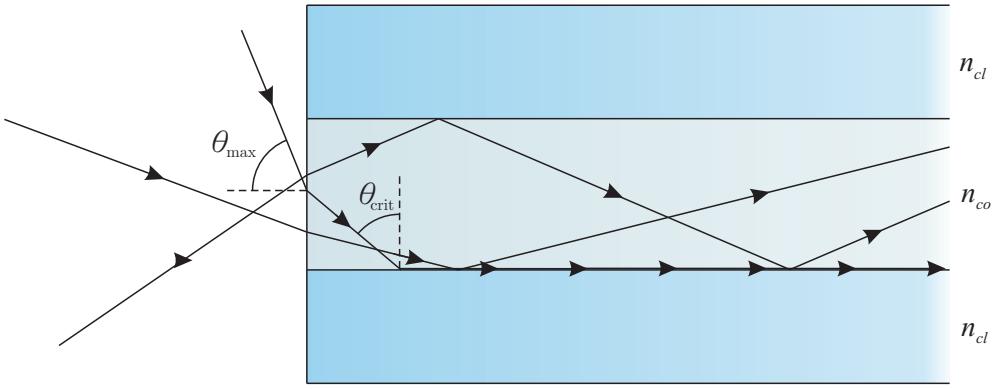

Figure 2.2: Light guided in a step-index fibre as described using the ray model. The value θ_{max} is as defined in equation 2.2, representing the maximum incident angle to couple into the fibre, with θ_{crit} being the resulting critical angle at the interface of the core and the cladding, as defined using Snell's Law.

cladding. This stepped profile can be made more complex, depending on the intended purpose of the fibre. For instance, the fibre could include additional high index layers in the cladding, or have a gradually changing refractive index across the fibre radius as the density of the dopant in the core gradually changes. This refractive index contrast can be quantified as

$$\triangle = \frac{n_{co} - n_{cl}}{n_{co}}, \tag{2.1}$$

where n_{cl} and n_{co} are the refractive indices of the cladding and core respectively.

The simplest model used to describe guidance in these conventional fibres and in PCF considers the light as a ray, or a vector, as shown in Figure 2.2. This ray is launched into a fibre at an angle which is within the range of acceptance angles, or the *numerical aperture* (NA) of the fibre, defined by the refractive index contrast as

$$NA = \sqrt{n_{co}^2 - n_{cl}^2} \simeq n_{local} \sin(\theta_{max}), \tag{2.2}$$

where n_{local} is the refractive index of the operating medium (most often air, but can be other media) and θ_{max} is the maximum launch angle for a ray which is still able

to couple into the fibre [24]. This equation is easily derivable using Snell's Law and a geometry where the ray is at the critical angle at the interface between the core and the cladding. Knowing the NA of a fibre is useful, as it defines the best choice of lens to achieve the maximum coupling into a fibre.

The light, modelled as a ray, then travels through the glass until it reaches the interface between the core and the cladding. If the angle of approach to the interface, as measured perpendicular to the interface boundary, is equal to or less than the critical angle, then the light is reflected back into the core, rather than refracted out into the cladding. This is known as *total internal reflection* (TIR) and is the simplest explanation of light propagation in a fibre.

2.3 Guidance in Photonic Crystal Fibres

The structural characteristics of a solid-core PCF were briefly discussed earlier in Chapter 1. The characteristic periodic arrangement of holes across the fibre cross section is known as a *photonic crystal*, with a defect, usually found in the centre, acting as a core. The dimensions of the photonic crystal, defined by the values of the pitch Λ and the hole size d, are on the scale of microns, and therefore comparable to the wavelength of the light propagating in the core defect.

This typical solid core PCF structure is in many ways analogous to a conventional step-index fibre, as the choice of the PCF pitch Λ and hole size d causes the average refractive index across the cladding region to fall, creating a step-index difference across the core defect, just as in conventional fibres.

However, the photonic crystal structure of PCF has several operational advantages over the glass doping approach of conventional fibres. The first is that the index contrast $\triangle$ can potentially be made much larger than in conventional fibres. The periodic hole structure can be adjusted to have large holes d with a small value of the pitch Λ to increase the fraction of the cladding taken up by air. This has the effect of significantly lowering the average refractive index across the periodic structure around the core defect, creating an index contrast which is much larger than conventionally achievable. It is notable that the holes of the periodic photonic crystal do not have to contain air, and can instead contain any practically chosen material to achieve the desired index contrast or dispersive profile.

The advantages of this large index contrast are twofold. Firstly, the contribution to the overall dispersion of the fibre from the waveguide is higher, allowing for far greater control of the exact dispersive behaviour through carefully engineering the dimensions of the photonic crystal. Secondly, The light propagating in the core is more highly confined, raising the intensity of the light in the core defect. This consequently causes more nonlinear processes to occur, allowing for those processes to be harnessed for the purpose of wavelength conversion. Dispersion is discussed in greater detail later in this Chapter, while the processes governed by nonlinearity are the subject of Chapter 3.

The guidance mechanism in solid core PCFs is similar to that of conventional optical fibres, arising from an index contrast between the cladding and the core. Therefore it could be described as "TIR-like". However, this interpretation becomes inappropriate, considering that the scale of the photonic crystal microstructure is usually of the order of the wavelength of the propagating light, making a ray-based model appear simplistic and hard to justify. It is therefore more appropriate to consider the propagating light as a wave, confined to the core in a *mode*.

2.4 Modes and the Propagation Constant

Considering light as a wave, rather than a particle-like ray or vector, allows for a more complete understanding of propagation and guidance in photonic crystal fibres. By solving Maxwell's equations for a fibre-like waveguide [25], a series of discrete modes are found as solutions. These modes are confined and guided in the core of the fibre, with the field decaying exponentially into the cladding region. A mode can be defined as an electromagnetic wave which propagates along the waveguide with unchanging parameters, except for the phase. Mathematically, this is

$$E(x, y, z, t) = F(x, y)e^{i(\beta(\omega)z - \omega t))}, \tag{2.3}$$

where the z-axis is defined as the direction of propagation along the fibre parallel with the core-cladding boundary, along which it is assumed that there is no change with propagation and therefore the transverse mode profile F is dependent only on x and y.

The element of the free space wavevector k_0 which is aligned along the z-axis is defined as the propagation constant, β. In the scalar approximation of equation 2.3 each spa-

tial mode distribution $F(x, y)$ corresponds to a single guided mode, with propagation constant β. However the electric field can have two orthogonal polarisation directions, which are degenerate in β in this approximation. For non-circular fibres a fully vector model shows that the polarization modes become non-degenerate. The β value therefore serves as a useful quantity to define mode propagation along the fibre.

As stated earlier, solutions to Maxwell's equations result in a discrete number of guided core modes, given as a result of the boundary conditions defined by the geometry of the fibre. Therefore only a limited number of values of β are valid within the fibre core, each one representing a guided mode. The refractive indices of the core and cladding of the fibre, as well as the wavelength of the propagating light, define the range within which guided modes are available, given by

$$n_{cl}k_0 \leq \beta \leq n_{co}k_0, \tag{2.4}$$

where k_0 is the free space wavevector, defined as

$$k_0 = \frac{2\pi}{\lambda_0} = \frac{\omega}{c}. \tag{2.5}$$

The lower value given in the equality in equation 2.4, $n_{cl}k_0$, is often referred to as the modal *cut-off*, as β values which fall below this value are no longer guided in the core, and instead form part of a continuum of modes in the cladding which are quickly attenuated from the fibre.

A fibre with only a single propagation constant value available within the range given in equation 2.4 is described as being *single mode*, while one with several available propagation constants is *multi-mode*. Of multiple guided modes, the one with the highest value of β is defined as the *fundamental mode*, characterised as having a Gaussian distribution in a circular fibre, with the lower β values being referred to as the *higher-order modes*, and having more complex spatial distributions in x and y.

Each mode experiences an effective refractive index, n_{eff}, depending upon the β value of that particular mode, through the relationship

$$\beta = n_{eff}(\omega)k_0 = \frac{\omega n_{eff}(\omega)}{c}. \tag{2.6}$$

Equations 2.4 and 2.6 therefore show that since each value of β experiences a different effective refractive index, it also experiences a slightly different *phase velocity*, v_{ph}. This results in a variation in propagation velocity for different guided modes, and therefore acts as a source of modal dispersion.

In 1971, D. Gloge developed method for calculating the number and transverse distributions of all the guided modes inside an optical fibre with "weak" guidance (i.e. where $\triangle$ in equation 2.1 is $\ll 1$) [26]. This calculation uses the two parameters

$$U = a\sqrt{k_0^2 n_{co}^2 - \beta^2} \tag{2.7}$$

and

$$W = a\sqrt{\beta^2 - k_0^2 n_{cl}^2} \tag{2.8}$$

where a is the fibre core radius. The U parameter represents the field behaviour inside the core of the fibre transverse to the direction of propagation, while the W parameter represents the transverse field behaviour in the cladding. These values can combined to define a further parameter

$$V^2 = U^2 + W^2. \tag{2.9}$$

Equations 2.7 and 2.8 can be solved to give the valid values of β for each guided core mode at a given k_0. These can be calculated using

$$U\frac{J_{l-1}(U)}{J_l(U)} = -W\frac{K_{l-1}(W)}{K_l(W)}, \tag{2.10}$$

and applying the relevant boundary conditions for the interface between the core and the cladding. Here J is a Bessel function of the first kind of order l and K is a modified Bessel function of the order l. The zero values of the J_l Bessel function define the points at which a mode reaches the cut-off in the fibre, where V is consequently equal to the cladding parameter W in equation 2.9, and the mode is no longer guided in the

core.

Equation 2.9 can then be expressed in terms of the fibre core radius a and the core and cladding refractive indices n_{co} and n_{cl} to give the *V Parameter*, which defines the number of guided modes for a given set of fibre parameters and at a certain wavelength,

$$V = \frac{2\pi}{\lambda} a \sqrt{n_{co}^2 - n_{cl}^2}. \tag{2.11}$$

In a PCF, the core radius is sometimes defined as being approximately $\sim 0.625\Lambda$ [27]. A fibre therefore can only guide a single, fundamental, core mode at a given wavelength if the V parameter is less than 2.405 [28], which corresponds to the first zero value of the J_0 Bessel function.

The V parameter can be used estimate the total number of guided spatial modes in a multi-mode fibre, through the relationship

$$N \approx \frac{V^2}{4} \tag{2.12}$$

As mentioned earlier, the number of guided spatial modes defined by equation 2.12 can be doubled to estimate the number of guided polarisation modes.

In addition to the concept of guided core modes described thus far, optical fibres exhibit a further two broad mode types; *cladding modes* and *leaky modes*. Both of these mode types do not typically guide along a long length of fibre, often being quickly attenuated out. Cladding modes are formed across the larger waveguide of the silica glass, limited by the outer edge of the fibre cladding and the surrounding environment or polymer coating. Cladding modes often leak out into the coating or are coupled out of the fibre by surface imperfections or bends, and are quickly lost. Leaky modes arise from core modes don't decay exponentially into the cladding, and instead display a degree of intensity overlap. The mode then suffers attenuation as light is coupled out into the surrounding region. This latter type of mode is present in hollow core fibres which guide light using only one bandgap cladding layer, and are described later in this Chapter and are relevant to research related in Chapters 7 and 8.

2.4.1 Birefringence in Optical Fibres

Birefringence can be introduced into the structure of an optical fibre by building defects along one axis of symmetry across the core. This can have several positive effects, including maintaining the polarisation of light propagating along the fibre, as well as a variation in the dispersion, and therefore potentially any nonlinear behaviour, along the defect axis compared with that of the orthogonal axis.

In conventional all-glass fibres, birefringence is introduced in several ways, such as using elliptical cores, or through the addition of rods on either side of the core that are made of a different glass, which introduces stress into the fibre along one axis, and therefore birefringence. Such fibres are sometimes referred to as "bow tie" or "panda" fibres [29].

In PCF, birefringence can be easily introduced through the alteration of holes on opposite sides of the core, either through over-inflation or under-inflation during fabrication, as was briefly outlined earlier in Section 1.4.1. These holes are sometimes referred to as the *Polarisation Maintaining* or *PM* holes, to distinguish them from the rest of the PCF cladding structure. Examples of such birefringent PCF are shown in Figure 2.3.

As a result of the defects, the air-filling fractions along these two axes are now slightly different, resulting in a difference in the effective refractive index, and hence propagation constant β, for the orthogonal polarisation modes aligned to each axis. Consequently they also experience different phase and group velocities, giving rise to the common definition for the two axes; the one with the lower refractive index being the *fast axis*, and one with the higher refractive index being the *slow axis*. The fast and slow axes are marked for each fibre in Figure 2.3.

The strength of the birefringence, B_m, in an optical fibre can be quantified through the relation

$$B_m = \frac{\beta_{fast} - \beta_{slow}}{k_0} = n_{fast} - n_{slow} \tag{2.13}$$

where β_{fast} and β_{slow} are the propagation constants experienced by light on the two orthogonal axes. For a typical birefringent "panda" fibre used in industry, a B_m value of the order of 10^{-4} is sufficient to maintain the polarisation of light propagating along either of the two axes [34].

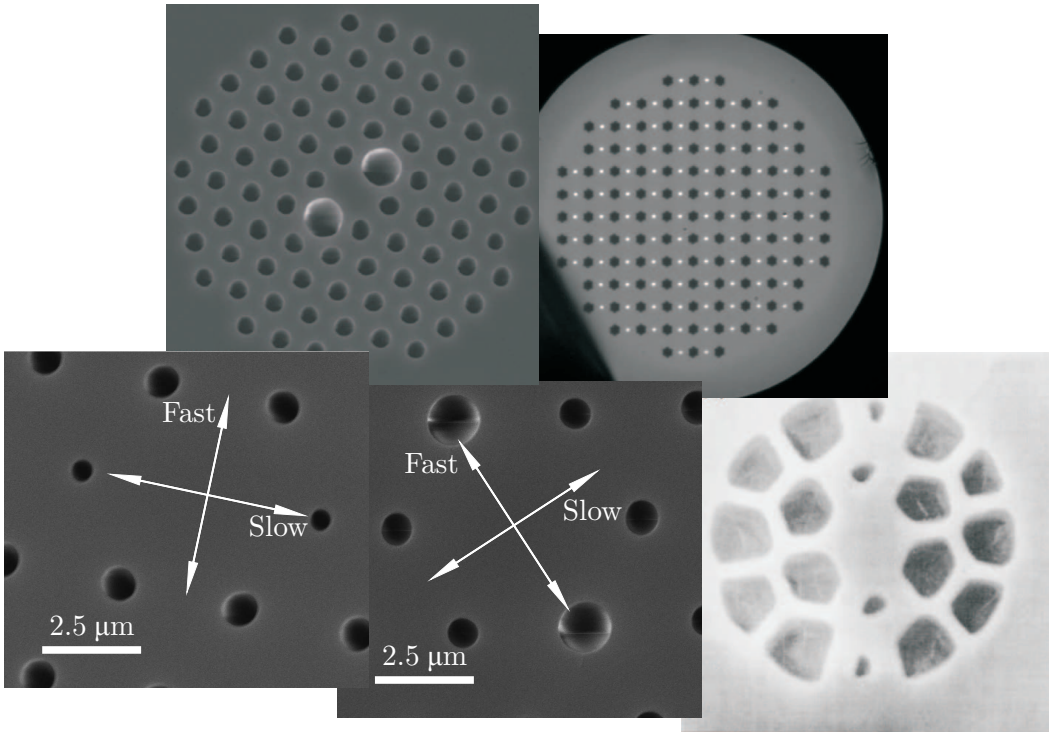

Figure 2.3: Some examples of birefringent PCF fibres. Clockwise from top right; a microscope image of a 98-core birefringent PCF [30], scanning electron microscope image of an early birefringent PCF [31], two scanning electron microscope images of birefringent four wave mixing fibres [32], and a highly birefringent PCF [33].

If linearly polarised light is aligned and launched along the fast or slow axis of a strongly birefringent fibre, it is guided with the linear polarisation preserved and aligned to that axis. This is as a result of any imperfections or bends in the fibre, which would usually lead to phase changes, being overcome by the strong birefringence. However, if the linear polarisation is initially aligned off of the fast or slow axes, then the polarisation vector elements aligned with the fast and slow axes experience different propagation constants, and therefore different phase velocities. This causes the polarisation elements to undergo a continuous relative phase shift during propagation, just as in commercial wave plates. The evolution of the polarisation as the light propagates goes first from linear to circular, then from circular to a linear that has been rotated through 90°, then back to circular, before finally returning to a linear polarisation with the same initial alignment. The length of fibre over which this cycle occurs is can be expressed as a *beat length* L_{BL}, defined as

$$L_{BL} = \frac{2\pi}{\beta_{fast} - \beta_{slow}} = \frac{\lambda}{B_m} \tag{2.14}$$

In a non-birefringent fibre, plane polarised light experiences the same phase changes for different vector elements during propagation as in the birefringent fibre. However, this is as a result of the physical layout of the fibre, external pressure being placed upon the fibre, or imperfections from defects in the glass, rather than being due to the microstructure of the fibre. The bends in, or pressure on, the fibre result in localised random variations in the refractive index, which then causes random changes in the phase of the propagating light. These changes are therefore not consistent, and any evolution of the polarisation during propagation is inherently unpredictable. As mentioned earlier, the deliberate defects in the microstructure of a birefringent fibre act to override these effects, maintaining the polarisation of the field along the full fibre length.

The size of the under or over-inflated holes in a birefringent PCF can be as much as 50%, although for effective polarisation maintaining behaviour only 10% is necessary [35, 36]. Overly large defects can even become a disadvantage, since the resulting guided modal distribution can become so distorted that it is difficult to efficiently couple a circular beam into the fibre modes, resulting in higher losses for that system [37].

2.5 Bandgap Guidance and the ARROW Model

In addition to the guiding of modes in fibres with a high index core, a further type of guidance can be harnessed through the formation of *Photonic Bandgaps*. These arise when a range of certain wavelengths and β values cannot propagate in the periodic structure of the fibre cladding, leaving them effectively confined to the core. One model used to describe this behaviour is known as *Anti-Resonant Reflecting Optical Waveguiding* (ARROW), and was first outlined in 1986 [38], although the application of the ARROW model to describe bandgap guidance in photonic crystal fibres was not considered until 2002 [39].

The utilisation of this effect has led to the fabrication of fibres with a core which does not need to be of a higher index than the surrounding cladding. These fibres are known as *Hollow Core Photonic Crystal Fibres* (HCPCFs) (briefly introduced earlier in

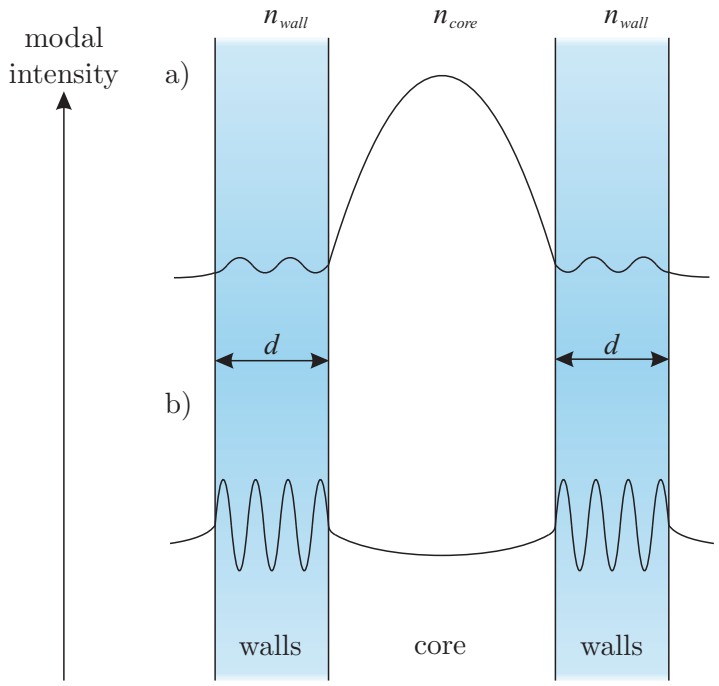

Figure 2.4: A one-dimensional representation of two anti-resonant waveguides on either side of a hollow core. Part a) shows a core mode off-resonance, failing to couple with the wall waveguide mode, and therefore confining light to the core region, and b) shows a core mode on-resonance, coupling with the wall waveguide mode, and attenuating the core mode.

Section 1.2), and are characterised by a core which consists of a central hole surrounded by a periodic silica cladding structure.

Light is launched into the core in a direction perpendicular with respect to the plane of periodicity of the cladding microstructure. Outside of the wavelength range of a given bandgap, a core mode is able to resonate with, and so couple to, the modes of the periodic cladding with the same β value. The periodic cladding microstructure effectively behaves as a series of high index waveguides, each surrounded by air. This coupling between the light in the core and cladding waveguides quickly attenuates the mode from the core as it leaks out, so that it fails to guide. However, in the case where the wavelength of the core mode is within the bandgap, there is no corresponding cladding microstructure mode with the same value of β for it to resonate and couple to, and therefore the mode is confined to the core. A one-dimensional representation of this effect is shown in Figure 2.4, where a core region is surrounded by a silica cladding wall structure on either side, each with a thickness d.

Figure 2.4 demonstrates how the walls surrounding the hollow core can be considered to be two silica waveguides surrounded by air, and as with a high index waveguide which is surrounded by a low index region, they have a number of guided modes, just as in a solid core fibre as described earlier in Section 2.4. The location of the guided modes within the waveguide for any given wavelength is therefore defined by the size, refractive index, and general shape of the waveguide [40, 41, 42]. In a HCPCF, the core is surrounded by several layers of these waveguides, with the overall anti-resonant effect being multiplied to result in a core mode which is fully confined and guided.

As previously stated, the wavelength location of these bandgaps is determined by the thickness of the wall waveguide, and follows the relationship [39]

$$\lambda_{resonant} = \frac{2n_{core}d}{m}\left[(n_{wall}/n_{core})^2 - 1\right]^{1/2}, \tag{2.15}$$

where d is the wall thickness, m is an integer for the resonant band number, and n_{core} and n_{wall} are the refractive indices for the core and wall respectively. This relationship assumes that the core diameter is far larger than the guided wavelength ($\lambda/a \ll 1$), and arises from considering each individual wall structure as a slab waveguide. Each "slab" has an associated V parameter, and forms a resonance for values of $V = m\pi/2$. Equating this with equation 2.11 and rearranging for the resonant coupling wavelength $\lambda_{resonant}$ produces equation 2.15.

Figure 2.5 is a representation showing the resulting resonant coupling wavelengths, where light is coupled out of the core. The values have been calculated using equation 2.15 for a one-dimensional anti-resonant waveguide with 3 μm thick silica walls, which are shown in red. An example of the resulting transmission bands along the core of the fibre is shown in blue. There are a clear series of anti-resonant regions, getting narrower for shorter wavelengths, where coupling from an adjacent core mode is not possible. Each red line represents the cut off of a mode in the waveguide (described earlier in Section 2.4), until above approximately 4 μm the waveguide guides only a single mode. The modal cut-off of the wall results in the observed steep edges for each bandgap.

However, losses in HCPCFs are not completely removed for the guided bands, as scattering off the imperfect silica glass surface of the core walls results in some degree of loss, especially for higher order modes. This is discussed further in Section 2.7.2.

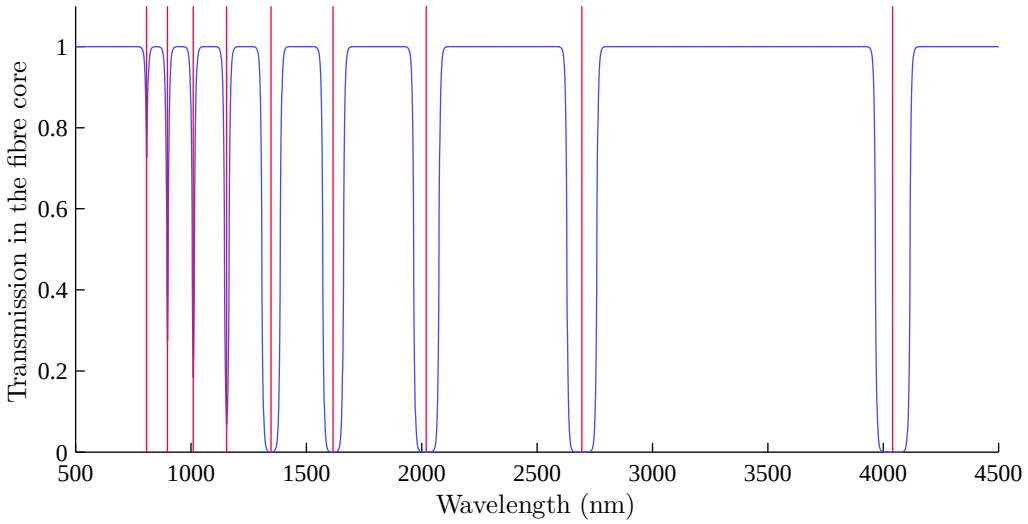

Figure 2.5: Calculated resonant wavelengths (shown in red) for an bandgap waveguide with 3 μm thick walls, and an example of the resulting transmission along the core of the fibre (shown in blue).

As introduced briefly earlier in Section 1.2, a new class of HCPCF has been developed, called *Negative-Curvature Fibres* (NCFs), or sometimes *Anti-Resonant Fibres* (ARFs). This type of fibre is characterised by containing only a single layer of anti-resonant waveguides around the core, rather than an array. This results in a core mode which does not decay exponentially into the cladding, as in conventional HCPCFs. They can therefore be described as not possessing "true" guided modes, despite still being confined by the anti-resonant effect of the single layer of silica walls. As a result, the core modes in these types of fibre are sometimes referred to as being leaky modes, although the degree of loss as a result of this can be engineered to be negligibly small.

For example, engineering the shape of the surrounding silica walls to minimise the resulting overlap with the core mode acts to reduce the loss in NCFs. As their name suggests, NCFs possess a negative curvature to their core walls, which acts to minimise the mode overlap and modify the guidance properties of the wall waveguides to reduce the coupling effect. The effect of the core shape on the core mode overlap is shown in Figure 2.6, where three NCF-like fibres, with a single layer of bandgap guidance structure, are shown. Each of the three different cores has a different shape, either a positive curvature, zero curvature, or a negative curvature, and the mode overlaps are compared. The negative curvature fibre clearly has the smallest overlap, and therefore further reduces coupling between the core and the waveguide of the walls. This effect of minimising the overlap between the core walls and the fundamental guided mode is

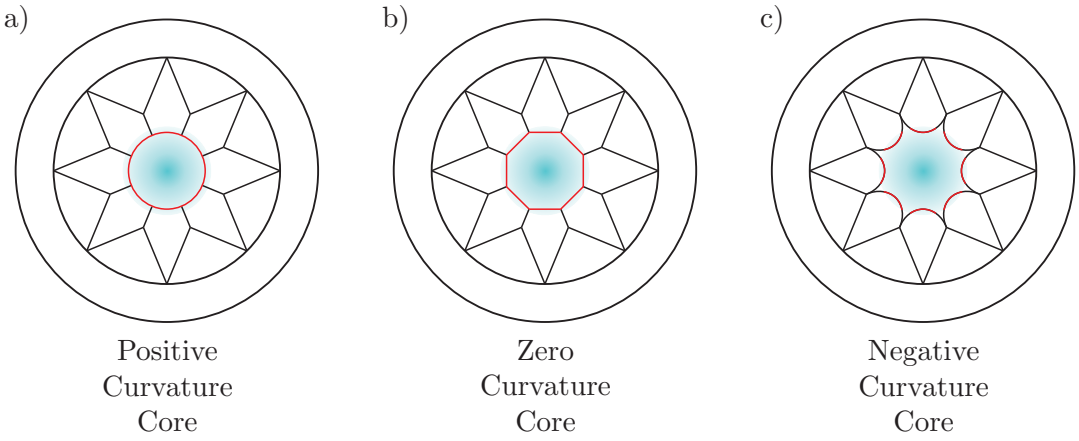

Figure 2.6: A comparison of three HCPCF structures with values of the core wall curvature that are a) positive, b) zero, and c) negative. The overlap between the silica walls and the core mode is shown in red, with the negative curvature demonstrated to possess the smallest overlap.

more effective with increasing degrees of negative curvature.

When operating at longer wavelengths in the mid-IR, where further losses arise from the high material absorption of silica (discussed later in Section 2.7), a small mode overlap with the fibre glass is even more desirable, as it can counter the effect of material absorption.

The first explicit experimental example of a negative curvature fibre was reported in 2011 by Pryamikov et al [15], who used a series of capillaries inside a larger capillary to form a negative curvature core. This 36 μm diameter core fibre allowed for guidance of approximately 60% out to just below 4 μm. Later work in 2011 used chalcogenide glass with a similar structure to achieve guidance out to 10.6 μm [43].

This structure was modified in 2012 for work published by the University of Bath [16], which achieved a minimum loss of 34 dBkm^{-1} at 3.05 μm and was able to guide light out to 4 μm, where the loss in solid silica is several orders of magnitude higher [44]. As with many fibres which do not possess several rings of cladding structure, bend losses were observed to become significant for turns with a diameter of less than 40 cm. This is due to the comparatively large connecting *nodes*, where the capillaries surrounding the walls join, which experience an increase in the mode overlap as the mode shifts to

the outside of the bend. This results in light coupling to the node and surrounding silica glass, and then being lost from the fibre. The general mechanism behind bend losses is discussed in Section 2.7.1. It is a version of this fibre that was used in the research presented later in Chapter 7, where it is described in greater detail.

Even more recently, researchers at the University of Bath have developed a negative curvature fibre with a higher resistance to bend losses, while preserving the low-loss guided bands [17]. This allowed it to be bent with a radius of as little as 2.5 cm and suffer only moderate additional losses. The fibre used a similar structure to that demonstrated by Pryamikov et al, but now with the internal capillaries fully separated, creating a "free" core boundary with no connecting nodes. This approach limits the coupling of light from the guided mode as it shifts to the outside of a bend, by further minimising the modal overlap and removing the large nodes that were the source of bend losses in earlier fibres [16, 15]. This fibre is used for the research described later in Chapter 8, where the structure and characteristics are covered in greater detail. Subsequent theoretical work has demonstrated that even lower bend losses in this type of fibre are possible [45], and can be achieved through the addition of smaller capillaries nested inside the existing structure to multiply the effect, theoretically reducing losses to under 0.1 dBm^{-1} between 3 μm and 3.5 μm.

2.6 Chromatic Dispersion

The effective refractive index experienced by light travelling in a medium such as silica is dependent on the frequency, ω, of that light. For a pulse made up of many different frequencies, the velocity experienced by each frequency varies, causing the pulse to spread out in time as some frequencies travel faster than others. This effect is known as *chromatic dispersion*, and is a direct result of the frequency dependence of the refractive index, $n(\omega)$.

To understand the behaviour of a pulse travelling along a silica optical fibre, the propagation constant β can be expanded into a Taylor series about a central frequency ω_0, giving

$$\beta(\omega) = n(\omega)\frac{\omega}{c} = \beta_0 + \beta_1(\omega - \omega_0) + \frac{1}{2}\beta_2(\omega - \omega_0)^2 + \frac{1}{6}\beta_3(\omega - \omega_0)^3 + ... \qquad (2.16)$$

where the differential of the propagation constant

$$\beta_m = \left(\frac{d^m \beta}{d\omega^m} \right)_{\omega=\omega_0} \quad m = 0, 1, 2, 3, ... \tag{2.17}$$

The first two differential coefficients, β_1 and β_2, are both related to the refractive index of the material through the relations

$$\beta_1 = \frac{1}{v_g} = \frac{n_g}{c} = \frac{1}{c} \left(n + \omega \frac{dn}{d\omega} \right) \tag{2.18}$$

$$\beta_2 = \frac{1}{c} \left(2\frac{dn}{d\omega} + \omega \frac{d^2 n}{d\omega^2} \right) \tag{2.19}$$

where v_g and n_g are the group velocity and the group index respectively.

The refractive index of a material, such as fused silica, is a fundamental result of the absorption resonances of the material structure at different frequencies, and can be estimated using the *Sellmeier equation* [46], given as

$$n^2(\omega) = 1 + \sum_{i=1}^{m} \frac{B_i \omega_i^2}{\omega_i^2 - \omega^2} \tag{2.20}$$

where the B_i coefficients are the strengths of the resonances at frequencies ω_i. This equation is empirically derived, with the sets of coefficients for different materials being determined experimentally. The values of these coefficients can then be used to plot an expected refractive index curve [47], as shown in Figure 2.7 as a function of wavelength.

Using the data from this refractive index curve along with the relation given in equation 2.18, the group index for silica can also be calculated, and is also shown in Figure 2.7. This means that for the envelope of a pulse travelling with a group velocity, v_g, equal to $^c/_{n_g}$, the different frequencies within that pulse will disperse as a result of β_2. This causes the pulse to broaden as the group velocities are different for each of the different frequency components of the pulse. This is known as *Group Velocity Dispersion*, and is conventionally defined either by $\beta_2(\omega)$, in $pskm^{-1}nm^{-1}$, or by D, defined as

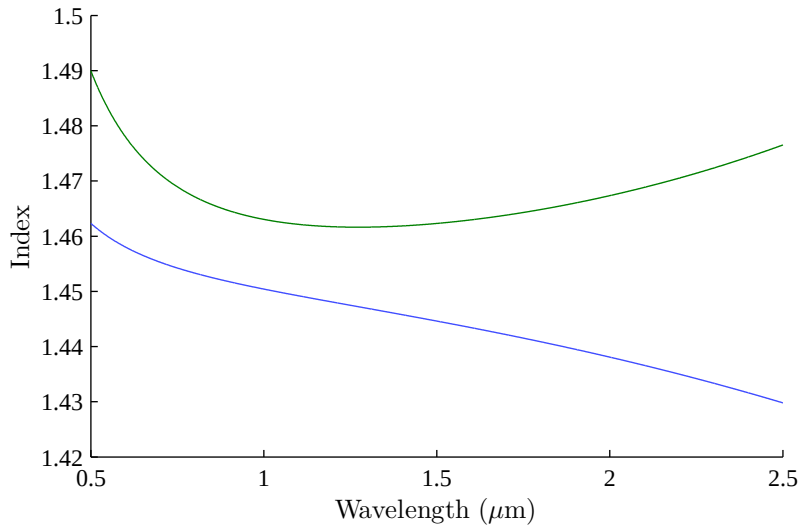

Figure 2.7: Plotted refractive index (blue) and group index (green) curves for pure silica.

$$D = \frac{d\beta_1}{d\lambda} = -\frac{2\pi c}{\lambda^2}\beta_2 = -\frac{\lambda}{c}\frac{d^2 n}{d\lambda^2}. \tag{2.21}$$

The resulting β_2 and D curves for fused silica are shown in Figure 2.8.

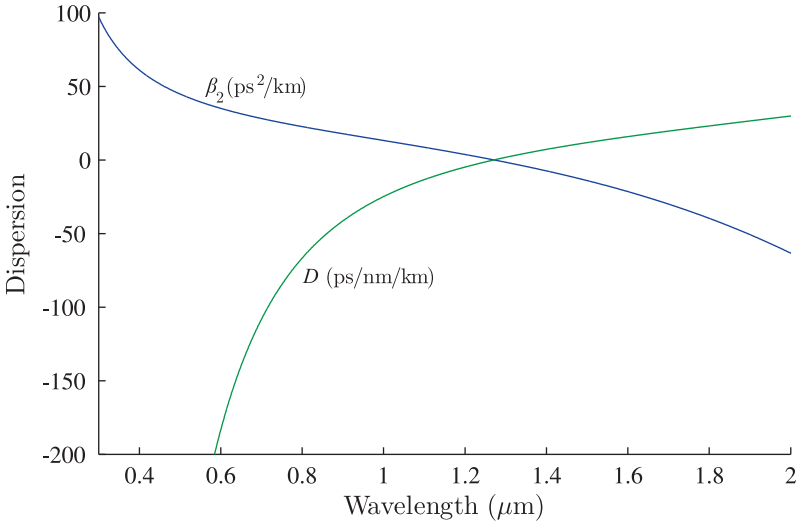

Figure 2.8: Plotted β_2 (blue) and D (green) curves for pure silica.

One notable element is that both β_2 and D curves pass through zero at the same wavelength, about 1.27 μm for fused silica glass [21]. This is known as the *Zero Dispersion*

Wavelength (ZDW), denoted as λ_{ZDW}, and arises from the point of inflection in the refractive index curve in Figure 2.7. The wavelength region where D is positive is conventionally referred to as the *anomalous* dispersion regime, while the region where it has a negative value is referred to as the *normal* dispersion regime.

In the normal dispersion regime, the lower frequencies (longer wavelengths) travel faster than higher frequencies (shorter wavelengths), causing a pulse to spread out with the comparatively redder wavelengths at the front of the pulse.

The behaviour is reversed for the anomalous dispersion regime, where the higher frequencies (shorter wavelengths) travel faster than the lower frequencies (longer wavelengths), causing the pulse to spread out with the bluer wavelengths at the front of the pulse.

Light travelling close to the zero dispersion wavelength does not experience either regime significantly. However, it is not completely free of dispersion, and does still experience some as a result of the β_3 term in equation 2.16 [46]

2.6.1 Waveguide Dispersion and Dispersion Engineering

As Chapter 3 describes, much of the nonlinear behaviour in optical fibres is driven or heavily affected by the dispersion profile of the fibre, such as the location of the ZDW which separates normal from anomalous dispersive behaviour. In conventional optical fibres, the size of the refractive index difference between the core and cladding, defined earlier in equation 2.1, can be chosen to alter the wave-guiding of the fibre, and therefore engineer the resulting dispersive behaviour. This is most often achieved through the doping of the core or the cladding to alter the refractive index [48].

This effect from the physical fibre structure on the overall dispersion of the fibre is referred to as *Waveguide Dispersion*, and acts separately and in addition to chromatic dispersion. This is most simply defined as the effect of the waveguide geometry itself on the propagating wave. In conventional optical fibres, the step in index between the core and the cladding is relatively small. This means that a propagating mode is not entirely confined to the core, with an edge element decaying into the cladding of the fibre. This is minimised for shorter wavelengths, where the mode remains predominantly in the core of the fibre and consequently experiences an effective index n_{eff} which is close to that of the core. However, longer wavelengths are more spread out, experiencing an n_{eff} which

is closer to that of the cladding. This wavelength dependence therefore has an effect on the dispersion of the fibre through β_2, resulting in shorter wavelengths experiencing anomalous dispersive behaviour, and longer wavelengths experiencing normal dispersive behaviour, contrary to chromatic dispersion.

However, the contribution from waveguide dispersion is relatively small in conventional optical fibres, due to the typically small index differences between the core and the cladding. This nonetheless allows for small amounts of dispersion engineering in conventional fibres, shifting λ_{ZDW} along as far as 1.55 μm, where commercial telecommunications fibres operate and silica has a minimum loss [49]. Such fibres are referred to as *Dispersion Shifted* fibres.

However, PCFs have the advantage of being able to alter the size of the refractive index difference, Δ, to a far greater degree than conventional all-glass fibres can, due to the high air-filling fraction of the cladding. By altering the size d and separation Λ of the holes in the cladding, the refractive index of the cladding can be significantly lowered, and the step size Δ can be customised to a greater degree.

This can then have the effect of significantly altering the effective index experienced by a mode compared to that of bulk silica, which can in turn have a dramatic effect on β_2. This shifts λ_{ZDW} to much shorter wavelengths and can even introduce a second λ_{ZDW} at longer wavelengths. Predicting the effect a specific structure will have on the dispersive behaviour of a fibre is potentially complex, but thanks to empirical approaches such as that demonstrated by Saitoh and Koshiba [50], the required structure can now be designed relatively simply. With careful design, a PCF structure can even be fabricated which displays a dispersion profile which remains in the normal regime over a wide wavelength range [51].

The wide range of potential custom dispersion curves makes PCF ideal for dispersion engineering, allowing for careful control of the dispersive behaviour of a fibre. This can then allow for the customisation of certain nonlinear effects, to generate behaviour which would be unobtainable in conventional optical fibres. The larger Δ value in PCFs allows for higher core intensities as the modal confinement is stronger, boosting the strength of the nonlinearity. Waveguide designs can be chosen which place the ZDW in the most appropriate spectral location for effects such as broad-band supercontinuum and the phase-matching for four-wave mixing. Both broad-band supercontinuum generation and four-wave mixing are described in detail in Chapter 3.

2.7 Fibre Loss

A major factor in the fabrication and use of all types of optical fibres is loss, usually measured using a logarithmic scale with units of dBkm^{-1} or dBm^{-1}. This then affects the power P propagating in the fibre after a distance L as

$$P = P_0 \exp^{-\alpha L} \tag{2.22}$$

where P_0 is the initial power and α is the loss per unit length, or *attenuation constant*. Most often the loss is defined in units of dBm^{-1}, and the relation

$$\alpha_{\mathrm{dB}} = -\frac{10}{L} \log\left(\frac{P}{P_0}\right) = 4.343\ \alpha \tag{2.23}$$

can be used to convert α to α_{dB}.

The loss in silica glass can be as a result of a variety of different effects, and is strongly wavelength dependent, as shown in Figure 2.9. As described earlier in Section 1.2, impure silica glass exhibits high losses across the whole spectrum due to a population of contaminants or impurities in the glass structure. For example, a common contaminant is the presence of oxygen-hydrogen (OH) groups, which introduce noticeable losses at 1380 nm, where the inherent losses of the glass are relatively low. This absorption around 1380 nm is shown as a green dotted curve in Figure 2.9. The pure silica glass suffers from several fundamental loss mechanisms over the transparency window from 0.2 μm to 2.5 μm, the first of which is *Rayleigh Scattering*, which becomes relevant at the short ultraviolet end of the window. This is shown as a blue-dashed curve in Figure 2.9.

Rayleigh Scattering arises from tiny density fluctuations in the amorphous glass, frozen into the structure during fabrication, which act to scatter light off the resulting small local shifts in the refractive index [21], scaling with wavelength as λ^{-4}. This acts as a fundamental limit for wavelengths up to about 1.5 μm for low-loss fibres.

At wavelengths longer than 1.5 μm, *Material Absorption* takes over as vibrational resonances in the glass start to become increasingly relevant, raising the fundamental glass loss until it becomes insurmountable beyond about 2.5 μm. This is shown as

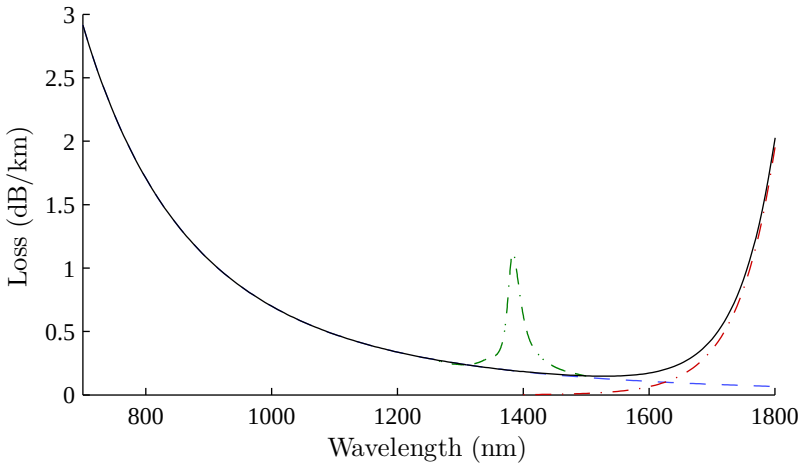

Figure 2.9: Loss spectrum for bulk silica, showing losses from Rayleigh Scatering (blue dashes), material absorption (red dotted-dashes), the absorption peak from the oxygen-hydrogen (OH) group impurity (dotted green), and the resulting inherent loss of the pure silica glass (black).

a red dotted-dashed curve in Figure 2.9. The intervening window between these two mechanisms, around 1.5 μm, is where the loss is at its lowest, and telecommunications fibres largely operate. The overall inherent loss of the silica glass, without impurities, is shown as a black curve in Figure 2.9.

However, even when the most care is taken to fabricate silica glass with the fewest impurities, some still present a problem. The most common impurity in modern optical fibres is the presence of OH groups arising from water molecules present during fabrication and later during storage. These groups have a fundamental vibrational absorption at 2.7 μm, which in turn has overtones in the silica low loss region around 1.5 μm, most notably at 1.38 μm [52]. The loss due to OH groups can be limited if sufficient steps are taken during the fabrication process to keep the local environment "dry", or free of water molecules and moisture in the air.

Additional losses from chemical groups in the glass can also be introduced over time as a result of high power laser exposure. Multiple photon absorptions by strained bonds in the glass can cause them to break, resulting in higher losses over regions of the spectrum where the broken bond has a resonance. These broken bonds can also then become the site of new chemical impurities, such as OH groups. This effect is known as *Photo-Darkening*, and is the subject of the theory described later in Chapter 4, and the research presented in Chapter 5.

2.7.1 Bend Losses

Losses can also come from the physical treatment of the fibre, such as bending. When a fibre is distorted into a tight bend with a sufficiently small radius of curvature, the guided mode can shift towards the outside edge of the core, increasing the overlap with the cladding modes. This can then be enough to begin coupling light out of the guided core modes, resulting in a higher loss over the length of the bend [53, 54]. This effect is more pronounced for longer wavelengths, where the fundamental mode is broader and overlaps more with the cladding of the fibre. Many of the higher order modes also suffer from bend losses more acutely, since the points of peak intensity for the mode are not found in the centre of the core of the fibre. This means that intensity at the nearest cladding boundary is then higher and the mdoe extends further into the cladding, worsening the loss effect. This can be harnessed practically to effectively "strip out" higher order modes by bending deliberately, leaving the fundamental mode behind as it is the mode least affected.

Bend losses can be positively harnessed to strip light out of higher order modes which, having a lower value for the propagation constant β, are more sensitive to small changes in the refractive index contrast than the fundamental mode. In addition, the spatial distribution of higher order modes generally places higher intensities closer to the core boundary, boosting the loss from that mode as the fibre is bent.

2.7.2 Loss in Hollow Core Fibres

When first developed, hollow core fibres were theorised to be free of any of the mechanisms which limit the losses in solid glass fibre. This was owing to the fact that the guided wave was propagating through air, and so was not subject to the same degree of Rayleigh Scattering or the vibrational absorptions found in silica glass. It was believed that the lowest achievable loss in hollow fibres could therefore be even lower than that achieved in solid core fibre.

However, as reported in two papers by Roberts et al. in 2005 [55, 56], the loss in hollow optical fibres would still be limited. This is due to a scattering effect arising from the roughness of the air-glass interface. The uneven surface at the interface causes the light in the guided core mode to be coupled out into the cladding, limiting the loss to a minimum of about 1.2 dBkm^{-1} [55], slightly higher than the minimum already

achieved in solid core fibre.

2.8 Gain in Optical Fibres and Other Media

Just as loss is the process causing light to decrease in intensity at a particular wavelength with propagation, gain is the process causing light to increase in intensity at a particular wavelength with propagation. The amount by which the intensity at a particular wavelength is increased as it propagates a given length is defined by the quantity called the *gain*. Gain is present in a fibre, or any other media, if a mechanism is acting whereby this intensity increase with length can occur. This is fundamental in all types of laser systems, where light is amplified in a *gain medium* at the chosen lasing wavelength.

In solid-core optical fibres, the silica of the core is often doped with a high-gain material, such as ytterbium or neodymium, to introduce a strong optical amplification. This is the most common basis behind commercial fibre laser systems [57], although nonlinear effects such as those described in the next Chapter can also be harnessed to serve as a source of gain, for instance in Optical Parametric Amplifiers (OPAs) and Optical Parametric Oscillators (OPOs) [58, 59].

This discussion will describe gain in the context of gas discharge laser systems, since this is directly relevant to the research presented later in Chapters 7 and 8.

Like loss, gain can be expressed in terms of the power at a particular wavelength propagating along a fibre in the same manner as equation 2.22,

$$P_x = P_0 \exp^{gL} \tag{2.24}$$

where the gain g is measured in m^{-1}, and the distance L is in meters. As with equation 2.23, this value can be converted into dBm^{-1} using the factor of 4.343.

To understand the behaviour of the gain in laser systems, it is necessary to consider the relative changes of the populations of the various energy levels in the gain medium. For a laser to operate, the gain medium requires a population inversion between the upper and lower excited states. In the context of a gas laser, this means that while the

atoms in that gas are largely unexcited and in their ground state, the small percentage which has been excited has a greater number of atoms in the upper lasing level than the number of atoms in the lower lasing level.

To achieve this population inversion, it is necessary to initially excite the atoms through pumping, either using an external light source or, in the case of gas discharge lasers, through an applied current density.

Initially, as the gain medium is first pumped, an electron of an atom in the gain medium is excited to the upper state at a given rate. It then spontaneously decays at a given rate defined by the average lifetime of that state, emitting a photon with an energy equal to the energy difference between the two states, before eventually reaching the ground state again. The gain is then solely defined by the spontaneous behaviour of the upper state and the excitation rate from the pump source. The larger the population inversion, the higher the gain, which is referred to in this regime as the *small-signal gain.*

However, the gain is adversely affected in the presence of a "seed" source, which acts to depopulate the upper state through stimulated emissions. The average lifetime of the upper state is then shortened as a result of these stimulated emissions, reducing the size of the population inversion and likewise resulting in the gain being reduced below the initial small-signal gain value. This is called *gain saturation.*

This seed source in fact originates from the population of photons initially emitted through spontaneous emission, and is potentially detrimental in terms of the gain. As the power of the pump source is increased, more atoms are excited to the upper state and more are spontaneously emitted, contributing to the overall output signal. Stimulated emissions then become increasingly important, as more and more photons are emitted and the population inversion is steadily reduced. When the pump source is relatively weak and relatively few photons are spontaneously emitted, this contribution to the population inversion from stimulated emissions is small enough to be negligible, leading to the aforementioned small-signal gain.

The relationship between the small-signal gain and the saturated gain for a given seed energy can be defined as [60]

$$g_{sat}(P,\lambda) = \frac{g_{sm}}{1 + (P_{seed}/P_{thr})}, \tag{2.25}$$

where $g_{sat}(P, \lambda)$ is the saturated gain for a given emission wavelength at a given seed power, g_{sm} is the small-signal gain, P_{seed} is the power of the seed (or the power at the emission wavelength), and P_{thr} is the seed threshold power for saturation. This threshold for the gain to saturate is defined as the intensity at which the population inversion is halved from its initial small-signal value. As is clear from equation 2.25, increasing the power of the emission wavelength above the threshold only results in an ever decreasing output gain.

Chapter 3

Nonlinearity in PCF

3.1 Introduction

This Chapter concerns optical nonlinearities and their role in optical fibres. As discussed earlier in Chapter 2, the ability to enhance the strength of nonlinear processes through tighter modal confinement is an advantage of PCF over conventional fibres. This has allowed for a wide range of devices to be developed which rely on nonlinear wavelength conversion processes to produce a desired output. However, the presence of nonlinearity is not always desired, and can act as an unwanted "leeching" effect in some systems. When this is the case, careful design of the PCF-based devices can act to minimise or screen out the unwanted processes. For example, the research presented later in Chapter 5 relies on a wide range of nonlinear processes to produce a supercontinuum, but evidence of unwanted Raman effects were also observed.

This Chapter begins by exploring the source of the nonlinear response in silica, with a description of the Kerr effect and how this gives rise to most nonlinear processes.

Some specific major processes are then described that are relevant to the research detailed in Chapter 5, including Four Wave Mixing, Raman Generation, and the behaviour when multiple effects combine in the fibre, resulting in the generation of a supercontinuum.

3.2 The Source of Nonlinearity in Fibre

As light propagates through a dielectric material, the polarisation response P of the material's bound electrons to the electric field E is linear, following the equation

$$\mathbf{P} = \varepsilon_0 \chi \mathbf{E}, \tag{3.1}$$

where ε_0 is the vacuum permittivity and χ is the material susceptibility, which varies with the electric field E. However, as the intensity of the propagating light increases to a point where the electric field is comparable to that of the inter-atomic electric field in the material, known as the Schwinger Limit [61], the response of the bound electrons becomes anharmonic, producing a material polarisation which is no longer linear with respect to the electric field. The relation can now be better defined as a Taylor expansion of the earlier linear relation, of the form

$$\mathbf{P} = \varepsilon_0(\chi^{(1)}.\mathbf{E} + \chi^{(2)}.\mathbf{EE} + \chi^{(3)}.\mathbf{EEE} + ...), \tag{3.2}$$

where $\chi^{(j)}$ is a $j+1$ rank tensor representing the j^{th} order susceptibility of the material [21, 62]. The linear response is represented by the $\chi^{(1)}$ term, and is usually the dominant, with each subsequent term reducing in strength compared with the last. The $\chi^{(2)}$ term is responsible for the strongest nonlinear responses in bulk crystals such as PPLN or BBO, while the dominant nonlinear response in PCF is driven by the $\chi^{(3)}$ term. This is because of the fact that silica glass possesses inversion symmetry, meaning that the energy required to displace of electrons in an electric field is symmetric in all directions, making the even j values of $\chi^{(j)}$ always equal to zero. However, in practice quadrupole and magnetic dipole effects in the silica glass do sometimes allow for even $\chi^{(j)}$ processes to occur, albeit very weakly [21].

Taking this into account, the nonlinear polarisation equation can be rewritten so that it only applies for silica waveguides such as PCF, and only including the most dominant $\chi^{(3)}$ term;

$$\mathbf{P} = \varepsilon_0(\chi^{(1)}.\mathbf{E} + \chi^{(3)}.\mathbf{EEE}) = \mathbf{P}_{linear} + \mathbf{P}_{nonlinear} \tag{3.3}$$

which now clearly comprises of a single linear and a single nonlinear term.

3.3 The Kerr Effect and the $\chi^{(3)}$ Nonlinearity in PCF

As light propagates through a material like silica, the refractive index can undergo an instantaneous change as a response to high optical intensities. This intensity-dependent behaviour of the refractive index is known as the *Kerr effect*.

The source of the Kerr effect can be derived from equation 3.3 and Maxwell's equations. Taking Maxwell's expression for electric flux density and the usual definition of the refractive index,

$$\mathbf{D} = \varepsilon_0 \mathbf{E} + \mathbf{P} = \varepsilon_0 n^2 \mathbf{E}, \tag{3.4}$$

and substituting in equation 3.3, results in an equation which links the susceptibility χ^j of the material to the total refractive index n. This is given as

$$n^2 = 1 + \chi^{(1)} + \chi^{(3)} E^2 \tag{3.5}$$

which can be approximated to be [63]

$$n \approx \sqrt{1 + \chi^{(1)}} + \frac{1}{2\sqrt{1 + \chi^{(1)}}} \chi^{(3)} E^2. \tag{3.6}$$

This is now in the form of a nonlinear refractive index [21, 62]

$$n = n_0 + n_2 E^2, \tag{3.7}$$

where $n_0 = \sqrt{(1 + \chi^{(1)})}$, represents the linear contribution to the refractive index. The second term is now intensity dependent, and has a nonlinear contribution to the refractive index, defined as

$$n_2 = \frac{3}{8n}\chi^{(3)}, \tag{3.8}$$

where it is assumed that the $\chi^{(3)}$ element is related to the co-polarised element of the tensor by $\frac{3}{4}\mathrm{Re}\left\{\chi^{(3)}_{xxxx}\right\}$. This assumes that field is linearly polarised, and therefore only a single element of $\chi^{(3)}_{xxxx}$ contributes to the refractive index [21, 63]. The Kerr effect is the underlying behaviour for many nonlinear responses, such as four wave mixing, modulation instability, self phase modulation and cross phase modulation. A typical value for n_2 in optical fibre at a wavelength of 1.064 μm is about 2.7×10^{-20} $\mathrm{m^2W^{-1}}$ for linearly polarised light [64, 65].

In the case of a real nonlinear waveguide, such as a PCF, the nonlinear refractive index n_2 can be incorporated into an expression to quantify the degree of nonlinearity in that waveguide, known as the *Nonlinear Coefficient* γ. This expression is

$$\gamma = \frac{n_2\omega_0}{cA_{eff}}, \tag{3.9}$$

where ω_0 is the central frequency of the propagating light, and A_{eff} is the effective mode area in the waveguide [63]. As equation 3.9 suggests, a smaller mode area will increase the degree of nonlinearity observed in a waveguide as the mode intensity consequently increases, and so engineering such waveguides to have smaller mode areas is advantageous. The mode area A_{eff} is defined as

$$A_{eff} = \frac{(\int_{\infty}^{-\infty}\int |E(x,y)|^2 dxdy)^2}{\int_{\infty}^{-\infty}\int |E(x,y)|^4 dxdy} \tag{3.10}$$

and can be minimised by increasing the difference in the core and cladding indices, and by minimising the core diameter.

The nonlinear coefficient can itself be used to define the distance over which nonlinear effects begin to become important, or the distance where the phase shift as a result of nonlinearity is equal to one radian. This is known as the *Nonlinear Length*, and is expressed as

$$L_{NL} = \frac{1}{\gamma P_0}. \tag{3.11}$$

This shows that in order to minimise the length of fibre needed for nonlinear effects to become relevant, either a high nonlinearity coefficient γ is needed, or a higher propagating power.

3.4 Four Wave Mixing

One of the most commonly used and well-understood processes that occur in nonlinear optical fibres is *Four Wave Mixing*, (FWM). This process is especially useful for devices which require wavelength conversion over relatively large spectral distances from the pump, and was investigated in optical fibres soon after the advent of low loss fibre systems [66, 67, 68, 69].

As the name suggests, four wave mixing arises from the interaction of four propagating photons or fields in the silica glass. The origins of the process are seen earlier in equation 3.3, where four separate fields are present in the nonlinear part of the equation; three electric field elements **E** and one from the material polarisation **P**.

Generally the FWM interaction can be described as being of one of two types. The first is one where three photons are annihilated to generate a fourth, an example of which is third harmonic generation, where three identical pump photons combine to produce a fourth with three times the frequency of the pump [21, 62].

However, this first type of FWM process is difficult to engineer in optical fibres, as a result of the difficulty in achieving efficient phase-matching, and is therefore less common than the second type of FWM process; where two pump fields interact to produce two other fields. This type of FWM is shown diagrammatically in Figure 3.1 for both nondegenerate and degenerate cases, where the pump photons are labelled as ω_1 and ω_2. In the nondegenerate case, where the pump waves are of two different frequencies, the effect is to generate two waves separated by the frequency difference Ω above and below the highest and lowest pump frequencies respectively. The lower generated frequency is referred to as the *Stokes* or *Idler* wave (ω_3 in Figure 3.1), and the higher generated frequency being the *Anti-Stokes* or *Signal* wave (ω_4 in Figure 3.1).

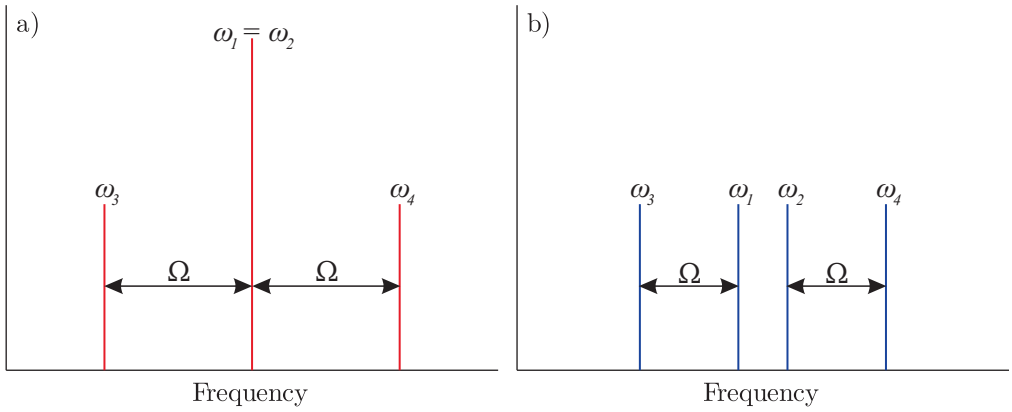

Figure 3.1: Example plots of the FWM waves, for both a) Degenerate and b) Nondegenerate cases. Pump waves are labelled as ω_1 and ω_2, while the Stokes and Anti-Stokes are labbelled as the ω_3 and ω_4 respectively.

In the degenerate case, where the two input photons are of the same pump frequency, the two resulting Anti-Stokes and Stokes photons generated are at different frequencies equally spaced above and below the pump.

The generation of the stokes and anti-stokes waves from the pump photons requires one of the corresponding electric field elements, from equation 3.3, to be found in the quantum noise of the material. This starting seed is therefore weak, and so the addition of even a very low powered seed source at either the Stokes or Anti-Stokes frequencies results in a larger amplification of the two side bands, as more Stokes or Anti-Stokes photons are generated with propagation. Without the presence of a seed source in addition to a pump, the weak seed generated from quantum noise can also be amplified using a cavity. This allows the initial weak signal to self-seed over many passes, amplifying to a point where a useful intensity of Stokes and Anti-Stokes fields can be coupled out.

3.4.1 Phase-matching

Since four wave mixing is a parametric process (or does not have an energetic interaction with the silica glass), it requires both energy and momentum to be conserved, resulting in a set of conditions referred to as *Phase-Matching*. The first of these, concerning the conservation of energy, is

$$\omega_3 + \omega_4 = \omega_1 + \omega_2 \tag{3.12}$$

where the pump frequencies ω_1 and ω_2 are equal for the degenerate case. The second phase-matching condition concerns the momentum of the interaction, and can be written as

$$\Delta k = \beta_3 + \beta_4 - \beta_1 - \beta_2 \approx 0 \tag{3.13}$$

where each of the β_x values are the propagation constants for each of the waves. As suggested by this second condition, it is a requirement that the interacting waves are as close to being in phase as possible for the interaction to be efficient and significant numbers of photons to be generated. Therefore, an ideal scenario is one where the mismatch in the phase, Δk, is effectively zero.

In a degenerate pumping case, and when there is an effect on the phase as a result of self-phase modulation and cross-phase modulation, equation 3.14 can be modified to an *Effective Phase Mismatch*, K, given as [21]

$$K = \Delta k + 2\gamma P_0 \tag{3.14}$$

where γ is the nonlinear coefficient defined in equation 3.9, and P_0 is the power of the pump waves.

Around the zero dispersion wavelength, these conditions result in a continuum of smallest possible $\Delta k/K$, which can be plotted in wavelength space. This phase-matching curve is determined by the dispersion of the fibre, so a specific pump frequency will generate specific stokes and anti-stokes frequencies, as shown in Figure 3.2. The region just short of the zero dispersion wavelength produces the largest frequency separation between the pump and sidebands, and so is most often the chosen spectral area of operation when conversion over a large spectral range is desired.

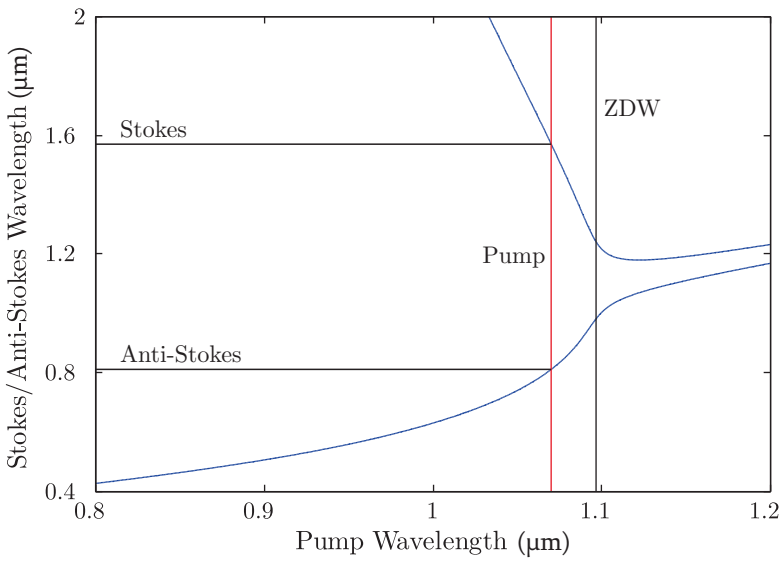

Figure 3.2: Example of a FWM phase-matching plot, showing the pump wavelength, the zero dispersion wavelength (ZDW), and the Stokes and Anti-Stokes wavelengths.

3.5 Raman Generation

The nonlinear mechanism of Raman generation is exploited in many modern optical devices, including Raman-based amplifiers [70, 71], lasers [72], detection and spectroscopic devices [73, 74]. First predicted in 1928 by C.V. Raman [75] and then experimentally demonstrated as a stimulated process in 1962 [76], it is also an important process when working with nonlinearities in optical fibres [77, 78].

Raman generation is a scattering process whereby light is inelastically scattered, emitting a photon down-shifted in energy, and therefore frequency. The lost energy is deposited into a vibration state of the material, as an optical phonon. Figure 3.3 shows the movement of energy between different levels during this process, with the pump wave and resulting stokes waves marked.

The location of the lower and upper vibrational states is defined by the host material, and is independent of the frequency of the probe photon. This results in a characteristic frequency shift, or *Raman response*, for different materials, making the process valuable for spectroscopy and detection applications. The strongest vibrational response for silica glass occurs when the frequency difference between the pump and the Raman Stokes wave is about 13.2 THz. This means that for a pump at 1064 nm, the first

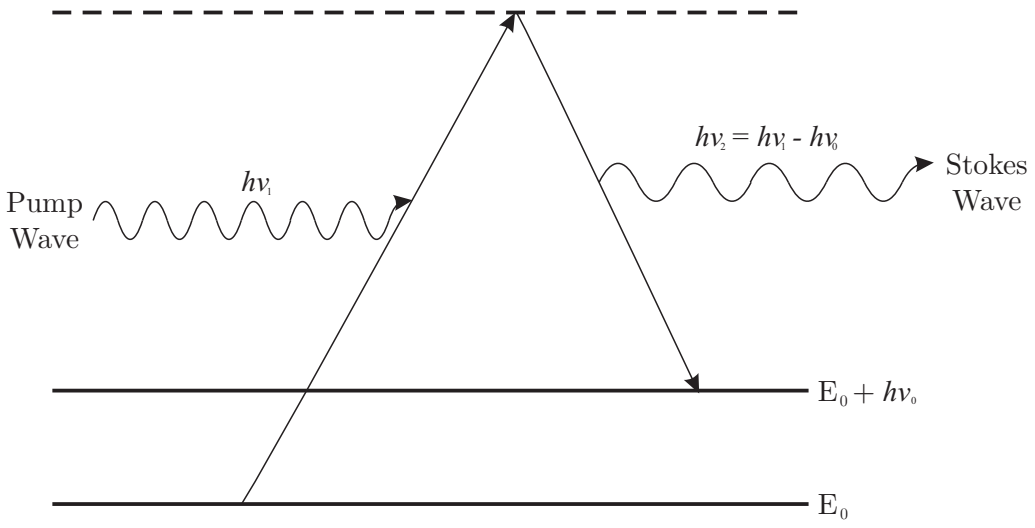

Figure 3.3: An example of Raman scattering between a pump wave with an energy of $h\upsilon_1$, a stokes wave with an energy of $h\upsilon_2$, and an optical phonon.

Raman peak would occur at 1116 nm.

In *Stimulated Raman Scattering* (SRS), an external Stokes wave above a certain threshold intensity is able to enhance the Raman scattering to create a stronger Stokes peak, which can then in turn seed a second spectral Raman peak. This can cascade down, each Stokes wave acting as a pump for the next level, forming a series of peaks in a "comb" [79, 80, 81], which can broaden through dispersion and contribute with other nonlinear processes to the generation of a *supercontinuum*. As in the spontaneous case, energy is lost to the material in the form of an optical phonon.

3.6 Supercontinuum Generation

A nonlinear system can be designed in such a way as to strongly display a range of different nonlinear processes over the same length of fibre, which can work over that length with dispersion to form a broad spectral band of light, known as a *supercontinuum*.

Although first observed in optical fibres as far back as 1976 [82], supercontinuum fibre sources have only recently become widely available commercially. This is largely as a result of the advent of PCF [83], which allows for the customisation of the fibre

microstructure, and therefore the dispersive profile, so the spectrum generated is as broader than previously achievable [84, 85]. These devices are capable of delivering any wavelength over many hundreds of nanometres, making them extremely versatile and successful [86, 87]. While often having a high degree of spatial coherence, their temporal and spectral coherence for longer pump pulses is often poor, unless great care is taken [88, 85].

This poor coherence arises from the initial processes involved in the generation of the supercontinuum; a long pump pulse, in the region of nano or pico-seconds, causes increased amounts of initial FWM, which is seeded from the quantum noise and therefore inherently "noisy". The resulting supercontinuum therefore displays increased amounts of spectral and temporal variation from pulse to pulse. For a shorter, femto-second pump pulse the dominant initial process is *Self-Phase Modulation* (SPM), arising as a result of the higher peak power of the pump. SPM is a manifestation of the Kerr effect described earlier in Section 3.3, where a pulse causes a shift in its own phase as a function of the intensity change with time ($^{dI}/_{dt}$), resulting in the generation of new red-shifted frequencies at the front of a pulse and new blue-shifted frequencies at the trailing edge of the pulse. This $^{dI}/_{dt}$ dependency means SPM is stronger for shorter, femto-second pulses compared with longer pico or nano-second pulses. Since SPM is caused by the more stable and deterministic Kerr effect means it results in an overall more spectrally coherent supercontinuum.

Various experimental approaches and fibre designs have been demonstrated to enhance the breadth of the supercontinuum spectrum or to reach shorter visible wavelengths or down into the UV, such as the use of more than one pump [89] or the tapering of the fibre [90]. Despite these different approaches, the most common is still to use a length of uniform PCF pumped with a single high peak power pulse just below the zero dispersion wavelength (ZDW), in the normal dispersive regime. In 2008, researchers at the University of Bath demonstrated that a uniform-structured supercontinuum fibre could be designed to generate light from 2700 nm down to 400 nm, producing the first true broadband "white light" source [91], as shown in Figure 3.4.

Some of the main nonlinear processes that lead to the generation of a broadband supercontinuum have already been discussed in this Chapter, namely the Raman response and four wave mixing (FWM). However the full process consists of additional effects that work together to generate the spectrum, including self phase modulation.

The work presented in Chapter 5 concerns the generation of a supercontinuum to use

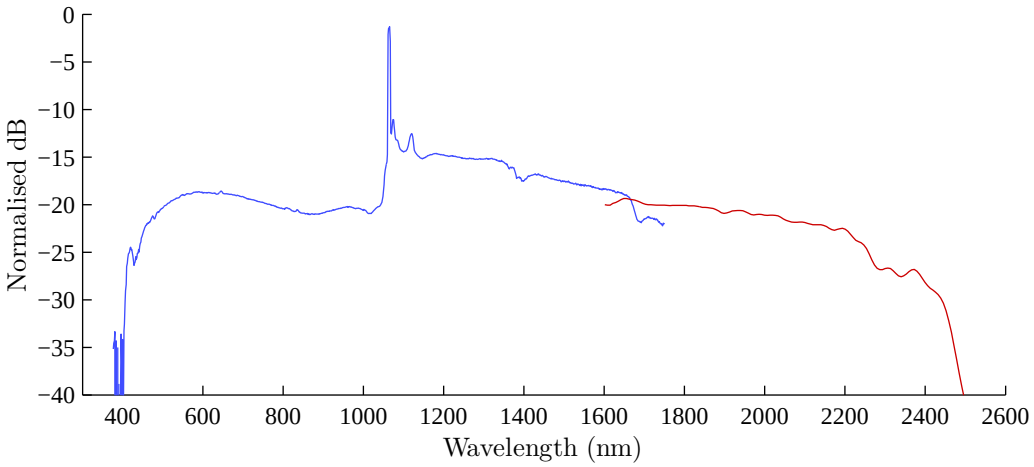

Figure 3.4: The "white light" supercontinuum demonstrated by the University of Bath in 2008, taken from the relevant publication.

as a method of inducing and monitoring defect formation in glass. The pumping laser used for that work emits pico-second pulses, and therefore the following description of the generation of a supercontinuum is for a scenario with such a pump source.

As previously noted, the dispersion profile of the fibre is conventionally engineered so that the pump is close to the zero dispersion wavelength, just inside the normal dispersion regime. This results in the efficient generation of side bands through four wave mixing, which in turn become the seed for the formation of optical solitons. Solitons in optical fibres can be defined as light pulses which propagate unchanged along an optical fibre. A "fundamental" soliton is one which undergoes no evolution at all as it propagates, while a "higher order" soliton is one which undergoes a cyclical evolution as it propagates along a given length of fibre. Solitons arise as a solution to the *Nonlinear Schroedinger Equation* (NLSE) [63], and are the result of SPM balancing the dispersion effects of the fibre. While SPM works to generate new red frequencies at the front of the pulse, dispersion acts to accelerate blue wavelengths to the front of the pulse. The result is that the two processes balance, and the soliton is left unchanged.

However, these solitons are then subject to the conditions of a real fibre, experiencing noise and small non-uniformities in the fibre microstructure, which results in the break up of the higher order solitons into a series of fundamental solitons, a process which is sometimes referred to as "soliton fission" [92]. The resulting population of fundamental solitons then experience stimulated Raman scattering, as the short wavelength blue edge of the soliton serves as a pump for the red leading edge. As a result the soliton

spectral packet shifts to longer wavelengths, in what is called *Soliton Self-Frequency Shifting* (SSFS) [93, 78, 94, 95], and pushes the supercontinuum spectrum as a whole out to longer wavelengths.

The short wavelength edge of the continuum, which has been generated through dispersive wave generation [91, 96], FWM, and SPM then experiences a trapping effect, as light in that region spatially and temporally overlaps with the SSFS solitons. While initially the group velocity of the light at shorter wavelengths was lower than that of the solitons, as the solitons propagate to longer wavelengths they experience an increasingly large group index, and consequently their group velocity falls. As the light at short and long wavelengths overlap and the group velocities reach a point where they match, the short wavelength light experiences the Kerr-driven refractive index change from the soliton, and shifts to shorter wavelengths through FWM.

This continues as the solitons self-frequency shift out to longer wavelengths, until they are attenuated by material absorption and lost. The breadth of the supercontinuum then depends on how far the solitons have propagated spectrally, and the location where the group velocity matches at the short wavelength end of the spectrum.

3.6.1 Group-Index Matching

Since the group velocity can be described in terms of the group index (equation 2.18), the importance of the material group index now becomes apparent in the engineering of the supercontinuum. Figure 3.5 shows three group index curves, one for bulk silica, one for an endlessly single mode PCF, and one for a silica wire with a diameter of 5 μm. The resulting group index curves for the PCF structures can be calculated from equation 2.18, and are observed to form a steeper long wavelength edge for an increasing air-filling fraction.

This means that as the solitons self-frequency shift up to the longer wavelengths and experience a larger group index, their matching short wavelengths get progressively shorter as the air-filling fraction increases, as shown in Figure 3.5. This ultimately means that the maximum wavelength of the soliton before it is attenuated matches with a group index at a shorter wavelength than previously, allowing the supercontinuum to extend further into the blue to as short a wavelength as 400 nm [91].

The fibres used in Chapter 5 have a high air-filling fraction such as described here,

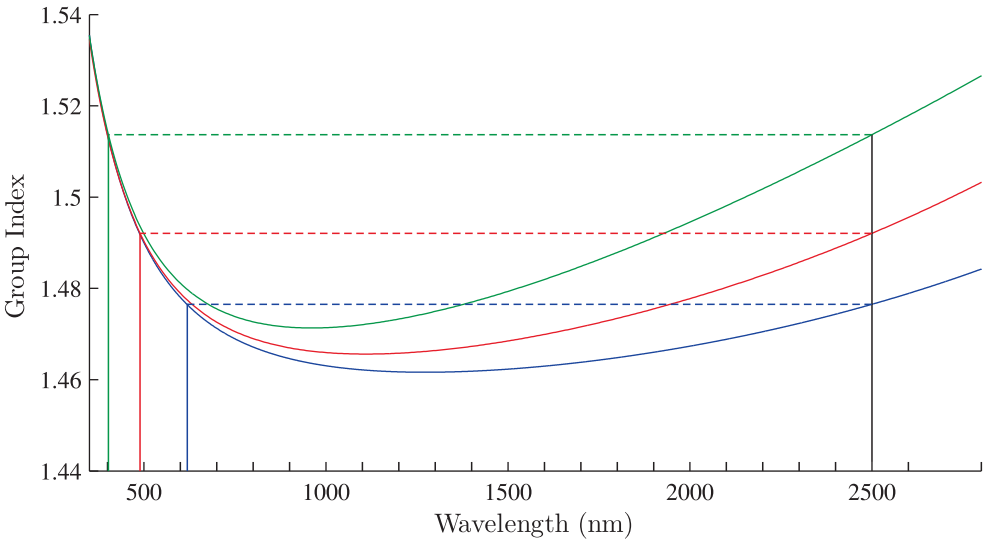

Figure 3.5: Three group index curves, one for bulk silica (blue), one for a endlessly single mode PCF (red), and one for a silica wire with a diameter of 5 μm (green). The matched wavelengths between the end of a typical supercontinuum at 2500 nm, and the progressively shorter blue wavelengths for each curve is shown.

allowing for a broad supercontinuum to be generated down to 400 nm, and so were instrumental in the investigation into photo-darkening effects in silica over a broad wavelength range.

Chapter 4

The Theory Behind Photo-Darkening in Optical Fibres

4.1 Introduction

Fibre optics have proven to be an ideal technology in the miniaturisation of laser systems, most famously through the development of fibre lasers [97]. In their most simple configurations, these devices carry an active lasing element, such as ytterbium, in the core of the fibre in the form of a dopant, and often use fibre Bragg gratings as mirrors to form potentially high power all-fibre laser sources [98]. Fibre lasers are now available that cover a wide range of specifications, and employ a number of different methods to meet commercial needs.

However, high power fibre lasers suffer from performance issues not present in other types of laser systems, due to the strong confinement of light, and consequently the high intensities, in the fibre core. One such issue is photo-darkening, where defects in the glass are formed as a result of the propagating light itself, in turn inducing increased losses over certain wavelength bands in the transmission spectrum of the fibre. This effect is particularly undesirable for several optical fibre based applications, including supercontinuum fibre laser sources, which provide a high power broadband "white light" output that can be filtered down to any wavelength as needed [99, 100].

4.2 Defect Formation in Silica

Damage to the silica glass arises as a consequence of the chemical structure of the silica and the flux of the high energy photons absorbed. Silica, SiO_2, is an amorphous solid containing a silicon atom bonded to four oxygen atoms in an approximately tetrahedral structure [101], sharing two oxygen atoms with a neighbouring structure in the same configuration. The natural angle of the O-Si-O bonds lies between 120° and 180° [102, 103], with an average at around 144° [104]. When the glass is drawn down to a fibre through a furnace, the silicon and oxygen atoms form chains which, due to heat and tension, become held at abnormal angles as the glass cools below the fictive temperature. These chains can link up to form rings of Si and O atoms, which puts a strain on both the bonds and the wider glass structure, so that any excitations of a sufficiently large energy can break those bonds. An example of both a complete Si-O ring in silica glass and a broken ring is shown in Figure 4.1.

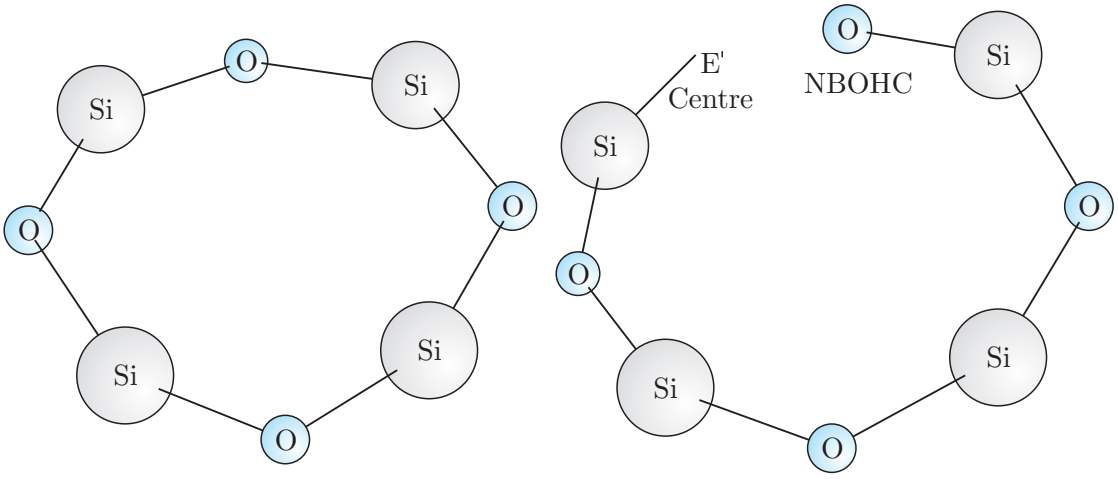

Figure 4.1: SiO_2 rings in fused silica glass, showing one complete ring with strained bonds, and a second that has been broken, forming a NBOHC and an E' centre.

Defects are known to be formed from the absorption of high energy particles [105] and single photons, such as gamma rays [106, 107], with the bond breaking energy being close to 8 eV [108]. Previous work has recently demonstrated that the absorption of multiple photons with lower individual energies can also create these defects, provided the photon flux is high enough [109]. Research at the University of Bath has recently shown that multi-photon absorption at 1064 nm can cause significant defects in silica glass [110].

A fibre laser that operates using a 1064 nm pump source has an individual photon energy of approximately 1.2 eV. When the photon flux increases to a point where the absorption of 8 photons in quick succession by a single bond becomes probable, the combined absorbed energy then exceeds the strained SiO_2 bond energy of 8 eV. The strained bond then breaks, forming a defect in the glass, which can have vibrational resonances which introduce unwanted additional absorptions within the transmission window of the glass.

The resulting glass defect is known as a *Non-Bridging Oxygen Hole Centre* (NBOHC) [111, 112, 113] or sometimes a *Colour Centre* [8, 114], and consists of an oxygen atom bonded to only one silicon atom, as shown in Figure 4.1. The resonances of the oxygen atom cause the defect to have a strong absorption band at 258 nm, and a weaker one at 630 nm [115, 116, 114]. Despite being weaker, the 630 nm band is potentially problematic for a device where transmission over this part of the visible spectrum is important. The defect also leaves a free-floating silicon bond, known as an *E' Centre*, which has a strong absorption at 213 nm [115].

The production of NBOHC sites and E' centres in silica glass usually occur in pairs, forming from the breaking of strained bonds in a Si-O ring, and can be described using the equation [113, 117, 118]

$$\equiv \text{Si—O—Si} \equiv \rightarrow \equiv \text{Si—O} \bullet + \bullet \text{Si} \equiv, \tag{4.1}$$

where $\equiv$ represents a trio of bonds between a Si atom and three O atoms, $\equiv$ Si—O$\bullet$ is a NBOHC, and $\bullet$Si $\equiv$ is an E' centre. There are a few other mechanisms by which an NBOHC site can be formed which does not also form an E' centre, but these are not relevant to the research presented in Chapter 5, and therefore are not described here.

4.3 Treatment Techniques

Techniques have been developed to treat or prevent the formation of defects like NBOHCs in optical fibres. These include doping the core with fluorine, which acts to break the stressed molecular rings and terminate them [119, 110] with the F atoms. This alters the vibrational resonances of the defect, and places the resulting absorption outside the transmission window of silica. Another approach is to thermally anneal the

glass after initial fabrication, allowing the molecular rings to reform and relax naturally, removing the population of strained bonds which could potentially be broken to form NBOHCs [120, 121, 122].

A third technique is to load the glass of the fibre with a population of molecules such as hydrogen, H_2 [123, 124, 125, 126]. These methods of gas delivery involve surrounding the fibre with H_2 at high temperatures or high pressures of up to 100 bar [127, 128, 129] or more, causing the gas to diffuse deep into the core of the glass fibre. If exposure to a high flux of photons is carried out soon after H_2 treatment [127, 128, 129], enough H_2 will still be present in the glass as it photo-darkens to immediately terminate the NBOHC sites with hydrogen as they are created, forming OH groups. This can also occur naturally over time in a fibre left exposed to the local atmosphere, where water molecules in the air provide the hydrogen. The resulting OH group does remove the NBOHC absorption around 630 nm, but unfortunately introduces a strong absorption around 1380 nm, which is the first overtone of the fundamental OH absorption at 2.7 μm [130]. The location of this first overtone is close to where silica is at its lowest intrinsic loss, and therefore adds an additional detrimental effect to the fibre transmission.

Research by Henschel et al. in 2002 [128] first suggested replacing hydrogen with deuterium, D_2, as the molecule for the loading process. The dynamics of the diffusion of deuterium into silica glass has been previously shown to be comparable to that of hydrogen [131, 132], and research has shown that this results in the same termination of the oxygen atoms at NBOHC sites, only now OD groups are formed [128]. Because deuterium has an extra neutron compared to hydrogen, the reduced masses of the two atoms are different, which in turn causes the vibrational resonant frequencies of the OD and OH groups to vary. This results in the OD groups having absorption bands at different wavelengths from the OH groups, and mostly lying in regions outside of the silica transparency window, and are therefore generally less detrimental to high power fibre systems. The fundamental absorption for OD groups is at 3.7 μm, and the overtones are likewise also at longer wavelengths compared to those of OH groups. The first OD overtone is located around 1880 nm, with a second overtone around 1265 nm. However, this second overtone is known to be much weaker, being around 1/60 of the strength of the first [133].

4.3.1 The OH $\rightleftharpoons$ OD Exchange Mechanism

An effect which is relevant for research on the treatment of silica fibres with D_2 is the OD $\rightleftharpoons$ OH exchange mechanism. This is a well known effect whereby established OH groups in the glass can be converted to OD groups when exposed to free D_2 atoms [134, 135, 133]. The exchange can be written as

$$2Si:OH + D_2(g) \rightleftharpoons 2Si:OD + H_2(g), \tag{4.2}$$

showing a process where D_2 gas diffuses into the silica glass and reacts with OH groups, releasing the hydrogen and forming an OD site in its place. The resulting hydrogen bonds with another displaced hydrogen to form a H_2 molecule, which then can diffuse freely through the silica glass. Reaction 4.2 also shows that the exchange is reversible, since the OH groups have a similar bond energy to the OD groups, and therefore a population of free H_2 could likewise displace the deuterium from the OD groups in the glass. However, the exchange mechanism is not spontaneous, requiring a population of H_2 or D_2 in the glass and some activation energy, such as heat, for the exchange to occur. As a result, the reaction is heavily dependent on the local temperature [134, 136] and the free gas populations, or the delivery of the activation energy through a flux of sufficiently energetic radiation [135].

As described, the formation of NBOHC sites and E' centres, and the photo-darkening absorption bands that arise as a result, are a significant problem in high power fibre laser systems. The treatment of a fibre by loading deuterium molecules into the core to counter the effects of this photo-darkening is often time consuming and requires specialist high pressure systems. Chapter 5 describes research carried out to develop a faster, yet still effective loading treatment using deuterium to prevent photo-darkening as a result of NBOHC sites and E' centres.

Chapter 5

A Deuterium-Loading Treatment for Photo-Darkening in Fibre-Based Laser Sources

5.1 Introduction

This chapter describes research carried out on the topic of treatments to prevent photo-darkening in silica photonic crystal fibres. As described in Section 4.2, this process causes irreversible damage to the silica of the fibre in the form of defects when exposed to high intensity laser light, creating a population of Non-Bridging Oxygen Hole Centres (NBOHCs), resulting from the breaking of stressed bonds in the glass. These NBOHCs introduce potentially detrimental absorption bands at certain wavelengths located in the visible spectrum. These sites can be terminated by hydrogen atoms in the glass, forming OH groups with a strong absorption at 1380 nm, which are themselves detrimental in telecommunications devices and supercontinuum fibre lasers.

Any approach to preventing the formation of stressed bonds, and therefore the NBOHC sites and the resulting absorption bands, would involve alterations to the fabrication process, which can be complex and difficult. However, it would be simpler to treat the glass with a chosen gas, allowing the broken strained silica bonds to be terminated with new groups made up of that chosen gas. The gas would need to be selected in order to form new groups that do not produce absorption bands in critical areas. The

absorption bands of these groups could instead be chosen to be located in unused parts of the transmission spectrum, where they could be effectively ignored.

As outlined in Section 4.3, one treatment for NBOHCs previously suggested is to expose the fibre to deuterium gas, D_2 [128]. The resulting oxygen-deuterium (OD) groups in the silica glass work to occupy many of the potential NBOHC sites that cause unwanted absorptions, making the fibre largely immune to the photo-darkening effect from high power lasers, and muting the OH group absorption bands. Instead, OD group absorption bands are introduced at longer wavelengths, compared to those of the usual OH groups which occupy the low loss transmission window of silica.

The primary aim of this research was to assess the effectiveness of a new technique for loading a PCF with deuterium gas. The current state of the art for deuterium loading involves submerging a silica fibre in the chosen gas at very high pressures of 100 bar or more [127, 128, 129], and can take several days to several weeks to achieve full loading [124, 128]. This is time consuming and requires specialist equipment, making it difficult to carry out. The technique presented here exploits the microstructure of PCFs, delivering the gas directly to within a few microns of the fibre core, resulting in a method which does not require high pressures or temperatures, and can be done with simple lab equipment in a few hours.

5.2 Approach

The approach for this work was to fabricate some supercontinuum fibre similar to one previously produced by the University of Bath [91], which is capable of generating light down to approximately 400 nm and up to approximately 2500 nm from a 1064 nm picosecond laser pump source. Two fibres were fabricated; one that was used for supercontinuum generation and remained untreated, and one which was annealed with deuterium during fabrication and prior to any supercontinuum generation [137, 138, 139, 140]. This annealing during fabrication of the second set of fibre allowed stressed silica rings in the glass to relax and terminated potential NBOHC sites with OD groups. Short lengths of these two fibres were then spliced to a high power fibre laser which acted as a pump for the supercontinuum, and left over many hours of exposure to induce photo-darkening and the formation of NBOHC sites and E' centres in the glass, until such a point that the process was observed to have saturated. A length of the untreated fibre was then loaded with deuterium using the new technique, at a few bar

of pressure and at room temperature, before also being exposed to the pump laser to generate a supercontinuum and induce photo-darkening.

The loss of these photo-darkened fibres was then assessed by carrying out a series of measurements using the "cut back" method, to confirm the location and strength of the absorption bands. It could then be verified that the OH bands were present in the untreated control fibre and were muted in the fibre that had been annealed with deuterium before splicing to the high power fibre laser. The D_2 loaded fibre loss was then compared with the annealed fibre to assess the extent of the photo-darkening, and hence the effectiveness of the D_2 loading technique in suppressing photo-darkening losses over the visible wavelength region and at 1380 nm.

Finally, the recorded losses for each measurement along the length of the fibres was compared. This allowed for a numerical estimate of the loss along the fibre length for each of the absorption bands at 630 nm, 1380 nm, and 1880 nm, and therefore a better understanding of the photo-darkening behaviour in each of the fibres.

5.2.1 Expectations

As described in Section 4.3, the vibrational modes of both OD and OH groups are well known [123, 130, 141], and so the location of attenuation peaks in a fibre with a high population of OH and OD groups can be predicted. The expected loss behaviour for untreated, annealed, and D_2 loaded fibres is shown in Table 5.1.

Detecting high losses around 630 nm indicates the presence of NBOHCs sites, as the oxygen atoms at the end of the broken SiO_2 rings have a strong and broad absorption around that wavelength. High losses at 1380 nm indicate the presence of OH groups, corresponding to the first overtone of the fundamental oxygen-hydrogen vibrational mode at 2.7 μm. A high loss at 1880 nm indicates the presence of OD groups in the glass, corresponding to the first overtone of the oxygen-deuterium fundamental vibrational mode at 3.7 μm. A second overtone of the OD groups is found at 1265 nm, albeit much weaker than the first.

Initially, the untreated fibre was expected to contain strained bonds within the glass structure, but relatively few NBOHCs and OH groups, resulting in consistent and flat loss values across the 630 nm and 1880 nm regions. A peak at 1380 nm was expected, since the glass contained a population of OH groups picked up during fabrication.

Fibre	Loss at 630nm	Loss at 1380nm	Loss at 1880nm
Untreated fibre (non photo-darkened)	None	Low	None
Untreated fibre (photo-darkened)	High	Moderate	None
D_2 Annealed fibre (non photo-darkened)	None/Low	None/Low	High
D_2 Annealed fibre (photo-darkened)	None/Low	None/Low	High
D_2 Loaded fibre (non photo-darkened)	None/Low	None/Low	High
D_2 Loaded fibre (photo-darkened)	None/Low	None/Low	High

Table 5.1: The expected loss at certain spectral regions for untreated, D_2 annealed, and D_2 loaded fibres.

After photo-darkening, the loss around 630 nm was expected to rise as the NBOHC population increased, and the 1380 nm peak was expected to increase moderately as some OH groups were formed from the NBOHC population, while the OD reference peak was expected to remain absent.

The D_2 annealed fibre was expected to behave differently, having initially possessed a large population of OD groups formed during the D_2 annealing process. This causes a strong absorption peak in the 1880 nm region, while the 630 nm region was expected to exhibit flat, normal loss values due to the glass being purged of potential NBOHCs during annealing. The 1380 nm peak was still expected to be present, although potentially lessened as a result of the high population of OD groups. After exposure to a high power laser, it was expected that this fibre would show little or no evidence of photo-darkening, as there would have been very few strained bonds remaining in the glass, inhibiting any sort of photo-darkening effects.

If the D_2 loading treatment process was successful, the resulting fibre was expected to exhibit low loss in the 630 nm region, and an OH peak at 1380 nm similar to that measured in an untreated, non photo-darkened piece of fibre. The 1880 nm peak was expected to be present and comparable in strength to that of the annealed fibre, showing that the population of OD groups in the D_2 loaded fibre was near to that of the D_2 annealed fibre, and had not been lessened by the exposure to high intensity photons.

5.3 Fabricating Supercontinuum Fibre

The fibre design chosen for this work was first produced at the University of Bath in 2008 [91]. As described earlier in Section 3.6, group index matching is used to generate a supercontinuum with a lower wavelength edge of approximately 400 nm, and an upper wavelength edge of around 2500 nm. This wide supercontinuum spectrum is ideal for investigating the location and strength of absorption bands in the silica glass as a result of OH and OD groups, particularly the region around 630 nm for NBOHCs, the area around 1380 nm for OH groups, and the region around 1880 nm for OD groups.

The two final fibres were fabricated from pure silica glass (Heraeus f300) using the stack and draw technique, as described previously in Section 1.4, and were designed with a solid core surrounded by 3 rings of capillaries. Both of the final fibre cladding microstructures had the same dimensions, each with holes with an average diameter of 4.5 μm, a pitch of 5 μm, and a core diameter of 4.5 μm. The stack was drawn to six usable canes, two of which were used to draw to the final fibres, each with a diameter close to 125 μm. A microscope image of the untreated fibre and the fibre annealed with D_2 is shown in Figure 5.1, where it is clear that the structures are very similar. This is significant because the generated supercontinuum must be as spectrally similar as possible in each fibre when pumped with the same 1064 nm laser source in order to maintain the comparability of the experiments. Since the supercontinuum generated is a direct consequence of the fibre dimensions, it is necessary that those dimensions are verified to be as similar as possible to ensure this.

The canes used to draw the untreated and D_2 annealed fibres both came from the same stack, ensuring the maximum possible similarity in the physical dimensions and characteristics of the two preforms as a result of the prior drawing phases.

Previous research has suggested that the OH groups present in a silica glass preform can be removed from the glass prior to the final fibre drawing phase by annealing with nitrogen [122], known as *nitrogen baking*. This nitrogen baking involves passing nitrogen gas through the preform as it is fed into the 1800°C furnace at a speed of 40 mm min^{-1}, and has been shown to be an effective method of significantly suppressing the 1380 nm loss peak in the final fibre [122]. Incorporating this element into the fabrication process for both the untreated fibre and the D_2 annealed fibre helped to further ensure that the two fibres were as close to identical as possible.

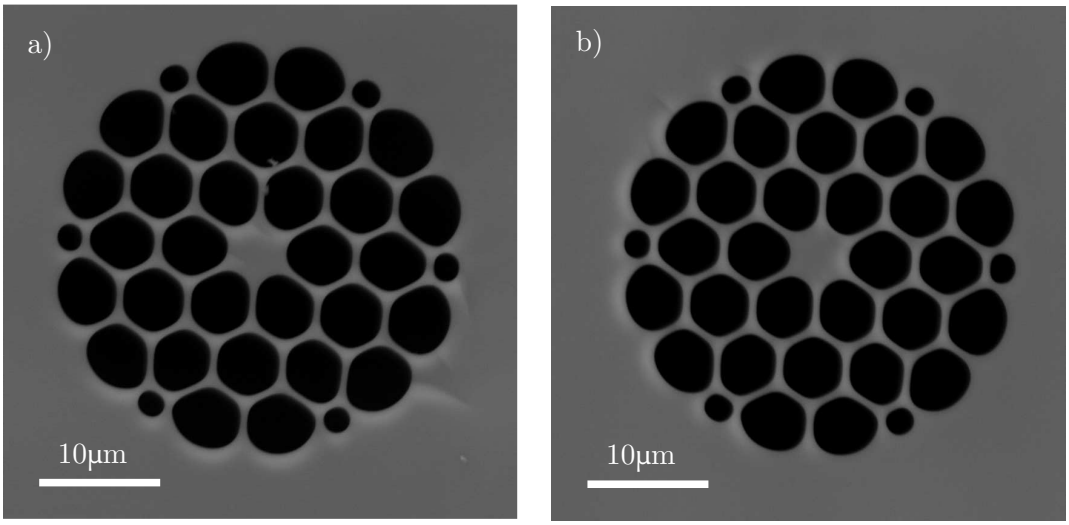

Figure 5.1: Scanning electron microscope (SEM) images of the fabricated supercontinuum fibres. a) shows the untreated fibre, and b) shows the D_2 annealed fibre.

As previously, the parameters used at this stage of drawing the two preforms to fibre was also kept the same. The speed that the preforms were fed into the furnace at were also kept constant at 4 mm min^{-1}, and the speed at which they were drawn down onto a spool was 25.9 m min^{-1}. The tension in the fibre was kept around 1.34 N by adjusting the furnace temperature. This ensured the preforms were both drawn at nearly the same "true" furnace temperature.

An additional consideration regarding the desire to use the same parameters for both fibres is the effect of the drawing process on the molecular structure of the glass. While other drawing parameters might produce the same fibre on a micro-scale, the population of strained Si-O bonds in the glass would be likely to vary significantly. When studying photo-darkening, it is desirable to maintain a similar population of potential NBOHC sites in the glass, so that a studied treatment can avoid appearing more effective than it is in reality as a result of a low population of strained bonds, and vice-versa. Maintaining the same parameters for both fibres ensures more than just matching their microstructures, and hence their nonlinear behaviour, and their loss, but also the number of potential NBOHC sites present in the glass.

5.4 Untreated Fibre

This section outlines the results for the inherent loss in the untreated fibre, the experimental method in exposing the fibre to a high power laser for an extended period of time, the experimental method for the measurement of the loss and the resulting loss data for the fibre after exposure.

5.4.1 Loss of Untreated Fibre

The inherent loss of the untreated fibre was measured prior to any photo-darkening to establish a baseline for subsequent data to be compared to. The cut back method was used to measure the loss, using a broadband xenon discharge lamp (Energetiq Inc., EQ99) as a source.

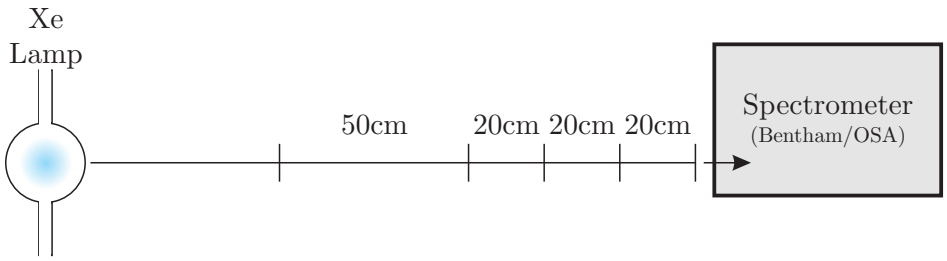

Figure 5.2: The setup and procedure for carrying out a loss measurement.

This method of measuring loss involves recording a broadband signal transmitted through a long piece of fibre, before cutting a length from the output end and measuring the transmitted signal again from the remaining piece. The difference between the two signals then represents the loss over the length of fibre that was removed, since the input end has not been moved and therefore the input coupling should be the same. The experimental setup and procedure for the loss measurement is shown in Figure 5.2. The transmission data was recorded using an Optical Spectrum Analyser (OSA)(Ando) for wavelengths from 400 nm up to 1700 nm, with longer wavelengths up to 2700 nm being recorded on a second spectrometer (Bentham, DTMc300).

Cut backs were taken using longer fibre samples of 301 m in length, and shorter fibre samples of 46 m in length. Each length was removed from the spectrometer, re-cleaved, and re-measured up to 5 times, allowing any fibre-to-spectrometer coupling losses to

be averaged out, and so increasing the accuracy of the measurement. The resulting loss data is shown in Figure 5.3, where data for different wavelength bands are shown in different colours and have been plotted together to form the full loss spectrum. The Bentham spectrometer measurements were all recorded at a resolution of 5 nm, with the 350 nm to 400 nm (shown in green) and 1700 nm to 2000 nm (shown in blue) sets taken over 46 m long cut backs, and the 800 nm to 1200 nm (shown in purple) and 1500 nm to 1700 nm (shown in yellow) were taken over 301 m long cut backs. The OSA spectrometer measurements were all recorded at a resolution of 10 nm, with the 400 nm to 800 nm (shown in red) and 1200 nm to 1500 nm (shown in orange) taken over 301 m long cut backs.

The loss below 1 μm is observed to be approximately 13 dBkm^{-1} $\pm$ 0.2 dBkm^{-1}. A peak at 1380 nm is clearly visible, and is characteristic of absorption by OH groups in the silica. With a maximum at around 40 dBkm^{-1}, the magnitude of this OH peak can be considered to be low enough so as to not disguise any other possible characteristics near that wavelength, such as the absorption by OD groups at 1265 nm, which would be expected to potentially appear after D_2 loading. This is the result of the nitrogen baking carried out to minimise OH content in the glass prior to drawing the final fibre. Any subsequent OH absorption can be compared to this starting value. The general loss curve is seen to behave as expected and as described earlier in Section 2.7, with higher loss at the short and long wavelength edges due to Rayleigh scattering and material absorption respectively. The loss around 1550 nm, which is expected to be close to the lowest over this window for silica, is around 4 dBkm^{-1} $\pm$ 0.2 dBkm^{-1}.

5.4.2 Photo-Darkening Exposure

For each of the laser exposures carried out to induce photo-darkening, 2.5 m to 3 m of fibre was spliced to the output of a high power fibre laser (Fianium ltd, 1064 nm, 5 ps, 20 MHz, maximum of 6W average power, 60 kW peak power). The configuration of the fibre and spectrometer for the photo-darkening exposure is shown in Figure 5.4.

A splice was considered to be of sufficiently high quality if it supplied a minimum power of 200 mW to the visible region of the supercontinuum spectrum (considered to be from 400 nm to 750 nm), out of a total average power in the supercontinuum of approximately 2.5 W. This value of 200 mW corresponded to a spectrum over that wavelength range which was of a sufficient intensity to clearly detect any photo-darkening effects. The

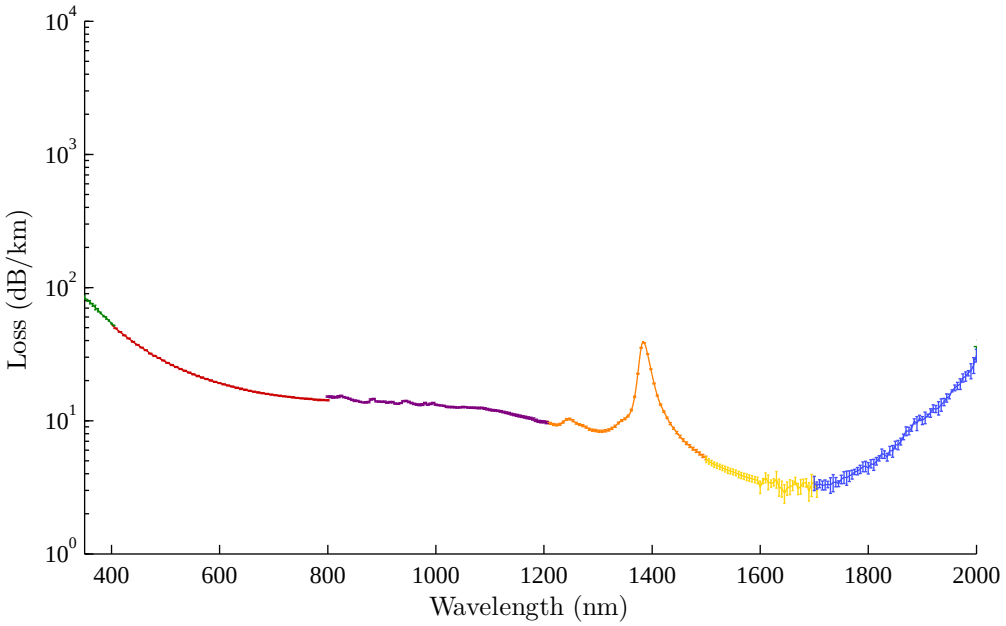

Figure 5.3: The loss curve for the untreated fibre. Loss was recorded from 350 nm to 400 nm (green), 400 nm to 800 nm (red), 800 nm to 1200 nm (purple), 1200 nm to 1500 nm (orange), 1500 nm to 1700 nm (yellow), and 1700 nm to 2000 nm (blue), with cut back lengths of either 301 m or 49 m. Data was recorded using both the OSA and the Bentham spectrometer, at resolutions of 5 nm or 10 nm.

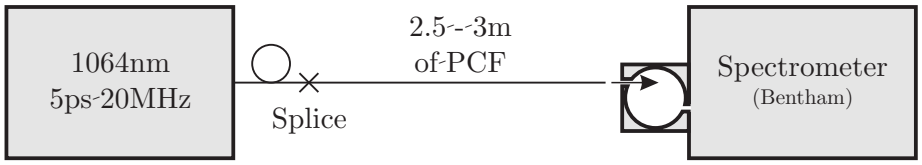

Figure 5.4: Experimental setup for the photo-darkening of the untreated, D_2 annealed, and D_2 loaded fibres.

power in the visible region was measured using four dichroic mirrors to separate the 400 nm to 750 nm range. This ensured that there was a sufficiently strong signal in the region around 630 nm to clearly discern any decrease in signal generation over time. In order to prevent damaging back reflection into the fibre laser, the supercontinuum fibre output end face was melted to produce a rounded edge.

Prior to exposure the spectrometer was fully calibrated using a standard bulb source.

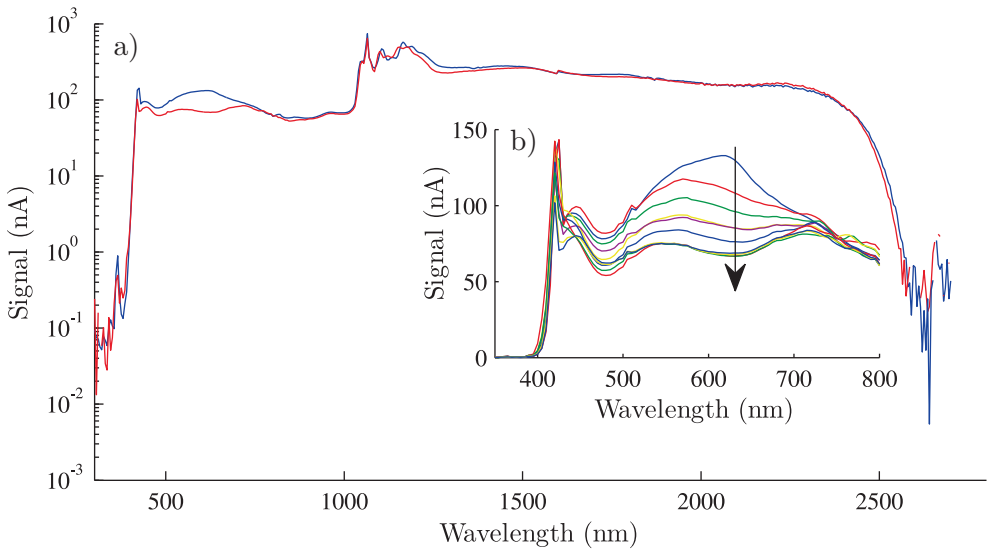

Figure 5.5: The change in the generated supercontinuum over time in the untreated fibre. a) shows the first (blue) and last (red) scans, with a noticeably different amount of generated signal around 630 nm. The observed discontinuity at 1600 nm for both data sets is the result of a change in detector, and is not a real change in intensity. b) shows the signal around 630 nm in 12 hr steps, highlighting the speed of photo-darkening over the first 36 hrs. The spectrometer resolution was 5 nm.

The fibre was then coupled into the Bentham spectrometer using an integrating sphere, and left for over 100 hours with the laser running continuously, with the spectrometer recording the supercontinuum generated every 30 minutes. This allowed for the damage and absorption in the fibre due to photo-darkening to be recorded over time. Figure 5.5 a) shows the first and last data scans for an untreated fibre under exposure.

Clearly the greatest change over the 100 hours of exposure is to the broad region around 630 nm, where the power has nearly halved. Figure 5.5 b) shows this in more detail, where each curve shows the generated supercontinuum in 12 hour steps. Most of the damage to the fibre appears to occur in the first 36 to 48 hours, after which the rate of damage slows and there is less change with each new scan.

The shape of both of the supercontinua include additional peaks in the region beyond the 1064 nm pump up to about 1200 nm. These peaks are due to Raman generation in the output fibre from the laser, prior to the splice to the PCF. Although they are unwanted and present a drain on the total power of the 1064 nm pump, they clearly do not reduce the pump to such an extent as to affect the breadth or quality of the

supercontinuum, which is clearly generating light at a short enough wavelength to be able to detect changes around 630 nm. For this reason their presence can be ignored. Other noticeable differences between the two supercontinua in Figure 5.5 a) can be attributed to small changes in the pump laser output power over time, which in turn has a resulting effect on the supercontinuum that is generated.

5.4.3 Untreated Fibre Loss After Photo-Darkening

After photo-darkening, the loss of the untreated fibre was measured. As with the earlier samples of untreated fibre, the measurement was carried out using the cut back method, again with a xenon lamp acting as the light source and two spectrometers to cover the full wavelength range from 350 nm to 2700 nm.

It was also desirable to know where in the fibre the most photo-darkening was occurring. To achieve this, three cut backs of 20 cm sections were taken from the spliced end of the fibre, followed by a cut back of 50 cm. Measurements were concentrated on wavelength regions known to have characteristic absorptions due to NBOHC sites, and OH and OD groups, starting with the 400 nm to 800 nm range, the OH peak at 1380 nm, and the OD peak at 1880 nm.

Unfortunately, the variation in the coupling efficiency to the spectrometer was comparable to the changes in transmission over such short lengths of fibre, which resulted in a mildly wavelength-dependent increase or decrease in the magnitude across the whole of the loss curve. The solution was to offset the loss in each data set to match the known background loss values of the fibre, shown earlier in Figure 5.3. The wavelength at which the data sets were offset to match with the known loss was chosen to be in an area known to be unaffected by photo-darkening. The result still clearly highlights the changes in the fibre loss brought about by photo-darkening in the fibre.

Figure 5.6 shows the loss measured over the 350 nm to 750 nm range using the Bentham spectrometer and the OSA, combined and averaged with error bars. The wavelength range recorded using the OSA was from 400 nm to 750 nm, resulting in a discontinuity below this wavelength.

The plot clearly shows a rise in the attenuation around 600 nm for the first 20 cm of fibre through which the pump pulse propagated (shown as the first 20 cm from the spectrometer in Figure 5.2), peaking at approximately 2 dBm^{-1} with an error of

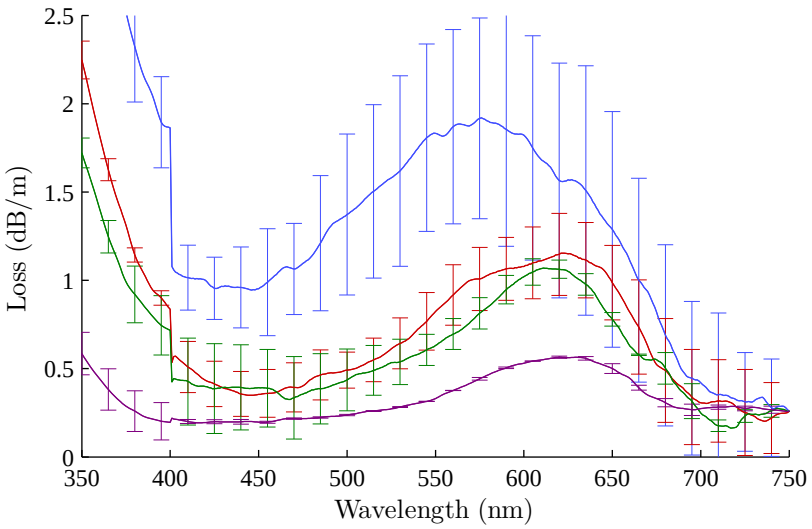

Figure 5.6: The loss of the untreated fibre over the 350 nm to 750 nm range after photo-darkening, for cut backs over the first 20 cm (blue), second 20 cm (red), third 20 cm (green), and the final 50 cm (purple) of fibre. Data was recorded by both the Bentham spectrometer (350 nm to 750 nm, resolution 5 nm) and the OSA (400 nm to 750 nm, resolution 1 nm), before being combined into one data set.

approximately 0.57 dBm^{-1}. This loss falls with each of the subsequent 20 cm sections of fibre, until there is very little evidence of photo-darkening in the final 50 cm, (the 60 cm to 110 cm section, shown in purple). This loss is most likely due to photo-darkening, since it is expected that the first 20 cm of fibre would contain the largest proportion of NBOHC sites, before steadily falling with fibre length until the final 50 cm cut back. The error bars are observed to become steadily smaller for each subsequent length of fibre, as the degree of photo-darkening decreases. This could be caused by a relatively large change in the density of NBOHC sites between cleaves taken during the measurement. The measurements taken further along the fibre show progressively smaller error bar values as the density of NBOHCs falls, until the final 50 cm, whilst also being a longer cut back and therefore more accurate, has the lowest density of defect sites.

The short wavelength edge below the 400 nm discontinuity, recorded solely using the Bentham spectrometer which is more sensitive than the OSA at this wavelength and therefore the cause of the discontinuity, is seen to rise steadily in the data, and is also strongest in the first 20 cm. This may be indicative of the absorptions at 213 nm and 258 nm from E' centres and NBOHC sites respectively, since it is clear from the 600 nm

to 630 nm loss peak that a population of NBOHC sites is present in the fibre. These absorptions at 213 nm and 258 nm are also known to be stronger than the 630 nm absorption, explaining the steepness of the 20 cm curve for shorter wavelengths.

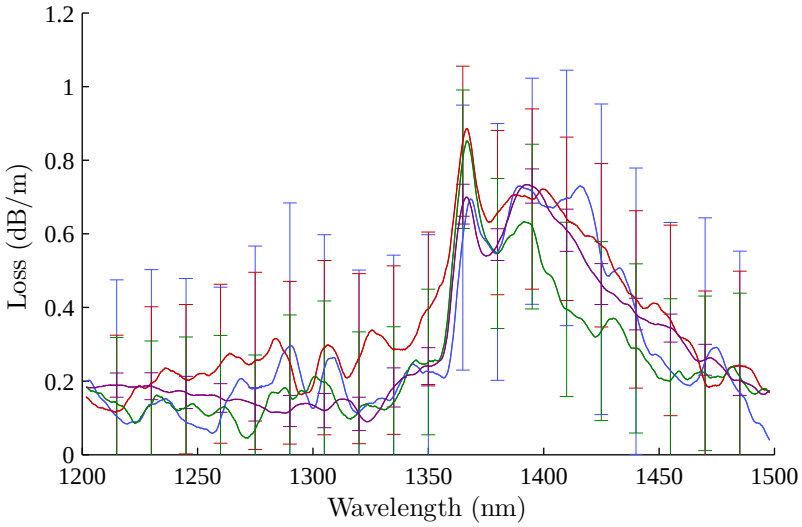

Figure 5.7: Graph of the loss of the untreated fibre at 1380 nm after photo-darkening, showing the first 20 cm (blue), second 20 cm (red), third 20 cm (green), and the subsequent 50 cm (purple) of cut back fibre with error bars. Data was recorded using the OSA, at a resolution of 10 nm.

The magnitude of the OH peak at 1380 nm is shown in Figure 5.7, and has clearly increased from the initial estimated loss value of 40 $dBkm^{-1}$, to an value closer to 700 $dBkm^{-1}$ after photo-darkening. However, unlike the 630 nm absorption band, the loss due to OH groups is approximately constant along the full length of the fibre, measuring around 0.7 dBm^{-1} with an error of $\pm$ 0.3 dBm^{-1}. Any variations in the average which might suggest the loss is not constant, such as the third 20 cm cut back (shown in green) being lower than the final 50 cm (shown in purple) around 1400 nm, still have error bars which overlap, showing the variation is not significant. This indicates that this higher population of OH groups formed in the glass during the period of time between the fabrication of the fibre and the photo-darkening exposure, and was due to the local environment rather than the photo-darkening. Moisture in the air where the fibre was stored could have diffused into the glass during the period between fabrication and measurement, forming OH groups and increasing the size of the 1380 nm absorption peak. This is supported by the observed second peak around 1370 nm, which is known to be caused by OH groups at the surface of the holes around the fibre core [131], which have marginally different vibrational resonance to the OH groups in the bulk of the glass.

In contrast to the data shown in Figure 5.6, the error bars at 1380 nm are seen to be relatively consistent along the full fibre length (except for the final 50 cm cut back, which is expected to have less variation compared to the 20 cm lengths). Since it is clear from the overall magnitude of the 1380 nm peak that the density of OH groups in the fibre is relatively consistent, despite the presence of NBOHC defect sites where more OH groups could form. This supports the previous hypothesis concerning NBOHC density variations between cleaves theorised when discussing Figure 5.6.

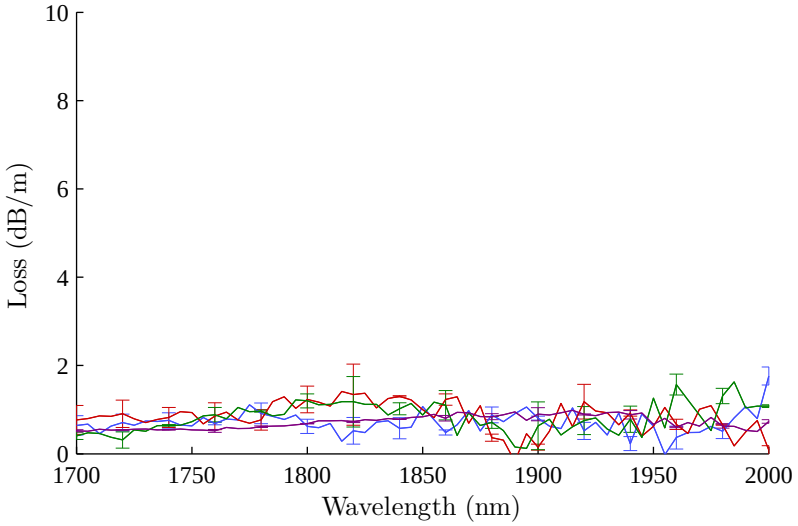

Figure 5.8: Graph of the loss of untreated fibre at 1880 nm after photo-darkening. The first 20 cm (blue), second 20 cm (red), third 20 cm (green), and the subsequent 50 cm (purple) are shown with error bars. Data was recorded using the Bentham spectrometer, at a resolution of 5 nm.

Finally, the loss in the region around 1880 nm is still found to be flat, having a value of around 0.7 dBm^{-1} with an error of $\pm$ 0.2 dBm^{-1}, as shown in Figure 5.8. This therefore verifies that there are still no OD groups present in the untreated fibre, and is expected given that the fibre has not been exposed to deuterium at any point in the measurement process.

5.5 D_2 Annealed Fibre

This section outlines the results for the inherent loss in the fibre annealed with D_2, the transmission data taken whilst the fibre was photo-darkened under high power laser exposure, and the resulting loss data for the fibre after exposure.

5.5.1 Loss of D_2 Annealed Fibre

As with the untreated supercontinuum fibre, the inherent loss of the annealed fibre was measured using the xenon lamp and the two spectrometers, taking cut backs of 150 m and 0.70 m in order to achieve good estimates of the loss over the wavelength window from 350 nm to 2000 nm. The resulting loss curve is shown in Figure 5.9. The Bentham spectrometer measurements were all recorded at a resolution of 5 nm, with the 350 nm to 400 nm (shown in green), the 800 nm to 1200 nm (shown in purple), and the 1500 nm to 1650 nm (shown in yellow) sets taken over 150 m long cut backs, and the 1700 nm to 2000 nm (shown in blue) taken over a 0.7 m long cut back. The OSA spectrometer measurements were all recorded at a resolution of 10 nm, with the 400 nm to 800 nm (shown in red) and 1200 n to 1500 nm (shown in orange) both taken over 150 m long cut backs.

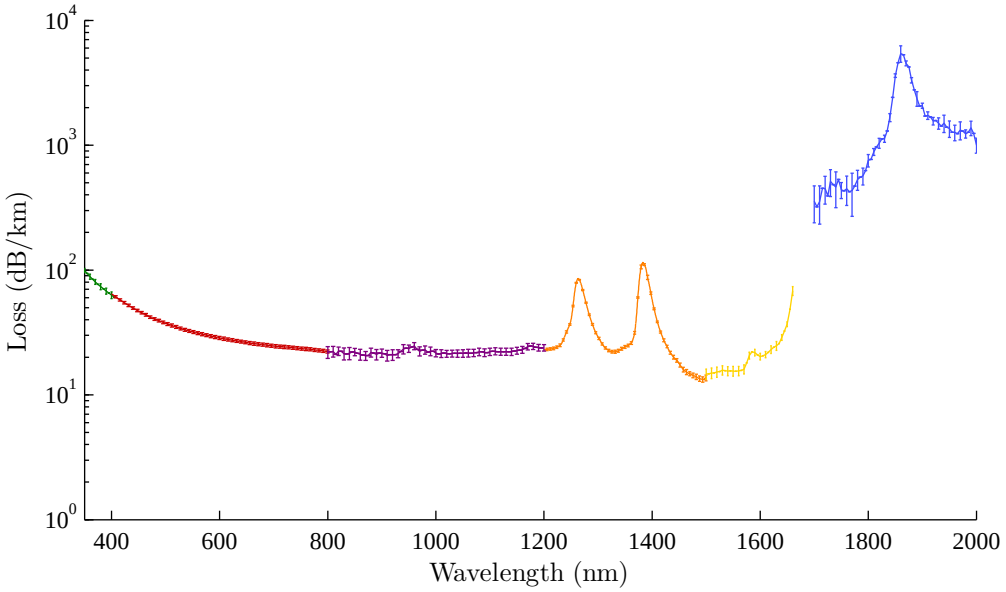

Figure 5.9: The loss curve for the fibre annealed with D_2. Loss was recorded from 350 nm to 400 nm (green), 400 nm to 800 nm (red), 800 nm to 1200 nm (purple), 1200 nm to 1500 nm (orange), 1500 nm to 1650 nm (yellow), and 1700 nm to 2000 nm (blue), with cut back lengths of either 150 m or 0.70 m. The OH absorption peak is visible at 1380 nm, and the absorption peaks resulting from the presence of OD groups are seen at 1265 nm and 1880 m. Data was recorded using both the OSA and the Bentham spectrometer, at resolutions of 5 nm or 10 nm.

The attenuation in the wavelength window below 1 μm is comparable to that recorded for the untreated fibre in Figure 5.3, with generally a slightly higher background loss in

the D_2 annealed fibre of approximately 21 dBkm^{-1} $\pm$ 0.5 dBkm^{-1} across this window, compared with approximately 13 dBkm^{-1} in the untreated fibre. The OH peak is clearly visible at 1380 nm and is also around 3 times higher than that measured in the untreated fibre, being about 115 dBkm^{-1} compared with approximately 40 dBkm^{-1} in the untreated fibre. This increase in the OH groups present in the annealed fibre directly after fabrication can be interpreted as being due to the local environment during the fibre draw and variations in the effectiveness of the nitrogen baking.

In addition to the 1380 nm OH peak, there is a significant absorption band at approximately 1265 nm of approximately 85 dBkm^{-1}. As described in Chapter 4, this arises from the second overtone of the OD groups present in the fibre, and is usually around 1/60 of the strength of the first overtone at 1880 nm. This is an early indication that there is a strong population of OD groups in the fibre, as desired.

Around 1550 nm, the loss is noticeably higher than in the untreated fibre, being around 15 dBkm^{-1} $\pm$ 0.2 dBkm^{-1}, compared with around 4 dBkm^{-1} in the untreated fibre. This is likely to be due to the D_2 annealing, with the very strong absorption around 1880 nm likely to be raising the loss across the region around that wavelength.

At longer wavelengths, the loss is observed to rise sharply, resulting in noise over a cutback of 150 m. Taking a much shorter cutback of 0.70 m allows for the loss in this region to be quantified, as seen in Figure 5.9. The gap in the data sets seen from 1650 nm to 1700 nm is as a result of a fault in the spectrometer at the time of recording, where no useful data over this range was recorded. However, the trend over this range is clear, and there are no expected absorption peaks over this 50 nm window. The peak at 1880 nm, resulting from the first overtone of the OD groups, is significantly higher than any of the other absorption bands in the chosen window from 350 nm to 2000 nm, with a maximum between 5000 dBkm^{-1} and 6000 dBkm^{-1}. It is notable that the strength of the 1880 nm peak is approaching exactly 60 times the strength of the 1265 nm peak, which is consistent with the theory developed from previous research into OD groups in silica glass [133]. This shows the D_2 annealing of the fibre was successful, a large population of OD groups now being present in the glass, and therefore few strained SiO_2 rings should remain, giving it protection from damage due to photo-darkening.

5.5.2 Photo-Darkening Exposure

As with the untreated supercontinuum fibre, the D_2 annealed fibre was spliced to the output of the high power fibre laser using an intermediate piece of ultra high NA fibre. As before, the quality of the splice was considered adequate once 200 mW or more of power was detected in the visible window of the spectrum from 400 nm to 750 nm, out of a total average power of approximately 2.5 W. The fibre end was again melted to prevent back reflection.

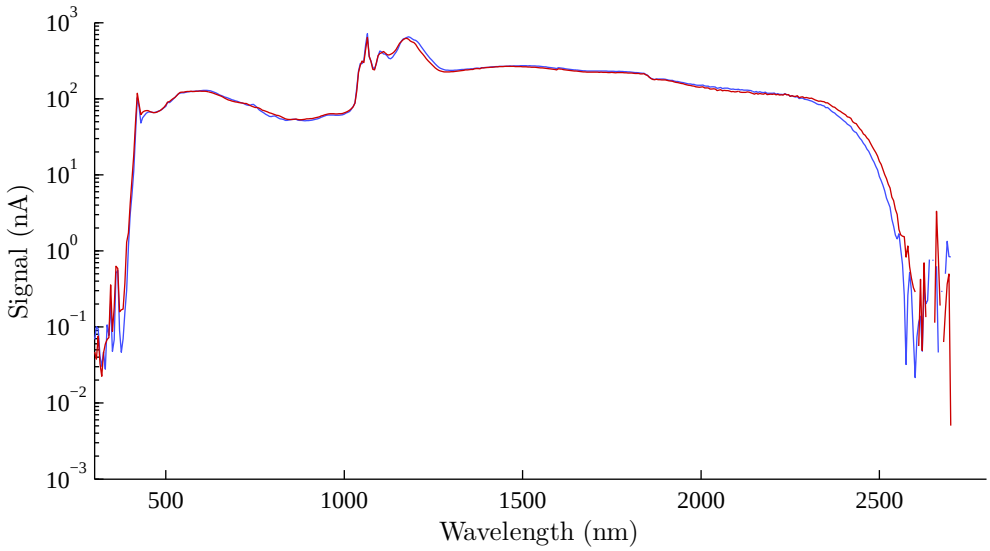

Figure 5.10: The supercontinuum generated over time in the fibre annealed with D_2, for the start (blue) and end (red) of the 100 hour exposure. Data was recorded using the spectrometer, at a resolution of 5 nm.

The fibre laser was then left to run continuously for 100 hours, with the spectrometer recording the supercontinuum generated every 30 minutes. The first and last scans of the supercontinuum are shown in Figure 5.10. Despite being stronger than in the untreated fibre, the absorption peak at 1380 nm is not visible in the supercontinuum spectrum. However, the very strong absorption peak at 1880 nm is observable as a slight dip in emission at this point. The strength of this high loss peak is potentially detrimental to the solitons generating the supercontinuum, as the intensity at wavelengths beyond this 1880 nm dip appears to fall when compared with the spectrum from the untreated fibre. However, the full extent of the spectrum is still preserved, with enough detectable light still present at the 400 nm and 2500 nm edges, and enough light is still visible at 630 nm to identify any photo-darkening effects. Relatively small additional variations in the general transmission strength across the whole supercon-

tinuum can be observed, and are interpreted as small fluctuations in the pump power over time. Finally, after 100 hours of high power laser exposure, the transmission at 630 nm remains high in this fibre, suggesting there is little or no photo-darkening.

5.5.3 D_2 Annealed Fibre Loss After Photo-Darkening

After photo-darkening, the loss of the D_2 annealed fibre was measured to verify that little or no photo-darkening had occurred, again using the cut back method in the same manner as the untreated fibre in subsection 5.4.3, with three 20 cm cut backs followed by a 50 cm cut back.

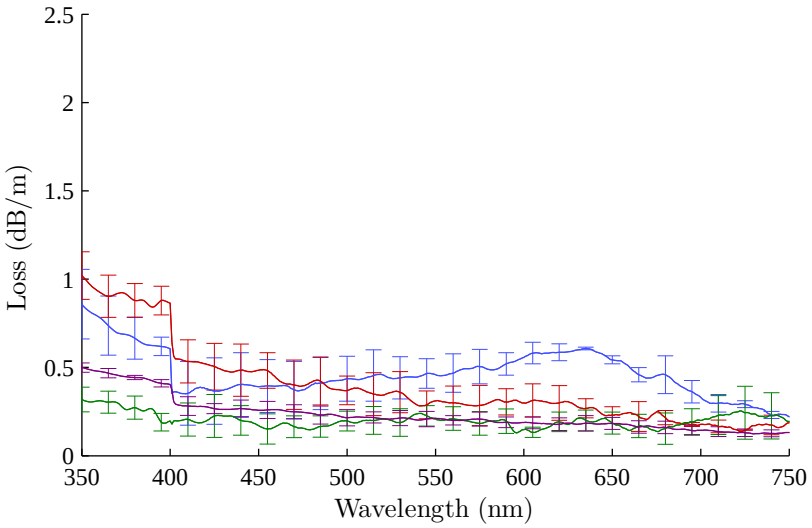

Figure 5.11: The loss of the D_2 annealed fibre over the 350 nm to 750 nm range after photo-darkening, for cut backs over the first 20 cm (blue), second 20 cm (red), third 20 cm (green), and the final 50 cm (purple) of fibre. Data was recorded by both the Bentham spectrometer (350 nm to 750 nm, resolution 5 nm) and the OSA (400 nm to 750 nm, resolution 1 nm), before being combined into one data set.

As before, the very short cut backs of 20 cm resulted in curves that suffered from a degree of variation due to coupling dependent losses. However, these variations were relatively small, and could be removed by point-matching each curve at a wavelength where the loss was expected to be unaffected by any photo-darkening and be at the noise level at around 0.2 dBm^{-1}. This resulted in an effective overlaying of the loss curves for each data sets, allowing for a direct comparison. Data was recorded using both the Bentham spectrometer and the OSA, before being combined and averaged

with error bars. Once again, a discontinuity is observed at 400 nm due to the shorter wavelength window of the OSA.

The loss curves for the 350 nm to 750 nm range are shown in Figure 5.11. The loss is significantly lower compared with that of the untreated fibre in Figure 5.6, although some evidence of photo-darkening is still present. The first 20 cm of fibre shows a maximum loss of approximately 0.6 $dBm^{-1} \pm 0.01$ dBm^{-1} above the background noise level of around 0.2 dBm^{-1} at 630 nm, almost a factor of 3.5 lower than that of the untreated fibre. The loss curves for the two subsequent 20 cm sections and the final 50 cm cut back quickly become flat around the noise level of approximately 0.2 dBm^{-1}, suggesting that very little photo-darkening has taken place beyond the first 20 cm. However, there is again evidence of loss at the short wavelength edge of the data recorded by the Bentham spectrometer below 400 nm. This is approximately 2.5 dBm^{-1} to 3 dBm^{-1} lower than the similar curve seen in the loss for the untreated fibre at 350 nm. This again could be due to the absorption bands at 213 nm and 258 nm from the comparatively smaller population of NBOHCs and E' centres.

The error bars for this data are observed to be relatively consistent over the fibre length, in contrast to the data over over the same rage in Figure 5.6. Again, this indicates that the variation in the size of the error seen in the untreated photo-darkened fibre was as a result of the large population of NBOHC sites. The error precisely at 630 nm is observed to be particularly small, and could simply be a result of coincidently very similar values at that narrow range of wavelengths over the multiple measurements.

The loss curve for the region around 1380 nm is shown in Figure 5.12. The OH peak is seen to have increased from approximately 115 $dBkm^{-1}$ in Figure 5.9, to closer to 900 $dBkm^{-1}$ to 950 $dBkm^{-1}$, with an error of approximately 190 $dBkm^{-1}$ for all cut back lengths. The only way this could be attributed to photo-darkening is over the first 20 cm of cut back fibre, since that length is the only one to show any evidence of increased loss over the 630 nm range. Therefore, as in the equivalent loss data for the photo-darkened untreated fibre, a likely explanation for the increase in the 1380 nm absorption is that during the time between the two loss measurements the glass has been exposed to a significant amount of moisture in the air. This could result in some OH groups being formed through diffusion into the glass. This is also again supported by the presence of the previously unseen second absorption peak near 1380 nm.

The 20 cm error bars over this wavelength range are observed to be relatively consistent, as seen previously in the untreated photo-darkened fibre. Once again, this is expected

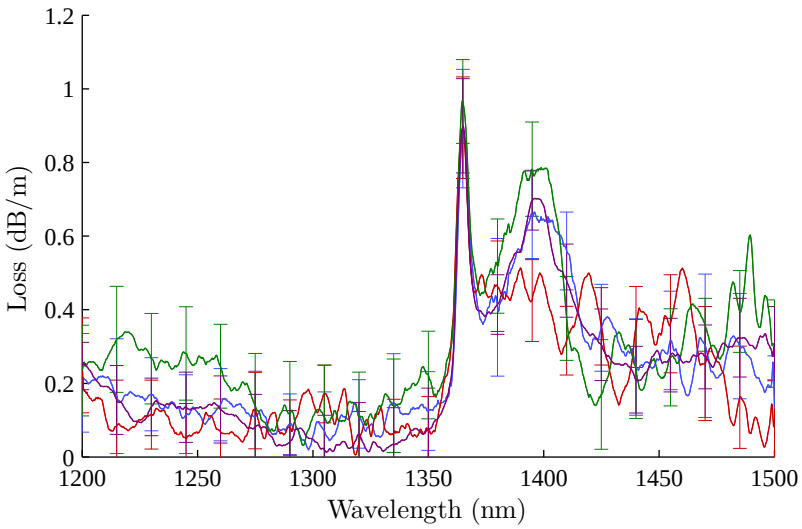

Figure 5.12: The loss recorded for the fibre D_2 annealed at 1380 nm after photo-darkening. The first 20 cm (blue), second 20 cm (red), third 20 cm (green), and subsequent 50 cm (purple) cut backs are shown. Data was recorded using the OSA, with a resolution of 10 nm.

considering the density of OH groups should remain approximately the same along the fibre length.

A notable absence from Figure 5.12 is the second overtone peak from the OD groups detected at 1265 nm earlier in Figure 5.9. This is because the strength of that absorption was measured to be around 85 $\mathrm{dBkm^{-1}}$, which is equivalent to about 0.09 $\mathrm{dBm^{-1}}$, which therefore falls well into the noise level around 0.2 $\mathrm{dBkm^{-1}}$ for the later measurement, and so is effectively undetectable over a cut back of only 20 cm.

The population of OD groups still present in the fibre can be verified from Figure 5.13. Here the peak from the first OD overtone is clearly still observable, with a strength of around 5 $\mathrm{dBm^{-1}}$ and an error of around 0.02 $\mathrm{dBm^{-1}}$, distributed effectively uniformly along the full length fibre. This is the same as measured earlier in Figure 5.9, and shows that there was no significant change in the population of OD groups in the D_2 annealed fibre during the high power laser exposure. This is further confirmed by the observation of the error bars being of a similar magnitude for all 20 cm cut back lengths.

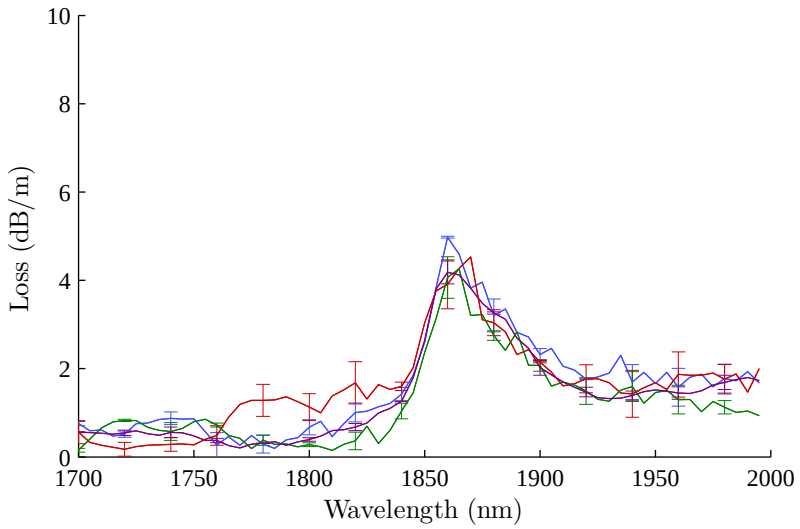

Figure 5.13: Graph of the loss of D_2 annealed fibre at 1880 nm after photo-darkening. The first 20 cm (blue), second 20 cm (red), third 20 cm (green), and the subsequent 50 cm (purple) are shown. Data was recorded using the spectrometer, at a resolution of 5 nm.

5.6 D_2 Loaded Fibre

This section describes D_2 loading of the untreated supercontinuum fibre with deuterium, detailing the method of loading and the justification for that approach, followed by the data recorded during the exposure of the fibre to the high power laser, as carried out for previous untreated and D_2 annealed fibres. The loss of the D_2 loaded fibre is then measured in the same manner as for previous fibres.

5.6.1 The Post-Treatment Methodology

The method chosen for the deuterium D_2 loading was similar to the method used in industry, as described earlier in Chapter 4. However, the methods of gas treatment of optical fibres through diffusion used in industry most often employ all solid silica fibres, not PCF. When treating a fibre it is most important for the gas to be present in the core in a sufficiently high concentration, since this is the region of highest optical intensity. For an optical fibre with a diameter of 125 μm, a gas molecule diffusing to the core has to travel around 62.5 μm. In addition, this diffusion process must occur on a relatively short time scale in order to be practical. The combination of these requirements, the

distance a molecule needs to diffuse, and the need for a sufficiently high concentration at the core, results in the high pressure of 100 bar and long treatment times of several days usually used in industry [129].

However, PCF has the advantage of having an air-filled cladding, providing channels along which gas can be pumped. This places the gas much closer to the core, therefore for a typical PCF with a core diameter of 4 μm to 5 μm the required diffusion depth is now only 2 μm to 2.5 μm. This makes the diffusion time much shorter, increasing the speed at which the concentration in the core rises, and reducing the need for very high temperatures and pressures.

5.6.2 Modelling Diffusion

A simple model of diffusion was employed in order to choose appropriate pressure, temperature and time parameters for the D_2 loading. Assuming a constant and uniform temperature, and a constant concentration of deuterium gas at the silica surface, Fick's second law for the concentration of a gas over time at a certain depth is

$$\frac{c(x,t)}{c_s} = 1 - \mathrm{erf}\left(\frac{x}{2\sqrt{Dt}}\right), \tag{5.1}$$

where c_s is the surface concentration, D is the diffusion coefficient of the gas, and t is the diffusion time. The diffusion coefficient for deuterium at room temperature is 7.36×10^{-12} cm^{2}s^{-1} [131], and is calculated for a given temperature using

$$D = 5 \times 10^{-4} \exp(-10.5/RT), \tag{5.2}$$

where R is the gas constant in kcal mol^{-1}, and T is the temperature in Kelvin. The values of -10.5 and 5×10^{-4} are both unique to deuterium, and originate from empirical data recorded by Lee et al. [136].

To estimate an appropriate temperature for the D_2 loading, the concentration at a depth of 2.5 μm over time was calculated for a range of temperatures from 293 K to 393 K. The result is shown in Figure 5.14.

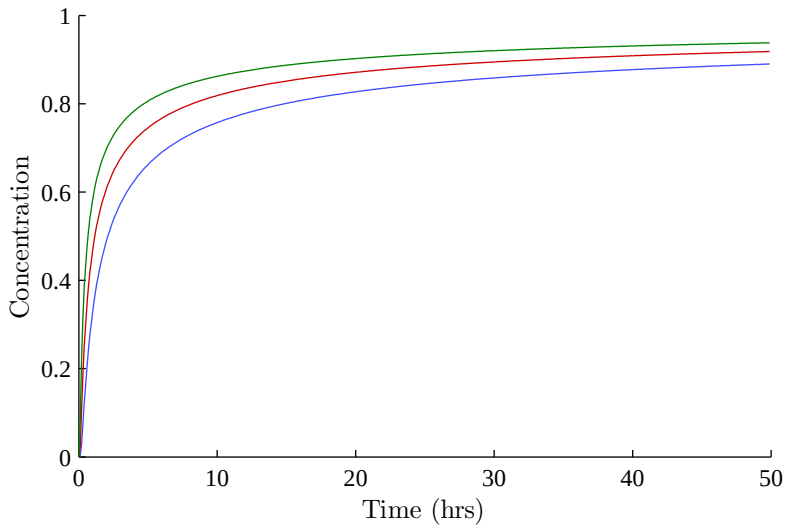

Figure 5.14: Graph of the concentration against time for a depth of 2.25 μm for several temperatures. Temperatures curves for 293 K (blue), 303 K (red), and 313 K (green) are plotted.

The calculated curve in Figure 5.14 for room temperature (shown in blue) shows the required time for the concentration in the PCF core to reach 80% of the concentration at the surface is around 18.4 hours. This time is significantly shortened as the temperature is increased, so that at a temperature of 313 K the calculated time taken for the core concentration to reach 80% is approximately 4.75 hours.

This is significantly faster than the usual diffusion times used in industry, which can take between several days and several weeks depending on the system [127, 128, 129]. Conventionally, such as in the writing of fibre Bragg gratings, pressures of up to 100 bar or more are needed, where the fibre is placed in an atmosphere of the gas, the molecules of which need to diffuse through the full radius of the fibre to reach the core. This all requires large pieces of specialist equipment, and can take a long time to carry out.

Figure 5.15 shows the gas concentration build up over time at room temperature for a depth of 2.25 μm, compared with more the conventional 62.5 μm depth needed for loading an all solid 125 μm fibre in industry. The 2.25 μm curve reaches high concentration values within only a few hours, whereas the 62.5 μm curve has barely reach 0.01% after 50 hours of diffusion. The need to accelerate this process is what drives the use of such high pressures and temperatures in industry, and this comparison shows why high pressures and temperatures were not necessary when D_2 loading a length of PCF that has a 2.25 μm radius core. Also, because the gas could be introduced through the

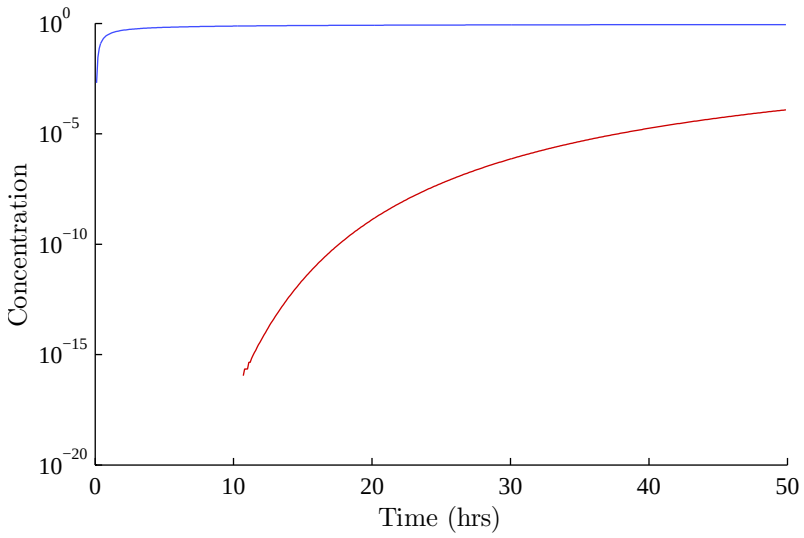

Figure 5.15: Comparison between the concentration build up over time at room temperature for a depth of 2.25 μm (blue), and a depth of 62.5 μm (red). 2.25 μm is analogous to the PCF fibre, loaded with D_2 through the microstructure holes, and 62.5 μm is analogous to an all-solid silica fibre, loaded from the outside as in industry.

holes of the microstructure, there was no need to immerse the fibre completely in a gas atmosphere, making the equipment needed much simpler.

Despite the high temperature dependence of the diffusion, as seen in Figure 5.14, carrying out D_2 loading at room temperature was considered to be sufficient and simpler than heating the fibre. In addition, it was expected that only a relatively low deuterium gas pressure in the fibre core would be needed to cover the majority of NBOHC sites, so achieving core gas pressures of tens of atmospheres would be unnecessary.

It was decided to introduce the deuterium at a pressure of 2 bar for 8.5 hours at room temperature, after which it was calculated that the deuterium gas pressure in the core would be approximately 1.4 bar, or a density of approximately 3.5×10^{25} molecules m^{-3} assuming an ideal gas at this pressure. The D_2 loading experiment is shown in Figure 5.16.

A length of 3 m of untreated supercontinuum fibre was chosen for loading. Due to the fact that the free deuterium gas in the fibre core would immediately begin to diffuse back out of the core after D_2 loading, the fibre was spliced to the pump laser prior to loading. This meant the gas could be introduced from only one end, as the other was

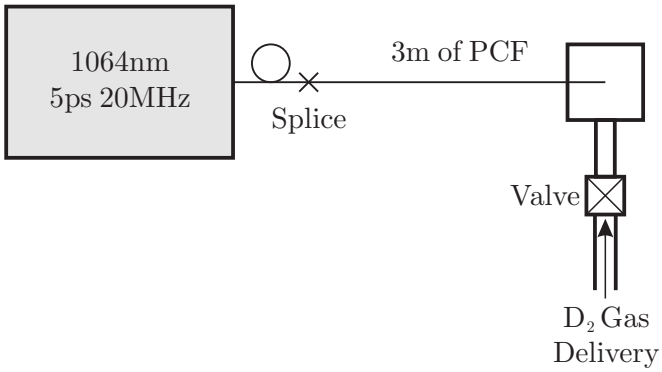

Figure 5.16: Diagram of the experimental setup for D_2 loading 3 m of fibre with D_2. Fibre was spliced to the output of the 1064 nm laser prior to loading.

then blocked. To verify the gas would load into the fibre in a fluid-like manner, the mean free path of the deuterium molecules was calculated using the equation

$$L_{mfp} = \frac{k_B T}{\sqrt{2}\pi m^2 p} \tag{5.3}$$

where k_B is Boltzmann's constant, T is the temperature in kelvin, m is the molecule diameter in meters, and p is the pressure in pascals. At 2 bar, this gives a mean free path of approximately 320 nm, and therefore it is reasonable to conclude that the fibre, with holes of around 5 μm in diameter, would fill in an even and fluid-like manner.

The deuterium was then introduced at a pressure of 2 bar through a gas cell attached to the end of the fibre. After 8.5 hours the fibre was removed from the gas cell and the end face was immediately sealed, since the deuterium would immediately begin diffusing back out of the fibre core, as described earlier in Chapter 4. The sealing of the end of the fibre meant that the rate of the outward diffusion of the deuterium gas would be slowed, maintaining a higher D_2 population in the glass for a longer period.

5.6.3 Photo-Darkening Exposure

Prior to exposure, the fibre laser used previously was replaced with one of a higher power. The formerly used laser had been damaged and was therefore not available to provide the exposure for the D_2 loaded fibre. The new laser, like the old one,

was a 1064 nm, 5 ps, 20 MHz model manufactured by Fianium Ltd. However, the maximum power of this model was 6 W, where as the previous model had been 4 W. However, setting the power level to 4 W on this new model did not reliably reproduce a supercontinuum broad enough to reach down to 400 nm, and therefore the total power was kept at the higher 6 W. This resulted in a higher 1064 nm peak in the supercontinuum, but the spectra were otherwise identical to those generated by the previous laser. As with the earlier splices, the power in the visible range from 350 nm to 750 nm was at least 200 mW, while the total average power in the supercontinuum was kept approximately equal to that of previous exposures.

The pump laser was switched on and left for 100 hours immediately after the D_2 loading period to induce photo-darkening in the fibre. The resulting changes to the supercontinuum over time is shown in Figure 5.17.

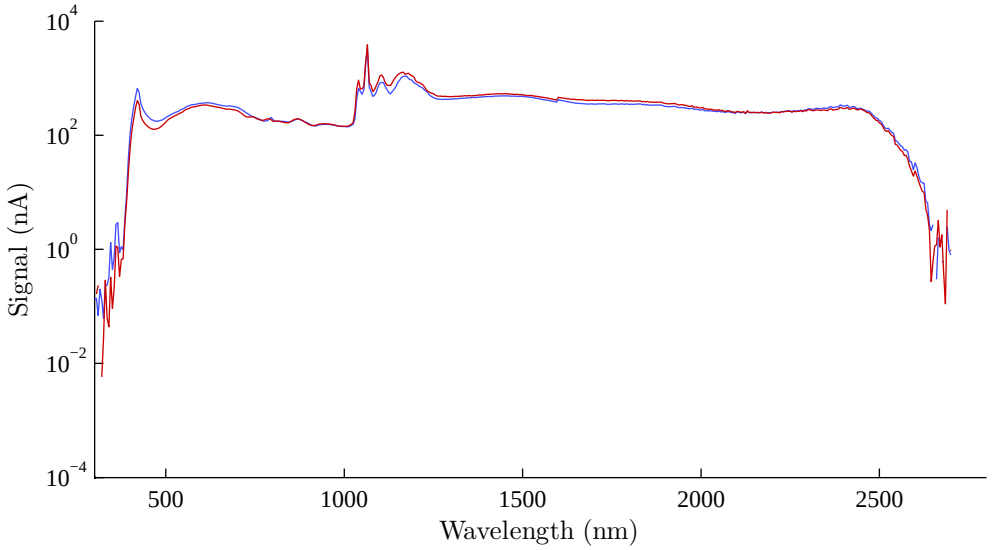

Figure 5.17: The generated supercontinuum from the D_2 loaded fibre, showing data from the start (blue) and the end (red) of the 100 hour exposure. Data was recorded using the spectrometer, at a resolution of 5 nm.

The intensity of the supercontinuum is seen to shift significantly over the 100 hour exposure time, falling in signal strength over the whole of the spectrum between 400 nm and 1000 nm, while the region towards the long wavelength edge is also seen to fluctuate over time. It is unlikely that this is an effect due to photo-darkening in the fibre, and more likely to be due to some heat-driven changes to the splice connecting the D_2 loaded fibre to the fibre laser, as a result of the higher pumping power. Alternatively, this could result from fluctuations over time in the output power of the fibre laser

itself. These two conclusions can be justified from the observation that the changes to the supercontinuum over time are approximately uniform across the whole spectrum, rather than centring on the development of the known photo-darkening absorption bands for NBOHC sites, as was seen in the data shown in Figure 5.5 for the untreated fibre earlier on in the chapter.

Aside from the changes to the whole supercontinuum as a result of suspected damage to the splice, there is little evidence of photo-darkening in the region from 600 nm to 630 nm.

5.6.4 D_2 Loaded Fibre Loss After Photo-Darkening

After exposure, the fibre loss was measured in the same manner as the untreated and annealed fibres, taking measurements from three 20 cm cutbacks followed by a final 50 cm cut back. The loss over the 400 nm to 800 nm range for both spectrometers is shown in Figure 5.18, again after having been combined and averaged. Once again, the small discontinuity observed at 400 nm is as a result of the shorter range of the OSA spectrometer.

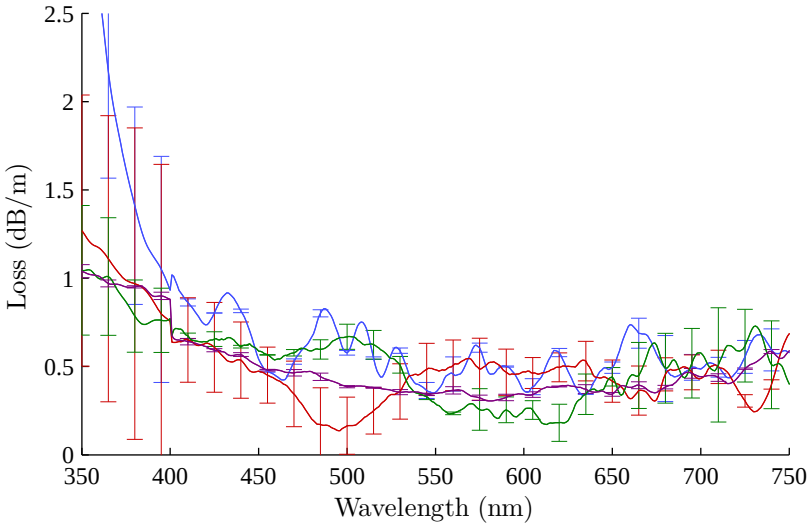

Figure 5.18: The loss of the D_2 loaded fibre over the 350 nm to 750 nm range after photo-darkening, for cut backs over the first 20 cm (blue), second 20 cm (red), third 20 cm (green), and the final 50 cm (purple) of fibre. Data was recorded by both the Bentham spectrometer (350 nm to 750 nm, resolution 5 nm) and the OSA (400 nm to 750 nm, resolution 1 nm), before being combined into one data set.

The loss over this wavelength range is shown to be almost completely flat, with no evidence of photo-darkening in the fibre over any of the cut back lengths. Compared with the loss in the untreated and D_2 annealed fibres, the D_2 loading shows similarly low loss to the D_2 annealed fibre in Figure 5.11, suggesting a strong presence of OD groups at generated NBOHC sites. However, the loss is seen to oscillate around the 0.2 $dBkm^{-1}$ to 0.5 $dBkm^{-1}$ region, with larger error bars than previously encountered, between 0.1 $dBkm^{-1}$ to 0.2 $dBkm^{-1}$ along the length of the fibre. This potentially as a result of the D_2 loading. While forming OD groups at the newly created NBOHC sites, the free D_2 in the glass may also be causing the increased variation in the measured loss values and the error. This could be tested by allowing the remaining population of free D_2 to diffuse out over time prior to measuring the fibre loss. Alternatively, the observed increase in the variation could be the result of an effect from the new laser, or a small variation in the xenon discharge lamp, both possibilities could be investigated further with repeat tests.

The data taken by the Bentham spectrometer also shows the same short wavelength increase in the loss at the 350 nm edge for the first 20 cm as seen in the other fibres. However, the strength of this loss curve is greater than seen previously, rising to above 3.3 dBm^{-1} for 350 nm, with an error of 0.5 dBm^{-1}. This suggests that the cause of this feature is in fact not the 213 nm and 258 nm absorptions from NBOHC sites and E' centres, since no population of NBOHC sites is inferred from the loss at 630 nm. It is notable that this behaviour was observed for each of the remeasured spectra for the first 20 cm prior to cutting back (described earlier at the start of Subsection 5.4.1), and it is therefore unlikely that the behaviour is the result of a single poor fibre cleave. It is also possible that the cause of this feature is not necessarily the same as that for the curves seen in the untreated and D_2 annealed fibres, since the magnitude of this curve is so much higher. Alternative explanations include an effect from residual D_2 present in the glass, or a physical change in the configuration of the Bentham spectrometer between the first 20 cm and the cut back to the second 20 cm. This could be further investigated by carrying out the same experiment using a different spectrometer, or by repeated D_2 loading experiments at a variety of lower pressures, and observing any resulting changes in the curve.

The expected location of the peak at 1380 nm is shown in Figure 5.19. However, no absorption peak is seen at 1380 nm, which would have indicated the presence of OH groups in the fibre. Instead, a strong peak of approximately 0.9 $dBm^{-1} \pm 0.2$ dBm^{-1} is seen around 1265 nm in the first 20 cm of the fibre, which matches the location

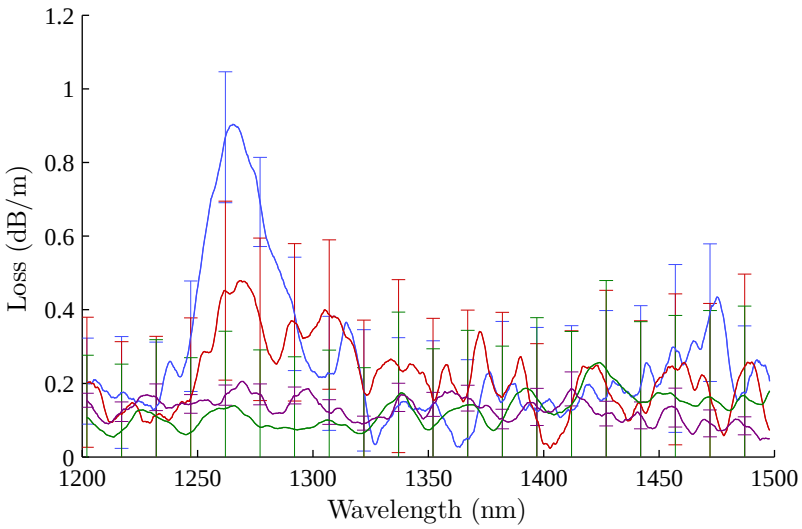

Figure 5.19: Graph of the loss at 1380 nm for the D_2 loaded fibre, recorded using the OSA at a resolution of 10 nm. The first 20 cm (blue), second 20 cm (red), third 20 cm (green), and the subsequent 50 cm (purple) are shown.

of a known absorption band for the OD group second overtone. Compared with the peak seen at the same spectral location in Figure 5.9 for the D_2 annealed fibre, this D_2 loaded 1265 nm peak in the first 20 cm is around 10.5 times greater in strength, being around 900 $dBkm^{-1}$ compared with 85 $dBkm^{-1}$ for the D_2 annealed fibre. This is strongly suggestive of a large population of OD groups in the glass over the first 20 cm of the fibre. This 1265 nm peak is then observed to be closer to 0.45 dBm^{-1} $\pm$ 0.2 dBm^{-1} over the next 20 cm piece, then falling off completely so that over the last 20 cm and the 50 cm of fibre the loss is flat, with the only variation being due to noise.

The error over this wavelength range is observed to be relatively consistent at around $\pm$ 0.2 dBm^{-1}, despite the changing density of OD sites along the fibre length. This is also a similar value to the error observed in the two other photo-darkened fibres, suggesting that any greater variation in error brought about by the presence of residual D_2 in the glass seen at shorter wavelengths does not appear to have an effect in this spectral region.

An explanation for the complete absence of the OH peak at 1380 nm is found in the expected exchange mechanism between OH and OD groups detailed earlier in Chapter 4. As the population of free D_2 in the silica glass was very high during the exposure period, it is possible that OH groups exchanged with the D_2, freeing up H_2 and forming OD

groups. However, an activation energy is required for the exchange [134, 136, 135, 131], suggesting either that the temperature was high enough in the fibre, as a result of the propagating high power pump, or that the high energy photons at the short wavelength edge of the supercontinuum were providing enough energy to enable the mechanism.

Even though this process is reversible and neither D_2 or H_2 has precedence over the other, the far greater population of D_2 resulted in a very low final population of OH groups, placing the strength of the characteristic 1380 nm absorption peak into the noise band.

Finally, the loss at 1880 nm was measured to confirm that OD groups were now present in the silica glass structure. The resulting loss curve is shown in Figure 5.20.

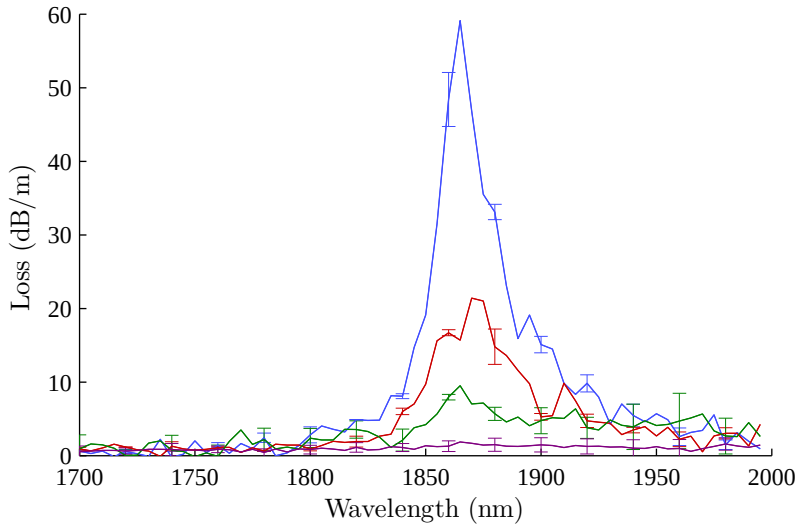

Figure 5.20: Graph of the loss at 1880 nm for the D_2 loaded fibre, using the Bentham spectrometer at 10 nm resolution. The first 20 cm (blue), second 20 cm (red), third 20 cm (green), and the subsequent 50 cm (purple) are shown. Data was recorded using the spectrometer, at a resolution of 5 nm. The y-axis has been necessarily rescaled compared to previous equivalent graphs for the untreated and D_2 annealed fibres.

The peak indicates the presence of OD groups in very large quantities in the first 20 cm, peaking at about 60 dBm^{-1} in strength, with an error of around $\pm$ 9 dBm^{-1}. Compared with that of the D_2 annealed fibre in Figure 5.13, this loss is around 12 times stronger, definitively demonstrating that a large population of OD groups have formed in the fibre during exposure to the high power laser. The 1880 nm peak is also approximately 60 times greater the strength of the 1265 nm peak, as expected from

previous research [131].

The second and third consecutive 20 cm sections of fibre and the final 50 cm all show peaks in the loss at 1880 nm that each decrease in size compared with the first, being 20 ± 2 dBm^{-1}, 10 ± 1.5 dBm^{-1}, and 1.2 ± 0.8 dBm^{-1} respectively. This shows the OD groups formed were immediately preceded by the formation of NBOHC sites in the first sections of fibre under exposure to photons from the high power pump, just as seen earlier in the untreated fibre. The presence of a large population of free D_2 in the glass allowed for these sites to immediately be converted to OD groups, explaining the observed length dependence of the 1265 nm and 1880 nm peaks, whereas in the D_2 annealed fibre the 1880 nm loss peak was homogeneous along the full fibre length.

5.7 Comparing Defect Contents

After photo-darkening and measuring the loss for each of the three untreated, D_2 annealed, and D_2 loaded fibres, a direct comparison could be made. From this an understanding of the concentration of NBOHC sites along the length of the fibres could be developed.

Figure 5.21 shows the loss values at different points along the length of each of the three fibres around 630 nm, using data shown previously in Figures 5.6, 5.11, and 5.18, and measured using the Bentham spectrometer and the OSA before being combined in those Figures. Due to the broad wavelength range of the NBOHC loss band around 630 nm, the data in each case was averaged over several values, from 628 nm to 632 nm.

As expected based on the data in Figure 5.6, Figure 5.21 shows that the average loss over this wavelength range for the untreated fibre, where there was no population of D_2 to deplete the NBOHC population, is observed to be higher than for either of the D_2 treated fibres, before appearing to decay away. The length data for this fibre shown in Figure 5.21 appears to follow a trend, and was consequently fitted with an exponential curve, shown in blue, which appears to correlate quite well. It should therefore be possible to make a prediction regarding the rate of change of the loss over this wavelength range.

Figure 5.21 includes an exponential decay curve (shown in blue), chosen to best fit within the error estimates of the data set. This is a similar form to equation 2.22 given

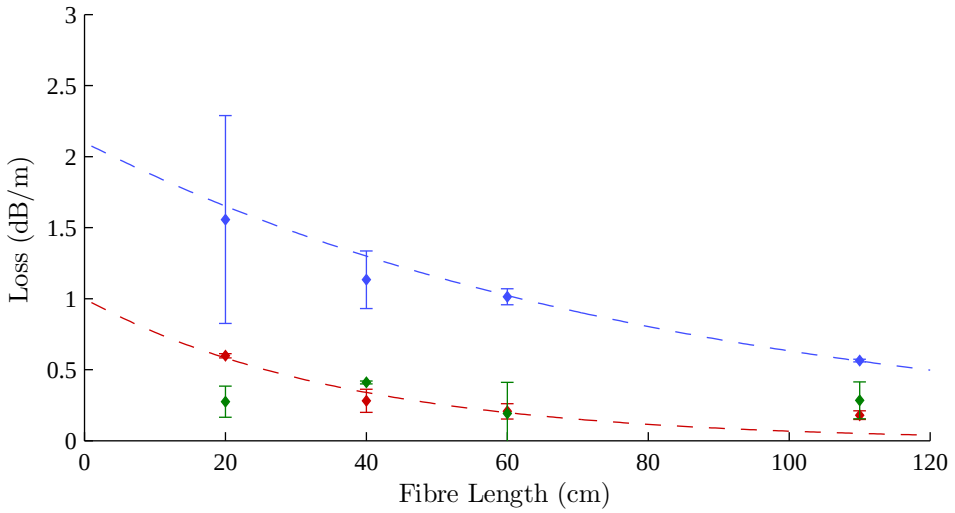

Figure 5.21: Loss values along the length for each of the untreated (blue), D_2 annealed (red), and the D_2 loaded (green) fibres around 630 nm, based on the averaged data recorded using the Bentham and OSA spectrometers. The loss and error values used were averaged over 628 nm to 632 nm. Exponential trend lines are included for the untreated (blue dashed) and D_2 annealed (red dashed) fibres.

earlier in Chapter 2, and is defined as

$$l_x = l_0 \exp^{-\sigma L}, \tag{5.4}$$

where loss values l are in dBm^{-1} and lengths L are in meters. From this, the constant representing the rate of change of loss in the fibre, σ, as a result of the changing density of NBOHC defects in the untreated fibre, can be estimated to be around 1.2 m^{-1}, or an effective "half life" of about 57.7 cm. The initial loss at the start of the fibre, l_0, where the population of defects would be expected to be at a maximum, is estimated to be around 2.1 dBm^{-1}. However, this value could be an overestimation if the photo-darkening exposure caused the NBOHC population, and hence the loss, to saturate at shorter lengths of fibre.

The data points for the D_2 annealed and D_2 loaded fibres, shown in red and green respectively in the plots of Figure 5.21, are observed to be generally lower than those of the untreated fibre. As in Figure 5.11, the data for the D_2 annealed fibre shows a small increase for the short fibre lengths, suggesting some photo-darkening took place,

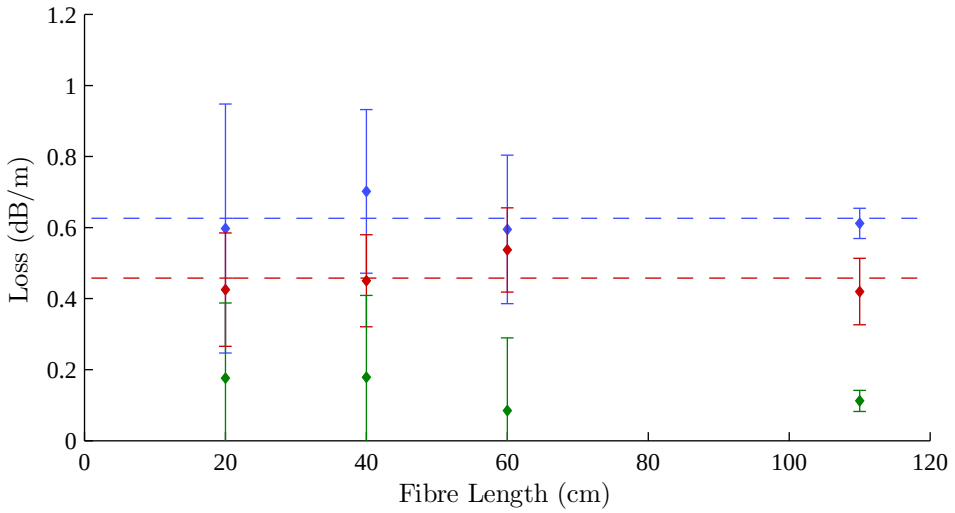

Figure 5.22: Loss values along the length for each of the untreated (blue), D_2 annealed (red), and the D_2 loaded (green) fibres at 1380 nm, based on data recorded using the OSA. The loss and error values used were presented earlier in the chapter, and were averaged from 1377 nm to 1383 nm. The average loss values for the untreated (blue dashed) and D_2 annealed (red dashed) fibres are also shown.

despite the purging of most strained bonds during the D_2 annealing process. As with the untreated fibre data, an exponential curve was fitted for the D_2 annealed fibre (shown in red). The data point at 110 cm was disregarded, due to there being no evidence of the OD absorption peak at this length in Figure 5.11 earlier, and was presumably too weak to appear above the noise floors of the two spectrometers. Using the same analysis as for the untreated fibre results in an estimated initial loss of 1 dBm^{-1} with a σ value of 2.7 m^{-1}, or a "half life" of 25.7 cm. This is more than half that of the untreated fibre, and shows that while the D_2 annealing process is effective at breaking strained bonds and replacing potential NBOHC sites with OD groups, it is still imperfect, and some NBOHC sites are still formed.

In contrast, the D_2 loaded fibre shows no evidence of an exponential decay along the length of the fibre, suggesting a population of NBOHC sites after photo-darkening exposure which is low enough as to be effectively undetectable using this method.

Figure 5.22 shows the absorption peak at 1380 nm for the three fibres, again plotted along the fibre length in each case, and using the data recorded on the OSA shown earlier in Figures 5.7, 5.12, and 5.19. The data was averaged over the 1380 nm absorption peak, from 1377 nm to 1383 nm.

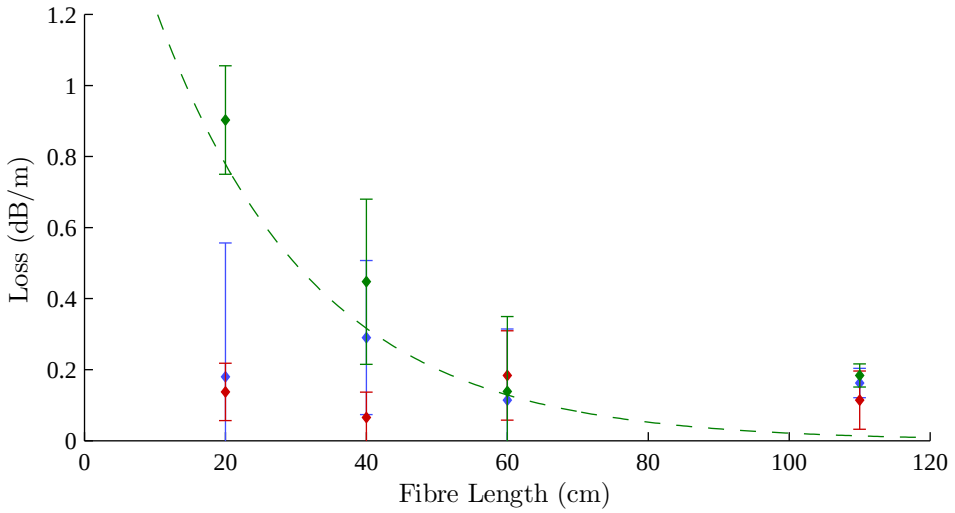

Figure 5.23: Loss values along the length for each of the untreated (blue), D_2 annealed (red), and the D_2 loaded (green) fibres at 1265 nm, based on data recorded using the OSA. The loss and error values used were presented earlier in the chapter, and were averaged from 1264 nm to 1266 nm. The fitted curve for the D_2 loaded (green dashed) fibre is also shown.

The values for the untreated fibre reflect the trend seen earlier in Figure 5.7, with the 1380 nm loss staying approximately constant along the fibres length. The average value of this loss, shown as the dashed blue line, is calculated to be approximately 0.62 dBm^{-1}, with a maximum error of $\pm$ 0.35 dBm^{-1}. The average loss at 1380 nm for the D_2 annealed fibre is shown as a dashed red line, and is calculated to be approximately 0.46 dBm^{-1}, with an error of $\pm$ 0.16 dBm^{-1}. As shown earlier in Figure 5.19, the loss at 1380 nm for the D_2 loaded fibre is low enough to be below the noise floor of the OSA, and therefore any average calculated of the values would be meaningless.

Figure 5.23 shows the loss values around 1265 nm along the length of the three fibres, also taken from Figures 5.7, 5.12, and 5.19. As discussed earlier, this wavelength is the expected location of the absorption peak of the second overtone of any OD groups present in the fibre.

The untreated fibre was observed in Figure 5.7 to not have a population of OD groups, and so the data point 40 cm, while having a higher average value and large error bars, can still be regarded as broadly consistent with that conclusion. The D_2 annealed fibre was also seen in Figure 5.12 to have no significant absorption peaks at 1265 nm, the second overtone of the OD groups being so weak as to fall below the general noise level of approximately 0.2 dBm^{-1} over short lengths of fibre. However, the D_2 loaded fibre

did show a significant absorption peak at 1265 nm in Figure 5.19, indicating a strong population of OD groups. Given that the NBOHC population in an untreated fibre was observed to decrease exponentially in Figure 5.21, the absorption peak at 1265 nm could be expected to also follow an exponential decay with fibre length, considering that OD groups are expected to form in regions where there is a high NBOHC defect population. The green dashed curve in Figure 5.23 fits the data points at 20 cm, 40 cm, and 60 cm, confirming this exponential decay trend. As in the earlier case of the D_2 annealed fibre in Figure 5.21, the data point at 110 cm was disregarded, since there was no evidence of the OD absorption peak at this length in Figure 5.19 earlier, and was likely to be too weak to appear above the noise floor.

The green curve takes the same form as in equation 5.4. Here the estimated rate of change of attenuation, σ, for the falling concentration of OD groups along the fibre, is around 4.5 m^{-1}, or an effective half life of 15.5 cm, with an initial loss l_0 of 1.92 dBm^{-1}. As in the case of the NBOHC defects, this initial loss estimation could be exaggerated if the NBOHC population was saturated over the first few centimetres of fibre.

Figure 5.24 shows the loss values along the lengths of the three fibres around 1880 nm, where the first absorption peak of OD groups is expected to be found. This data was again taken from Figures 5.8, 5.13, and 5.20, and was originally recorded using the Bentham spectrometer.

It was previously verified in Figure 5.13 that the untreated fibre showed no evidence at 1880 nm of OD groups anywhere along the fibre. The D_2 annealed fibre was shown to possess an absorption peak at around 5 dBm^{-1} for all the tested fibre lengths. After averaging the D_2 annealed data from 1875 nm to 1885 nm for Figure 5.24, the average loss was calculated to be approximately 4.14 dBm^{-1}, with an error of $\pm$ 0.3 dBm^{-1}, and is shown in Figure 5.24 as a red dashed line. The OD population in the D_2 annealed fibre would not be expected to show an exponential decay, as observed in the D_2 loaded fibre, since those OD groups were formed in the glass before photo-darkening, and so are not linked to the NBOHC defect population.

As seen in the 1265 nm data in Figure 5.23, Figure 5.24 shows a clear exponential decay relationship for the D_2 loaded fibre. The green dashed curve highlighting this relationship is expected to share the same rate of change of loss constant σ as that used to fit the 1265 nm data in Figure 5.23, which was approximately 4.5 m^{-1}. The initial loss, l_0, at the start of the D_2 loaded fibre is expected to be 60 times stronger than the second OD group overtone at 1265 nm, and so was set to be approximately

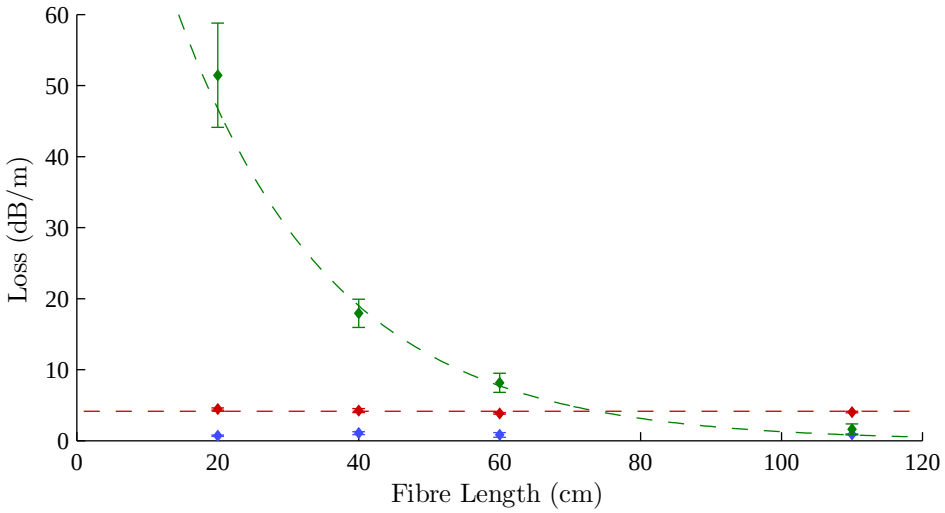

Figure 5.24: Loss values along the length for each of the untreated (blue), D_2 annealed (red), and the D_2 loaded (green) fibres at 1880 nm, based on data recorded using the Bentham spectrometer. The loss and error values used were presented earlier in the chapter, and were averaged from 1875 nm to 1885 nm. The average loss value for the D_2 annealed (red dashed) fibre and the fitted curve for the D_2 loaded (green dashed) fibre are also shown.

115 dBm^{-1}. This curve is observed to also fit the 1880 nm data well, and therefore the initial loss values l_0 for both 1265 nm and 1880 nm, and the attenuation constant value of 4.5 m^{-1}, or a half life of about 15.5 cm, can be considered as realistic parameters for describing the rate of fall in concentration of OD group population along the length of the D_2 loaded fibre.

5.8 Summary and Conclusions

To summarise and conclude, two structurally identical supercontinuum fibres were fabricated and nitrogen baked. One fibre was left untreated and one was annealed with D_2 to form a population of OD groups in the glass. The loss was measured for both fibres and it was verified that the fibre annealed with D_2 showed evidence of having OD groups present in the glass through a strong absorption peak around 1880 nm.

Both fibres were pumped by a high power laser at 1064 nm for 100 hours, each generating a wide supercontinuum which was periodically recorded by a spectrometer. Strong evidence of photo-darkening was observed in the untreated fibre through a drop over

time in the spectral intensity around 630 nm, while comparatively little evidence of photo-darkening was seen in the equivalent data for the D_2 annealed fibre. This was verified in both fibres through loss measurements carried out over several short cut-backs. Most photo-darkening was seen to occur in the first 20 cm of both fibres, after which the loss at 630 nm fell away exponentially, showing that the photo-darkening is driven by the high flux of photons from the 1064 nm pump [110]. The observed photo-darkening in the D_2 annealed fibre shows the process was effective, but not completely able to remove potential NBOHC sites from the glass. The strength of the absorption peak at 1880 nm in this fibre after high power laser exposure, from the second overtone of the OD groups, was shown to be unaffected by the laser exposure.

A length of untreated fibre was then loaded with D_2 at a pressure of 2 bar for 8.5 hours, before also being pumped by the 1064 nm laser to induce photo-darkening. The loss was then again measured, revealing a very strong absorption band at 1880 nm of around 60 dBm^{-1}, 12 times stronger than in the D_2 annealed fibre. No evidence of photo-darkening was observed in the D_2 loaded fibre compared with both the untreated or pretreated fibre cases. This is interpreted as the result of the population of free D_2 atoms present in the glass, binding to the NBOHC sites as they are created, thus forming the OD groups and their characteristic absorption bands at 1880 nm and 1265 nm. The characteristic OH absorption peak at 1380 nm is absent in the D_2 loaded fibre, and is explained as being due to the exchange mechanism between OH and OD groups in the silica glass (detailed in Chapter 4). It is theorised that the high power 1064 nm pump laser or the high energy photons in the supercontinuum provided the energy for the exchange mechanism to occur.

The relative strengths of the 1880 nm OD group absorption peaks in the D_2 annealed and D_2 loaded fibres was also observed to be significantly different, with the D_2 loaded fibre displaying 12 to 13 times the loss of the D_2 annealed fibre. This could be partially explained by the exchange mechanism between OD and OH groups, acting to boost the OD group population in the D_2 loaded fibre, whereas the D_2 annealed fibre lacked a large population of free D_2 during exposure to harness this effect. In addition, the D_2 annealing process could have also "relaxed" a number of strained bonds from the glass, as well as breaking strained bonds at potential NBOHC sites and forming OD groups. This would account for the difference in OD group populations between the D_2 annealed and D_2 loaded fibres, while still allowing for the D_2 annealed fibre to undergo some photo-darkening, as the final population of strained bonds were broken during the laser exposure.

The loss measured for different wavelengths was then plotted for different cut back lengths for each fibre, allowing for a direct comparison of the loss behaviour. This confirmed that the D_2 loaded fibre was successfully binding to NBOHC sites to form OD groups, as the photo-darkening behaviour in the untreated and D_2 annealed fibres followed an exponential trend, as did the OD peak at 1880 nm in the D_2 loaded fibre. This data was fitted with a curve and an estimated "half life" for the changing loss with length was then calculated for the photo-darkened NBOHC sites in the untreated and D_2 annealed fibres, as well as the OD groups in the D_2 loaded fibre. It was found that the loss around 630 nm in the untreated photo-darkened fibre, and presumably therefore the density of NBOHC sites, fell to half after about 58 cm. This is compared to the D_2 annealed fibre, where same absorption fell to half after about 26 cm. The OD group density in the D_2 loaded fibre, arising from OD formation at NBOHC sites and measured through the absorptions at 1265 nm and 1880 nm, halved after only about 16 cm. Unfortunately, because the absorption due to a single NBOHC site and a single OD group are not known, it is difficult to quantify the actual population density for each.

The difference in the loss "half lives" for the untreated fibre and the D_2 loaded fibre might be surprising, considering it would be expected that the OD groups in the D_2 loaded fibre substitute for the NBOHC sites. However, the additional process of the exchange mechanism between the OD and OH groups would increase the OD population density beyond that of the NBOHC sites. This might also follow an exponential relationship if the exchange were enabled by photons from the pump source.

The data for the D_2 loaded fibre showed that the new technique chosen to load the fibre with D_2 succeeded in suppressing the negative photo-darkening effects due to OH group formation to a point as being undetectable over the measured fibre lengths. This was more effective than that of the annealing method, which was unable to completely suppress the unwanted photo-darkening. The use of PCF allows for a relatively low D_2 treatment pressure of only 2 bar, carried out at room temperature for a relatively short time of only 8.5 hours, where previously far higher pressures and temperatures were necessary, over far longer periods [127, 128, 129].

This allows for more practical gas treatments for high power fibre systems to prevent photo-darkening effects, requiring only a small amount of table top equipment and short treatment times. A fast and effective method of loading the glass with deuterium is also particularly attractive for supercontinuum systems. As demonstrated here, a fibre can be treated after splicing to a supercontinuum device, using the supercontinuum

laser source itself to enable the formation of a large population of OD groups from NBOHC sites in the glass. Subsequent performance and supercontinuum bandwidth was also shown to be unaffected by the resulting strong OD absorptions at 1265 nm or 1880 nm.

5.9 Further Work

Further work that could be carried out on this topic includes a full understanding of the minimum population of free D_2 required to suppress the OH group formation and remove all NBOHC sites. The strength of the 1880 nm peak for the D_2 loaded fibre, and the suppression of the 1380 nm OH peak, suggests that 2 bar of pressure may be higher than is actually necessary to achieve the desired effect. Further research could aim to specify a more appropriate lower treatment pressure.

Research could also be carried out to understand the role of residual D_2 in the glass after loading and photo-darkening. If the excess gas is allowed to diffuse back out of the fibre over time after exposure to the pump source, does it affect the resulting loss data. For instance, does the 1380 nm OH peak slowly return, again as a result of the exchange mechanism between OD and OH groups.

Additional further work could be carried out observing NBOHC site formation during photo-darkening exposure, only now with a real-time termination of NBOHC sites with OD groups. This would be achieved by splicing the fibre to the fibre laser output, and then loading and sealing the fibre with D_2, and immediately exposing the glass to the high intensity 1064 nm pump laser during the diffusion period. It is expected that NBOHC sites could then be terminated with OD groups as they are formed, and the resulting spectral behaviour directly recorded in the same manner as carried out in the research described here.

Chapter 6

The Theory Behind Gas Discharge Lasers in Optical Fibres

6.1 Introduction

This Chapter concerns the theory behind gas discharge lasers, with a particular focus on systems using discharge tubes with internal diameters of less than 1 mm, where the gain in such lasers is expected to be higher than for tubes with larger internal diameters. The higher gain in these systems makes them ideal for harnessing lasing lines which are otherwise difficult to access, as well as the practical advantages offered through miniaturisation. This could prove to be useful for commercial applications where the inherently narrow linewidth of gas lasers is required. This is directly relevant to the research presented in Chapters 7 and 8.

The content of the Chapter covers the descriptions of the different mechanisms and processes that occur within the discharge, and the balance required between those processes to maintain the stability of a discharge over long periods of time. The importance of the electron temperature and gas pressure in discharge tubes with a sub-millimeter diameter, and how these values vary for different choices of gas, are described. Two different regimes of gas excitation are then explored; direct current (DC) and radio frequency (RF) field excitation, including the mechanisms, advantages and disadvantages

of each. Finally, the details of lasing for specific gas mixtures of helium neon (HeNe) and helium xenon (HeXe) are considered, again in the context of discharge tubes with a sub-millimeter internal diameter.

6.2 Previous Research

The concept of using an electrical discharge to achieve population inversion in a gas was first proposed by Fabrikant in 1939 [142], and later proposed as a method of building a laser in 1959 and 1960 [143, 144]. This was not achieved practically until 1961, when Javan, Bennett and Herriott [145] demonstrated an RF electrical discharge laser using a HeNe gas mixture. This laser operated at 1.15 μm, and used a discharge tube with a diameter of 1.15 cm and a length of 80 cm.

Since then, it has been recognised that gas discharge lasers with narrower tube diameters possess a higher gain [146, 147, 148, 149], and so one strand of gas laser research concentrated on achieving narrower discharge tubes. In 1971 Smith demonstrated a HeNe laser operating at 633 nm [150], with an inner discharge tube diameter of 430 μm, made from a specially straightened glass capillary. Due to instabilities encountered when using only a DC source as the excitation, this system used a combination of DC and RF to maintain the discharge. The difficulty in achieving stable discharges in narrow discharge tubes, and the increasing loss for narrower waveguides, resulted in relatively few papers being published in the following years. Smith presented a HeXe laser operating at 3.5 μm in 1973 [151], again using a combination of DC and RF excitation, inside a discharge tube of 250 μm. Other research achieved laser oscillation in tubes with inner diameters of 510 μm in 1975, and 490 μm in 1976 [152, 153]. In 2008, Shi et al. demonstrated stable discharges in straight discharge tubes of 260 μm in diameter and 26.2 cm in length, as well as flash discharges in tubes with smaller diameters [154, 155]. Their work also showed that DC excitation could be achieved with breakdown voltages of the order of tens of kilovolts.

6.3 Dynamics of a Gas Discharge

The breakdown of a gas into a gas discharge, sometimes referred to as a glow discharge, is most simply defined as the partial ionisation of a population of atoms in the gas by

an applied electric field. This occurs first through the production of a population of primary electrons by the applied field, either emitted from partially ionised atoms in the gas or from a cathode plate. The electrons are then accelerated by the field, colliding with neutral atoms to both produce a population of secondary electrons and excite the atoms to a higher energy state.

In a sufficiently excited gas discharge, these atoms can achieve a population inversion at certain metastable energy levels. The atoms then emit photons as electrons transition from those states to lower energy states, allowing the gas in the discharge to lase. Systems such as this can harness either the neutral or ionised atomic populations to lase, depending on the fraction of ionised atoms in the gas compared to the remaining neutral atoms.

6.3.1 Collisions in a Gas Discharge

Collisions in a gas discharge are responsible for the transfer of energy between electrons and atoms in the gas, as well as the production of the free electron population through ionisation. There are many different collision processes that can potentially participate, depending on the atomic species present and the electron energy distribution, and these can generally be broken down into several types; elastic collisions, inelastic collisions, and superelastic collisions.

Elastic collisions between electrons and atoms occur throughout the discharge, as the electrons (having a far lower mass than the atoms) move with a greater random velocity, occasionally encountering an atom and interacting with it to alter its kinetic energy and direction of motion. While there is a transfer of kinetic energy as a result of this type of collision, there is no change to the internal energy state of the atom, and so elastic collisions are not directly responsible for the excitation or ionisation of the atomic species.

Inelastic excitations occur through collisions between fast (high energy) electrons and atoms, as well as collisions between atoms. In the case of collisions between electrons and atoms, the energy is transferred from the fast electron to excite the atom into a higher energy state, lowering the energy of the electron. Inelastic collisions between fast electrons and neutral atoms can also ionise atoms as well as excite them, adding to the overall electron population and serving as a source of free electrons to counter the electron loss processes in the discharge.

In the case of collisions between atoms, the energy is exchanged from an excited atom to another atom of the same or different species, leaving the second atom in an excited state. An example of an inelastic energy transfer between atoms would be

$$A' + B \rightleftharpoons A + B' \pm \Delta E_{\infty}, \tag{6.1}$$

where ΔE_{∞} is the energy difference between the excited states of atoms A and B. In order for exchanges of this type to occur frequently in a gas discharge, the energy difference needs to be small, as in the exchange between the Helium 2^3S_1 level and the Neon $3S_2$ level in a HeNe laser (discussed further in Subsection 6.5.1).

Collisions between atoms can also be a mechanism for ionisation and electron production, through the *Penning effect* [156]. This occurs when an atom in an excited metastable state collides with unexcited atom, transferring energy and ionising that atom, releasing an electron. This effect can be described as

$$A^* + B \longrightarrow A + B^{+'} + e^-, \tag{6.2}$$

and becomes possible in systems where the ionisation energy of atom B is less than the excited metastable energy of A^*, such as in a HeHg gas discharge [157], and to some extent in HeXe gas discharges [158].

Superelastic collisions are a further type of collision process present in a gas discharge. In this case a free electron collides with a neutral atom which is currently in an excited state, de-exciting the atom and transferring energy to the electron. This can potentially be a problem for the discharge dynamics of a gas laser. If the de-excited energy state is the metastable upper level in the desired lasing mechanism, then the superelastic collisions act to deplete that upper level, damaging the population inversion. Conversely, superelastic collisions can be favourable if they act to de-populate the lower energy levels in a lasing mechanism, acting as a boost to the population inversion.

The wide variety of collision processes that can occur in gas discharges is increased further still in the presence of molecules, such as in CO_2 gas lasers, although they are not relevant to this work and so are not described here.

The mean free path of an electron in a gas discharge is defined as the average distance

travelled by the electron between collisions. This can be defined mathematically for a gas mixture containing two species of particle, usually electrons and atoms or ions, using [159, 160]

$$\lambda = \frac{1}{N\pi \left(r_1 + r_2\right)^2 \left(1 + {}^{v_2^2}/_{v_1^2}\right)^{1/2}} \tag{6.3}$$

where N is the total number of particles cm^{-3}, r_1 and r_2 are the radii of the two types of particle, and v_1 and v_2 are their random velocities. This can be simplified when applied to electrons in a gas, so $r_1 = r_e \ll r_2 = r_{atom}$ and $v_1 = v_e \gg v_2 = v_{atom}$, reducing equation 6.3 to

$$\lambda_e = \frac{1}{N\pi r_{atom}^2} = \frac{1}{N\sigma_e}, \tag{6.4}$$

where σ_e is the electron-impact cross-section of the atom. The cross-section σ_e is actually energy dependent, due to the interaction between the electrons and the electron cloud and nucleus of the atom. As a result, the cross-sections for elastic, inelastic, and superelastic collisions in different atomic species vary with the average free electron energy. Figure 6.1 shows this curve for several noble gases, taken from research carried out in 1933 by Brode [161].

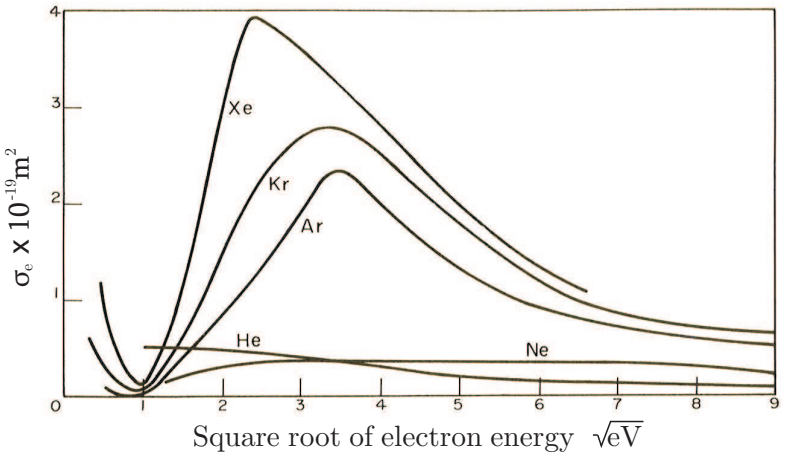

Figure 6.1: The curve of σ_e for changes in the square root of the electron energy, and therefore T_e, for each noble gas [161].

The mean free path of the electrons in the gas, as linked to the impact cross-section σ_e in equation 6.4, can be used to find the electron collision frequency f_e. The collision frequency is defined as

$$f_e = N\sigma_e v_e, \tag{6.5}$$

where v_e is the random velocity of the electrons, and is defined by the average energy of the electrons, or the electron temperature. Practically calculating f_e is difficult however, due to the energy dependence of the electron impact cross-section.

6.3.2 The Electron Temperature, $\mathbf{T_e}$

The mechanisms and processes present in a gas discharge rely strongly on the size and properties of the free electron population. Therefore to understand the physics behind a gas-discharge laser, it is necessary to understand the electron behaviour. The stability of the discharge is heavily reliant on the production and depletion rates of the free electron population, as well as on the average kinetic energy of the free electrons, known as the *Electron Temperature*, or T_e. High electron temperatures generally result in a greater degree of instability in a discharge, as it can result in higher depletion rates as fast electrons can reach and collide with the walls from a greater distance into the bulk gas, ultimately causing the discharge to fail. The higher energy of the electrons can also contribute to significant heating of the gas envelope as increasing amounts of energy are deposited into the material, potentially resulting in damage. High values of T_e are determined by the type of applied electric field, the electric current through the discharge, the pressure of the gas, and the different atomic species present in the gas.

The electron density and temperature of a stable glow discharge is most often in the range from 10^{16} m^{-3} to 10^{20} m^{-3} and 10,000 K to 100,000 K [148]. It is necessary for stability that the discharge maintains a quasi-neutral charge, meaning that the population density of the free electrons is approximately equal to the population density of the ionised atoms, and is distributed evenly throughout the RF driven discharge, and in the positive column section of the DC driven discharge. The various regions of and the functional differences between RF and DC driven discharges, such as the positive column, are discussed later in Section 6.4.

When the electron population is high, usually above 10^{16} m^{-3}, and in thermodynamic equilibrium, the electron temperature can be defined by applying a Maxwellian distribution to the electron velocities, leading to

$$\frac{m_e \left\langle v_2^2 \right\rangle}{2} = \frac{3kT_e}{2}, \tag{6.6}$$

where $\left\langle v_2^2 \right\rangle$ is the mean square velocity of the free electrons, m_e is the electron mass, and T_e is given in degrees kelvin. The effect on the electron velocity from the applied field is small, meaning the thermal energy dominates and electron motion is therefore predominantly random in direction rather than directed towards the anode.

6.3.3 The Debye Length

An issue relevant when considering discharges in discharge tubes with small diameters is the Debye length, λ_D. This is defined as the distance from the walls of the discharge tube over which effects from the walls of the cell are important, affecting the local quasi-neutrality of the discharge in that region. Beyond this distance the charged particles in the gas discharge are effectively screened from the walls by the other charges in the gas, maintaining a quasi-neutrality. In cells with larger diameters of more than 1 mm, this effect near the walls is largely irrelevant since the bulk volume of the gas is so much larger than the volume within one Debye length of the walls. However, in systems where the cell radius is small enough for the volume within the Debye length to be comparable to the volume of the bulk gas, the effect at the cell walls becomes more important. Using a few assumptions about the behaviour of the gas [162], the Debye length can be obtained from Poisson's equation;

$$\lambda_D = \left[\frac{k_B \epsilon_o}{ne^2 \left[\frac{1}{T_e} + \frac{1}{T_+} \right]} \right]^{\frac{1}{2}}, \tag{6.7}$$

where k_B is Boltzmann's constant, T_+ is the ion temperature, or average kinetic energy of the partially ionised atoms, and n is the total density of particles. If it is assumed that the more massive ions in the gas are moving very slowly or are effectively stationary, then their contribution can be removed and the expression can be simplified to [163]

$$\lambda_D = \left[\frac{k\epsilon_o T_e}{n_e e^2}\right]^{\frac{1}{2}} = 69\sqrt{\frac{T_e}{n_e}}\text{meters} \tag{6.8}$$

which, given the aforementioned ranges of electron temperatures T_e and electron densities n_e, results in values of λ_D over a range from approximately 500 nm to several hundred microns. If the Debye length is comparable to or larger than the radius of the discharge tube used, which is possible in small bore systems, then the bulk discharge is unable to screen the effects of the discharge tube walls, and they start to change the behaviour of the discharge.

6.3.4 The Electron Temperature and the *pd* Product

As mentioned earlier, the average electron temperature T_e, and thus the average velocity of the electrons in the discharge, is linked to the dimensions of the discharge tube and the gas pressure, in addition to the applied field and choice of atomic species. This can be shown by equating the rate of free electron production through ionisation in the discharge to the rate of free electron loss through diffusion, for the dimensions of a given discharge tube.

It is assumed that there is net charge neutrality in the discharge, that the mean free paths of the electrons and ions are less than the radius of the discharge tube, and that the discharge tube has a radius which is larger than the Debye length. The number of ions produced per cm^3 per second is equal to

$$q = \alpha n_e, \tag{6.9}$$

where α is the ionisation rate per electron and n_e is the electron concentration per cm^3. If the discharge tube is assumed to be cylindrical, and the rate of production is equal to the rate of diffusion loss, meaning that the discharge is stable, then

$$\frac{kT_e}{e}\left(\frac{d^2 n_e}{dr^2} + \frac{1}{r}\frac{dn_e}{dr}\right) + \left(\frac{\alpha}{b^+}\right) n_e = 0 \tag{6.10}$$

where r is the radius of the discharge tube, and b^+ is the ion mobility [146]. The

solution to this equation is a zero-order Bessel function with boundary conditions of $n_e = 0$ at $r = R$, which gives

$$\frac{\alpha}{b^+} = \frac{kT_e}{e}\left(\frac{2.405}{R}\right)^2. \tag{6.11}$$

The rate of ionisation α is described as being dependent upon the gas pressure p, the electron temperature T_e, the ionisation potential V_i (in volts), and the initial slope of the ionisation mean free path curve a (in volts^{-1}). Work by von Engel [146] states that α is approximately equal to

$$\alpha \approx 600\left(\frac{2}{\pi}\right)^{\frac{1}{2}}\left(\frac{e}{m_e}\right)^{\frac{1}{2}} apV_i^{\frac{3}{2}}\left(\frac{kT_e}{eV_i}\right)^{\frac{1}{2}} e^{-{}^{eV_i}/_{kT_e}}, \tag{6.12}$$

and can therefore be substituted into equation 6.11 and simplified, so

$$\left(\frac{kT_e}{eV_i}\right)^{\frac{1}{2}} e^{{}^{eV_i}/_{kT_e}} = 1.2 \times 10^7 \left(CpR\right)^2, \tag{6.13}$$

where C is a constant equal to $|\frac{aV_i^{\frac{1}{2}}}{b^+ p}|^{\frac{1}{2}}$. The values of V_i, a, and p are in volts, cm, and Torr respectively. For simplicity when applying this to experiments, the radius R can be converted to the internal diameter d of the gas discharge tube, and so will be referred to as such for the remainder of this work. This relationship can then be plotted, showing how the electron temperature per volt of ionisation potential T_e/V_i generally changes with Cpd, and is shown in Figure 6.2.

The curve in Figure 6.2 shows that the electron temperature becomes increasingly high as the values of p and d get smaller. It is notable that reducing a discharge tube diameter from a value of the order of a few centimetres to one of the order of a few microns results in approximately a factor of ten increase in the value of T_e/V_i. This is because of the increased rate of loss of ions in smaller-bore discharge tubes due to the cell walls, resulting in fewer collisions between free electron and atoms, higher free electron velocities, and therefore a higher average value of T_e.

As the value of pd gets smaller, equations 6.4, 6.8, and 6.13 show that the electron mean

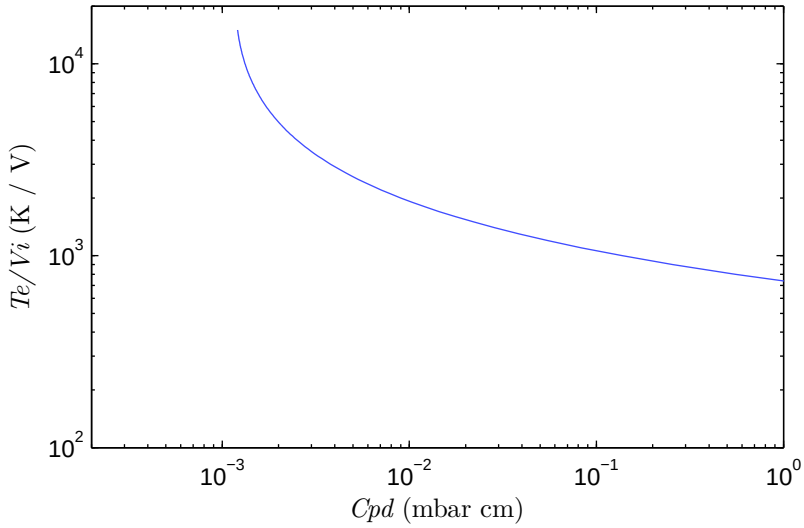

Figure 6.2: The curve of T_e/V_i for changes in Cpd, calculated from equation 6.13. Values have been converted from equation 6.13 so the plot is for the diameter d of the tube and pressure p is in mbar rather than Torr.

free path, the Debye length, and the electron temperature all get larger, resulting in a discharge tube diameter below which the electron temperature is so high and the Debye length so large that the discharge dynamics can no longer be predicted with any certainty. This is because, as stated earlier, the bulk of the discharge can no longer maintain quasi-neutrality within one Debye length of the discharge tube walls, and the average electron energy is so high that the electron mean free path approaches the discharge tube radius, and unpredictable losses at the walls become a source of instability across the discharge as a whole.

When designing gas laser systems with diameters of less than 1 mm, it is necessary to maintain the optimum value of pd in order to set the size of T_e such that the collision cross-section is maximised, as shown in Figure 6.1. Therefore, the pressure p is increased to compensate for the lower value of d, raising the number of atoms present and the number of electron collisions, limiting the electron temperature.

Due to the dependence of equation 6.13 on the nature of the gas, through V_i and a, the value of T_e for a given pd can be significantly different for different gases.

Unpublished work by R. T. Young in 1968 [147], shown later by Willett [148] in 1974 and below in Figure 6.3, shows how the electron temperature curve changes against pd for various noble gases.

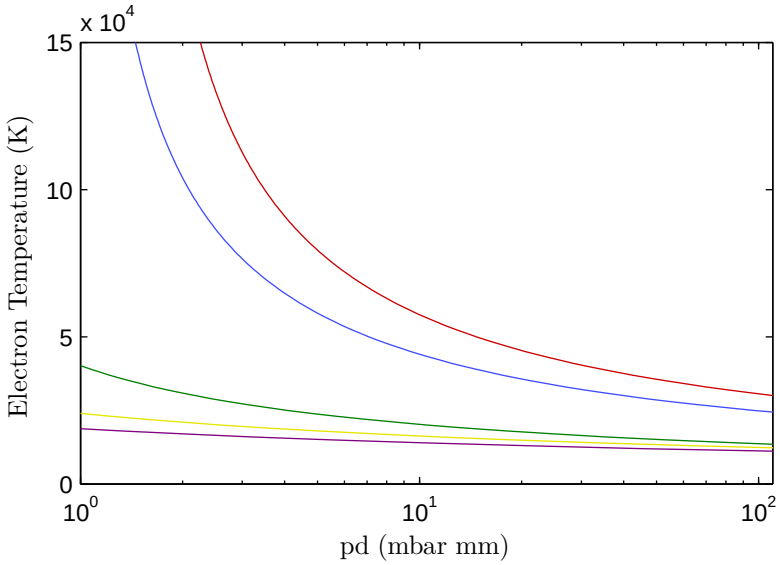

Figure 6.3: The change in T_e for changes in pd for He (red), Ne (blue), Ar (green), Kr (yellow), and Xe (purple), taken from unpublished work by R. T. Young in 1968 [147].

Ne and He are observed to have the highest T_e values for lower values of pd, for example having approximate predicted electron temperatures of around 112,000 K and 76,000 K for pure He and Ne respectively at a pd of 3 mbar mm. Xe, Kr and Ar however, are predicted to have far lower average electron temperatures, with a 5:1 mixture of HeXe having an approximate predicted value of T_e of 25,000 K to 30,000 K for a pd value of 3 mbar mm [147]. Young's predictions of electron temperature have been found to be similar to experimental values [164, 165] for pd values of 2.5 mbar mm or above.

The reason for the lower electron temperatures in Xe, Kr and Ar is that the collision cross-sections for these gases are larger compared to those of He and Ne, as shown earlier in Figure 6.1 [161]. Higher cross-sections result in a greater frequency of collisions, and therefore a lower value of T_e. Xe, Kr and Ar also have higher ionisation efficiencies than He or Ne, which also effectively lowers the value of T_e through the constant C in equation 6.13. This implies that a HeNe gas laser operating with a low pd value is likely to experience a higher electron temperature and potentially more instability as the electron loss rate at the walls increases.

The gain for different emission lines is linked to the electron temperature, and consequently the operating pressure of the gas. This is due to the T_e dependence of the electron impact cross-section, shown in Figure 6.1, which defines the collision frequency

and therefore rate of upper state excitation in the atomic species. If T_e is itself pressure dependent, then the alteration in pressure that results in a different value of T_e will also affect the gain.

From the peak values for each gas in Figure 6.1, an estimate for the ideal local electron temperature, and therefore an ideal value of *pd*, can be found. The curve for He and Ne are both essentially flat over the range of electron energies, and therefore there is no obvious ideal electron energy for these gases. The curve for Xe is more pronounced, with a clear peak in the collision cross-section at the equivalent of around 6.25 eV, which can be expressed as an electron temperature of approximately 72,000 K. However, Figure 6.3 shows that the electron temperature for pure Xe at low *pd* values is much lower, at around 20,000 K. Therefore, to achieve the higher electron temperatures needed to increase the cross-section when using gas cells as small as a hollow optical fibre, it is likely that the Xe gas would need to be mixed with another gas such as He, which has a much higher value of T_e at low *pd* values, as shown in Figure 6.3. The electron temperature would then be largely determined by the He content, although the presence of Xe is expected to lower the value of T_e from the pure He value [166]. Therefore, to reach 72,000 K on the He curve in Figure 6.3, the *pd* would need to be a maximum of approximately 4 mbar mm, but ideally lower. This value then serves as an estimated upper limit for the ideal *pd* values in HeXe, with lower values being preferable.

6.3.5 The *pd* product and the Gain

As mentioned earlier, the measured gain values of several laser systems have previously been observed to increase for decreasing discharge tube diameter for a given value of *pd* [167, 147, 148, 149]. This has been a large motivator in the research towards gas lasers that operate in small discharge tubes. The mechanism which causes this increase in the gain has been contested by different research groups since the early 1970s, largely falling into one of two explanations.

The first was proposed by Bennett in 1965 [168], stating that the increased gain is due to an increase in the de-excitation rate of the lowest metastable energy level in the lasing mechanism. This state often has a long lifetime due to the sharing of an angular momentum quantum number with the ground state, and therefore de-excitation is forbidden from occurring spontaneously. The de-excitation then requires a collision

with an electron or the wall of the discharge tube in order to occur. Bennett proposed that in smaller discharge tubes, the diffusion rate to the walls is higher and consequently the rate of de-excitation is higher, freeing the de-excitation of the upper energy levels and raising the gain.

The second mechanism was proposed by Willett in 1971 [169, 148]. He argued that the population of metastable states in narrow discharge tubes would be the same as in larger tubes, and gain was not as a result of this de-excitation mechanism. Instead, he proposed that the increased gain was simply the result of the raised pressure necessary to compensate for the lower diameter and still maintain the same *pd* value. A greater density of atoms directly leads to a higher electron population, which results in larger populations for all states in the lasing mechanism, which in turn raises the gain. This explanation of Willett's, rather than Bennett's, is currently considered to be the most likely description of the physical process occurring.

6.4 Types of Excitation Process

The methods of applying an electric field to the discharge tube generally fall into one of two approaches: a direct current (DC) field, or a radio frequency (RF) field. An excitation by a DC field requires the electrodes to be directly exposed to the gas in the cell, and is generally easier to achieve experimentally in discharge tubes with a large internal diameter. It is for this reason that most commercial gas lasers utilise a DC field as the excitation source. As a result many systems with discharge tubes that have narrow internal diameters use the alternative RF excitation method in order to avoid having to directly expose the gas to the electrodes in such a small space.

6.4.1 RF Excitation

The biggest practical advantage gained by RF excitation is from the electrode configuration. DC excitation carries the risk of contamination of the gas with atoms ablated from the electrodes over time, which is not a problem encountered in RF driven systems, having the advantage of being able to couple energy to the gas without any direct electrode exposure. However, it is true that careful choice of the electrode material in modern DC-excited gas laser systems can remove the danger of gas contamination. RF excitation also does not suffer from cataphoretic effects like some DC systems.

The RF excitation method does have some disadvantages, including the need for specialised electrical circuitry to produce the RF signal, the difficulty in specifying the electrical parameters of the excitation, such as the current, and the reported increase in difficulty of maintaining a discharge over time for narrow-bore discharge tubes [148, 170, 149].

Excitation using an RF field was common in early work on gas lasers, particularly in gas discharge systems with smaller discharge tube diameters, where direct exposure of the electrodes to the gas proved difficult to achieve.

Several basic characteristics of the RF discharge are fundamentally different from those of a DC discharge, as discussed in the next section. The first is that the RF field is alternating periodically, resulting in a smaller proportion of the electron and ion population being swept to the electrodes and lost, as is the case in DC discharges. This lower rate of loss allows for discharges to be maintained for lower field strengths. Secondly, electrons released as a result of secondary effects (such as electron emission from the walls of the discharge tube) do not contribute to the discharge, unless they are emitted in a direction that is in phase with the RF field.

The oscillation of the free electron population is in phase with the driving RF field and moves about a mean position; it therefore gains zero average power from the field. If an oscillating electron then experiences a collision with an atom, it can become out of phase with the driving field, resulting in a net power gain and an increase in the energy of the electron. Collisions in an RF system can drive up the energy of electrons in this way until the collisions are sufficiently energetic to ionise or excite neutral atoms in the gas.

According to work by G. Francis in 1960 [171], the most important factors in the breakdown and maintenance of an RF discharge are the gas pressure p, the dimensions of the discharge tube, and the frequency and wavelength of the applied field. Additional factors also include the power supplied by the field.

The gas pressure defines the mean free path of the electrons, which in turn defines the collision frequency between electrons and the neutral atoms. For low gas pressures where the mean free path of the electrons is greater than the length or radius of the discharge tube, there are many electrons colliding with the discharge tube walls. This can result in the destabilisation of the discharge, where the electron population of the breakdown cannot be maintained in a steady state, and the discharge eventually fails.

Therefore, higher pressures where the mean free path is less than the length or radius of the discharge tube are preferable. In this scenario, there are many more collisions between electrons and atoms, which ionise or excite neutral atoms in the discharge as desired.

If the driving frequency of the field is a lot lower than the electron collision frequency, $f_{RF} \ll f_e$, then the electrons have many collisions during one cycle. This can potentially result in the slow diffusion of electrons to the walls of the discharge tube, moving radially in a random walk transverse to the direction of the applied field (which runs parallel to the tube length). At the tube walls they are effectively lost from the electron population. If the amplitude of the field is very large, then the electrons are strongly accelerated after each collision, directly driving a fraction into the walls after a collision with a higher kinetic energy, which may potentially result in damage to the tube in addition to the reduction of the electron population.

If the driving frequency of the field is much larger than the electron collision frequency, $f_{RF} \gg f_e$, the the electrons stay effectively stationary with each cycle and only spread out through diffusion. Despite this they still undergo many collisions with neutral atoms, but are less likely to be lost at the cell walls.

If the frequency of the applied field is pushed up towards the microwave regime, the effect from the field on the discharge changes. The geometry of the discharge tube becomes important, acting as a microwave cavity, and the electron temperature becomes much higher than for lower frequency fields [172]. Work by Motornenko [173] also shows that the excitation of certain atomic levels also increases for very high frequencies above 10 GHz.

6.4.2 DC Excitation

The second method of applying a field to induce a breakdown in a gas is DC excitation. In this case a pair of electrodes are directly exposed to the gas, with the breakdown occurring between them as a potential difference is applied. The stability of DC excited gas-breakdown is again dependent on the energy and stability of the free electron population, requiring the ionisation rate to equal the depletion rate along the length of the discharge.

The drift velocity from one electrode to the other for the ion species can result in cat-

aphoretic effects in gas mixtures of more than one species, destabilising the discharge. This problem is commonly overcome with the addition of a return tube to circulate the gases [150].

Due to the constant alignment of the field in the DC excitation regime, the gas discharge takes on several defined spatial characteristics, particularly in the region around the cathode, due to the static nature of the excitation field. The largest of these spatial characteristics in the glow discharge are defined as the *negative glow* region and the *positive column*. The latter of these usually makes up the majority of the glow discharge and is where the lasing emission occurs.

The spatial distribution of the glow discharge is shown in Figure 6.4 [146], including various "dark" and "glow" regions, as well as the varying electric field strength and potential along the length of the discharge.

In a steady-state glow discharge, the electric field strength is at a maximum at the cathode. Here electrons are emitted from the cathode and accelerated towards the anode by the strong electric field E, while the potential V is observed to build relatively steeply moving away from the cathode. However, this initial region of acceleration does not allow the electrons to gain sufficient kinetic energy to induce photon emission from any neutral atoms they collide with. Therefore the region immediately around the cathode is observed to be "dark" and does not give off any glow, being referred to as the *Aston dark space*, and is labelled in Figure 6.4.

Once the electrons have travelled far enough, the average kinetic energy is sufficiently high to excite neutral atoms through collisions. These atomic excitations result in photon emission, and so a thin bright layer is observed, known as the *cathode layer*.

In the region beyond the cathode layer, known as the *cathode dark space*, the electrons have a greater kinetic energy than the maximum excitation energy of the gaseous atoms, so little or no light is emitted. Instead, inelastic collisions between the primary electrons from the cathode result in a growing population of secondary electrons.

The region following the cathode dark space shown in Figure 6.4 is the *negative glow*, where the remaining primary cathode electrons collide inelastically with the gas, ionising more electrons into the secondary population and losing energy. Here the positive and negative space charge densities peak due to this ionisation, and the negative current density reaches a constant maximum, while the potential V now rises more slowly

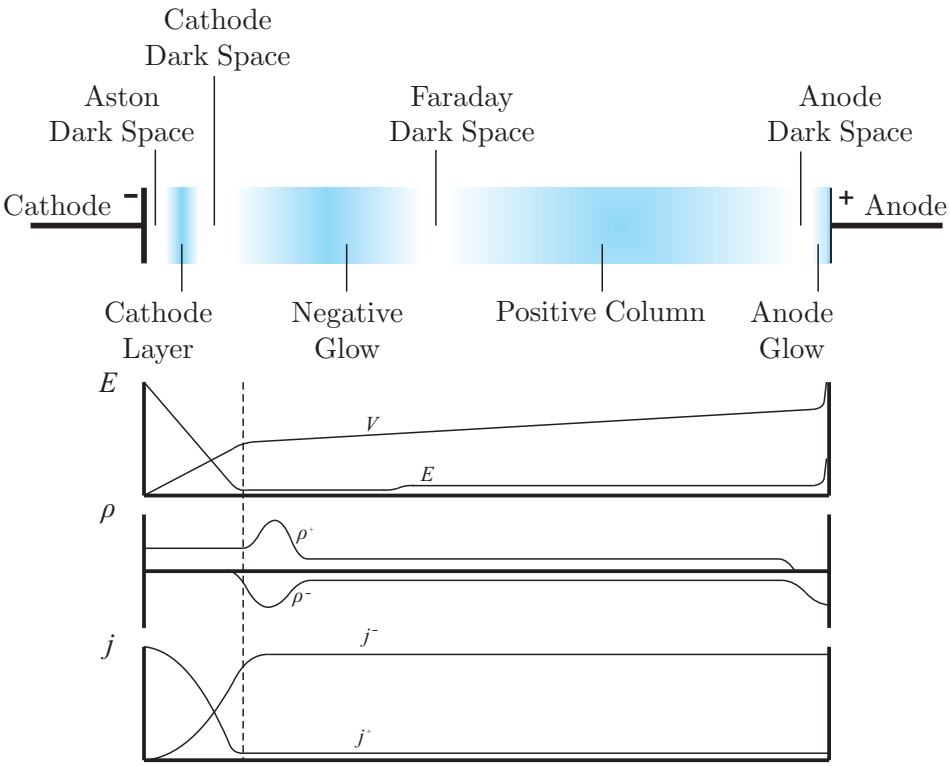

Figure 6.4: The distribution of a glow discharge, showing the various dark regions, the negative glow and the positive column (each region not to scale). The distribution of the potential (V), electric field (E), space charge densities (ρ^+ and ρ^-), and current densities (j^+ and j^-) along the length of the discharge is also shown below the diagram.

than previously. With the primary electrons now at a lower energy, and experiencing a low electric field, all electrons collide and excite the atoms of the gas, resulting once again in photon emission and another glow region.

Further along the discharge, the negative glow begins to fall away as the electrons recombine with atoms partially ionised in the production of the secondary electrons. This forms the *Faraday dark space*, and consists mostly of lower energy, secondary electrons being accelerated by the electric field E, which is now beginning to slowly increase again.

Once the electron population has reached the necessary threshold energy, collisions with neutral atoms in the gas are enough to excite and populate the upper energy levels for various lasing transitions. Emissions across these transitions produce a pho-

ton population, starting the *positive column*, which continues for the majority of the discharge length to the anode. It is in this region that the laser photons are emitted and stimulated emission in a cavity forms the population inversion needed for certain lasing transitions.

The positive column exists in a steady state, namely one where the rate of ionisation of electrons is equal to the rate of electron loss as a result of recombinations and diffusion to the walls of the envelope. The column often has a uniform appearance as a result of the weak electric field E, so the direction of motion of the electrons is generally random, with a small drift velocity towards the anode.

The behaviour near the anode consists largely of electron collisions, as the potential V and electric field E peak. Positive ions are repelled from the anode, forming a negative space charge, which gives off a glow as the electrons in the strong E field excite neutral atoms around the anode, known as the *anode glow*.

The relative size of the regions described so far can vary based on the potential applied along the discharge and the physical dimensions of the cathode [148]. However, the positive column most often forms the largest part of the gas discharge and is governed by the diffusion behaviour of the gas and electrons.

6.5 Laser Transitions in Certain Noble Gases

Gas lasers using neutral noble gases as a lasing medium have been a subject of research since the very beginning of laser development [145]. Two of the most common systems, both in research and commercially, are those operating with a HeNe gas mixture and those with a Xe or HeXe gas mixture [145, 174]. Despite both having some strong gain lines, this is due more to either the location of certain emission lines in the visible spectrum (in the case of Ne), or the ease of achieving stable electrical breakdowns (in the case of Xe). Both gas mixtures are chosen as a part of the research described in Chapters 7 and 8, and so the mechanisms for each at the emission lines of interest are described here.

6.5.1 Helium Neon Laser Systems

Helium-neon based gas lasers are very common, having an accessible line at 632.8 nm in the visible region which has historically proven useful in a variety of different devices. He and Ne were chosen as the gas lasing medium for the first gas laser demonstrated in 1960 [145]. Although this gas laser harnessed the 1.15 μm line, the emission line around 632.8 nm was quickly observed to have a higher gain than other lines in the visible region, and so 632.8 nm lasers have been widely used since first being demonstrated by researchers at Bell Labs in 1962 [175]. The work described later in Chapters 7 and 8 includes work on another HeNe laser transition with much higher gain than the 632.8 nm line [176, 177]; the 3.39 μm transition.

As shown earlier in Figure 6.3, He and Ne possess higher electron temperatures for a given range of *pd* values, compared with the other noble gases. This, coupled with their lower ionisation efficiencies as a result of their lower collision cross-sections, makes it potentially difficult to start and maintain a gas discharge using He and Ne.

The lasing mechanism behind both the 632.8 nm and 3.39 μm transition is shown in Figure 6.5. In an electrically-driven HeNe laser, energy is delivered to the He atom through inelastic electron collisions, exciting the atom from its ground state to the 2^1S_0 energy level. This state is metastable, and possesses a long lifetime before de-exciting back to the ground state.

While in this excited state, the He atoms can potentially collide with Ne atoms in the gas, transferring their energy to the Ne atoms (as described earlier in Subsection 6.3.1). Fortuitously, the energy levels of Ne are arranged such that the $3S_2$ state has very nearly the same energy as the helium 2^1S_0 state, resulting in a transfer of energy from the He atom to the Ne atom at this state. This transfer mechanism is of primary importance in a HeNe laser system, since without the presence of He in the gas, the excitation cross-section for the neon $3S_2$ level is much smaller, making pure Ne lasers very difficult to build and thus rare [178].

The population of the neon $3S_2$ state increases with more of these collisions, since in a typical HeNe system there is usually a greater population of He atoms than Ne atoms, and this metastable state has a long lifetime. This reaches a point where there is a population inversion between the neon $3S_2$ state and both the lower energy $2P_4$ and $3P_4$ states, a prerequisite for lasing.

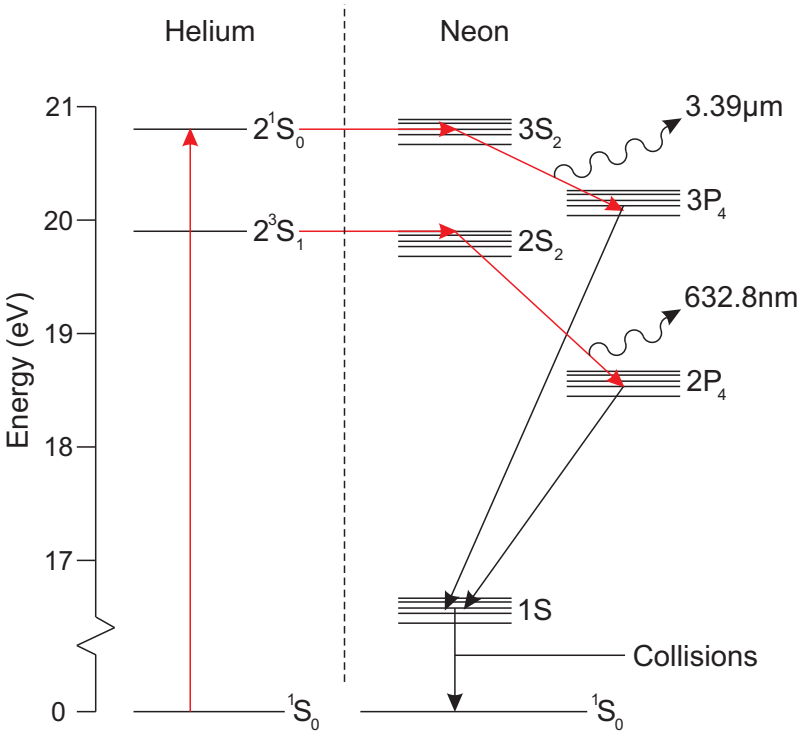

Figure 6.5: The energy levels in a HeNe laser operating on either the 632.8 nm line or the 3.39 μm line.

Transitions from the neon $3S_2$ state to the $2P_4$ and the $3P_4$ states result in photons being emitted at 632.8 nm and 3.39 μm respectively, both of which can then be harnessed by a highly reflecting cavity to induce stimulated emission and form a laser.

The $2P_4$ and $3P_4$ lower energy states both have shorter lifetimes than the $3S_2$ upper energy state, and quickly depopulate to the $1S$ band of states. A spontaneous transition from one S state to another S state is forbidden due to the common angular momentum quantum number, so the final de-excitation back to the ${}^1S_0$ ground state occurs through a collision with an electron in the discharge.

As discussed earlier in Subsection 6.3.5, the gain of the 3.39 μm line is observed to increase for a given value of pd as the diameter of the discharge tube is decreased. This is a roughly inversely proportional relationship, and HeNe mixtures operating at the 3.39 μm line have shown gain as high as 20 dBm^{-1} [176].

6.5.2 Helium Xenon/Pure Xenon Laser Systems

Xenon gas, like many of the other noble gases, is a common choice as a lasing medium [174, 179, 180, 181]. With 54 bound electrons in the neutral Xe atom, plenty of energy level transitions are available, several of which have been previously measured to have a high gain [182, 179, 183, 167]. The first mid-IR neutral Xe gas lasers operated on the 2.062 μm line [174], and several emission lines in the mid-IR wavelength region have since been exploited as lasers [184, 185, 180].

Chapters 7 and 8 concern research using Xe as a lasing medium, with a focus on the transitions in the region between 3 μm to 4 μm, particularly the 3.5 μm line, which has been shown to have very high gain of as much as 60 dBm^{-1} to 70 dBm^{-1} [182, 179, 167].

Unlike HeNe laser systems, the presence of He in a HeXe laser is not necessary to easily induce lasing, and numerous pure Xe systems have been demonstrated [179, 180]. However, it has been observed that the gain in pure Xe systems is not as high as in HeXe systems [179, 167], due to the He serving as an additional source for the electron population, both directly and through Penning collisions between excited He atoms and Xe atoms. The He also works to increase the stability of the gas discharge, by de-exciting the free electrons with the highest energy through collisions. This results in a more stable electron population, which in turn stabilises the electron temperature, and the gas discharge as a whole. Xenon tends to discharge relatively easily, due to the ionisation efficiency being higher than many other noble gases, and as shown in Figure 6.1, the collision cross-section for neutral Xe is much higher than for Ne or He, and peaks at a lower average electron energy.

The wavelength region of interest, from 3 μm to 4 μm, is known to have several strong emission lines with potentially high gain in small bore gas laser systems [182, 179, 167, 151]. Figure 6.6 shows the energy level configuration between the $3D$ and $2P$ orbitals, where many of the mid-IR transitions are found.

As with the HeNe lasing mechanism, the initial excitation of the Xe atoms is from high energy electron collisions in the gas discharge. This excites the bound electrons in the atom from the ground state to the $3D$ orbital, specifically the $3D_1^{'}$ for the 3110 nm emission line, $3D_1^{''}$ for the 3370 nm emission line, $3D_4$ for the 3500 nm line and the 3885 nm emission lines.

Photons are then emitted as electrons transition to their third, lower energy states on

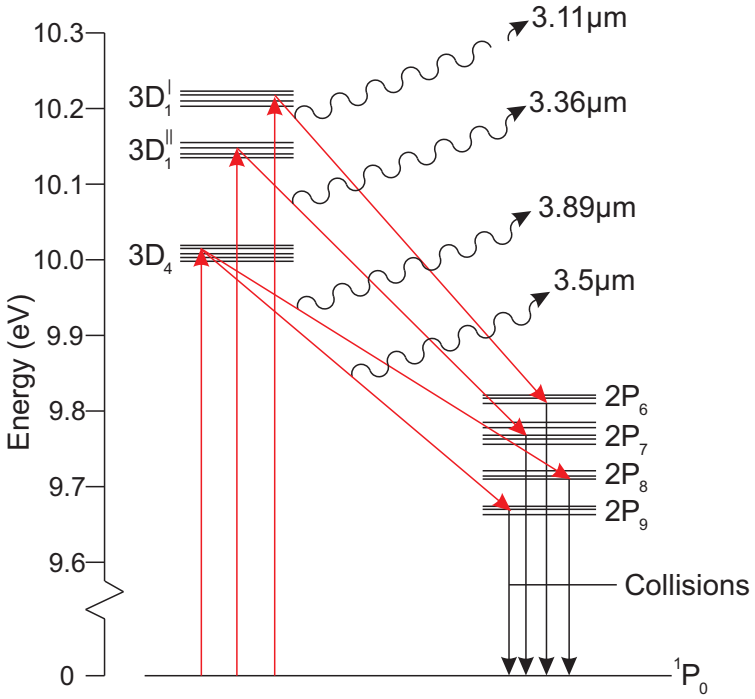

Figure 6.6: The energy levels in a Xe or HeXe laser operating mid-IR. The 3.11 μm, 3.36 μm, 3.5 μm, and 3.89 μm lines are highlighted

the $2P$ orbital; the $2P_6$ for the 3110 nm emission line, $2P_7$ for the 3370 nm emission line, and $2P_9$ for the 3500 nm line and the 3885 nm emission lines. Since any spontaneous transition from these lower energy states back to the ground state is forbidden, the final de-excitation occurs through collisions with electrons in the discharge.

As in the case of HeNe lasers operating within narrow discharge tubes, the gain for the 3.5 μm HeXe lasing line has been observed to increase for decreasing diameter, and again this is a roughly inversely proportional relationship for a given value of pd.

This gain-diameter relationship, and the useful nature mid-IR lines, makes the development of HeNe and HeXe gas lasers in narrow discharge tubes an attractive prospect for research, and is the topic concerning Chapters 7 and 8.

Chapter 7

Fibre Gas Discharge Lasers: An RF Excitation Method

7.1 Introduction

The work described in this chapter was presented as a poster at the AIPT Conference hosted by Aston University, Birmingham, in 2013 (see Publications and Conference Presentations 2).

This chapter details the research carried out towards developing a fibre-based gas discharge laser, driven by a radio frequency (RF) electrical field. The fibre chosen for the system was a newly developed negative curvature photonic crystal fibre, capable of guiding light in the mid-IR between 3 μm and 4 μm. Neutral noble gases were chosen for their high gain emission lines in the mid-IR region from 3 μm to 3.5 μm.

7.2 Approach

As described earlier in Chapter 6, when the internal diameter of a gas laser tube is made smaller, it becomes harder to initiate and maintain electrical discharges. This is due to the resulting change in the electron temperature T_e and electron collision cross-sections for the different atomic species present in the gas. However, if the pressure of

the gas is raised to compensate for the smaller internal diameter of the gas cell, then the same value of T_e and collision cross-sections can be maintained, preserving the performance of the laser. An additional advantage for the emission lines in noble gases such as neon or xenon, as discussed in Chapter 6, is that the gain is roughly inversely proportional to the discharge tube internal diameter for a given value of pd. This therefore potentially opens up a range of lasing wavelengths that are usually difficult to access due to otherwise relatively low gain in discharge tubes with larger internal diameters. Access to these wavelengths, as well as the advantage of miniaturing such systems into an optical fibre, can potentially be applied to commercial devices where the inherently narrow linewidth offered by gas laser systems is beneficial.

Additionally, previous research was limited by the optical losses of the glass capillaries used as discharge tubes [150], which scale as r^{-3} and became too high beyond a certain capillary length or below a certain diameter. The advent of hollow core PCF (HCPCF) largely solved this loss problem, but presented the additional problem in that the core diameters were typically only a few tens of microns, small enough that the stabilisation of gas discharges proved very difficult. The more recent development of negative curvature fibres (NCF) presents an opportunity to solve this problem, since the loss of these hollow fibres is low and the core diameter can be as large as 100 μm or more. Like some hollow-core PCFs, NCF fibres are also capable of guiding light in the mid-IR [16], where silica glass is usually highly absorbing and inherently lossy. This means long interaction lengths can be used, and laser wavelengths harnessed that are usually out of reach, making a narrow-bore fibre-based noble gas laser in the mid-IR an attractive device to develop. This serves as sufficient motivation for this research.

The most common approach to conventional electrical gas lasers is to use a direct current (DC) source as the excitation. Earlier, in Chapter 6, it was outlined how this form of excitation can be experimentally difficult for systems with a small internal diameter, most importantly because of the need for the direct exposure of the electrodes to the gas. Practically, this would involve drilling holes in the fibre, which is both difficult to achieve and hard to reliably repeat. In addition, discharge lengths are then fixed and cannot be adjusted using the same piece of fibre.

By contrast, an RF excitation approach would offer the advantage of being able to couple power from the driving field directly through the glass to the gas inside the fibre, initiating a gas breakdown. It was judged that RF excitation would be more practically achievable and provide more flexibility in the location of the electrodes along the fibre. This also would allow for multiple sets of electrodes to be used, alternating

the connections to the RF source as done by Mielenz et al. [186], so that the discharge could be extended to longer lengths along the same fibre.

Therefore, the approach was to develop an RF source to feed into a tunable resonant circuit, the output of which in turn was attached to electrodes which were wrapped around the outside of the fibre. The negative curvature fibre chosen to act as the gas cell was able to guide light generated by the gas discharge in the mid-IR between 3 μm and 4 μm. This fibre was attached to a vacuum system to evacuate and introduce the required gas mixtures. Electrodes were wrapped around the outside of the fibre and placed along with the resonant circuit inside a Faraday cage to contain the RF field. The system also kept the optical path from the fibre clear so light could be coupled in and out at either end. This allowed for the spectrum of the light generated in the discharge to be recorded, and the potential for detection of the gain for different lines based on different discharge parameters and lengths.

7.3 RF System Experimental Setup

The setup for the RF experiment involved several different elements: an electrical system to generate a high voltage radio frequency signal, a Faraday cage to effectively confine that signal and prevent the field interfering with any surrounding equipment, a pair of electrodes to couple energy through the silica glass from the radio signal to the gas inside the fibre, and finally a vacuum system to evacuate the fibre and deliver the desired gas mixture and pressure.

7.3.1 The RF Electronics

The RF excitation field was generated by a series of electrical components connected by co-axial cables, with the initial signal taken from a CB radio (MoonRaker FA5000). The full electrical setup is shown in Figure 7.1.

The CB radio produced an RF signal at 27 MHz, on EU Channel 14, which was then passed on through a coaxial cable to a standing wave ratio (SWR) meter (Zetagi). An SWR meter measures the mismatch in the ratio between backward and forward voltages, and is used for impedance matching a circuit to achieve the maximum forward power transfer between a transmitted signal and the circuit load. A matching circuit

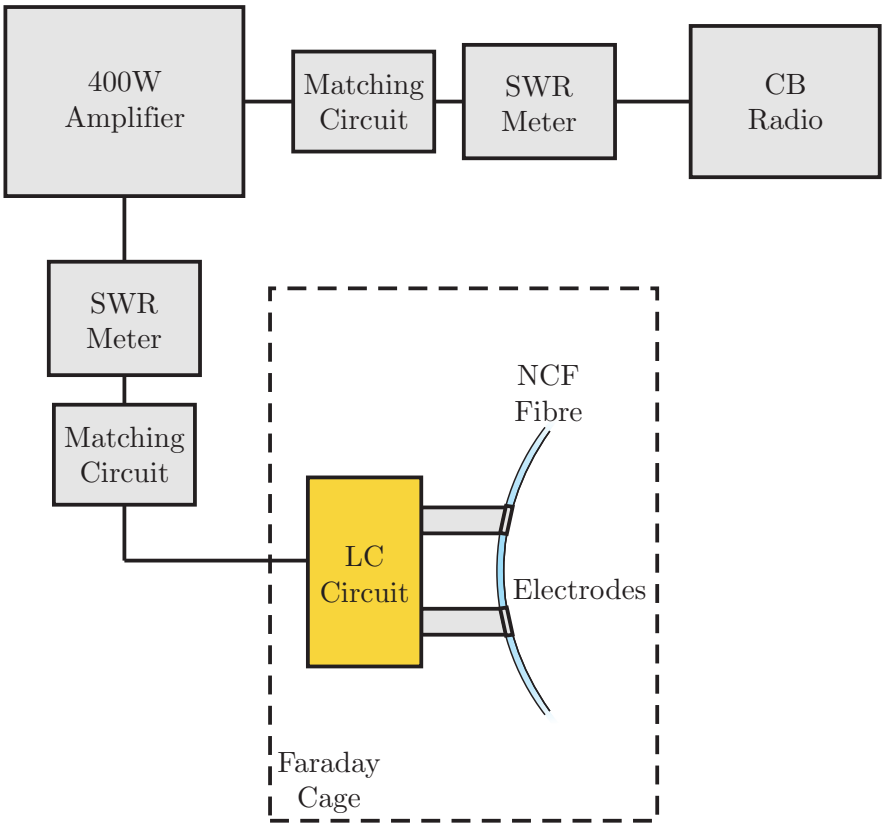

Figure 7.1: The electrical setup of the RF system, including the CB radio, SWR meters and the 400 W amplifier, connected to the LC circuit inside the Faraday cage.

connected directly after the SWR meter allowed for the impedance to be adjusted so the forward power transfer was maximised.

The SWR meter was in turn attached to a 400 W variable amplifier (RM KL-400), which increased the power of the RF signal. After this a second SWR meter and matching circuit allowed for further impedance matching between the amplifier and a resonant circuit inside the Faraday cage. In addition to increasing the efficiency of the power transfer to the resonant circuit, this second SWR meter and matching circuit also prevented any damage to the power amplifier due to excessive back reflections.

The resonant circuit was custom made on a small piece of strip-board, designed as a simple inductor-capacitor (LC) circuit. The circuit design is shown in Figure 7.2. A capacitor chain was chosen to distribute the applied voltage over many components,

so as not to exceed the voltage rating of individual parts. The chain was made up of two parallel arms, the first consisting of a series of six 2.2 pF capacitors and a 100× voltage probe for measuring the voltage amplitude of the circuit.

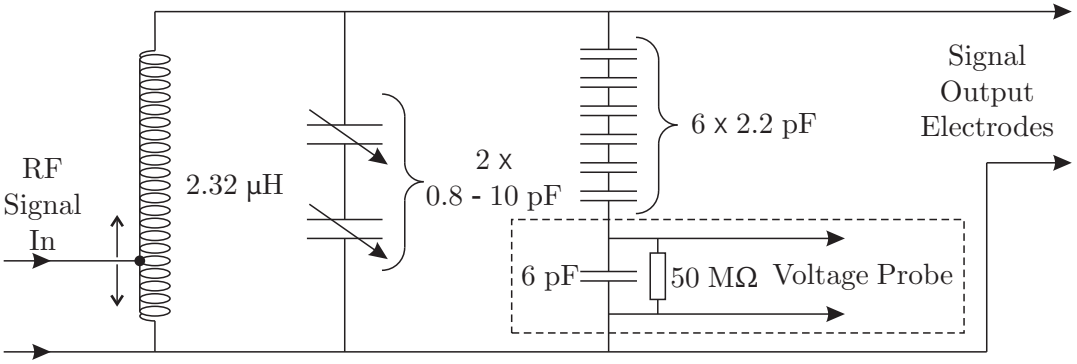

Figure 7.2: Electrical diagram of the LC circuit.

The probe had a capacitance of 6 pF, and therefore the total capacitance on that arm was approximately 0.36 pF. The second arm of the capacitor chain was made up of two identical mechanically variable capacitors. These capacitors consisted of a cylindrical glass casing surrounded by an anode section at one end. A cathode made up of a screw system at the other end moved a cylindrical metal rod forwards and backwards inside the casing, allowing for the degree of overlap between the cathode and the anode to be altered, and so in turn changing the capacitance. The capacitive range of the variable component was from 0.8 pF to 10 pF, resulting in a total capacitive range for both arms being from 0.75 pF to 5.35 pF. The maximum load for each variable capacitor was 5 kV, which was higher than the expected maximum potential of the RF source. However, they were designed to operate in a DC system, and so suffered from coronal discharging around the outside casing. To solve this, anti-corona lacquer was applied over the surface, followed by a layer of heat shrink to cover any sharp metallic corners.

The inductor was made using copper wire, SWG 19 (or approximately 1 mm in diameter), shaped into a torus with an average total diameter of 15 cm, and a coil diameter of 1.5 cm. A torus shape was chosen over a simpler straight coil design due to the lower fraction of the field that occupies space outside of a torus compared with that of a straight coil. The walls of the Faraday cage could potentially interfere with the inductor field, resulting in an unwanted effect on the resonant circuit based on specific placement, so the greater field confinement of a torus-shaped inductor was considered more favourable. The coil contained a total of 44 turns, and the total inductance could

be calculated using the equation [187]

$$L = 0.01595N^2 \left[D - \sqrt{D^2 - d^2} \right], \tag{7.1}$$

where N is the number of turns, D is the mean diameter of the toroid (in cm), and d is the diameter of one coil (in cm). The coil therefore had an estimated total inductance of 2.32 μH. Figure 7.2 shows a section of the inductor connecting across the input of the LC circuit. This short was made by the signal input wire which could be connected to different turns of the inductor coil, allowing for the inductance of the circuit to be adjusted. Due to the small number of turns in the inductor across the connection, the contribution of that section to the overall inductance and resonance of the circuit was negligible, and could be ignored.

Both the variable capacitors and inductor allowed for the resonant frequency of the circuit to be tuned, and using the relation

$$f_{res} = \frac{1}{2\pi\sqrt{LC}}, \tag{7.2}$$

the range of resonant frequencies could be calculated to be from 45 MHz to 120 MHz. However, the local environment, such as the Faraday cage itself, the electrodes and the wires contributed further on the scale of pF to the total capacitance, which affected the resonant frequency of the circuit. The resonant frequency range was therefore lower, so the RF frequency at 27 MHz was included. The location of the shorting lead of the inductor and the value of the variable capacitors allowed for the exact resonance to be finely tuned.

The voltage probe was connected to an oscilloscope to monitor the amplitude of the signal, which could be adjusted and maximised for each setting of the 400 W amplifier by altering the variable capacitor. The probe value on the oscilloscope could be multiplied up by a factor to give an estimate of the true RF field potential at the output of the LC circuit. By assuming that the charge on each capacitor plate in the voltage probe chain was the same, and using the general relation $Q = {}^{C}/_{V}$, this factor was found to be 17.4 times the probe value.

Unfortunately, the RF system was unable to directly measure the current flowing

through a discharge, which made it difficult to understand the underlying dynamics and stability of the breakdown. Instead, observations of stability were made based on how long the discharge could be sustained, and the required applied field potential, as described further in Section 7.6.

7.3.2 The DC Source

In RF gas discharge systems with large internal gas cell diameters of several cm or more, the RF field alone is frequently sufficient to initiate the discharge. However, in small diameter systems a second source is often required to initiate the breakdown [150], acting to ionise a small population of electrons which can then be oscillated by the RF field. Initial experiments using this system included the use of a modified piezo-electric kitchen stove igniter, which applied a brief DC field of several kilovolts to the region around the fibre, resulting in the breakdown of the gas into a discharge.

In later experiments this ignition source was replaced with a variable DC source with output potentials of up to 10 kV. As well as having a wire probe to direct the applied field to the vicinity around the fibre, the DC source (Applied KiloVolts, 3590 series) also included an output coaxial port from which the potential could be monitored using a voltmeter. In the event of the field arcing to either of the electrodes, an additional port could be used to monitor the current flow in the same way, and a ballast resistor of 2 MΩ was attached in series with the probe output to limit the current to under the source maximum of 0.5 mA. The layout and connections of the 10 kV DC source is shown in Figure 7.3.

The output probe from the DC source could be placed within 5 mm of the fibre, and the potential increased until the breakdown of the gas in the fibre initiated the discharge. After this point the DC source could be switched off, and the discharge maintained by the RF field.

7.3.3 The Faraday Cage

In order to limit the radio waves to the immediate volume around the fibre, electrodes, resonant circuit and 10 kV DC source, a Faraday cage was built. This was made from sheets of steel with a hexagonal array of 5 mm wide holes. This hole size is far smaller

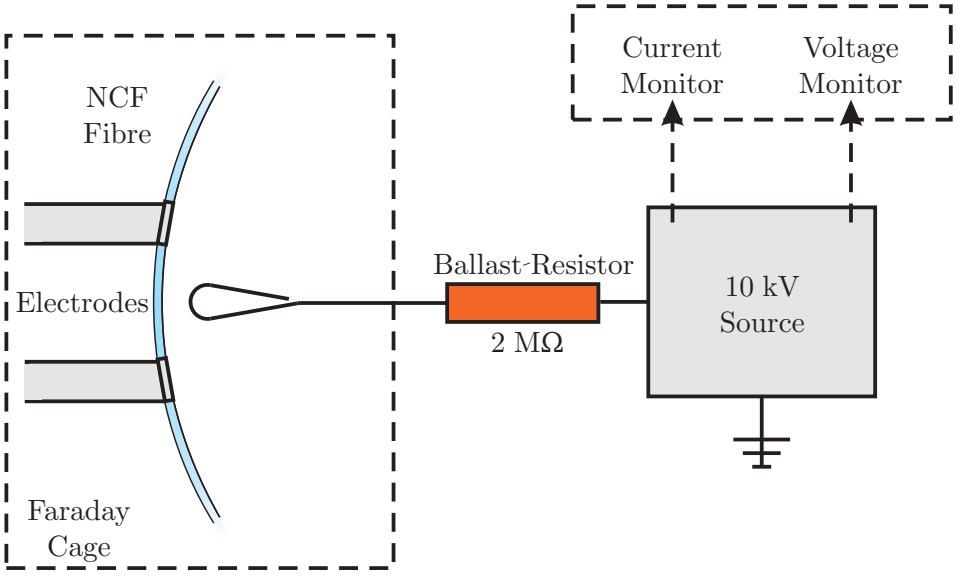

Figure 7.3: Diagram of the 10 kV DC source, including the outputs for voltage and current monitoring, and the 2 MΩ ballast resistor to limit the maximum current under arcing to to under 0.5 mA.

than the wavelength of the radio waves, which is about 11 m for a field oscillating at 27 MHz, and so allowed for the direct observation of the cage interior without compromising the effectiveness of the field confinement. These holes also acted as a way to feed the fibre in and out of the cage, as well as the signal delivery and probe cables for the resonant circuit, and the lead for the 10 kV DC source.

A schematic of the Faraday cage is shown in Figure 7.4. A removable lid was built into the design, allowing for easy access to the fibre and the resonant circuit, whilst maintaining the ability to close the cage securely and minimise any signal leakage from within.

7.3.4 The Electrodes

The main advantage of using RF excitation over DC excitation, as described in Section 6.4, is the fact that in an RF system the electrodes do not need to be directly exposed to the gas, being able to instead couple directly through the silica glass to the gas inside. This means the electrodes used can be simply placed around the outside of the fibre, making it easier to prepare experimentally and allowing for the length of the

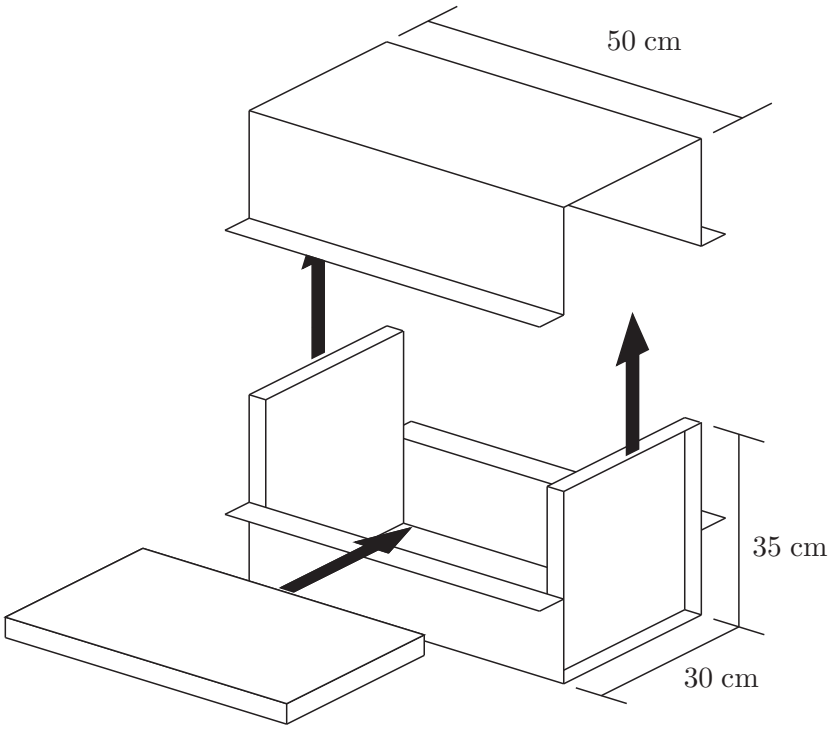

Figure 7.4: Diagram of the Faraday cage of the RF system, showing the removable lid and the slide in shelf, which holds the LC circuit and the fibre.

discharge to be variable with electrode placement.

After stripping a section of fibre of its polymer coating, small pieces of aluminium foil were wrapped tightly around the bare glass of the fibre, as shown in Figure 7.5.

Aluminium was chosen as the electrode material primarily because of its flexibility and low cost. When the system was on and discharging, the aluminium wrapped sections of the fibre effectively created a pair of coaxial capacitors, with the glass acting as the dielectric between the discharging gas and the aluminium electrode. The capacitance of these coaxial electrodes can be defined using the relation

$$\frac{C}{L} = \frac{2\pi k \varepsilon_0}{ln[\frac{b}{a}]}, \tag{7.3}$$

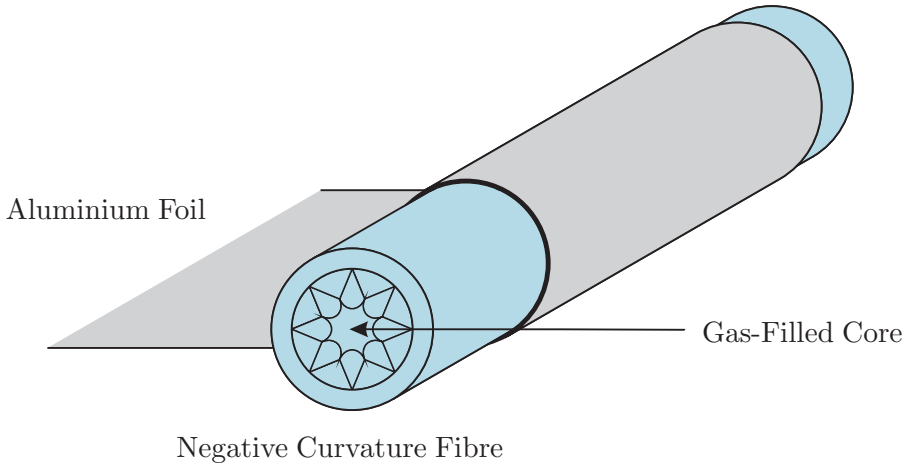

Figure 7.5: Diagram of the aluminium electrodes.

where k is the dielectric constant for that material, known to be around 3.8 for silica [188], and a and b are the inner and outer radii of the fibre, given as 45 μm and 60 μm respectively. Ignoring the thin internal structure of the fibre for simplicity, and taking electrodes which are 5 mm long, this results in an approximate individual electrode capacitance of 146 nF.

7.3.5 The Vacuum System

The fibre was attached to a vacuum system at either end, allowing for the evacuation and delivery of the desired gas mixture at the desired pressure. This had to be achieved whilst still maintaining optical access to the ends of the fibre, allowing the spectral output, generated by the gas discharges and guided by the fibre, to be recorded.

The configuration of the vacuum system is shown in Figure 7.6, with the turbo pump, pressure gauges, and valves labelled.

The system was built from KF-16 and KF-25 vacuum parts, attached to a rotary turbo pump (Oerlikon Leybold Vacuum, TurboLab 80), and was able to reach a low pressure of 10^{-4} mbar at either end of the fibre, where pressure gauges were located.

To connect the fibre to the vacuum system and still keep the optical path in and out of the discharge clear, two blocks were designed and built, each fitted with an evacuation pipe and a gauge for monitoring pressure. One block was additionally fitted with an

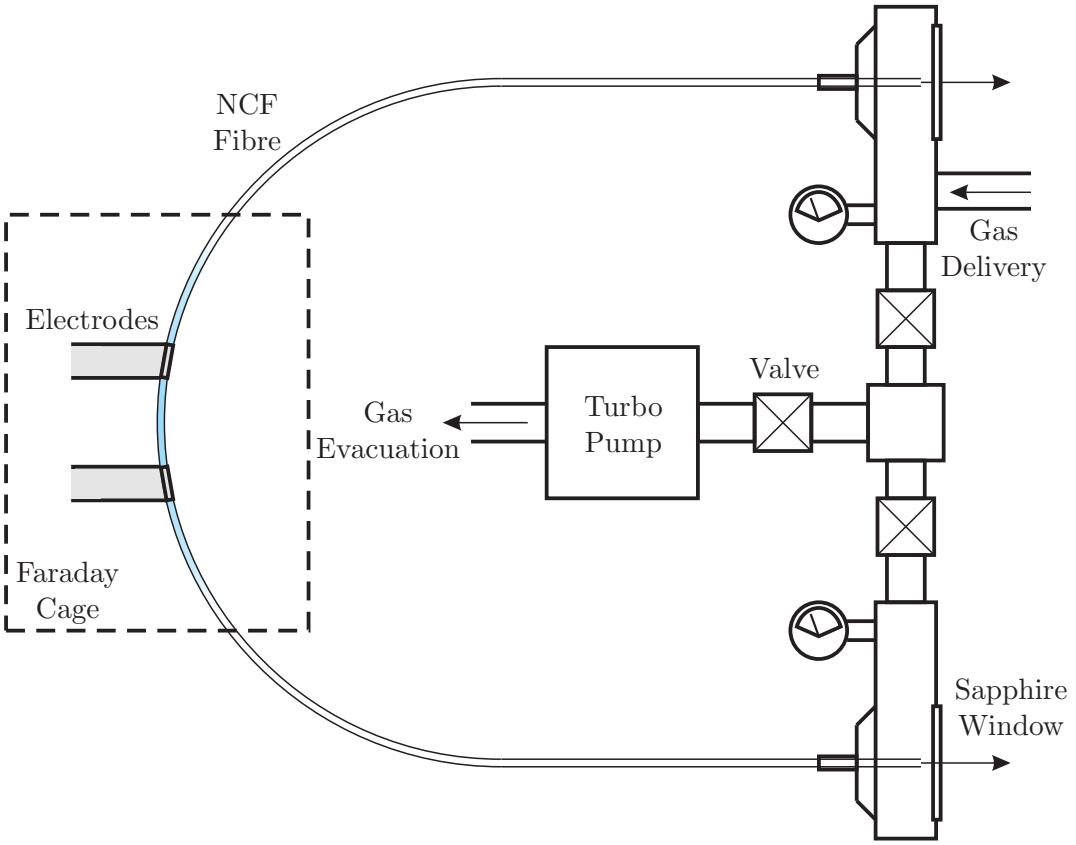

Figure 7.6: Diagram of the vacuum system configuration.

input pipe for gas delivery. The section of each block directly in front of the end of the fibre was removed and replaced with a sapphire window, allowing for a clear optical path for coupling light in and out. One block was designed to connect directly to the input slit of a spectrometer capable of detection in the mid-IR (Bentham, DTMc300), allowing for efficient signal collection from the fibre.

A removable fibre holder was included with each block, allowing for the fibre to be mounted inside the block in a consistent position with each discharge test. A seal was formed around the outside of the fibre by passing the fibre through a bung inside the holder, and then compressing it using a screw. The design for the blocks and the removable fibre holders is shown in Figure 7.7.

The final configuration required a fibre length of 2 m, connected to holders at either end of the vacuum system in a semi-circle, passing through the Faraday cage, where a section was stripped of polymer, electrodes applied to the outside, and connected to

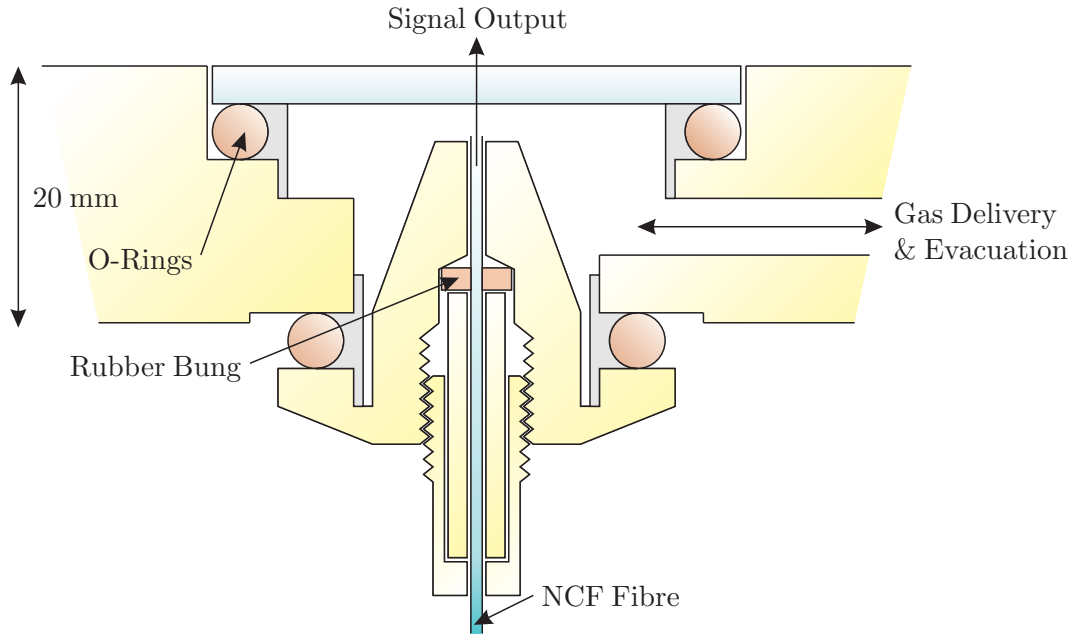

Figure 7.7: Diagram of the removable fibre holders used in the vacuum system.

the RF circuit.

7.4 The Negative Curvature Fibre

The fibre used for this research was a novel negative curvature hollow core fibre (NCF) developed in 2012 by F. Yu at the University of Bath [16]. Using bandgap guidance, described earlier in Section 2.5, light is guided along the fibre in a series of bands, separated by regions of high loss. One band of transmission covers the region from 3 μ to 4 μm, making it ideal for generating and guiding light from high-gain mid-IR emission lines of noble gases. The mid-IR transmission band of the fibre is shown in Figure 7.8 a). The attenuation at 3.5 μm is seen to be less than 0.1 dBm^{-1}, which was considered low enough to make it appropriate for this research.

The spikes observed in the attenuation curve of Figure 7.8 a) between 3.3 μm and 3.7 μm were noted and explained in the publication presenting this fibre [16]. They are reported as being the result of trace amounts of chlorine, left over from the fabrication process of the pure silica glass. The chlorine then slowly out-gases from the glass over time, occupying the hollow-core as HCl gas. It is the absorption lines of the HCl that

cause the observed spikes in the loss, and are therefore not "real", or expected to be present in a fibre which has been evacuated and filled with a noble gas mixture.

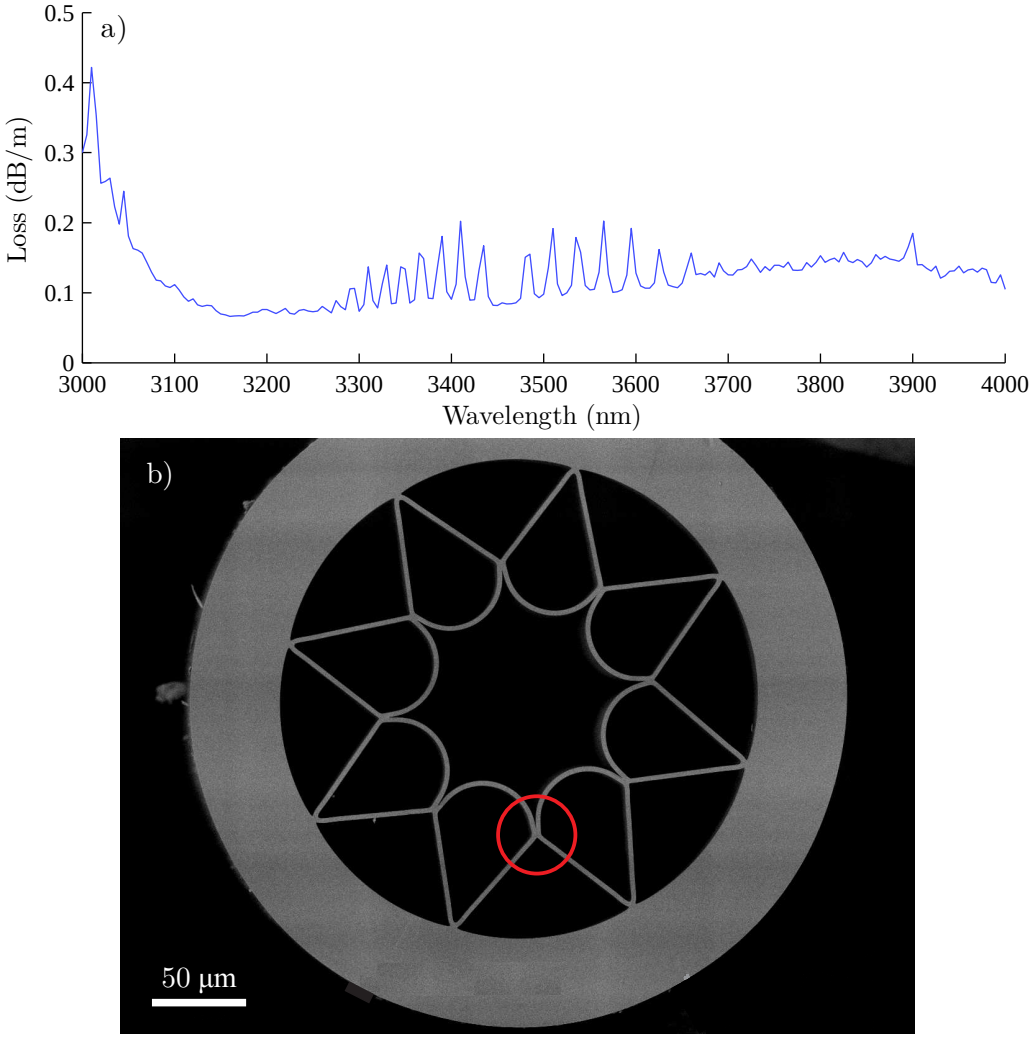

Figure 7.8: a) Negative curvature fibre attenuation curve for the band covering 3 μ to 4 μm and b) an SEM image of a fibre with the same structure, fabricated at the University of Bath [16]. A connecting "node" is circled in red.

An SEM of the fibre structure is shown in Figure 7.8 b). The core radius at its narrowest was measured to be about 96 μm, a curvature of $26^{-1}\mu\text{m}^{-1}$ and an overall outer fibre diameter of about 350 μm. This placed it at the lower edge of the range of tube inner diameters used in previous research on this topic [150, 151, 155, 154].

However, it was reported by F. Yu that the fibre suffered from high losses for bend radii of less than 20 cm. This was the result of the "nodes" connecting the internal capillaries

of the fibre to each other, as marked in Figure 7.8 b). This made it necessary for the fibre to be held fixed, and with a minimum radius of curvature of 20 cm, in order to avoid significant losses in transmission. In the vacuum system described earlier, the bend radius was set to 50 cm to prevent this problem. Furthermore, care was taken to keep the fibre in a fixed position during the recording of spectra, to avoid any fluctuations in the transmitted signal strength.

7.5 Gas Mixtures and Pressures

As described in Section 6.5, noble gas mixtures of HeNe and HeXe were chosen, due to the presence of several emission lines in the mid-IR range for Ne and Xe which have previously been reported to have high gain [176, 177, 179, 167].

Gas mixtures of HeXe were used as the lasing medium in several early gas lasers [174, 179, 180], and as described in Chapter 6, Xe has the advantage of having relatively low contribution to electron temperature, estimated to be of the order of 10,000 K to 15,000 K for the range of *pd* values given earlier in Figure 6.3. Xe also potentially has electron collision cross-sections of up to 4×10^{-19} m^2 [161], several times larger than the other noble gases. The emission line at 3.5 μm was expected to have a particularly high gain based on previous research [182, 179, 167].

As discussed in Chapter 6, the maximum ideal *pd* value for HeXe is predicted to be 4 mbar mm, which corresponds to a pressure of approximately 40 mbar in this fibre. However, it may not be possible to maintain a discharge at this pressure using this equipment. For a narrow-bore RF system operating with HeXe as the discharging gas, the optimum pressure to initiate and maintain a stable discharge is dependent on the frequency and amplitude of the RF driving field, as well as the exact dimensions of the gas cell, and is not easily defined. It was expected that the collision frequency f_e of the electrons in the discharge would be significantly larger than the driving frequency of 27 MHz, which would result in many collisions per cycle of the field. The electrons would then undergo a diffusion to the fibre walls. If the field potential was too high, then the electrons near the walls would be accelerated into the glass to be lost, potentially damaging the fibre. For this reason it was thought that the pressure increase of the gas should be made even larger than that needed to maintain the same electron temperature (see Section 6.3.4). While equation 6.5 shows that a greater pressure would increase the collision frequency further still, the greater number of atoms would cause more

collisions per cycle, de-exciting fast electrons more efficiently before they reached the fibre walls. The presence of He in the gas mixture would also contribute to this de-excitation effect, so gas mixtures with high He content could display more stability.

The gas mixture of HeNe was also used as a discharge medium, due to the emission line at 3.39 μm which is known to have a high gain [176, 177]. HeNe has been used extensively in previous research, both in large gas cells and in smaller systems [145, 175, 150]. However, Ne is known to have a higher operating electron temperature than Xe for a given value of pd, of the order of 40,000 K to 80,000 K from Figure 6.3 shown earlier in Chapter 6, and a lower collision cross-section of the order of 0.5×10^{-19} m^2 [161]. This potentially makes HeNe gas mixtures more unstable in tubes with narrow internal diameters.

Again, the optimum pressure for discharge initiation and stabilisation for a narrow-bore RF system using HeNe is not well known, and as with the HeXe mixture, the collision frequency in HeNe was expected to be much larger than 27 MHz. This, in conjunction with the higher working electron temperatures of He and Ne, would potentially risk damage to the walls of the fibre at lower pressures. Therefore, raising the working pressure of the HeNe mixtures above what would usually be expected would reduce the electron temperature, potentially minimising any damage as a result of high energy electrons colliding with the internal walls of the fibre.

7.6 RF Electrical Discharge Initiation, Stabilisation, and Characteristics

Prior to any attempt at initiating a discharge in the gas, the LC circuit was tuned using one of the the variable capacitors, adjusted to maximise the amplitude of the output from the voltage probe. Failure to do this resulted in a weak field being emitted from the electrodes, and breakdown of the gas would not occur.

As mentioned in Subsection 7.3.2, RF systems using narrow tubes often require a DC source to initiate the discharge, and the 10 kV variable DC source served that purpose for the majority of this work. Initial discharges achieved breakdown for a DC potential of 3 kV to 5 kV, after which the RF field took over. During a discharge, the SWR meters and matching circuits of the RF system allowed for the measurement and adjustment of the power reflected backwards, which was minimised in order to increase the strength

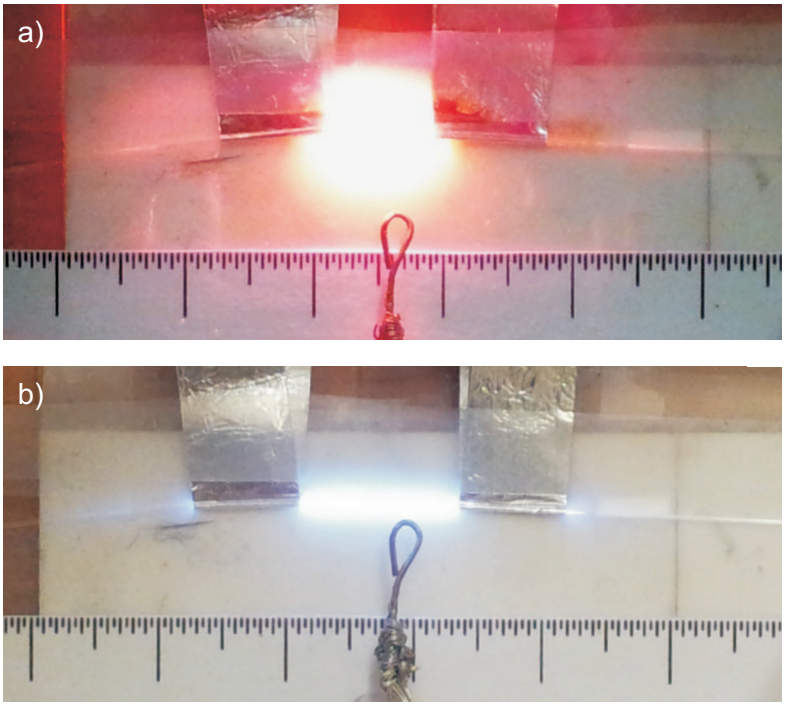

Figure 7.9: a) A short discharge of 9 mm in 125 mbar 5:1 HeNe. b) A similar short discharge of 13 mm in 100 mbar 2:1 HeXe. In both images, the large scale units are 1 cm, the DC wire loop is in the centre, with the RF electrodes at the top, and electrodes were 8 mm wide.

of the RF field at the electrodes.

Electrode separations of a few millimetres achieved breakdowns in both HeXe and HeNe relatively easily for lower amplifier settings, corresponding to RF field potential of around 1.4 kV. However, if left at this potential for several seconds, the discharges were prone to failing and flickering out. This could be overcome with the DC source, set to only 1 or 2 kV, providing enough of a field to stabilise the discharges for longer periods. It was found that HeNe discharges had a significantly shorter average lifetime, rarely more than thirty seconds, compared to HeXe discharges, which could be kept stable for several minutes at a time. Discharges in pure Xe could also be initiated and sustained, although this gas mixture often suffered from greater instability than HeXe.

Higher settings on the amplifier, corresponding to RF potentials of up to a maximum of 2.6 kV, generally improved the stability of the discharges, particularly in HeXe, and often did not require the DC source to sustain the discharge. Discharges using HeNe suffered from frequent burn outs at higher amplifier settings, where the fibre physically

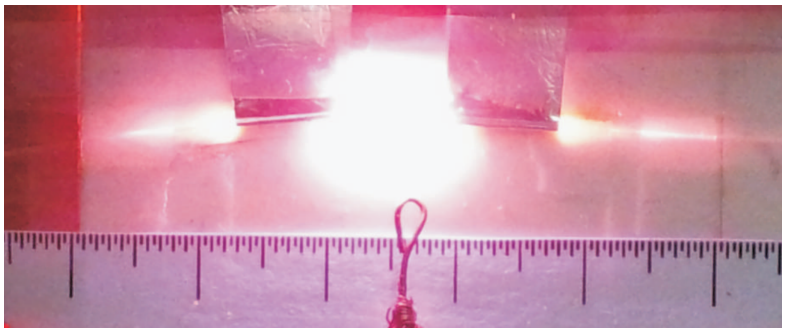

Figure 7.10: A longer discharge of in 125 mbar 7:1 HeNe, where the field potential is set to a high value of 2500 kV. The large scale units are 1 cm, the DC wire loop is in the centre, with the RF electrodes at the top, and electrodes were 8 mm wide.

melted from the heat, although the stability of the discharges was improved if a burn out did not occur. The problem of fibre burn outs in the system, and the solutions implemented, are discussed in the next Section.

In attempting to produce longer gas discharges, stabilisation proved more challenging and required both the RF field and the DC source to be set at larger values. Examples of discharges in both HeNe and HeXe are shown in Figure 7.9, with Figure 7.9 a) showing a discharge across two 8 mm electrodes with a separation of 9 mm in 5:1, 125 mbar HeNe, and Figure 7.9 b) showing a discharge across two 8 mm electrodes with a separation of 13 mm in 2:1, 100 mbar HeXe.

Both discharges show the generation of light continuing right to the ends of the electrodes, before quickly tailing off further along the fibre. This observation was consistent for RF potentials of 1600 V or more, and discharges were observed to continue beyond the end of the electrode for the highest RF potentials, as shown in Figure 7.10, suggesting that the breakdown extends along the full length from the start of the first electrode to the end of the second in those cases. However, discharges such as the one shown in Figure 7.10 frequently resulted in a burn out after a few seconds.

It was difficult to achieve longer gas discharge lengths in HeNe compared with HeXe and pure Xe, which displayed different degrees of greater stability. However longer discharge lengths were desirable, as they would produce a stronger output of optical signal at the fibre end, which would make detection and analysis of the emission lines easier. Longer discharges in HeXe of up to 12 mm were achieved, again using the DC source as an aid for stabilisation, and with the amplifier running at the higher

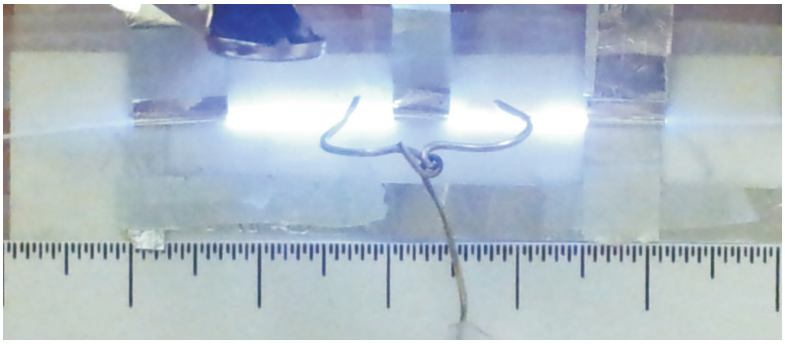

Figure 7.11: A longer discharge of in 110 mbar 3:1 HeXe, using three electrodes where the outer two have matching polarities. The large scale units measure 1 cm apart, the DC wires are at the centre of each separation, and the RF electrodes are at the top. Electrode widths are 7 mm, 4 mm, and 6 mm, with separations of 13 mm and 11 mm moving left to right.

RF potentials. To extend the length beyond 25 mm to 30 mm, a third electrode was added, with the middle electrode having the opposite polarity to the outside two. This approach has been applied before in RF systems [186]. An example of a discharge of this type is shown in Figure 7.11, where a HeXe gas mixture of 3:1 at a pressure of 110 mbar is discharging at 2100 kV between three electrodes, with widths of 7 mm, 4 mm, and 6 mm and separations of 13 mm and 11 mm from left to right. This configuration was found to be hard to maintain in HeXe, frequently flickering out after several seconds, and was less successful in HeNe, where discharges would not initiate at all.

The difficulty in stabilising HeNe discharges compared to HeXe discharges is likely to be due to the lower electron collision cross-sections for He and Ne, which required higher than normal pressures to compensate and initiate the discharge. However, equation 6.5 shows that this higher pressure results in a higher collision frequency, and therefore a faster rate of diffusion of electrons to the walls of the fibre, where there is then a greater rate of loss. The higher electron loss rate then results in a failure to maintain the discharge, causing it to flicker out, or for higher field strengths the number of electron collisions increasingly damages the fibre walls, resulting in a burn out [148].

The same effect was far less pronounced in the HeXe mixtures, where the high electron collision cross-section of Xe meant that large pressures were not required to initiate a discharge. This kept the electron loss rate low and therefore stability was easier to achieve. The presence of He in the gas mixture served as an aid to stability by elastically and inelastically colliding with the faster electrons before they diffused to

the walls of the fibre. In pure Xe mixtures the larger cross-section again aided stability, but lacked the stabilising effect from the He, and so those gas discharges displayed higher instability than the HeXe discharges.

7.7 Heat Management

As mentioned in the previous Section, a high rate of electron collisions with the walls of the fibre often resulted in damage and the burn out of the discharge as the fibre structure melted. Microscope images of a fibre damaged in this way are shown in Figure 7.12. Here it is clear that the fibre structure has been destroyed by the heat from the discharge over a relatively large region, rather than a short, clean break in the fibre at a specific point. As discussed earlier, this was found to be a far more common problem in HeNe discharges compared with HeXe or pure Xe discharges.

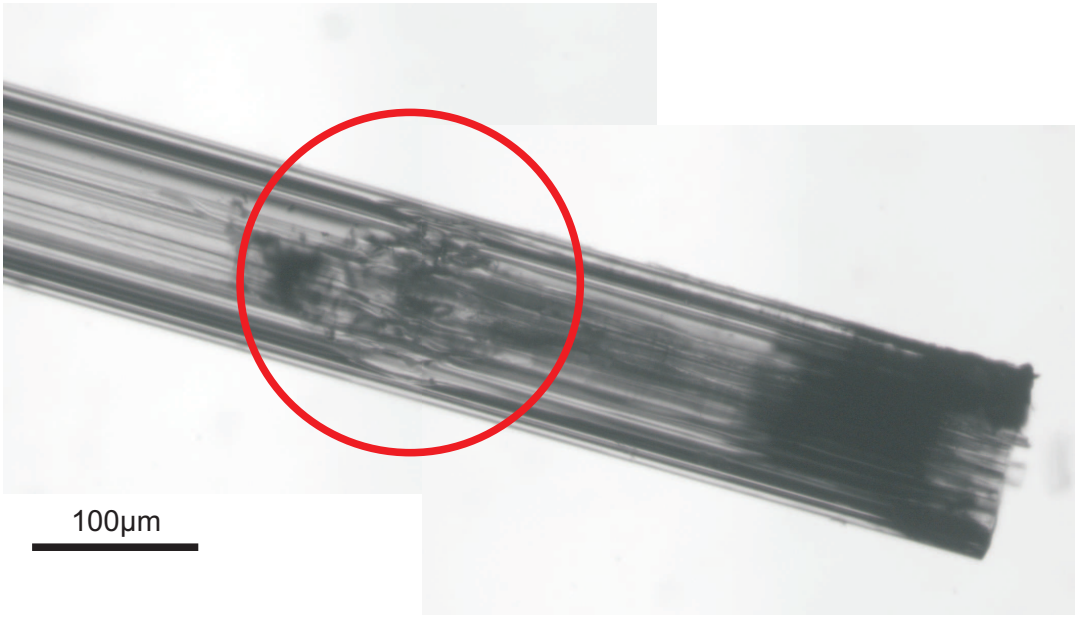

Figure 7.12: Microscope images of the melted fibre after a burn out. The damaged region is circled in red.

This burn out problem was most common when the RF field potential was at its higher values, 2 kV and above. However, this level of field potential was necessary to maintain discharges beyond a certain length. Any lower field setting resulted in flickering and instability of the discharge. Therefore a solution to the build up of heat in the fibre walls was needed.

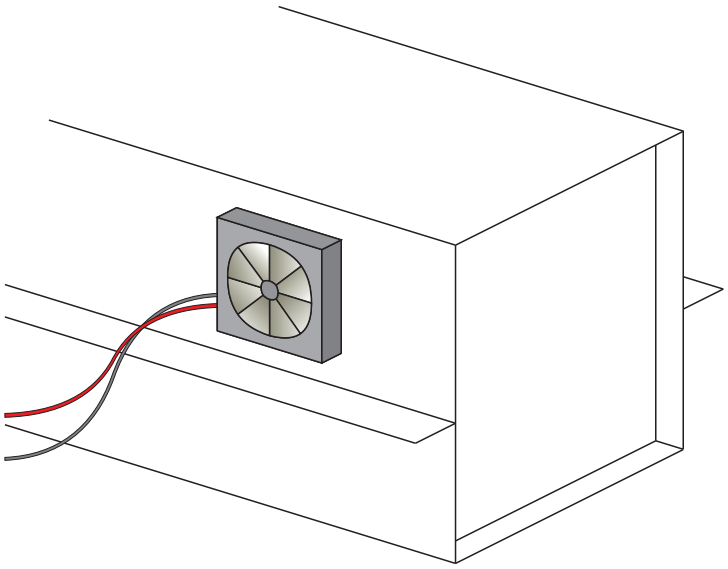

Figure 7.13: Diagram or image of the fan on the outside of the Faraday cage.

One possible solution was to alter the electrical setup of the experiment in order to raise the driving frequency of the field closer to the collision frequency. This would shorten the path length of the electrons and the number of collisions per field cycle, minimising the effect of the diffusion of the electrons to the walls of the fibre. However, this would be expensive, requiring a replacement of most of the electrical components with equipment which could operate in the GHz range.

Therefore a second solution was implemented to minimise the heat damage. This involved introducing a method of cooling the fibre and dissipating the heat, simply by attaching a fan to the outside of the Faraday cage. This ensured a continuous flow of air could move over the fibre, acting to mitigate the build up of heat in the fibre between the electrodes, as shown in Figure 7.13.

This simple solution was very effective for both pure Xe and HeXe mixtures, and helped to lessen the problem in HeNe mixtures, allowing for longer and more stable discharges. However, HeNe discharges still suffered from this problem at the highest RF field potential, and instabilities in the discharge remained even if burn outs no longer occurred.

7.8 Gas Pressure and Breakdown Voltage

As mentioned earlier in Section 7.5, the optimum gas pressure for discharge stability in RF systems with sub-millimetre internal diameters depends on the frequency and amplitude of the driving field, as well as the dimensions of the gas cell and the purity of the gas mixture.

In order to understand the ideal gas parameters for this system, an investigation was carried out recording the minimum RF field potentials necessary to initiate and sustain the discharge for a range of different ratios and pressures. In each case the field was initiated by the DC source, which was subsequently turned off, leaving the RF field to maintain the discharge. If the discharge did not fail within a few seconds, and remained steady for more than ten seconds without flickering, it was judged to be "stable" and the potential recorded. For each discharge the electrodes were of a fixed size and separation, and when they needed replacing, such as after a burn out, the same configuration was replicated.

After a series of different field potentials were recorded for given pressures and ratios of HeNe and HeXe, conclusions could be made as to the ideal gas mixture pressure and ratio based on the stability of the discharge. Notably, significant variations in potentials were observed over multiple discharges at the same given gas pressures and mixtures. This is likely to be due to small uncontrollable variations in other parameters, such as the exact electrode size, how closely the electrodes were wrapped around the fibre, the purity of the gas mixture, and the precise current flow along the discharge. As mentioned earlier, unfortunately RF systems are unable to directly monitor current, making comparisons of the dynamics of different discharges difficult.

7.8.1 HeXe: 5 mm Separation Discharges, Large He Content

The data for a range of pressures is shown in Figure 7.14, for ratios of 100:1, 50:1 and 25:1 of HeXe. Mixtures with a high He content were initially chosen in the belief that the He would aid the stability of the discharge, as shown in previous work [174, 179, 184, 189] and discussed earlier in Section 7.5. The electrodes chosen in each case were 5 mm wide, with a separation of 5 mm, so the total discharge length was 15 mm.

The high ratios of HeXe are shown to generally require higher potentials over a broad

range of pressures, with 100:1 only working in the range from 150 mbar to 350 mbar. At the low end of this pressure range the required field was high, dropping slightly in the mid range around 253 mbar, and rising again at the higher pressures up to 350 mbar. Above and below these pressure limits the discharge failed to fire for any field potential, or resulted in a fibre burn out.

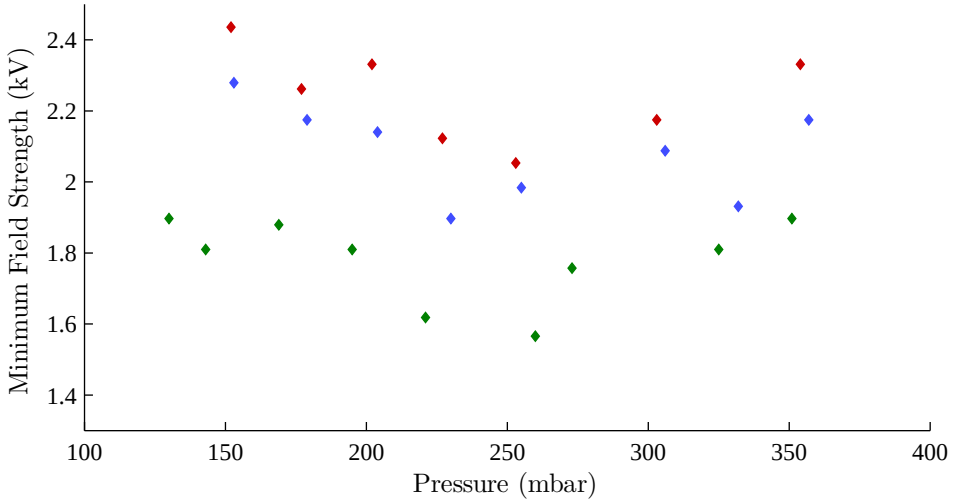

Figure 7.14: The minimum field potentials needed to sustain a HeXe discharge for a range of different gas ratios and pressures. Ratios of HeXe shown are 100:1 (red), 50:1 (blue), 25:1 (green). Electrodes were 5 mm wide with a separation of 5 mm.

The same behaviour is observed in the 50:1 and 25:1 data, with the difference that the lower ratios required increasingly lower potentials to remain stable. This appears to show a trend towards gas mixtures with a higher proportion of Xe discharging more easily, and is in keeping with some of the previous research carried out on HeXe gas lasers, where the working ratios are around 20:1 or below [174, 179, 151].

7.8.2 HeXe: 10 mm Separation Discharges, Low He Content

To investigate how far this trend progressed, and if discharges could be sustained over longer lengths of fibre, additional data was taken for gas mixtures with a larger Xe content, over a electrode separation of 10 mm. This resulted in a total discharge length of 20 mm, including the 5 mm electrodes. The same procedure was followed as previously, with the DC source initiating the breakdown before being turned off, and the discharge needing to be sustained for at least ten seconds before being considered

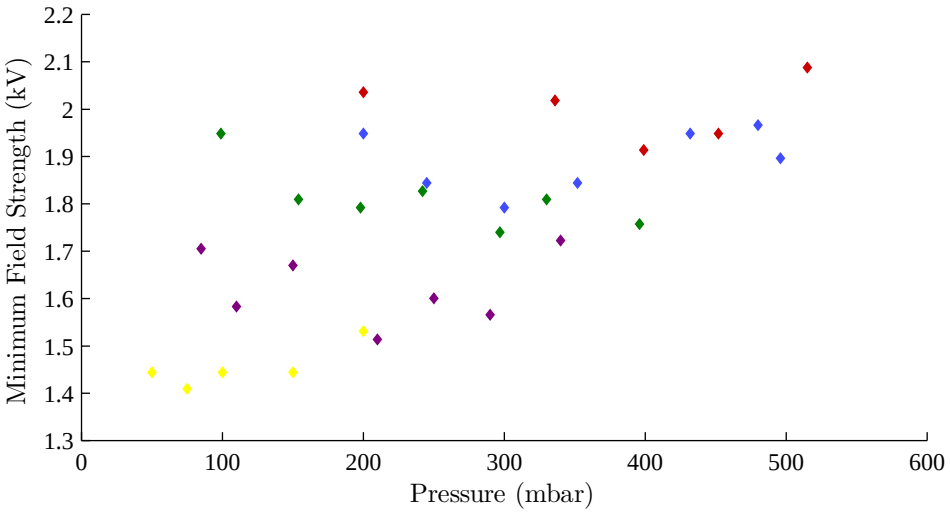

Figure 7.15: The minimum field potentials needed to sustain a HeXe discharge for gas ratios containing a greater proportion of Xe. Ratios of HeXe shown are 20:1 (red), 15:1 (blue), 10:1 (green), 4:1 (purple), and pure Xe (yellow). Electrodes were 5 mm wide with a separation of 10 mm.

"stable".

Figure 7.15 shows the resulting data points for HeXe gas ratios of 20:1, 15:1, 10:1, 4:1, and pure Xe. Again, the minimum field potentials recorded generally fell as the Xe content increased. In addition, the minimum pressure at which a discharge could be sustained was also observed to generally fall with rising Xe content. This can potentially be explained by the higher ionisation efficiency of Xe compared with He, and the larger collisional cross-section of Xe, which could result in a higher electron production rate in mixtures with a greater proportion of Xe.

However, an increase in instability was observed in the pure Xe discharges, which frequently failed sooner than those with some content of He, and were also highly prone to burn outs at pressures above 150 mbar to 200 mbar. This is likely to be due to the absence of the He to act as a stabiliser, through the de-excitation of fast electrons.

Discharges in HeXe over even longer lengths of fibre also appear to be possible from this data, given the relatively low field levels required for these ratios, compared with the maximum available field potential of the system.

7.8.3 HeNe: 5 mm Separation Discharges, Low He Content

A similar investigation was then carried out using HeNe gas mixtures, starting with ratios closer to those used in previous research on narrow diameter gas discharges [150, 145]. The same procedure and criteria were applied to the discharges as in the HeXe case, using an electrode size and separation of 5 mm and 10 mm respectively.

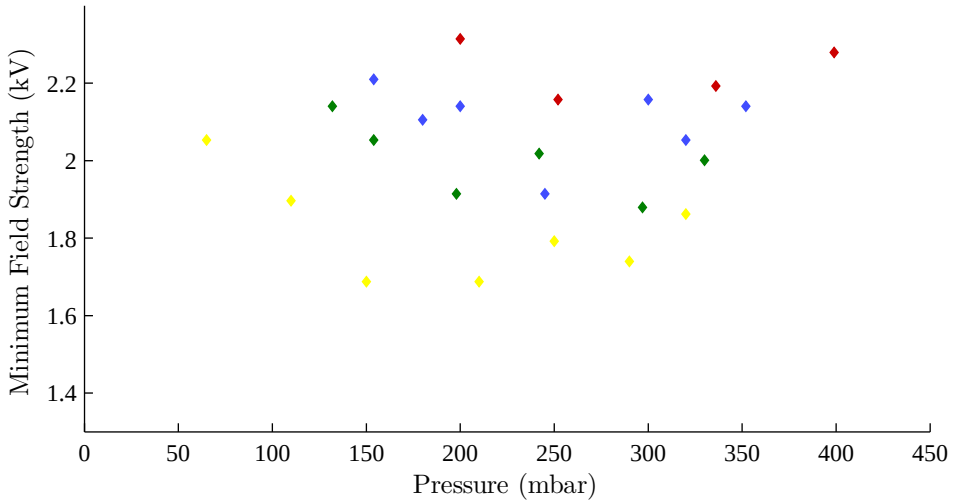

Figure 7.16: The minimum field potentials needed to sustain a HeNe discharge for a range of gas ratios and pressures. Ratios of HeNe shown are 20:1 (red), 15:1 (blue), 10:1 (green), and 4:1 (yellow). Electrodes were 5 mm wide with a separation of 10 mm.

Figure 7.16 shows the resulting data for HeNe gas mixtures, using ratios of 20:1, 15:1, 10:1, and 4:1. The same trends seen in the HeXe data are also present for HeNe, with a generally falling field potential for greater proportions of Ne. Higher pressures were far more likely to suffer a burn out for mixtures with less He, again possibly due to the stabilising effect of He in those gas mixtures.

The minimum field potential needed to sustain a discharge again appears to generally increase with pressure, until discharges either did not occur or became highly unstable. At lower pressures the necessary potential again tended to be high or discharges would not initiate, often flashing briefly without becoming stable.

7.9 Concluding Discharge Initiation and Stabilisation

To conclude, discharges were achieved in HeXe and HeNe gas mixtures for a range of ratios and pressures. It was found that pressures of at least 100 mbar were required to initiate and maintain a discharge for both HeXe and HeNe. Both gas mixtures suffered burn outs and instability at higher pressures and failed to start at lower pressures, despite larger field potentials.

The relatively high pressures needed to initiate discharges with this system resulted in working *pd* values which were higher than in previous research, ranging from approximately 5 mbar mm to 33 mbar mm for HeXe and 5 mbar mm to 40 mbar mm for HeNe. Considering the ratios used at these *pd* values, this corresponds to approximate theoretical electron temperatures ranging from 15,000 K to 20,000 K for HeXe mixtures, and 35,000 K to 90,000 K for HeNe mixtures [147]. Previous work has operated gas lasers using these noble gases with more conventional *pd* values of 2.7 mbar mm to 8 mbar mm [150, 151], which have theoretical electron temperatures of 15,000 K to 20,000 K and 80,000 K to 130,000 K in HeXe and HeNe respectively. Unfortunately, the necessary operating pressures in this RF driven system results in a range of *pd* values which are likely to be higher than the ideal values predicted earlier in Chapter 6 of less than 4 mbar mm to maximise the collision cross-section of Xe.

HeXe was observed to be relatively easy to initiate for ratios of under 15:1, with the minimum sustainable pressure dropping to under 100 mbar for pure Xe. Discharges of 10 mm in length could be sustained for several minutes without significant fluctuations in stability for HeXe, although discharges of pure Xe displayed higher levels of instability in comparison.

The general behaviour of the HeNe discharges was frequently quite unstable compared to those of HeXe. While discharges in HeXe could be maintained for several minutes, HeNe discharges often failed to last as long. This comparatively short lifetime made it difficult to record output spectra from the HeNe discharges.

7.10 HeXe and Pure Xe Gas Discharge Spectra

Having achieved discharges in HeXe which were stable for several minutes, spectra of the emitted photons could be recorded from the output at the end of the fibre.

The output block containing one fibre holder, described earlier in Section 7.3.5, could be attached directly to a spectrometer, with the signal emitted from the fibre coupling out of the sealed block through a sapphire window. This allowed the spectra generated from the discharge to be recorded.

Several mixtures and pressures were used to generate and record HeXe spectra. However, even in the most stable HeXe discharges, it was found it be difficult to reliably record spectra before a discharge would fail. Therefore, a systematic study of the various mixture ratios, pressures, and discharge lengths was not practically attainable using this RF excitation approach. Instead, several different combinations were recorded to ascertain if any produced noticeably more signal than others.

7.10.1 5:1 HeXe 128 mbar Discharge, 5 mm Separation

The spectra from a discharge of 5:1 HeXe, at a pressure of 128 mbar, were recorded for several potentials using the spectrometer and are shown in Figure 7.17.

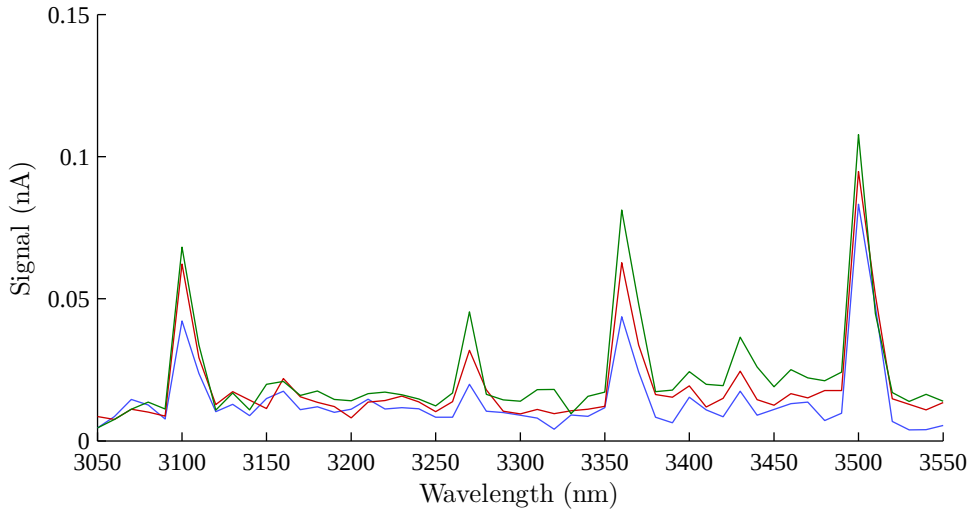

Figure 7.17: The spectrum between 3050 nm and 3550 nm recorded from a 5:1 HeXe discharge at 128 mBar, for field potentials of 1.53 kV (blue), 1.88 kV (red), and 2.05 kV (green). The spectrometer resolution was set to 10 nm. Electrodes were 5 mm wide with a separation of 5 mm.

Only the field potential was changed between each recording, with the fibre, electrodes, and gas mixture remaining the same in each case. The spectrum clearly shows a series of peaks, located at 3105 nm, 3270 nm, 3370 nm, and 3500 nm with two more possible

peaks at 3160 nm and 3425 nm. These all correspond to known lines of Xe located to within a few nanometres of each recorded peak [182], verifying that the Xe in the discharge is emitting photons which are coupling into and being guided by the fibre.

The emission spectra for the RF field potentials of 1.53 kV, 1.88 kV, and 2.05 kV all show the same emission lines, with a noticeable increase in each of the 3105 nm, 3270 nm, 3370 nm and the 3500 nm lines in each case. The large spectrometer resolution of 10 nm was chosen due to the lifetime of the discharge and the time taken by the spectrometer to record the spectra.

7.10.2 Pure Xe 110 mbar Discharge, 5 mm Separation

Discharge spectra were also recorded for pure Xe gas mixtures for field potentials of 1.51 kV and 1.91 kV, at a pressure of 110 mbar, and are shown in Figure 7.18. As before, the fibre and gas mixture was the same for each recorded spectra, only the field potential was increased. The electrode configuration also remained the same as for the 5:1 HeXe mixture data shown earlier in Figure 7.17, being 5 mm wide electrodes with a separation of 5 mm. The choice of 10 nm as the spectrometer resolution is again due to the short lifetime of the discharge.

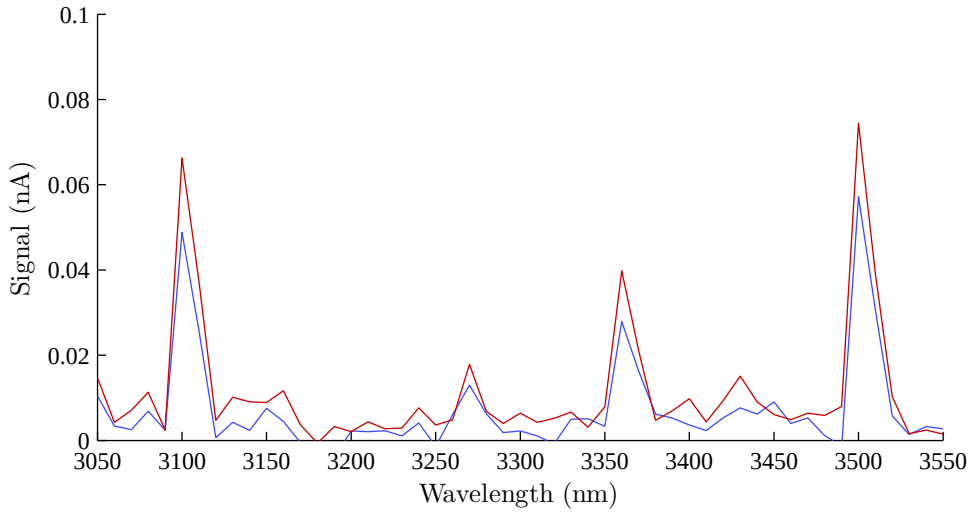

Figure 7.18: The spectrum between 3050 nm and 3550 nm recorded from a pure Xe discharge at 110 mBar, for field potentials of 1.51 kV (blue), and 1.91 kV (red), and a spectrometer resolution of 10 nm. Electrodes were 5 mm wide with a separation of 5 mm.

Both spectra again show the same distinctive peaks as in the 5:1 HeXe data, with strong emissions at 3105 nm, 3270 nm, 3370 nm, and 3500 nm. When the signal strength above the noise for each line is compared with the 5:1 HeXe data, marginally more light is observed at 3105 nm and 3500 nm, with approximately the same signal strength at 3270 nm and 3370 nm. This difference in signal strength is small enough to be within the discharge-to-discharge variation, preventing any conclusions regarding the effect the proportion of He in the gas might have on the line emission strength.

7.10.3 1:1 HeXe 125 mbar Discharge, 12 mm Separation

In order to generate and collect a larger signal, several spectra were taken for a longer discharge of 1:1 HeXe at a pressure of 125 mbar. The electrodes for this set of discharge data were 10 mm and 6 mm wide, with a separation of 12 mm, producing a total discharge length of 32 mm. Data was recorded for field potentials of 1.75 kV, 2.15 kV, and 2.38 kV, and the recorded spectra are shown in Figure 7.19.

The general signal strengths for all three spectra are noticeably larger than for the shorter discharge lengths shown in Figures 7.17 and 7.18. However, while the 3270 nm, 3370 nm, and 3500 nm lines are observed to have increased by around a factor of two, the 3105 nm line appears to have remained at approximately the same strength as the discharge length is doubled. This could be due to the fact that the *pd* value was greater than optimum for the gain on this line, affecting the collision cross-section and limiting the excitation rate of the 3105 nm line.

As the potential is increased, the emission strength is again observed to rise on all lines, albeit by a different amount for each peak. The 3500 nm line, already the strongest line, increases the most, followed by the 3370 nm line. Small increases in 3105 nm and 3270 nm are also observed.

The image of the discharge shown in Figure 7.19 b), also appears to show the length of the discharge extending out beyond the electrode on one side. This is potentially the result of fast electrons being accelerated by the field beyond the electrode, colliding with Xe atoms and emitting photons as in the region between electrodes. As mentioned earlier, this effect was only observed for the higher field potentials, such as 2.38 kV for the example shown in Figure 7.19 b), therefore supporting the possible explanation concerning fast electrons collisions beyond the electrodes.

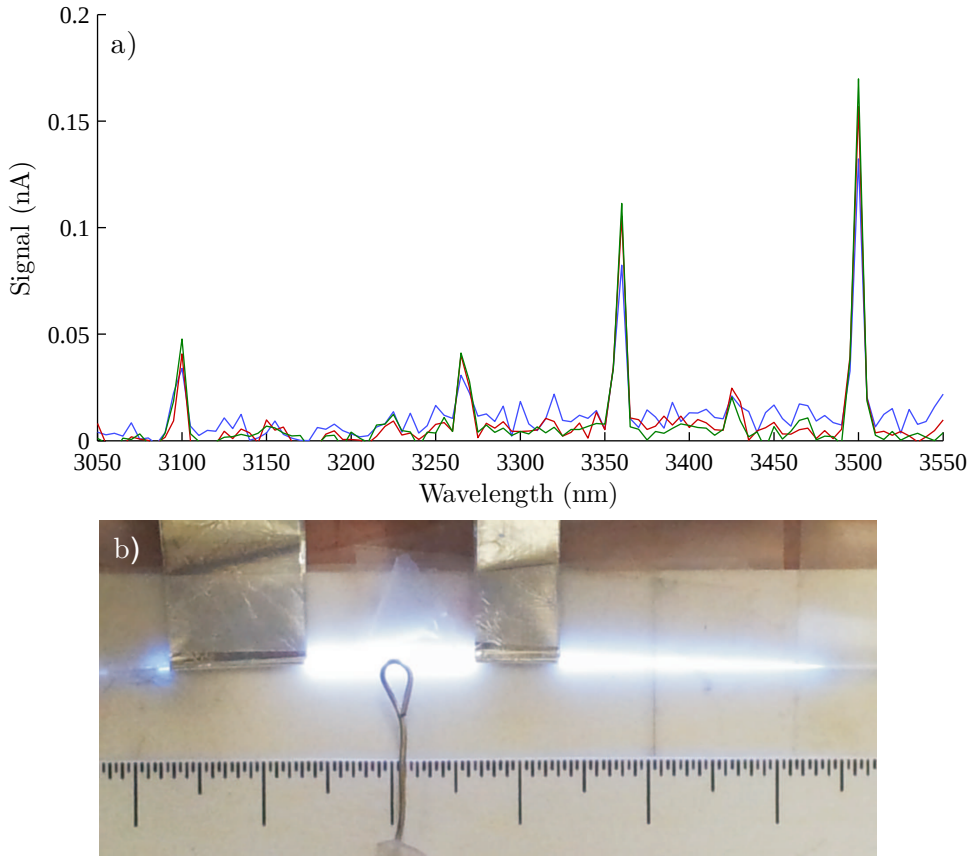

Figure 7.19: a) The spectrum between 3050 nm and 3550 nm recorded from a 1:1 HeXe discharge at 125 mBar, for field potentials of 1.75 kV (blue), 2.15 kV (red), and 2.38 kV (green), at a spectrometer resolution of 10 nm. Electrodes were 10 mm wide with a separation of 12 mm. b) An image of the discharge at a field potential of 2.38 kV, showing the discharge length to be approximately 50 mm in length.

7.10.4 Comparing Gas Mixtures and Signal Strengths

The signal strength data from Figures 7.17, 7.18, and 7.19 can now be plotted and directly compared. Figure 7.20 shows the maximum signal recorded at each discharge voltage for each of the major peaks in the earlier spectra.

Comparing this data allows for some conclusions to be drawn regarding the effect from the variation of the Xe partial pressure, the total gas mixture pressure, the electrode size, the electrode separation, and the discharge voltage, on the strength of the emission signal.

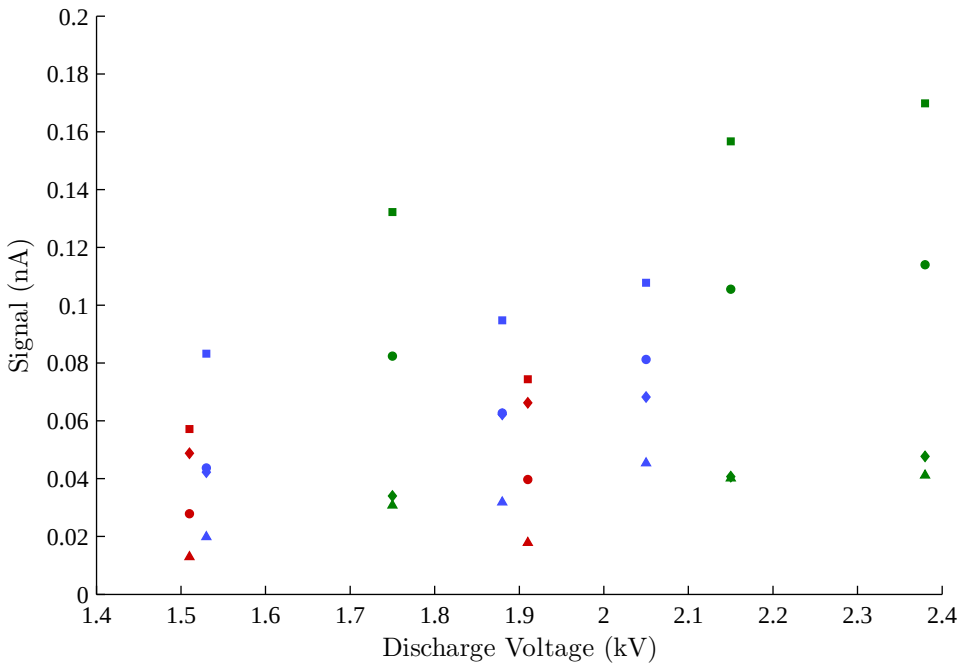

Figure 7.20: The data from Figures 7.17, 7.18, and 7.19, consolidated and plotted as the detected signal strengths for the discharge voltages applied. The gas mixtures, electrode size, and electrode separations shown are 128 mbar 5:1 HeXe with 5 mm sized electrodes and 5 mm separation (blue), 110 mbar pure Xe with 5 mm sized electrodes and 5 mm separation (red), 125 mbar 1:1 HeXe with 10 mm sized electrodes and 12 mm separation (green). The wavelengths shown are 3100 nm (diamonds), 3270 nm (triangles), 3370 nm (circles), and 3500 nm (squares).

Figure 7.20 shows that in all the discharges there is a clear increase in detected signal for each increase in voltage. This is most prominent on the 3370 nm (circles) and 3500 nm (squares) lines, which are also the lines with the highest overall signal strengths. This relationship is unsurprising, since it is already understood that the voltage of the RF field is coupling to the Xe gas and causing it to breakdown into a discharge, therefore an increase in the field voltage would be expected to increase the population of excited Xe atoms, and in turn the number of photon emissions. It is also unsurprising that the 3370 nm and 3500 nm lines are the most sensitive to changes in the RF field potential, as they are already the strongest emission lines, suggesting the upper levels of those transitions are excited relatively easily by the field. These are also the lines expected to display the higher amounts of gain [182, 179, 183, 150], which is also as a result of the large population inversion achieved by efficient excitation of their upper states.

The three data sets also use different partial pressures of Xe and total pressures, 16% of 128 mbar (blue), 100% of 110 mbar (red), and 50% of 125 mbar (green). Previous research has suggested that the presence of helium in the gas mixture increases the resulting gain [148], but this may not be reflected in the initial signal strength of the different peaks. As the overall pressure is increased, more Xe atoms are available to be excited and so more photons are emitted. However, as discussed in Chapter 6, increasing the pressure alters the electron temperature T_e, which in turn affects the resulting collision cross-section and the gain. In addition, the contribution of He to the gas mixture acts to increase T_e, and therefore its absence results in an effective T_e which is lower than ideal for Xe. These elements might explain why the data points for the 100 mbar pure Xe are generally lower than the other two sets, despite having a much higher degree of Xe present.

The size and separation of the electrodes appear to each affect the signal strength differently. It is clear from equation 7.3 that the 10 mm long electrodes used in the 125 mbar 1:1 data, being twice the length of the other two data sets, would operate with twice the capacitance. However, to ensure that the LC circuit had a resonant frequency of 27 MHz, the variable capacitors were adjusted to compensate for this increased contribution to the capacitance of the circuit from the longer electrodes. Therefore, the only possible practical benefit of the longer electrodes could be to increase the contact area with the fibre, and minimise any micro-gaps between the electrode and the silica glass. Unsurprisingly, the separation of the electrodes appears to have a more direct effect on the signal. As expected, the longer the discharge, the more signal is generally detected across all lines, as shown by the 125 mbar 1:1 data, which has a separation of 12 mm. However, the separation increase from 5 mm to 12 mm does not appear to simply increase the signal by a proportional amount. This could possibly be the result of the different amount of Xe present in the gas mixture for this data set compared with the two other data sets, or the result of variations between data sets in the loss caused by the high bend sensitivity of the fibre, despite best efforts to keep the fibre straight and level between the breakdown regions and the spectrometer.

Overall, it is hard to draw specific conclusions as to the relationship between the signal strength and the gas mixture, partial Xe pressure, and electrode separation. The fact that the detected signal strength will vary to some degree due to fibre bend losses, and the inability of this method to measure the true current density in the fibre for each breakdown, are also sources of uncertainty.

The short discharge lengths achieved using the RF excitation approach, in addition to

these uncertainties regarding the different gas mixtures, could be made less significant by the detection of high gain on the 3500 nm emission line, as expected from previous research. In this case, short discharge lengths could prove to be sufficiently long to detect such high gain, and hence allow for a more precise understanding of the breakdown characteristics. Therefore, an experiment was designed to perform a gain measurement on the lines over this wavelength range.

7.11 HeXe Gain Measurement

Having detected several spectra from discharges of pure Xe and HeXe of up to 12 mm in separation, a measurement was made to determine the extent of the gain on the detected lines.

In order to carry out the measurement, it was necessary for a second Xe discharge to be generated inside the fibre, further separated along the fibre with respect to the first. This would allow for spectra to be recorded from each of the Xe sources separately, and compared to the signal that resulted from both sources emitting simultaneously. When one discharge was active, light would be generated and guided along the fibre to the spectrometer as usual, so two spectra could be taken, one for each discharge. When both discharges were active simultaneously, light generated in one discharge would propagate through the other before arriving at the spectrometer. This would result in some degree of amplified spontaneous emission, which in the presence of gain on an emission line would show a total signal strength which was larger than the sum of the individual signals from each discharge. By keeping the positioning of the fibre the same for each discharge combination, the loss would be expected to remain constant and therefore not affect the gain measurement. Experimentally this required a second set of RF equipment and a second LC resonant circuit, identical to the one used to generate discharges up to this point, which would generate a second discharge further along the fibre.

Figure 7.21 shows the experimental layout for the gain measurement, including the two discharges, each inside a separate Faraday cage. Because each circuit would be emitting an RF signal which was very close to the same frequency, the second cage was built, made of the same steel sheeting as the original cage and to the same design. This shielded the two RF sources from each other as well as from the wider environment. In addition, the two channels on the CB radio chosen as the sources for the RF signals

were detuned as far from each other as possible to minimise interference which would affect the gain measurement. This detuning could be compensated for using the LC circuits, ensuring the RF field potential was undiminished inside the fibre.

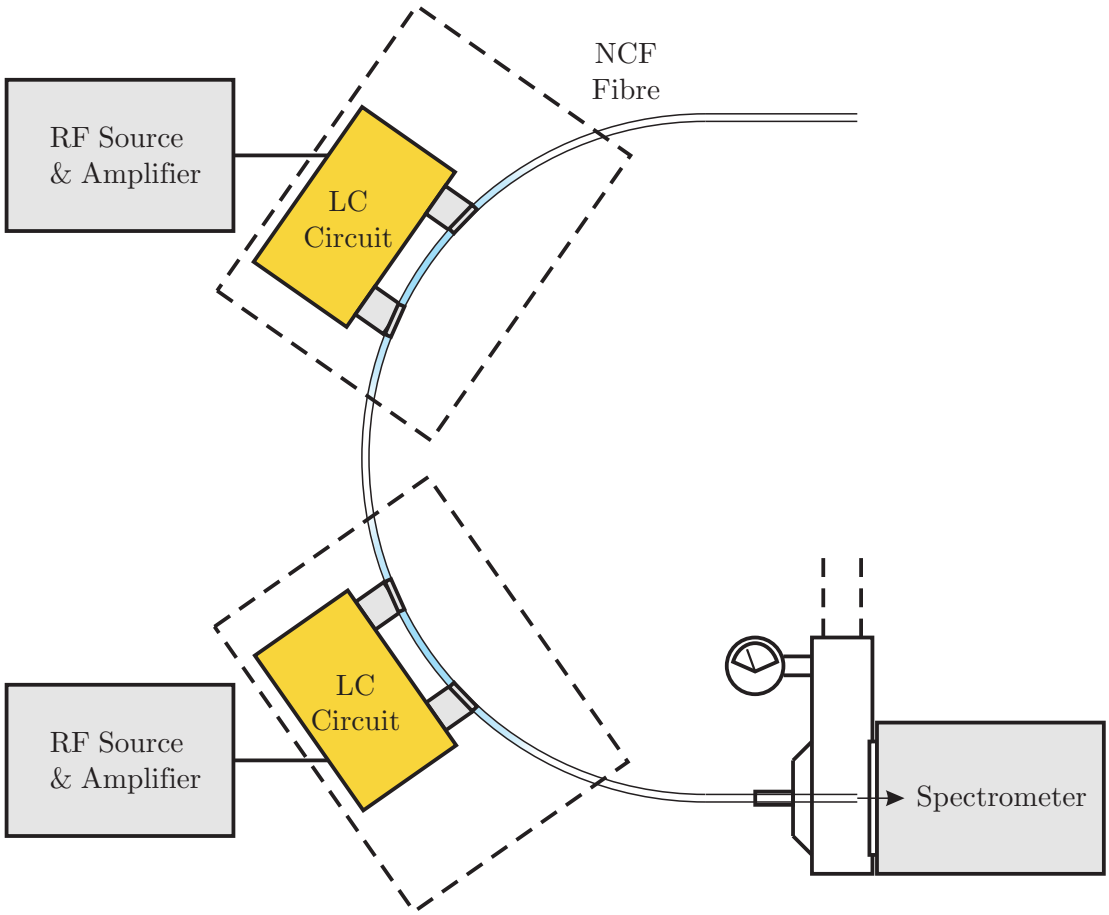

Figure 7.21: The experimental setup of the gain measurement, with two RF sources and a dividing wall inside the Faraday cage.

It was experimentally verified that the shielding between RF sources was sufficient, and that any interference was minimal. One RF source was switched on and the voltage probe was monitored through an oscilloscope as the second source was switched on. The amplitude and stability of the waveform on the oscilloscope was observed to remain unchanged as each of the circuits was tested.

The first discharge length consisted of 7 mm wide electrodes separated by a gap of 10 mm, resulting in a total discharge length of 24 mm. The second discharge length consisted of 8 mm electrodes separated by 13 mm, making a total discharge length of 29 mm. The gas chosen was 120 mbar of pure Xe, and was kept in the fibre for both

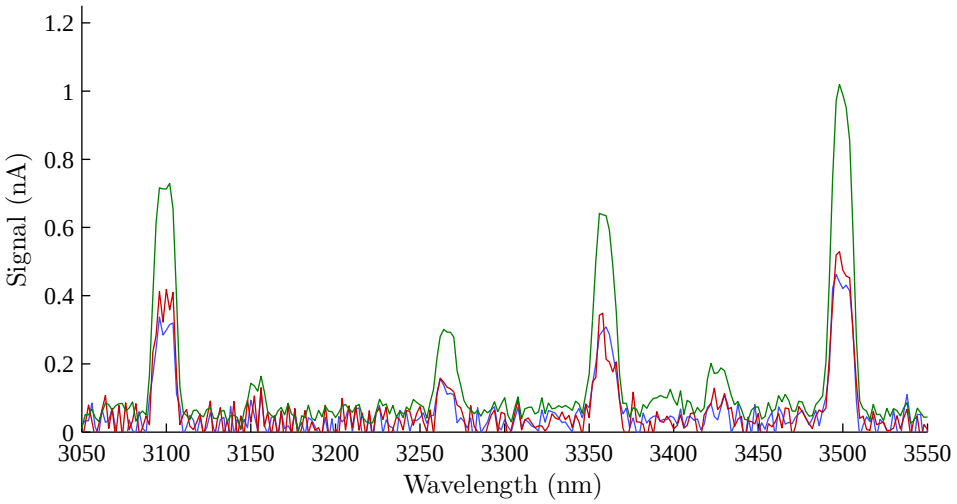

Figure 7.22: The spectra generated inside the fibre by each of the discharges individually, compared with the spectra generated by both discharges active simultaneously. Discharge 1 (blue) operated at a potential of 1.22 kV, while discharge 2 (red) operated at a potential of 1.48 kV. Both discharges running simultaneously (green) were at the same field potentials as in the individual cases. The spectrometer resolution was set to 2 nm, with a slit width of 10 nm.

the individual discharges and the simultaneous discharge.

The results of the gain measurement are shown in Figure 7.22. Discharge 1 operated at a potential of 1.22 kV, while discharge 2 operated at a potential of 1.48 kV. These RF field potentials were the same in both individual and simultaneous cases. Again the four peaks at 3105 nm, 3270 nm, 3370 nm, and 3500 nm are observed, with weaker emissions again observed around 3160 nm and 3425 nm. The height of the 3105 nm peak in both of the individual lines is again observed to be relatively strong compared to all but the 3500 nm line, as was seen earlier in Figure 7.18. The third spectrum, showing the signal from both discharges simultaneously, is significantly larger on all lines for the length increase from 24 mm and 29 mm to 53 mm.

The maximum signal strengths for each peak of the three spectra are plotted in Figure 7.23, allowing for a direct analysis of any potential gain on the detected Xe emission lines. The 3105 nm line (shown in blue) has a maximum signal value of 0.729 nA, which is 0.027 nA, or about 3.5%, less than the sum of the individual maxima. The noise for these spectra is observed to be of the order of 0.1 nA, placing this difference within the noise band, possibly indicating a small amount of either absorption or gain over this short increase in length. The line at 3270 nm (shown in green) has a maximum signal

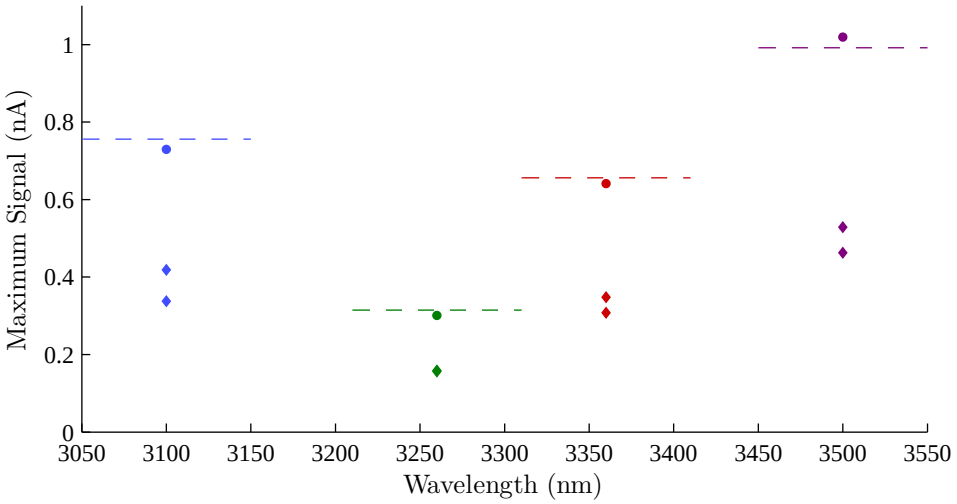

Figure 7.23: The maximum signal detected for each major emission wavelength, comparing each discharge individually (diamonds) with both discharges together (circles). The sum of the signal strengths for discharge 1 and discharge 2, and therefore the threshold for detecting any gain, is shown as a dotted line for each wavelength. The detected signal strengths for the individual discharges on the 3270 nm line were very similar, both being around 0.158 nA, and therefore effectively overlap.

of 0.301 nA, which is 0.013 nA, or about 4.3%, less than the sum of the individual signals. This is again within the noise band, and so does not reveal much regarding the gain on this line. The maximum signal strength for the 3370 nm peak (shown in red) is 0.641 nA, which is again short of the individual sum by 0.015 nA, or about 2.3%, and again within the noise band of 0.1 nA. Finally, the signal at 3500 nm (shown in purple) is 1.012 nA, which is 0.028 nA, or about 2.8%, above the sum of the individual signals at the same wavelength, which is again within the variation of the noise. It is also notable that the signal strength of each peak was expected to display some variation between discharges, and is therefore another possible reason for the small discrepancy between the expected signal strength and the detected signal for both discharge lengths.

This suggests that for an increase in discharge length from 24 mm and 29 mm to a length of 53 mm, there is not enough gain or absorption on these lines to be statistically significant or conclusive. If longer discharges could be sustained, and therefore stronger signals recorded from the emission lines, then the noise uncertainty could be removed and a clearer assessment of the gain for each line could be made.

It is also notable that while every effort was made to ensure that each discharge behaved

the same way both times they were initiated, there would inevitably have been some small differences in the signal strengths from discharge to discharge. These differences could have been the result of heating in the LC circuits, a small degree of leakage through the dividing wall from one side of the Faraday cage to the other, or small changes in the field potential as a result of fluctuations in the 400 W amplifiers. Even if these changes were small, they could counteract or conceal the extent of any gain over such a short length increase.

7.12 Summary and Conclusions

To conclude, it has been shown in previous research that noble gas lasers with a reduced internal diameters display higher gain [179, 167, 149, 150, 151, 148]. With this relationship in mind, a 27 MHz RF system was constructed using a CB radio as a source. An LC circuit was connected to the system and used to deliver a maximum potential of 2.6 kV to two electrodes wrapped around the outside of a hollow negative curvature fibre with a core diameter of 96 μm. The fibre core could be evacuated using a vacuum system, and gas mixtures of HeNe or HeXe could be introduced at a chosen pressure. A DC source was used to emit a field of up to 10 kV to initiate a gas breakdown within the fibre, which was then maintained using the RF field. Light generated between 3 μm and 3.5 μm by the emission lines of the gas species, were guided along the fibre with an attenuation of 0.1 dBkm^{-1}, to be emitted from the fibre ends.

An investigation was carried out to find the optimum range of HeNe and HeXe gas ratios and pressures to achieve stable breakdowns. It was found in each case that the range of pressures over which stable discharges could be achieved was greater than the ideal maximum pressure of approximately 4 mbar mm, suggested earlier in Chapter 6. This was probably due to the chosen operating frequency for the RF system being significantly lower than the collision frequency of the electrons in the gas, resulting in a high rate of loss of the free electrons through diffusion to the fibre walls.

The light that was generated by the gas and guided in the fibre could be coupled out of the vacuum system through a sapphire window, and collected by a spectrometer, allowing for spectra to be recorded. A range of gas mixtures and pressures were chosen, rather than a more detailed systematic approach, due to the general difficulty in consistently initiating and maintaining discharges for the time required to record spectra. Spectra were recorded for several HeXe gas mixtures, pressures, and discharge lengths;

5:1 HeXe at 128 mbar over 15 mm, pure Xe at 110 mbar over 15 mm, and 1:1 HeXe at 125 mbar over 28 mm. No HeNe gas discharge spectra were recorded, due to the long term instability in even the most stable of the HeNe discharges. Xe lines were detected at 3105 nm, 3270 nm, 3370 nm, and 3500 nm in all spectra. The strength of the detected lines generally increased with field potential as expected, but were observed to vary with discharge ratio. The emission at 3105 nm was seen to remain at approximately the same strength when the discharge length was increased by 13 mm in the 5:1 HeXe spectra, shown in Figure 7.19. This could be attributed to the line exhibiting poor gain for this value of pd, due to a low excitation rate of the upper level for the 3105 nm transition. The 3500 nm line was shown to be the strongest of the lines observed, followed by the 3370 nm line. It was expected from prior research that the 3500 nm line has the highest gain over this wavelength range, potentially as high as 60 dBm^{-1} [179, 167].

The peak signal strengths and field potentials for each of the emission lines of the recorded spectra were plotted together for comparison. The signal strength for the 3370 nm and 3500 nm lines were observed to be the most sensitive to the field potential applied to the fibre, and is attributed to the efficient excitation of the upper states for those lines by the RF field. It was observed that the pure Xe discharge showed noticeably less signal than the HeXe mixtures, despite having more Xe. This is interpreted as being due to the lower electron temperature T_e in the gas, which reduced the collision cross-section of the Xe and therefore reduced the strength of the resulting signal. The presence of He in the mixture acts to raise T_e to a point where the Xe collision cross-section is larger, and a stronger signal is emitted across all lines. The size of the electrodes were not expected to directly affect the signal strength, but could potentially aid the discharge in achieving breakdown through better contact with the fibre. The separation distance between the electrodes was expected to increase the signal as a result of more excited Xe atoms in the larger discharging portion of fibre. However, this was not observed to be a proportional increase compared with the shorter discharge lengths at similar field potentials. This was attributed to the variation between discharges in the fibre loss from bending, making any conclusions regarding possible gain based on the comparison difficult.

The equipment was therefore modified to carry out a gain measurement on the observed Xe lines. The spectra from two discharges, first separately and the together, were recorded and analysed. It was found that the signal strengths on all lines did not suggest significant gain, falling within the noise band of $\pm$ 0.1 nA in all cases. This is

likely to be the result of the short lengths of the discharges, which generated relatively weak signals with respect to the noise. In order for clear gain to be measured over these length scales, the gain would have to be at least 10 dBm^{-1}, which given the high operating pressures, is possibly unlikely. This is because the higher pressures of 100 mbar or more needed to sustain discharges in this system also increased the *pd* value to around 9.6 mbar mm, and therefore reduced the electron temperature. At a reduced value of T_e, the collision cross-section in Xe is reduced, and is no longer the optimum for significant gain, despite the reduced internal diameter of the gas cell, and therefore a lower value of the gain would be expected.

Possible solutions to this problem which allow the pressure of the discharge to be lower, and therefore optimised for gain, include the increase of the RF driving frequency from 27 MHz to a value closer to the collision frequency. This would prevent the free electrons from diffusing to the walls of the gas cell over one cycle, reducing the electron loss rate. Lower stable pressures could then be accessed, where the gain is higher and more clearly detectable in short discharges. An alternative solution would be to achieve longer discharges, so any relationship between length and signal strength, which indicates gain, would be more obvious. However, this was found to be difficult using this system, as instabilities in the discharge became larger as the discharge length was increased. One configuration which was attempted was to connect multiple electrodes along the fibre, alternating in polarity, similar to a configuration previously demonstrated [186, 150]. However, this was also found to be difficult to initiate, often being unstable and frequently led to burn outs.

Finally, an alternative which could potentially solve all the problems described would be to instead use a DC excitation system. While this would require the direct exposure of the gas to the electrodes emitting the field, it would remove the electron diffusion and burn out problems, increasing the stability and allowing for lower pressures to be used to achieve a more optimum *pd* value. This increased stability could also allow for longer discharges to be achieved, and relatively recent work has demonstrated discharge lengths in narrow capillaries of up to 26.2 cm are possible [155]. The electrical equipment would be far simpler, not requiring any resonant tuning or impedance matching. Additionally, the current density could be directly measured in a DC discharge, allowing for a more detailed understanding of the discharge dynamics.

For these reasons, further research towards a fibre gas discharge laser replaced the RF source with a DC source. The details and results of that research are the subject of Chapter 8.

Chapter 8

Fibre Gas Discharge Lasers: A DC Excitation Method

8.1 Introduction

The work described in this Chapter was presented at the Conference on Lasers and Electro-Optics (CLEO) 2014 as a post-deadline paper (see Publications and Conference Presentations 3), and at the Speciality Optical Fibres and Applications conference (SOF) 2014 (see Publications and Conference Presentations 4).

This Chapter continues the work aimed at developing a fibre based gas laser. Earlier in Chapter 7, an RF field was used as the source of excitation to induce the gas breakdown inside the fibre. This approach was found to suffer from several experimental difficulties, including complex electrical equipment, an inability to directly monitor the current in a breakdown, short discharge lengths, and a high level of instabilities. In this Chapter the more conventional DC excitation method is used, where these previous difficulties are overcome.

8.2 Approach

As described in Chapter 6, the DC excitation method requires the electrodes to be directly exposed to the gas inside the fibre. This approach was previously rejected due to the perceived difficulties of meeting this requirement, either by drilling holes in the fibre to allow electrode access, or by placing the electrodes at the end of the fibre while leaving the optical path clear.

However research using an RF excitation highlighted a number of unforeseen difficulties. As discussed earlier in Chapter 6, electron temperatures are higher in RF driven discharges for small gas envelopes, resulting in an increased number of fast electron wall collisions, which can cause catastrophic fibre damage. Such damage was experimentally observed in the internal structure of the fibre in Figure 7.12. Additional problems were encountered due to the unreliability of the electronics and their lack of current control, and furthermore, very short discharge lengths made any sort of gain measurement difficult.

The experimental approach of recent research [154, 155] was considered. In both these publications by Shi et al., discharges of up to 26.2 cm in neutral noble gases were achieved in straightened tubes with an inner diameter of 260 μm, using the DC excitation method with breakdown voltages of the order of 10 kV. This is significantly lower than previously thought necessary using a pair of electrodes at each end of a waveguide. Flash glow discharges of 2.9 cm in length were also observed in straight discharge tubes with a diameter as small as 20 μm, but could not be sustained. The choice of electrode configuration in this work was also considered to be excessively far from the fibre, which added an unnecessarily large cathode and anode voltage drop to the discharge voltage, suggesting the breakdown voltage could be lowered further still. The choice of gases, Ar and He, was not ideal for electrical discharges in tubes with small diameters, both having a higher electron temperature than other noble gases available. In addition, it was recognised that a DC system would allow for a high degree of precise current control, which was a central problem to the RF excitation work.

Chapter 6 highlights the work published in 1973 at Bell Labs by Smith et al. [151], where a gas mixture of He and Xe isotopes was used in a short, narrow capillary waveguide to form a gas laser at 3.5 μm. Gain measurements at this wavelength suggested a peak for HeXe mixtures of 5:1, at pressures of approximately 6.5 Torr (approximately 8.7 mbar) in a specially-straightened tube with an inner diameter of 250 μm. The principle of

preserving the *pd* value to maintain the same electron temperature in the discharge for a given gas mixture, and therefore the optimum gain, allows for an estimation of the pressure need when working with a negative curvature fibre of a smaller diameter. However, the gases used in the work by Smith et al. were particular isotopes, and so some variation when using the equivalent natural noble gases was expected. This would arise from the increased mass of the atomic ion species and the resulting change to the positive ion mobility, which in turn could affect the general stability and dynamics of the discharge.

It was believed that the experimental approach of recent research [154, 155] could be perfected, while the earlier work by Smith et al. [151] could provide a reasonable starting point for choosing HeXe gas mixtures and pressures. Working on the basis of the results of these publications, it was hypothesised that a system could be built around a negative curvature PCF to deliver long, stable discharges, allowing for simpler spectra detection and greater ease in investigating the length dependences of the discharge.

8.3 Electrical Setup

The electrical setup required for the DC approach was simpler than that used in the RF system, and is shown in Figure 8.1. A variable 40 kV DC supply (UltraVolt, 40A series), rated to a maximum current of 0.75 mA, was used as a source. The supply provided output ports from which the current and the supply output voltage could be monitored and recorded through data logging software.

The supply was then connected to a series of high resistance boxes, each made up of a number of individual 1 MΩ resistors, rated to 750 V and 3 W, connected in series. The use of many 1 MΩ resistors rather than a smaller number with larger values was to spread the maximum 40 kV load voltage so the total potential across any one resistor was never more than 730 V, limiting the minimum resistance to 55 MΩ. The resistors allowed for the current of the system to be regulated through the variable supply voltage and the choice of resistance boxes used, and functioned as a ballast resistor for the discharges. Four resistance boxes were constructed, each with different resistance values, allowing for different combinations to be used in order to vary the range of discharge currents available. The boxes were filled with potting compound to prevent arcing between resistors, and served to prevent any breakages in the links between resistors. Boxes were labelled A B C and D, with values of 18 MΩ, 27 MΩ,

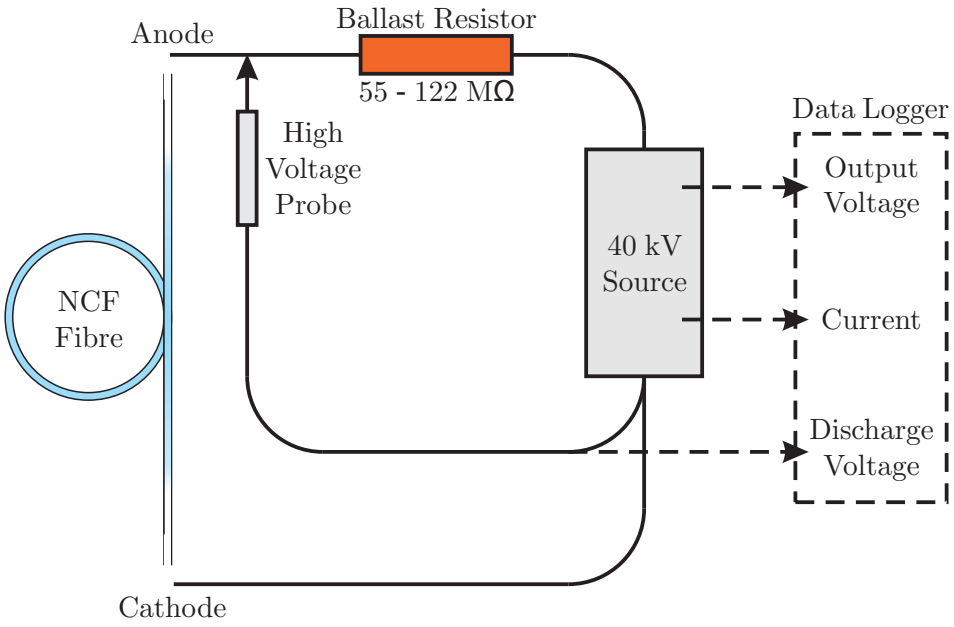

Figure 8.1: Diagram of the electrical DC system setup.

37 MΩ, and 40 MΩ respectively. For the majority of experiments, boxes C and D were chosen, with a combined resistance measured as 77 MΩ ± 2 MΩ.

The combined ballast resistor was connected to the anode pin, and the voltage across the discharging fibre could be measured using a x1000 high voltage probe, also attached to the anode pin, while the ground of the probe and the 40 kV supply were connected to the cathode. The changes in this voltage over time were also recorded using data logging software.

8.4 The Vacuum System

The vacuum system was kept nearly the same as in the RF system, only now an additional 1/4" plastic tube and valve was used to isolate the positively charged metal tubing holding the anode from the rest of the vacuum system. The modified vacuum setup is shown in Figure 8.2.

Low pressures of the order of 10^{-4} mbar could be reached at the points where pressure gauges were placed; at the end of the plastic tube and at the cathode end of the fibre.

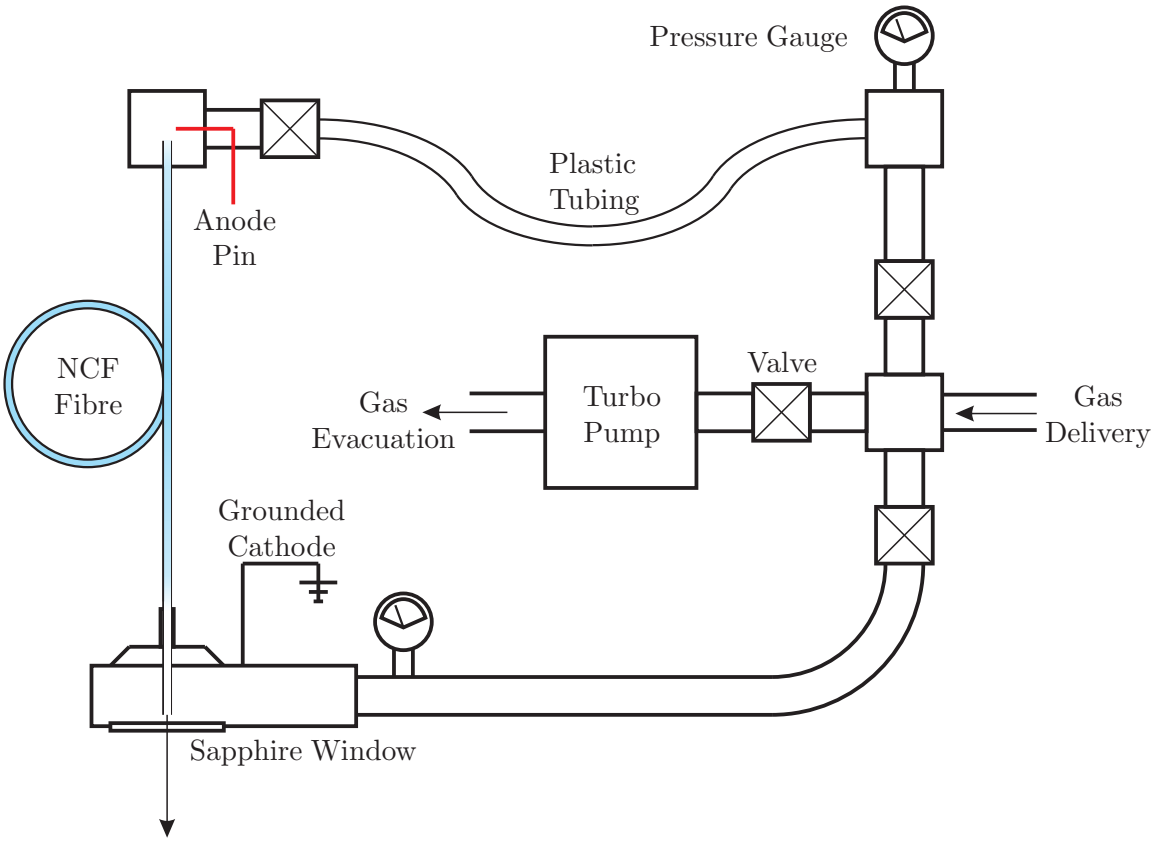

Figure 8.2: Diagram of the vacuum setup for the DC system.

These gauges allowed for a measure of the gas mixture pressure to within 0.01 mbar.

The mean free paths of the gas mixtures at discharge pressure for Xe, HeXe, and HeNe were calculated using

$$L_{mfp} = \frac{k_B T}{\sqrt{2}\pi m^2 P} \tag{8.1}$$

where k_B is Boltzmann's constant, T is the temperature in kelvin, m is the particle diameter in meters, and P is the pressure in pascals. From this the mean free paths of Xe, He, and Ne at 12 mbar of gas pressure can be calculated to be approximately 4 μm, 9 μm, and 7.5 μm respectively. From this we concluded that the fibre, having a core diameter which was much greater than these values, would fill in a fluid-like manner and quickly equalise to the desired pressure.

8.5 The Anode and Cathode Designs

The anode pin directly next to one end of the fibre was a 1 mm thick tungsten wire. It was found that sharpening the end of the wire to a point or cutting it flat achieved the same degree of stability in discharges, whereas a splintered end required a significantly higher voltage to achieve breakdown. The anode was positioned outside of the optical path at the fibre output, so it would not obstruct the signal emitted from that end. The anode configuration is shown in Figure 8.3, along with the surrounding housing to maintain the vacuum at the end of the fibre.

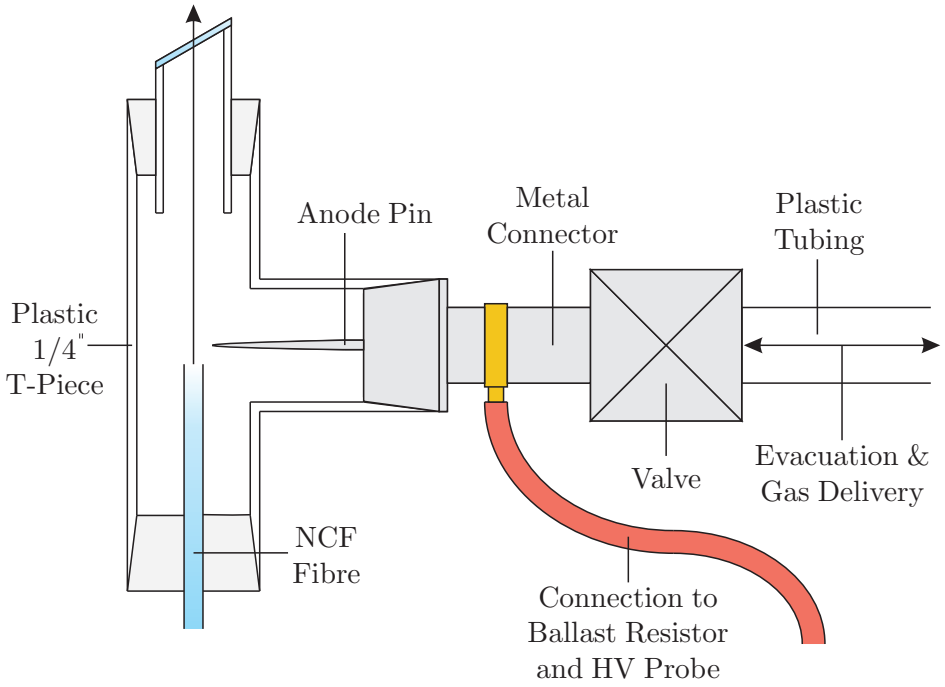

Figure 8.3: The configuration of the anode pin and surrounding housing.

The fibre was held inside an 1/4" PFA vacuum T-piece (Swagelok), using a nylon bung, with the far end of the T-piece available for coupling light out of the fibre via a Brewster window. A metal connector was attached at the perpendicular arm of the T-piece, followed by a valve and the length of flexible plastic tubing. The anode pin was connected to the inside of the metal connector, allowing the high voltage probe and the ballast resistor to be connected externally.

The brass fibre holder previously used in the RF research served as a cathode, and was grounded accordingly. The shape and arrangement of the cathode housing was shown

earlier in Chapter 7, Figure 7.7. The dynamics of the discharge at the cathode end, such as the cathode layer, was spread around the cathode plate, and as the fibre was cleaved level with the opening in the cathode housing, this would remain constant for all lengths of fibre tested.

This configuration meant that the gas filled fibre was directly exposed to the anode pin at one end, and at the cathode end the fibre was able to discharge to the grounded brass holder. The optical path was therefore not impeded at either end of the fibre, allowing for emission measurements to be made using the spectrometer, as in the previous RF work.

8.6 A New Negative Curvature Fibre

A new negative curvature fibre, fabricated at the University of Bath [17] and similar to a design also demonstrated by Pryamikov et al. [15, 19], was introduced for this DC excitation research. Like the earlier fibre used in the RF work, this fibre used bandgap guidance with a negative curvature core (described in Section 2.5) to guide light in the same mid-IR range.

The attenuation of the fibre over the 3 μm to 4 μm range, is shown in Figure 8.4 a). The loss remains low over the whole band, reaching a minimum around 3.45 μm, with a loss of approximately 0.15 dBm^{-1}. Spikes observed in the loss from 3.3 μm to 3.7 μm are the same as those seen in the attenuation measurements of the first negative curvature fibre from the RF work, as seen earlier in Figure 7.8 a). As in that fibre, the cause was the presence of HCl in the hollow core, itself a result of residual chlorine from the fabrication of the silica glass, and should not be considered a part of the "real" loss when the fibre is evacuated.

Figure 8.4 b) shows an scanning electron microscope image of the fibre. The structure, unlike the one shown earlier in Figure 7.8 b), did not have a core with a continuous boundary or a conventionally recognisable cladding region. Instead, this fibre simply consisted of 10 equally spaced capillaries attached to the walls of a larger capillary. These smaller capillaries were measured to have a wall thickness of 3 μm and a outer diameter of 36 μm. The overall fibre measured 273 μm in outer diameter, with a minimum core diameter of 119 μm. As with the fibre used in Chapter 7, the curvature of the capillaries minimised the degree of glass overlap with the fundamental mode in

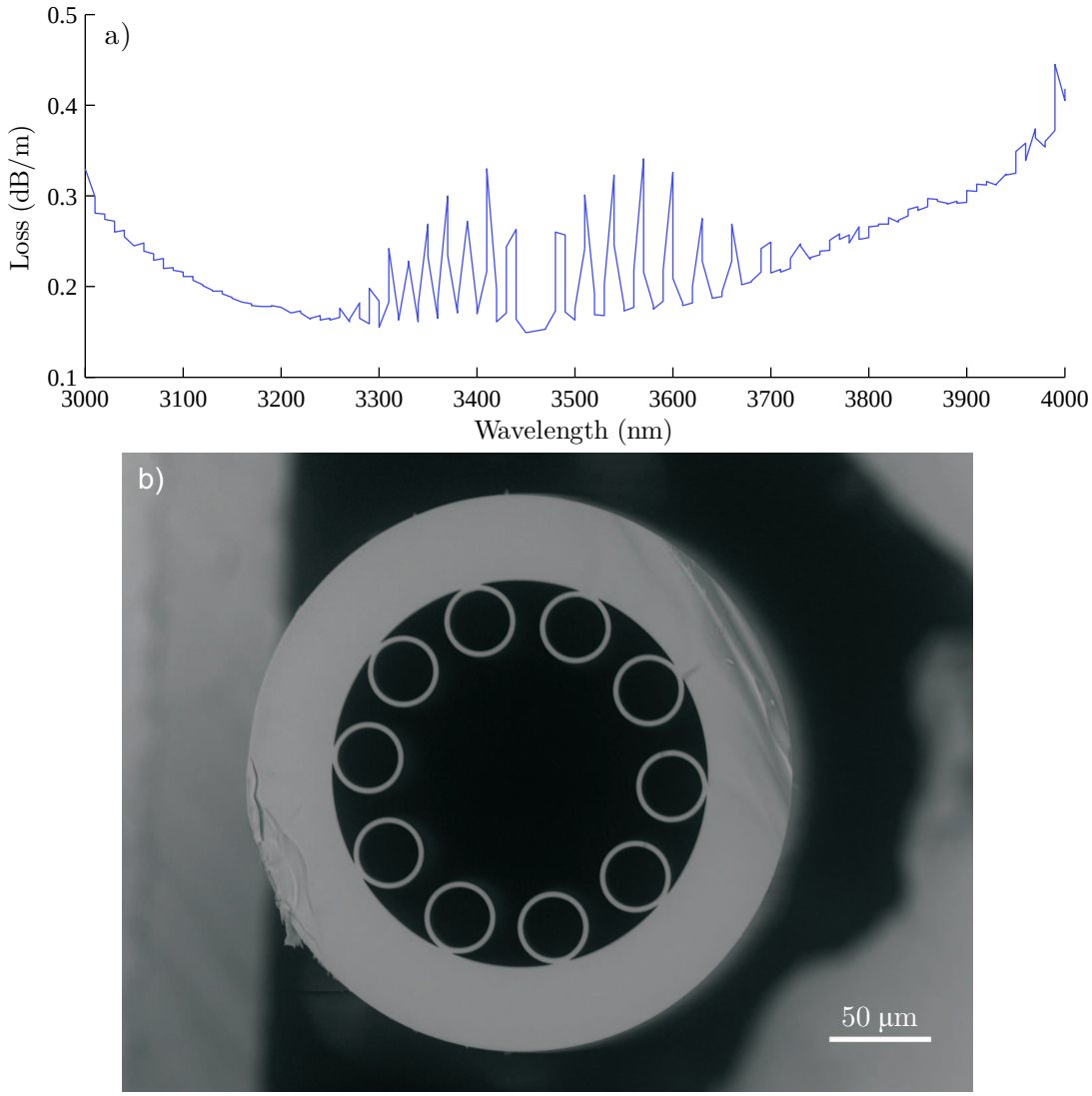

Figure 8.4: a) The fibre attenuation curve from 3 μm to 4 μm, and b) an SEM of the fibre used, fabricated at the University of Bath.

the fibre core, keeping the losses from the fibre low.

The primary advantage of this fibre design was that it suffered from bend losses to a far lesser extent than the one described in Section 7.4 and used previously for the RF work. Figure 8.5 shows the transmission bands along a length of straight fibre compared with a case where the fibre is bent over a half turn with a bend radius of 10 cm. Losses are observed to be significant for the higher order bands occupying the shorter wavelength regions, but for the band of interest, starting at 2.8 μm and ending at 4.1 μm, the change in transmission as the fibre is bent is far smaller, being about

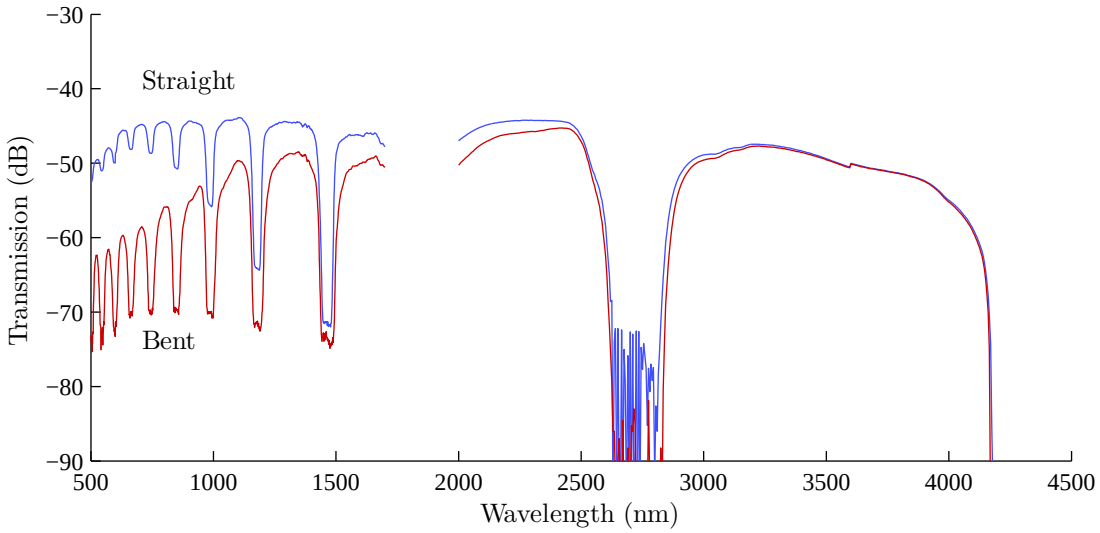

Figure 8.5: Graph of the change in transmission when the fibre is bent with a radius of 10 cm. The straight case (blue) shows little change in the mid-IR compared to the bent fibre transmission (red).

0.1 dB ± 0.02 dB.

Using this fibre allowed for a greater degree of flexibility in lab procedures; where previously the fibre had to be kept completely still to maintain a consistent optical signal, now a long length of fibre could repositioned or even coiled as required without any significant change to the signal strength.

8.7 Gas Mixtures and Pressures

The problems previously encountered with the RF excitation in Chapter 7, relating to the electrons colliding with the internal fibre walls at low pressures, were not anticipated to be as severe in the DC excitation. This is because the DC source does not oscillate, and instead continuously accelerates electrons longitudinally along the fibre, reducing the degree of diffusion transversely to the walls and potentially allowing for lower pressures to be used.

As in the research described in Chapter 7, the gases chosen were mixtures of HeNe, HeXe, and pure Xe. As stated earlier in Section 8.2, previous research [151] using a similar DC excitation system suggested that mixtures of HeXe in a ratio of approxi-

mately 5:1 would yield high gain on the 3.5 μm line for a pressure of around 6.5 Torr (approximately 8.7 mbar). However, this was in a specially straightened glass capillary with an inner diameter of 250 μm, using particular isotopes of He and Xe rather than their natural counterparts, so these ratio and pressure values could only be interpreted as approximate starting points. Given the narrower internal core diameter of the fibre, a HeXe ratio of 5:1 at a working pressure of 12 mbar was chosen as a starting point for this research.

This can be compared with the discussion regarding the theoretical ideal *pd* value derived from Figures 6.1 and 6.3 earlier in Chapter 6, where it was predicted that the ideal electron temperature for a Xe discharge would be approximately 72,000 K, corresponding with a maximum *pd* value of 4 mbar mm for HeXe mixtures.

The presence of He in HeXe mixtures acts as a stabiliser, due to the collisions with fast electrons, preventing those electrons from impacting on the core walls to the point of damaging the fibre. This also limits the rate of loss to the free electron population and thereby improves the general stability of the breakdown. The presence of He is also expected to raise the electron temperature of the discharge, as can be observed from the unpublished 1968 work by Young shown earlier in Figure 6.3. In a fibre with a core diameter of 119 μm, a gas mixture at a pressure of 12 mbar corresponds to a *pd* value of around 1.43 mbar mm, which is well below the predicted maximum ideal value of 4 mbar mm, and so this low value was therefore expected to be in a region where the electron temperature would be favourably high, ensuring a higher Xe collision cross-section, and consequently higher gain.

This means that pure Xe laser systems operating on the same 3.5 μm line would be expected to have a slightly lower gain than that of the HeXe laser systems [179, 183, 167]. Despite this, it was decided to investigate the discharge behaviour of pure Xe in addition to HeXe to observe any differences in breakdown and behaviour between the two. Considering that low pressure values for pure Xe would produce higher electron temperatures, the pressure of 2 mbar was chosen for discharges using only this gas.

HeNe gas lasers, operating with a DC excitation source, typically use a ratio of approximately 10:1 and have a pressure of only a few millibar for tube diameters of more than 1 cm. For narrow-bore systems of less than a few millimetres, the population of Ne necessary is higher, suggesting a ratio of 5:1 or more [164]. Likewise, the ideal pressure is also higher (to preserve the *pd* value and electron temperature, see Figure 6.3 in Chapter 6), although for a DC system this is still expected to only lie in the range of

10 mbar to 20 mbar for a fibre of approximately 100 μm in diameter. Gas mixtures and pressures of HeNe were chosen with this general region in mind, with the intention of optimising later to maximise the single pass signal at the HeNe 3.39 μm line.

8.8 DC Electrical Discharge Initiation, Stabilisation and Characteristics

Previous research on DC driven discharges using noble gases (but not HeXe, Xe or HeNe mixtures) in narrow capillaries achieved a maximum discharge length of 26.2 cm [154]. With this in mind, a fibre length of 30 cm was chosen to test the system and establish stable gas discharges.

These initial electrical gas discharges over 30 cm of fibre proved successful, using the chosen HeXe gas ratio of 5:1 and pressure of 12 mbar. The colour of the discharges was observed to be a bright blue, the expected colour for a Xe discharge in the visible part of the spectrum [190]. Figure 8.6 shows a photo of the cathode end of the fibre during a stable HeXe discharge which demonstrates this characteristic colour. The presence of contamination in the system with air was apparent when the discharge colour was observed to be more purple. This is the typical discharge colour of nitrogen [191], hence indicating the presence of air. Although this did not affect the electrical behaviour of the discharge, it was found to be detrimental to the discharge stability if present in sufficiently large quantities. The precise constituent, or constituents, of the air which caused this instability was difficult to identify, and therefore care was taken to prevent any leakages and ensuring the vacuum was sufficiently high for each discharge test.

An example of the electrical behaviour in a clean HeXe discharge for both the supply and discharge currents against voltages is shown in Figure 8.7 for a 30 cm length of fibre using a 12 mbar, 5:1 HeXe mixture.

As expected, the discharge voltage closely matches the supply voltage prior to breakdown. However, a small amount of current is observed to flow along the length of the gas filled fibre, increasing slightly as the supply voltage rises from zero to the breakdown voltage. This corresponds to a resistance of the order of 1000 MΩ, and is therefore likely to be current flowing along the probe, which has this impedance value.

The gas breakdown is seen at a discharge voltage of 14.5 kV, sharply dropping to

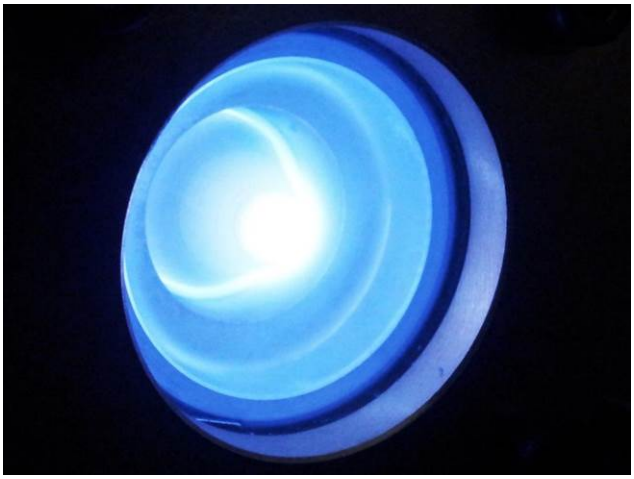

Figure 8.6: An image of the cathode end of the fibre during a stable HeXe discharge.

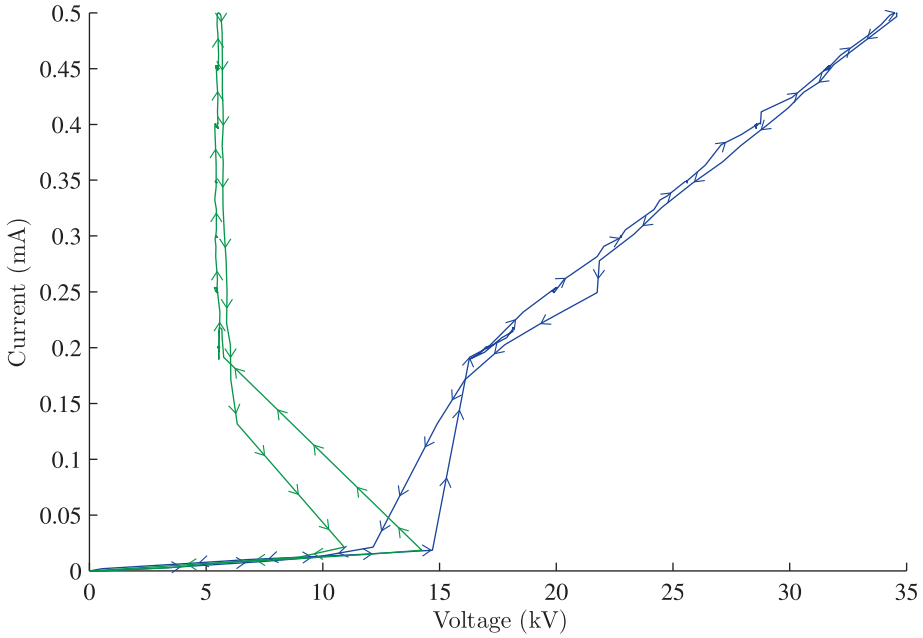

Figure 8.7: A graph of current against voltage for the Supply (blue) and Discharge (green) Voltages for a 30 cm discharge in 12 mbar 5:1 HeXe. Arrows denote direction of supply voltage increase and decrease.

6 kV as the current flow along the fibre quickly rises up to 0.2 mA. As the current is increased, the supply voltage increases roughly linearly as expected. The discharge voltage is seen to remain nearly constant at 6 kV throughout, with only a mild slope showing the negative resistance typical of a discharge [192]. A hysteresis is observed as

the current is reduced, the discharge remaining in effect down to 0.13 mA, well below the switch on current of 0.2 mA, and switches off at around 12.5 kV.

Figure 8.8 shows the recorded electrical characteristics during the same discharge as a function of time, again showing the current, supply and the discharge voltages.

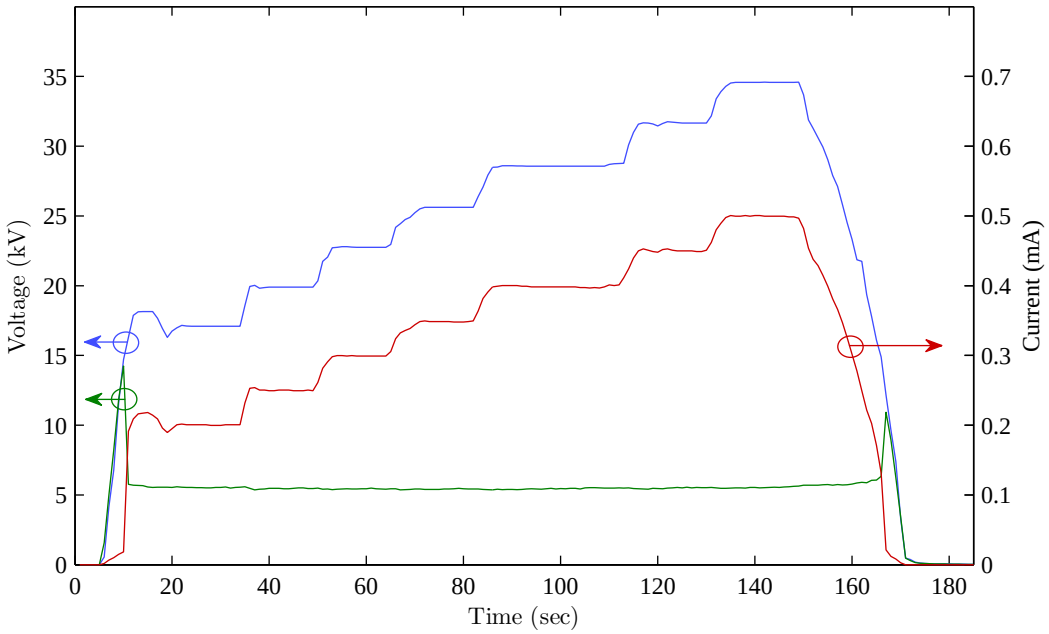

Figure 8.8: A 30 cm HeXe discharge showing the current (red), supply output voltage (blue) and discharge voltage (green) behaviour with time.

Here it is again evident that the discharge voltage remains stable around 6 kV throughout the discharge, which lasts for a little under 170 seconds. This is despite the current being altered, by adjusting the output of the 40 kV supply, in steps of 0.05 mA up to a maximum of 0.5 mA, before being quickly brought down to a shut off at 0.13 mA. It is also worth noting that the current steps are stable, with no significant fluctuations over time between deliberate changes. These values of current provide a range of current densities for this fibre, from 11×10^6 mA m^{-2} to 45×10^6 mA m^{-2}. This is comparable to the current density of 7.1×10^6 mA m^{-2} used in previous research [151], for a current of 0.35mA and a tube diameter of 250 μm.

The example shown in Figures 8.7 and 8.8 demonstrates the stability of the gas discharges in this system over time, as well as the fine control and stability of the current, and the hysteresis of the discharge voltage over a full cycle. By collecting this data for all discharges the breakdown voltage, operating current and discharge voltage could be

recorded, the current set and the stability closely monitored.

With respect to different gas mixtures, ratios of 5:1 HeXe at 12 mbar were generally found to be the most stable and the easiest to discharge, in that the breakdown voltage was relatively low and the stability was found to be generally high, with very little flickering. This is as expected based on previous research described in Chapter 6. However, the pure Xe gas would discharge for the chosen pressure of 2 mbar, but without the stability over long periods, making the recording of emission spectra and electrical data more difficult. This was again expected based on the stabilising role of He in HeXe systems, which states that the electron temperature is slightly higher for pure Xe systems and can cause instabilities in the gas discharge [147, 148].

The discharges from HeNe mixtures proved to be the hardest to achieve, suffering from fluctuating breakdown voltages from discharge to discharge, and frequent flickering or sudden extinguishing of the discharge. This behaviour was observed to be heavily dependent on the purity of the gas; the presence of even small amounts of air in the vacuum system was even more detrimental than in the HeXe discharges, resulting in a bright purple colour to the discharges from atmospheric nitrogen, and no stability to the discharge. Additionally, due to the higher electron temperatures in HeNe systems compared with HeXe systems, and the structure of the cathode which confined the fibre and inhibited heat dissipation, the discharges were prone to cause fibre damage at the cathode end.

8.9 Emission Spectra for Different Lengths

Now that the system was capable of achieving stable discharges over 30 cm lengths of fibre (a new record in terms of the length of a gas discharge in sub 200 μm diameter tubes), the next step was to attempt to record emission spectra from the discharging gas.

The cathode end of the fibre was connected to a brass block with a sapphire output window. The block was built with the ability to be fixed to the entrance slit of a spectrometer (Bentham, DTMc300, used as a single monochrometer), allowing light to be collected as it was emitted from the fibre.

8.9.1 50 cm Gas Discharges

HeXe discharges in a fibre of 50 cm in length were then carried out, using the same mixture of 5:1 and pressure of 12 mbar as previously in 30 cm discharges. The current was set to 0.25 mA, being the lowest current that consistently produced stable discharges and therefore a current density closest to that used in [151]. The breakdown voltage was recorded as being 13.2 ± 0.2 kV, with the discharge voltage again remaining constant at 7.8 ± 0.2 kV for the duration of the discharge. The emission spectrum for a 50 cm length HeXe discharge is shown in Figure 8.9 (in blue), with error bars showing the variation between gas discharge for each major peak.

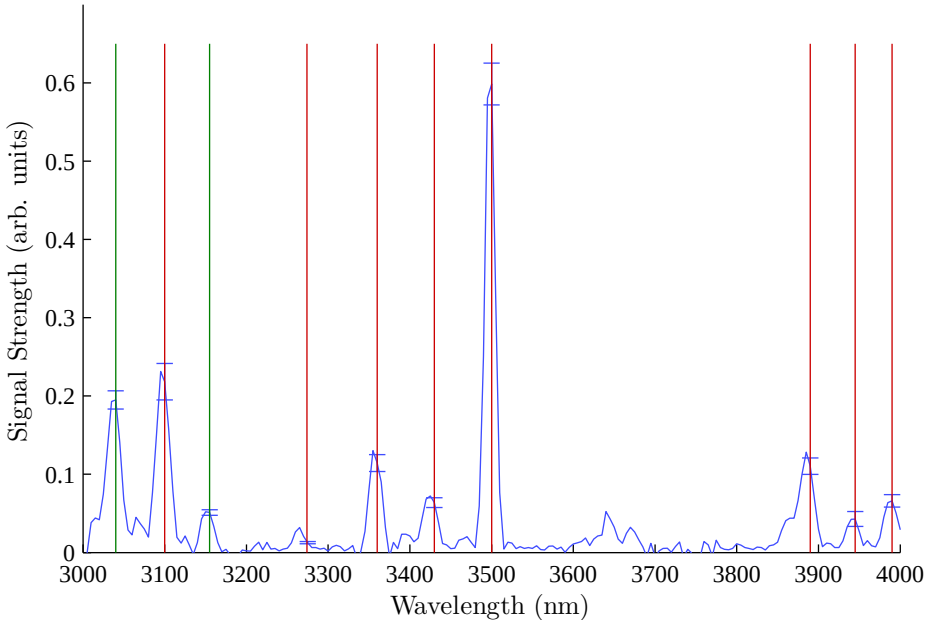

Figure 8.9: The emission from a 50 cm HeXe discharge (5:1, 12 mbar, 0.25 mA, spectrometer resolution 5 nm) shown in blue, with the expected Xe emission lines, shown in red for those that have been observed in previous research to lase, and green for those which have only been observed [182]. Error bars are shown for the most significant peaks.

The range runs from 3 μm to 4 μm, and clearly shows several significant peaks in the output. Overlaid with the known emission lines of Xe over that range (see Section 6.5.2), it is clear that the Xe gas is discharging and that it is spontaneously emitting at the lines expected, based on previous research [182, 193, 194, 195]. The slight shift in wavelength for each of these peaks from the expected locations is within the spectrometer resolution of 5 nm for the measurement. The signal strength for each peak was observed to vary from discharge to discharge, and showed a strong dependence

on the degree of contamination in the system with air, represented in the figure by error bars for each of the major peaks. The variation was found to be in the range of 4.3% to 10% of the emission strength, depending on the peak, with the 3500 nm peak having the lowest variation of 4.3%. When repeated evacuations and gas discharges were carried out, signal strength was seen to generally increase.

The strongest peaks are observed around 3040 nm, 3105 nm, 3370 nm, 3425 nm, 3885 nm, and a very strong peak at 3500 nm. Based on previous research [182], the 3105 nm, 3370 nm, and the 3500 nm lines are expected to have the highest gain, and it is these lines that are observed to have the highest peaks, with the addition of 3040 nm and 3885 nm.

These match the lines detected in the RF work described in Chapter 7 fairly well. The 3105 nm, 3370 nm, and 3500 nm are all clear in this DC data, whereas the lines detected at 3270 nm and 3425 nm are again very weak compared to the other major lines. The weakness on the 3270 nm line is more apparent when compared with the earlier spectra (for example Figure 7.22), where this line appeared to be slightly stronger relative to other emission lines. The reason for this could be a higher gain on another line that shares the same upper level, resulting in more stimulated emissions in preference of that other line at the expense of the 3270 nm line. In the RF work there may have been less stimulated emission occurring to cause this, owing to the much shorter discharge lengths achieved in that work. The 3040 nm and 3885 nm lines were not within the spectral range chosen for the RF work, and so were not detected.

8.9.2 80 cm Gas Discharges

Discharges of 80 cm were also achieved, using the same HeXe gas conditions. Again, the current was set to 0.25 mA, and the breakdown voltage was record as being 15.5 kV $\pm$ 0.2 kV, while the discharge voltage was found to be steady at 12.2 kV $\pm$ 0.2 kV for the duration of the discharge.

Figure 8.10 shows the emission spectrum for the 80 cm length of discharge, shown in green and compared to the earlier 50 cm spectrum shown in blue. Again, the variation between signal strength from discharge to discharge is shown as error bars for each of the major peaks. For this discharge length, the fluctuation fell in a larger range of between around 4.3% and 35%, with the 3500 nm emission line again having the lowest variation of 4.3%. This indicates that the degree of contamination in the gas from air

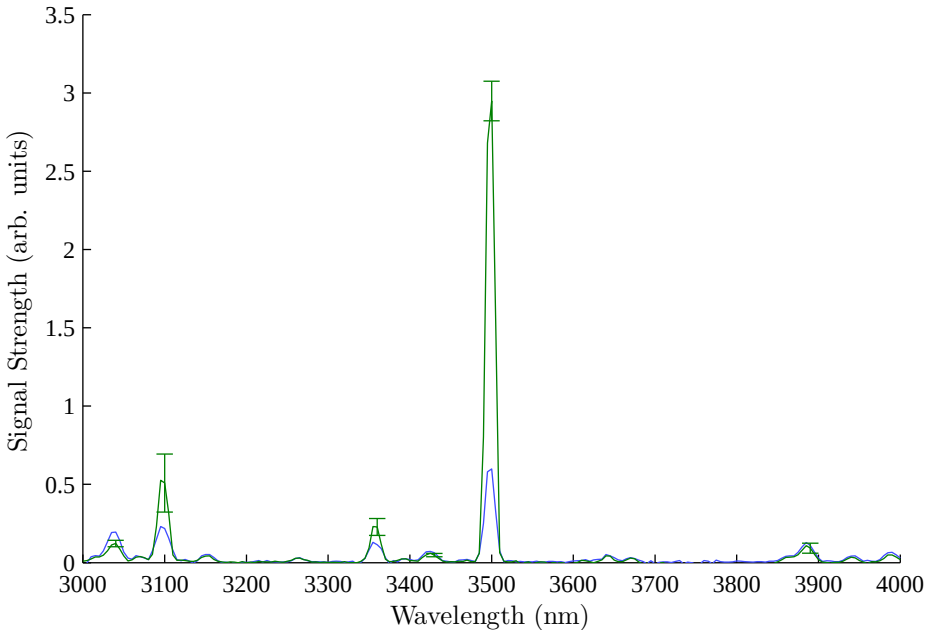

Figure 8.10: The emission from an 80 cm HeXe discharge (5:1, 12 mbar, 0.25 mA, spectrometer resolution 5 nm) shown in green, with the 50 cm emission spectra shown in blue. Error bars are shown for the most significant peaks of the 80 cm spectrum.

has a greater effect on the signal strengths for the longer discharge lengths, although the 3500 nm line appears to be the least affected.

However, a large increase in the overall signal strengths of the 3105 nm, 3370 nm and 3500 nm lines is observed, with the 3105 nm and 3370 nm lines increasing by approximately the same degree, whilst the 3500 nm line increases by a far larger factor of around five. All of these increases are greater than the proportional increase in the length, suggesting the possibility of gain from a greater degree of stimulated emission on these lines.

Other features observed in Figure 8.9 are seen in Figure 8.10 to remain almost the same or, as in the case of the 3040 nm line, to actually decrease. This decrease could be explained as the result of low gain on this line (as expected in Section 6.5.2) alongside the natural variation of the signal strength from discharge to discharge.

8.9.3 100 cm Gas Discharges

To further investigate the dependence of the signal strength on the length of the gas discharge, a fibre length of 100 cm was tested. As with the 50 cm and 80 cm lengths, the current was set to 0.25 mA, and the breakdown voltage was recorded as 21.2 kV $\pm$ 0.2 kV, with a steady discharge voltage during breakdown of 12.4 kV $\pm$ 0.2 kV. Figure 8.11 shows the resulting spectra between 3 μm and 4 μm. As in the other spectra, error bars show the variation between several discharges for each emission line. The fluctuation range is now seen to be between around 3.3% and 18%, with the 3500 nm line again having the lowest value of 3.3%. It is possible that for this length any net gain on these lines is beginning to compensate for the negative effects of contamination of the gas with external air.

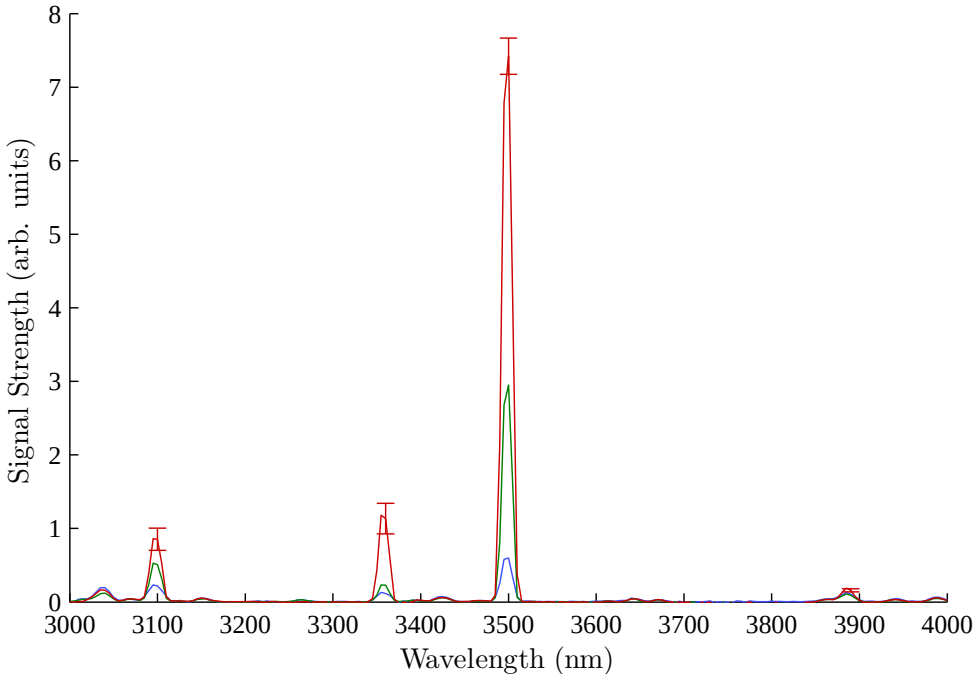

Figure 8.11: The emission from an 100 cm HeXe discharge (5:1, 12 mbar, 0.25 mA, spectrometer resolution 5 nm) shown in red, with the earlier 80 cm and 50 cm emission spectra shown in green and blue respectively. Error bars are shown for the most significant peaks of the 100 cm spectrum.

The trend in overall signal strength seen in Figure 8.10 is seen to continue here, with the same lines increasing significantly with the 20 cm increase in fibre length. The two lines at 3105 nm and 3370 nm are observed to have now increased by a factor of more than two as the length of the fibre is doubled, indicating the possible presence of gain.

The line at 3500 nm is seen to increase even more significantly than previously, now having a signal strength that is more than ten times larger than originally recorded for the 50 cm discharge in Figure 8.9.

8.9.4 Comparing the Signal Growth On Different Lines

The lines observed to show clear super-linear growth in Figures 8.10 and 8.11 are then directly compared in Figure 8.12. The strengths of the signals on the 3040 nm, 3105 nm, 3370 nm, 3500 nm and 3885 nm lines are all shown, each being an average at least three separate data sets. The 3500 nm line includes extra lengths and is averaged over a greater number of data points, allowing for an exponential curve to be fitted. Error bars are shown for all lines, but are observed to be most significant for the 3500 nm line, due to the greater number of points in that set. Each repeated discharge consisted of a newly cleaved fibre at both ends, new gas mixture, and adjusted anode and cathode positions. All the data shown has been normalised to the signal strength at 50 cm to allow for a direct comparison of signal growth on each line.

The black dashed line represents a proportional signal increase with length, where there is no net loss nor gain. All the emission lines except the 3500 nm line are seen to increase by less than the proportional value from 50 cm to 80 cm, indicating a degree of overall loss. However, the 3105 nm and 3370 nm lines are seen to rise above this proportional boundary at 100 cm as the gain becomes dominant. Separating these two effects and estimating the precise loss and gain values for these lines is difficult with the limited data set available, but it is assumed the loss is approximately the same as that measured earlier for the fibre in Figure 7.8, at about 0.1 dBm^{-1}.

It is clear that the 3500 nm line (in blue) shows the strongest growth, displaying an even greater proportional increase in the signal from 80 cm to 100 cm than the initial signal from 50 cm to 80 cm. This results in a signal that is almost 12 times stronger than that recorded for half the length. The growth of the signal with length is shown to fit an exponential relationship, as would be expected in the presence of gain. The fitted curve is of the form given earlier in Chapter 2, when discussing gain, and again in Chapter 5

$$P_x = P_0 \exp^{gL} \tag{8.2}$$

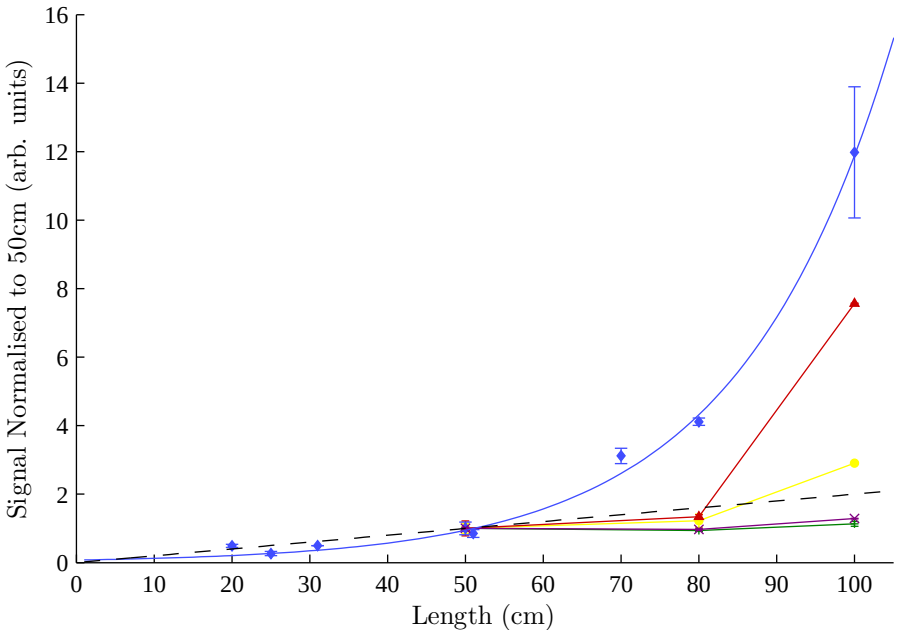

Figure 8.12: The signal strength for the 3040 nm (green crosses), 3105 nm (yellow circles), 3370 nm (red triangles), 3500 nm (blue crosses) and 3885 nm (purple diamonds) lines for each discharge length, all with error bars and normalised to the signal strength at 50 cm for direct comparison. For comparison, a proportional increase line is plotted (black dashed). The 3500 nm line has a fitted exponential curve (blue line).

where gain value is in m^{-1} and lengths are in meters. The value of g for the fitted curve is 5.06 m^{-1}. This can be converted to a value with units in dBm^{-1}, using the coefficient of 4.343 given earlier in Chapter 2, equation 2.23, yielding an estimated gain for this data set of around 21.9 dBm^{-1}. This gain estimation is analysed in more detail in the next section.

The 3370 nm line (in red) is observed to increase by only a modest amount between 50 cm and 80 cm, but is much stronger from 80 cm to 100 cm, reaching more than seven times the initial 50 cm signal strength. This suggests the 100 cm gas discharge was long enough to display the characteristic exponential curve for the stimulated emission, greatly increasing the single pass signal and demonstrating the strong gain on that line.

A similar, although less pronounced, effect is seen on the 3105 nm line (in yellow), where again a modest increase from 50 cm to 80 cm is followed by a stronger response from 80 cm to 100 cm. This is again suggestive of the exponential relationship that is typical in the presence of gain, resulting in a signal that is three times stronger than

that of the initial 50 cm.

For comparison, Figure 8.12 also shows the signal growth of the 3040 nm and 3885 nm lines (in green and purple respectively), which are observed to grow by only a marginal amount as the length of the gas discharge is increased. These lines can therefore be interpreted as having little or no gain to exploit in a gas discharge laser.

As described earlier in Section 6.5.2, the 3500 nm transition in Xe shares its upper energy level with the transition at 3885 nm. If the observed increase in the emission strength was due to a fluorescent effect, then an equal proportional increase would be expected for this line also. However, this line is only seen to double in strength between the 50 cm and 100 cm spectra, ruling out any kind of fluorescent effect.

It is additionally notable that the cathode dimensions remained unchanged for all discharge lengths. This confirms that the length dependence observed in the spectra of Figures 8.9, 8.10, and 8.11 can all be considered to be the result of photons generated in the positive column of the gas discharge, rather than photons generated as a result of cathode dynamics.

After considering these points, it is concluded that the data observed is indicative of significant gain on the 3500 nm line of around 22 dBm^{-1}, confirming it as a good candidate for lasing. The lines at 3105 nm and 3370 nm also display some indications of gain.

8.10 Repeatability of Signal Strength on the 3500 nm Xe Line

Having observed a strong signal increase with gas discharge length for several lines of Xe, and calculated an estimate for gain on the 3500 nm line, it was desirable to assess the repeatability of the signal detected for various lengths.

The signal at 3500 nm from discharges of HeXe (5:1 at 12 mbar) was monitored at a current of 0.25 mA for a range of different discharge lengths, from 20 cm up to 100 cm, and with a number of repeats to verify the consistency of the signal behaviour. Each repeat constituted a new fibre, newly cleaved at both ends, a new gas mixture, and newly adjusted anode and cathode positions relative to the fibre. This data set, previ-

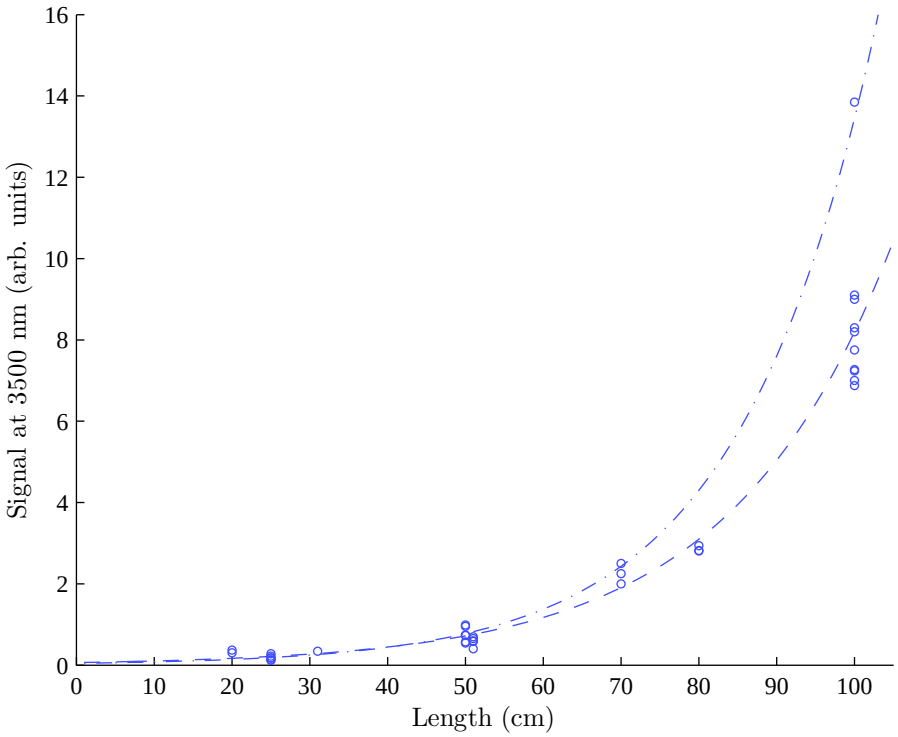

Figure 8.13: The signal strength at 3500 nm (10 nm bandpass) for a range of separate discharges of HeXe (5:1 12 mbar) and for a range of different lengths of gas discharge. Many of the data points have very similar signal strengths, and so partially overlap on the plot. Two exponential fitted curves are plotted for the data set, one excluding the highest data point achieved at 100 cm (dashed), and one excluding the lower values at 100 cm (dot-dashed).

ously included in the averaged data for the 3500 nm line shown earlier in Figure 8.12, is shown in Figure 8.13.

Despite the wider spread of data points at longer lengths, the same super-linear behaviour seen on this line in the last section is still clearly observable. In addition, it shows the relative repeatability of the large signal strength for the longer lengths of fibre at 70 cm, 80 cm, and 100 cm, where even the weakest signals still follow the same general trend of exponential behaviour with increasing length.

The absolute variation in the detected signal for different discharges is clearly larger for the longer lengths of fibre. However, this signal variation is found to be approximately equal when expressed as a percentage of the average signal detected for that length, and consistently falls between 20% to 25%. The main cause of this variation from discharge to discharge is believed to be contamination to the gas mixture. As mentioned in

Section 8.8 and Section 8.9.1, it was found during experiments that the detected signal strength correlated with the amount of air contaminating the system, observed as the degree of purple colouring in the discharge as a result of the breakdown of atmospheric nitrogen. In these cases the electrodes and fibre were kept the same, with the only difference between discharges being the gas mixture, which in addition to the colouring of the discharge, suggests the signal variation is the result of leaks or impurities. By taking steps to minimise the presence of air from leaks, such as repeatedly filling and evacuating the fibre with He before filling with the chosen HeXe mixture, the detected signal strength was generally seen to increase.

The first and most obvious step was to ensure that all seals were sufficiently tight and that no leaks were present. The second step was to repeatedly evacuate the system after it had been opened to the atmosphere, for instance when the fibre was replaced or the pin anode was adjusted. By filling the system and fibre with the desired gas mixture, discharging and recording the signal strength, and then again evacuating the system and repeating the process, the remnant population of atmospheric air in the fibre was continually reduced. This generally resulted in higher recorded signals, highlighting the link between the two.

Figure 8.13 also shows two fitted exponential curves, the first corresponding to the large cluster of lower signal values at 100 cm, representing approximately the gain value most often observed, shown as a blue dashed line. The curve has an attenuation constant g of 4.86 m^{-1}, which can be converted to approximately 21.1 dBm^{-1} using the coefficient of 4.343 used in the previous section and first stated in Chapter 2. The second disregards the 80 cm and lower 100 cm values, and corresponds only to the largest signal recorded, representing the highest observed potential gain value, shown as a blue dotted-dashed line. This line has an attenuation constant g value of 5.7 m^{-1}, which can be converted to approximately 24.75 dBm^{-1}. These two upper and lower end values fit well with the earlier gain estimate of approximately 22 dBm^{-1} given in the previous section, which was calculated from the average of the whole data set for the 3500 nm emission line.

Both fitted curves in Figure 8.13 do not appear to show evidence of the detrimental effect of gain saturation. This is because in such a case, the trend would be expected to become linear above a certain fibre length. However, the estimated gain values of around 21 dBm^{-1} to 25 dBm^{-1} fall far short of that reported previously by Smith et al. [151], and this could be explained by a saturation in the gain. Alternatively, the gas pressure, the discharge current, and the Xe and He pressures could also account

for these lower than expected gain values.

8.11 Summary and Conclusions

To summarise and conclude this work, a DC excitation system was developed using a 40 kV source and a series of high resistance boxes for current control. The fibre used for the research was a newly developed negative curvature fibre, fabricated at the University of Bath, with a core diameter of 119 μm and was capable of guiding light over 3 μm to 4 μm range with negligible bend losses. A vacuum system allowed for the fibre to be evacuated and filled with the required gas mixture, and a pin anode and a plate cathode applied the field to the gas in the fibre.

Stable discharges were achieved in HeXe and pure Xe mixtures, with HeXe proving to be stable for long periods of time. A series of spectra were then recorded for a variety of discharge lengths, showing several peaks associated with known emission lines of Xe. The longest stable discharge achieved was 100 cm, and is therefore the longest stable gas discharge achieved so far in sub-millimeter diameter discharge tubes, the previous being 26.2 cm in length [155, 154]. Spectra for each length showed a strong super-linear increase in the recorded single pass signal strength for several emission lines between 3 μm to 4 μm, indicating the presence of gain, particularly on the 3500 nm line, as expected from previous research [182, 179, 151].

Further analysis has shown that the data suggests a gain value of between 21 dBm^{-1} and just below 25 dBm^{-1}, varying from discharge to discharge as a result of impurities in the gas. This is comparable to the value reported in previous research by Bridges et al. [179], where they detected gain of between 20 dBm^{-1} and 60 dBm^{-1} in a 7 mm inner diameter tube. It was reported that this range was dependant on driving method, He content, and Xe pressure. However, this is in contrast to the far higher gain detected by Smith et al. [151], which was closer to 1000 dBm^{-1}. As discussed earlier in this Chapter, this research used a combination of RF and DC excitation, as well as isotopes of Xe, both of which could be important in achieving these higher gain values.

There are multiple possible reasons for the lower gain values estimated here. It is very likely that the pressure and He content are not optimised for this diameter of discharge tube, and a gas system where the maximum Xe cross-section is achieved would yield a larger gain value. This is highlighted by the shape of the Xe cross-section curve seen

earlier in Figure 6.1 in Chapter 6, where the collision cross-section is seen to peak over a relatively narrow range of electron energies. The driving current also has a modest effect on the resulting gain, and it is possible that an increase from the chosen value here of 0.25 mA would increase the gain further.

The possibility of gain saturation was also briefly discussed earlier. This effect would result in a lower resulting value than expected from other research, but there is little direct evidence of this in the data presented here. The presence of gain saturation would result in the signal strength displaying less and less exponential growth for increases in fibre length, potentially becoming more linear. While this has not been observed in a discharge over a meter, it could potentially be present, but undetectable in discharges over only a meter in length.

This work has ultimately demonstrated that stable DC driven gas discharges inside narrow hollow core fibres, using noble gases, is achievable. Lengths of up to a meter have for the first time been shown, with longer lengths potentially possible for larger DC driving potentials in similar systems. Indications of gain have been observed in the spectral data recorded for several lines of Xe in the mid-IR. Novel negative curvature optical fibres can be used as the discharge tube in such systems, allowing for long interaction lengths and laser operating wavelengths in the mid-IR.

8.12 Further Work

This work could be extended to include a cavity, forming a fully operating fibre gas discharge laser operating with HeXe at 3500 nm, driving the output power up to a higher value. However, time constraints prevented this final step and further optimisation from being undertaken as a part of this work.

The first issue faced in the completion of a cavity to achieve oscillation would be the necessity of having mirrors external to the gas system. The fibre used has a very low numerical aperture, estimated to be only 0.019 at 3500 nm, and so over a distance of 10 cm from the fibre end face the spot size is still under 5 mm in diameter. While this is initially an advantage, it would pose a practical problem when aligning a mirror at the anode end of the discharge, due to this small beam spot size. Additionally, problems would potentially arise from the mount holding the anode connection not being sufficiently secure to maintain a consistent beam spot position. The initial end

cavity mirror would have to be placed at the anode end, since the cathode is attached to the spectrometer monitoring the signal. An alternative would be to use a 3500 nm centred filter, along with a smaller separate 3500 nm detector, removing the need for the cathode end to be connected to a spectrometer. This would allow some degree of free space propagation from the anode end to a mirror, so a 3500 nm signal could be filtered from the cavity for signal monitoring. These constraints makes the formation of a cavity difficult, but not impossible, and subsequent work carried out at the University of Bath has achieved double-pass measurements of the gain in this system [196].

With a working HeXe laser, the optimum gas mixture and pressure could be probed in order to achieve the ideal *pd* value to maximise the Xe collision cross-section in the fibre, allowing for a better understanding of the discharge mechanics in narrow-bore gas cells of this size. Further optimisation of the gain could then also be achieved, either by reaching the higher levels predicted by earlier research, or by understanding the mechanisms that are resulting in gain saturation.

The multitude of additional lines in Xe below 3 μm is also a possible topic for future research. Xe possesses an emission line in the longer wavelength region at 5.6 μm, which reportedly displays an even stronger gain than the 3.5 μm line [197]. This is also an attractive future target since the wavelength is further into the IR, where material absorption of the silica glass is even stronger.

Likewise, mixtures of HeNe could then be investigated, with a focus on the Ne 3390 nm line. This work has shown that discharges in HeNe are difficult to maintain, being very sensitive to impurities from air as a result of leaks and having a higher electron temperature than Xe and HeXe discharges. However, if discharges could be stabilised, then the same system could deliver a 3390 nm HeNe laser, optimised for mixture and pressure like the HeXe and Xe gases. Further lines in Ne below 3 μm are then also a possibility.

Visible wavelengths from transitions in both Xe and Ne are possible as well, although these would suffer from the fibre sensitivity to bend losses over this region. Continuing development in custom fibre design means this sensitivity problem could be overcome in time.

There are a range of additional neutral noble gases which could also be harnessed in the same manner, such as argon and krypton, so this system could be adapted for many lasing wavelengths.

Appendix A

Publications and Conference Presentations

1. P. J. Mosley, S. A. Bateman, L. Lavoute, W. J. Wadsworth. Low-Noise, High-Brightness, Tunable Source of Picosecond Pulsed Light in the Near-Infrared and Visible. Optics Express, 19(25):25337-25345, 2011.

2. S. A. Bateman, F. Yu, J. C. Knight, W. J. Wadsworth. Towards an Electrically-Pumped Fibre Gas Laser in the 3 - 4 μm Range. In conference; Aston Institute of Photonic Technologies Conference (AIPT) (Aston University, Birmingham, UK), Poster Session, 2013. *Winner of Best Poster Presentation*

3. S. A. Bateman, W. Belardi, F. Yu, C. E. Webb, W. J. Wadsworth. Gain from Helium-Xenon Discharges in Hollow Optical Fibres at 3 to 3.5 μm. In conference; Conference on Lasers and Electro-Optics (CLEO), Session STh5C.10, The Optical Society, 2014. *Post-Deadline Paper*

4. S. A. Bateman, W. Belardi, F. Yu, C. E. Webb, W. J. Wadsworth. Gain from Helium-Xenon Discharges in Hollow Optical Fibres at 3.5 μm. In conference; Speciality Optical Fibres and Applications (SOF), Session SoM4B.3, The Optical Society, 2014.

5. A. Love, S. A. Bateman, W. Belardi, C. E. Webb, W. J. Wadsworth. Double Pass Gain in Helium-Xenon Discharges in Hollow Optical Fibres at 3.5 μm. In conference; Conference on Lasers and Electro-Optics (CLEO), 2015. *Subsequent Publication*

References

[1] J. Hecht. *City of Light*. Oxford University Press, 1st edition, 1999.

[2] J. Tyndall. *Notes On Light*. William H. Wheeler, 1870.

[3] K. C. Kao. Dielectric-Fibre Surface Waveguides for Optical Frequencies. *Proceedings of the Institution of Electrical Engineers*, 113:1151–1158(7), July 1966.

[4] Nobelprize.org. The Nobel Prize in Physics. `http://www.nobelprize.org/nobel_prizes/physics/laureates/2009/`, 2009. [Online; accessed 27-Sept-2014].

[5] K. C. Kao and M. W. Jones. Spectrophotometric Studies of Ultra Low Loss Optical Glasses II: Double Beam Method. *Journal of Physics E: Scientific Instruments*, 2(4):331–335, 1969.

[6] E. Snitzer. Optical Maser Action of Nd^{+3} in a Barium Crown Glass. *Phys. Rev. Lett.*, 7:444–446, 1961.

[7] J. Stone and C. A. Burrus. Neodymium-Doped Silica Lasers in End-Pumped Fiber Geometry. *Applied Physics Letters*, 23(7):388–389, Oct 1973.

[8] P. Kaiser. Drawing-Induced Coloration in Vitreous Silica Fibers. *Journal of the Optical Society of America*, 64:475, 1974.

[9] J. C. Knight, T. A. Birks, D. M. Atkin, and P. St. J. Russell. Pure Silica Single-Mode Fibre With Hexagonal Photonic Crystal Cladding. In *Optical Fiber Communication Conference*, page PD3. Optical Society of America, 1996.

[10] R. F. Cregan, B. J. Mangan, J. C. Knight, T. A. Birks, P. St. J. Russell, P. J. Roberts, and D. C. Allan. Single-Mode Photonic Band Gap Guidance of Light in Air. *Science*, 285(5433):1537–1539, 1999.

[11] H. Inaba, T. Kobayasi, M. Hirama, and M. Hamza. Optical-Fibre Network System for Air-Pollution Monitoring Over a Wide Area By Optical Absorption Method. *Electronics Letters*, 15(23):749–751, November 1979.

[12] A. Cheung, W. Johnstone, and D. Moodie. Gas Detection Based on Optical Correlation Spectroscopy Using a Single Light Source. *Measurement Science and Technology*, 17(5):1107, 2006.

[13] W. L. Barnes, S. B. Poole, J. E. Townsend, L. Reekie, D. J. Taylor, and D. N. Payne. Er^{3+}-Yb^{3+} and Er^{3+} Doped Fiber Lasers. *Journal of Lightwave Technology*, 7(10):1461–1465, Oct 1989.

[14] A. Tunnermann, T. Schreiber, and J. Limpert. Fiber Lasers and Amplifiers: An Ultrafast Performance Evolution. *Applied Optics*, 49(25):F71–F78, Sep 2010.

[15] A.D. Pryamikov, A.F. Biriukov, A.F. Kosolapov, V.G. Plotnichenko, S.L. Semjonov, and E.M. Dianov. Demonstration of a Waveguide Regime for a Silica Hollow-Core Microstructured Optical Fiber with a Negative Curvature of the Core Boundary in the Spectral Region Beyond 3.5 μm. *Optics Express*, 19, 2011.

[16] F. Yu, W. J. Wadsworth, and J. C. Knight. Low-Loss Silica Hollow Core Fibers for 3 - 4 μm Spectral Region. *Optics Express*, 20(10):11153–8, May 2012.

[17] W. Belardi and J. C. Knight. Hollow Antiresonant Fibers with Low Bending Loss. *Optics Express*, 22(8):9514–9519, 2014.

[18] A. Hartung, J. Kobelke, A. Schwuchow, K. Wondraczek, J. Bierlich, J. Popp, T. Frosch, and M. A. Schmidt. Double antiresonant hollow core fiber - guidance in the deep ultraviolet by modified tunneling leaky modes. *Optics Express*, 22(16):19131–19140, Aug 2014.

[19] A. D. Pryamikov. Negative Curvature Hollow Core Fibers: Design, Fabrication, and Applications. In *Conference on Fiber Lasers XI - Technology, Systems, and Applications Location: San Francisco, CA*, volume 8961, 2014.

[20] T. A. Birks, D. M. Atkin, G. Wylangowski, P. St. J. Russell, and P. J. Roberts. 2D Photonic Band Gap Structures in Fibre Form. In CostasM. Soukoulis, editor, *Photonic Band Gap Materials*, volume 315 of *NATO ASI Series*, pages 437–444. Springer Netherlands, 1996.

[21] G. P. Agrawal. *Nonlinear Fiber Optics*. Academic Press, 4th edition, 2007.

[22] C. Xiong and W. J. Wadsworth. Polarized Supercontinuum Generation in a Birefringent Photonic Crystal Fiber Pumped By a 1064 nm Microchip Laser. In *Lasers and Electro-Optics Society, 2007. LEOS 2007. The 20th Annual Meeting of the IEEE*, pages 816–817, Oct 2007.

[23] L. Cognolato. Chemical Vapour Deposition for Optical Fibre Technology. *Journal de Physique IV*, 5(C5):975–987, 1995.

[24] E. Hecht. *Optics*. Addison Wesley, 1st edition, 2002.

[25] J. C. Maxwell. A Dynamical Theory of the Electromagnetic Field. *Philosophical Transactions of the Royal Society of London*, 155:459–512, 1865.

[26] D. Gloge. Weakly Guiding Fibers. *Applied Optics*, 10(10):2252–2258, Oct 1971.

[27] T. A. Birks, D. Mogilevtsev, J. C. Knight, P. St.J. Russell, J. Broeng, P. J. Roberts, J. A. West, D. C. Allan, and J. C. Fajardo. The Analogy Between Photonic Crystal Fibres and Step Index Fibres. In *Optical Fiber Communication Conference and the International Conference on Integrated Optics and Optical Fiber Communication*, page FG4. Optical Society of America, 1999.

[28] T. A. Birks, J. C. Knight, and P. St.J. Russell. Endlessly Single-Mode Photonic Crystal Fiber. *Optics Letters*, 22(13):961–963, Jul 1997.

[29] K. H. Tsai, K. S. Kim, and T. F. Morse. General Solutions for Stress-Induced Polarization in Optical Fibers. *Journal of Lightwave Technology*, 9(1):7–17, Jan 1991.

[30] J. M. Stone, F. Yu, and J. C. Knight. Highly Birefringent 98-Core Fiber. *Optics Letters*, 39(15):4568–4570, Aug 2014.

[31] A. Ortigosa-Blanch, J. C. Knight, W. J. Wadsworth, J. Arriaga, B. J. Mangan, T. A. Birks, and P. St. J. Russell. Highly Birefringent Photonic Crystal Fibers. *Optics Letters*, 25(18):1325–1327, Sep 2000.

[32] L. Lavoute. Birefringent Four Wave Mixing Fibres Fabricated at the University of Bath.

[33] P. Romagnoli, C. R. Biazoli, M. A. R. Franco, C. M. B. Cordeiro, and C. J. S. de Matos. Integrated Polarizers Based on Tapered Highly Birefringent Photonic Crystal Fibers. *Optics Express*, 22(15):17769–17775, Jul 2014.

[34] K. Tajima and Y. Sasaki. Transmission Loss of a 125 μm Diameter PANDA Fiber with Circular Stress-Applying Parts. *Journal of Lightwave Technology*, 7(4):674–679, April 1989.

[35] Z. Zhu and T. Brown. Experimental Studies of Polarization Properties of Supercontinua Generated in a Birefringent Photonic Crystal Fiber. *Optics Express*, 12(5):791–796, Mar 2004.

[36] W. Jin, Z. Wang, and J. Ju. Two-Mode Photonic Crystal Fibers. *Optics Express*, 13(6):2082 – 2088, 2005.

[37] T. Nasilowski, T. Martynkien, G. Statkiewicz, M. Szpulak, J. Olszewski, G. Golojuch, W. Urbanczyk, J. Wojcik, P. Mergo, M. Makara, F. Berghmans, and H. Thienpont. Temperature and Pressure Sensitivities of the Highly Birefringent Photonic Crystal Fiber with Core Asymmetry. *Applied Physics B*, 81(2-3):325–331, Mar 2005.

[38] M.A. Duguay, Y. Kokubun, T.L. Koch, and L. Pfeiffer. Antiresonant Reflecting Optical Waveguides in SiO_2-Si Multilayer Structures. *Applied Physics Letters*, 49(1), 1986.

[39] N. M. Litchinitser, A. K. Abeeluck, C. Headley, and B. J. Eggleton. Antiresonant Reflecting Photonic Crystal Optical Waveguides. *Optics Letters*, 27(18):1592–1594, Sep 2002.

[40] F. Luan, A. K. George, T. D. Hedley, G. J. Pearce, D. M. Bird, J. C. Knight, and P. St. J. Russell. All-Solid Photonic Bandgap Fiber. *Optics Letters*, 29(20):2369–2371, Oct 2004.

[41] T. P. White, R. C. McPhedran, C. Martijnde Sterke, N. M. Litchinitser, and B. J. Eggleton. Resonance and Scattering in Microstructured Optical Fibers. *Optics Letters*, 27(22):1977–1979, Nov 2002.

[42] N. M. Litchinitser, S. C. Dunn, B. Usner, B. J. Eggleton, T. P. White, R. C. McPhedran, and C. Martijn de Sterke. Resonances in Microstructured Optical Waveguides. *Optics Express*, 11(10):1243–1251, May 2003.

[43] A.F. Kosolapov, A.D. Pryamikov, A.S. Biriukov, V.S. Shiryaev, M.S. Astapovich, G.E. Snopatin, V.G. Plotnichenko, M.F. Churbanov, and E.M. Dianov. Demonstration of CO_2-Laser Power Delivery Through Chalcogenide-Glass Fiber with Negative-Curvature Hollow Core. *Optics Express*, 19(25):25723–25728, Dec 2011.

[44] J. M. Florence, C. C. Allshouse, F. W. Glaze, and C. H. Hahner. Absorption of Near-Infrared Energy by Certain Glasses. *Journal of Research of the National Bureau of Standards*, 45(2), 1950.

[45] W. Belardi and J. C. Knight. Hollow Antiresonant Fibers with Reduced Attenuation. *Optics Letters*, 39(7):1853–1856, Apr 2014.

[46] D. Maucuse. *Light Transmission Optics*, chapter 8 and 12. Van Nostrand Reinhold, New York, 1982.

[47] G. Ghosh, M. Endo, and T. Iwasaki. Temperature-dependent sellmeier coefficients and chromatic dispersions for some optical fiber glasses. *Journal of Lightwave Technology*, 12(8):1338–1342, Aug 1994.

[48] R. Lundin. Dispersion Flattening in a W Fiber. *Applied Optics*, 33:1011–1014, 1994.

[49] B. J. Ainslie and C. R. Day. A Review of Single-Mode Fibers with Modified Dispersion Characteristics. *Journal of Lightwave Technology*, 4(8):967–979, Aug 1986.

[50] K. Saitoh and M. Koshiba. Empirical Relations for Simple Design of Photonic Crystal Fibers. *Optics Express*, 13(1):267–274, Jan 2005.

[51] L. E. Hooper, P. J. Mosley, A. C. Muir, W. J. Wadsworth, and J. C. Knight. All-Normal Dispersion Photonic Crystal Fiber for Coherent Supercontinuum Generation. In *Conference on Lasers and Electro-Optics 2010*, page CTuX4. Optical Society of America, 2010.

[52] O. Humbach, H. Fabian, U. Grzesik, U. Haken, and W. Heitmann. Analysis of OH Absorption Bands in Synthetic Silica. *Journal of Non-Crystalline Solids*, 203:19–26, August 1996.

[53] D. Marcuse. Field Deformation and Loss Caused by Curvature of Optical Fibers. *Journal Optical Society America*, 66(4):311–320, Apr 1976.

[54] L. Faustini and G. Martini. Bend Loss in Single-Mode Fibers. *Journal of Lightwave Technology*, 15(4):671–679, Apr 1997.

[55] P.J. Roberts, F. Couny, H. Sabert, B. J. Mangan, D. P. Williams, L. Farr, M. W. Mason, A. Tomlinson, T. A. Birks, J. C. Knight, and P. St.J. Russell. Ultimate Low Loss of Hollow-Core Photonic Crystal Fibres. *Optics Express*, 13(1):236–244, Jan 2005.

[56] P. Roberts, F. Couny, H. Sabert, B. Mangan, T. Birks, J. C. Knight, and P. st. J. Russell. Loss in Solid-Core Photonic Crystal Fibers Due to Interface Roughness Scattering. *Optics Express*, 13(20):7779–7793, Oct 2005.

[57] H.M. Pask, R. J. Carman, D. C. Hanna, A. C. Tropper, C. J. Mackechnie, P.R. Barber, and J. M. Dawes. Ytterbium-Doped Silica Fiber Lasers: Versatile Sources for the 1-1.2 μm Region. *Selected Topics in Quantum Electronics, IEEE Journal of*, 1(1):2–13, Apr 1995.

[58] C. Tang, W. R. Bosenberg, T. Ukachi, R. J. Lane, and L.K. Cheng. Optical Parametric Oscillators. *Proceedings of the IEEE*, 80(3):365–374, Mar 1992.

[59] J. E. Sharping, M. Fiorentino, P. Kumar, and R. S. Windeler. Optical Parametric Oscillator Based on Four-Wave Mixing in Microstructure Fiber. *Optics Letters*, 27(19):1675–1677, Oct 2002.

[60] S. Hooker and C. Webb. *Lasers*. Oxford University Press, 2010.

[61] J. Schwinger. On Gauge Invariance and Vacuum Polarization. *Physics Review*, 82:664–679, Jun 1951.

[62] R. W. Boyd. *Nonlinear Optics*. Academic Press, Boston, 2nd edition, 2003.

[63] R. Thompson, C. Leburn, and D. Reid (Eds.). *Ultrafast Nonlinear Optics*. Springer, 2013.

[64] D. Milam and M. J. Weber. Measurement of Nonlinear Refractive Index Coefficients Using Time Resolved Interferometry: Application to Optical Materials for High Power Neodymium Lasers. *Journal of Applied Physics*, 47(6):2497–2501, Jun 1976.

[65] K. S. Kim, W. A. Reed, K. W. Quoi, and R. H. Stolen. Measurement of the Nonlinear Index of Silica-Core and Dispersion-Shifted Fibers. *Optics Letters*, 19(4):257–259, Feb 1994.

[66] R. H. Stolen, J. E. Bjorkholm, and A. Ashkin. PhaseMatched ThreeWave Mixing in Silica Fiber Optical Waveguides. *Applied Physics Letters*, 24(7), 1974.

[67] C. Lin. Designing Optical Fibers for Frequency Conversion and Optical Amplification by Stimulated Raman Scattering and Phase-Matched Four-Photon Mixing. *Journal Optical Communications*, 4(2), 1983.

[68] N. Shibata, R. Braun, and R. Waarts. Phase-Mismatch Dependence of Efficiency of Wave Generation Through Four-Wave Mixing in a Single-Mode Optical Fiber. *Quantum Electronics, IEEE Journal of*, 23(7):1205–1210, Jul 1987.

[69] Nuno A. Silva, Nelson J. Muga, and Armando N. Pinto. Evolution of First-Order Sidebands From Multiple FWM Processes in HiBi Optical Fibers. *Optics Communications*, 284(13):3408 – 3415, 2011.

[70] M. N. Islam. Raman Amplifiers for Telecommunications. *IEEE Journal of Selected Topics in Quantum Electronics*, 8(3):548–559, May 2002.

[71] Y. Feng, L. Taylor, and D. B. Calia. Multiwatts narrow linewidth fiber raman amplifiers. *Optics Express*, 16(15):10927–10932, Jul 2008.

[72] K. O. Hill, B. S. Kawasaki, and D. C. Johnson. LowThreshold CW Raman Laser. *Applied Physics Letters*, 29(3):181–183, 1976.

[73] E. Finot, T. Brul, P. Rai, A. Griffart, A. Bouhlier, and T. Thundat. Raman and Photothermal Spectroscopies for Explosive Detection. In *Proc. SPIE Micro- and Nanotechnology Sensors, Systems, and Applications V*, volume 8725, pages 872528–872528–12, 2013.

[74] C. M. McGoverin, T. Rades, and K. C. Gordon. Recent pharmaceutical applications of raman and terahertz spectroscopies. *Journal of Pharmaceutical Sciences*, 97(11):4598–4621, 2008.

[75] Sir C. V. Raman. A New Type of Secondary Radiation. *Indian Journal Physics*, 2:387, 1928.

[76] E. J. Woodbury and W. K. Ng. Ruby laser operation in the near ir. *Proceedings of the Institute of Radio Engineers*, 50(11):2365–2383, Nov 1962.

[77] R. H. Stolen and E.P. Ippen. Raman Gain in Glass Optical Waveguides. *Applied Physics Letters*, 22(6), 1973.

[78] R. H. Stolen, W. J. Tomlinson, H. A. Haus, and J. P. Gordon. Raman Response Function of Silica-Core Fibers. *Journal of the Optical Society of America B*, 6(6):1159–1166, Jun 1989.

[79] T. Udem, R. Holzwarth, and T. W. Hnsch. Optical Frequency Metrology. *Nature*, 416:233–237, 2002.

[80] J. Ye and S. T. Cundiff. *Femtosecond Optical Frequency Comb: Principle, Operation and Applications*. Springer, 2005.

[81] L. Ying, H. Jing, L. Jinyong, W. Wenliang, and J. Zongfu. Generation of Raman Sidebands Aided by a CW Stokes Signal. *Optics & Laser Technology*, 58(0):215 – 219, 2014.

[82] C. Lin and R. H. Stolen. New Nanosecond Continuum For Excited-State Spectroscopy. *Applied Physics Letters*, 28:216, 1976.

[83] R. S. Windeler J. K. Ranka and A. J. Stentz. Visible Continuum Generation in Air-Silica Microstructure Optical Fibers with Anomalous Dispersion at 800 nm. *Optics Letters*, 25(1):25–27, 2000.

[84] W. J. Wadsworth, N. Joly, J. Knight, T. Birks, F. Biancalana, and P. St. J. Russell. Supercontinuum and Four-Wave Mixing with Q-Switched Pulses in Endlessly Single-Mode Photonic Crystal Fibres. *Optics Express*, 12(2):299–309, Jan 2004.

[85] J. M. Dudley, G. Genty, and S. Coen. Supercontinuum Generation in Photonic Crystal Fiber. *Rev. Mod. Phys.*, 78:1135–1184, Oct 2006.

[86] P. St. J. Russell. Photonic Crystal Fibers. *Science*, 299:358–362, 2003.

[87] J. C. Knight. Photonic Crystal Fibers. *Nature*, 424:847–851, 2003.

[88] L. E. Hooper, P. J. Mosley, A. C. Muir, W. J. Wadsworth, and J. C. Knight. Coherent Supercontinuum Generation in Photonic Crystal Fiber with All-Normal Group Velocity Dispersion. *Optics Express*, 19(6):4902–4907, Mar 2011.

[89] V. Tombelaine, P. Leproux, V. Couderc, and A. Barthlmy. Generation in Holey Fibers by Dual-Wavelength Sub-Nanosecond Pumping. *Photonics Technology Letters*, 18:2466–2468, 2006.

[90] A. Kudlinski, A. K. George, J. C. Knight, J. C. Travers, A. B. Rulkov, S. V. Popov, and J. R. Taylor. Zero-Dispersion Wavelength Decreasing Photonic Crystal Fibers for Ultraviolet-Extended Supercontinuum Generation. *Optics Express*, 14:5715–5722, 2006.

[91] J. M. Stone and J. C. Knight. Visibly "White" Light Generation in Uniform Photonic Crystal Fiber Using a Microchip Laser. *Optics Express*, 16(4):2670–2675, Feb 2008.

[92] E. A. Golovchenko, E. M. Dianov, A. M. Prokhorov, and V. N. Serkin. Decay of Optical Solitons. *Journal of Experimental and Theoretical Physics*, 42:87, 1985.

[93] Kodama Y. and Hasegawa A. Nonlinear Pulse Propagation in a Monomode Dielectric Guide. *Quantum Electronics, IEEE Journal of*, 23(5):510–524, May 1987.

[94] G. P. Agrawal and C. Headley. Kink Solitons and Optical Shocks in Dispersive Nonlinear Media. *Physics Rev. A*, 46:1573–1577, Aug 1992.

[95] N. Nishizawa and T. Goto. Experimental Analysis of Ultrashort Pulse Propagation in Optical Fibers Around Zero-Dispersion Region Using Cross-Correlation Frequency Resolved Optical Gating. *Optics Express*, 8(6):328–334, Mar 2001.

[96] I. Cristiani, R. Tediosi, L. Tartara, and V. Degiorgio. Dispersive Wave Generation by Solitons in Microstructured Optical Fibers. *Optics Express*, 12:124–135, 2004.

[97] I.N. Duling. Sub-Picosecond All-Fibre Erbium Laser. *Electronics Letters*, 27:544–545(1), March 1991.

[98] Y. Tang, C. Huang, S. Wang, H. Li, and J. Xu. High-Power Narrow-Bandwidth Thulium Fiber Laser with an All-Fiber Cavity. *Optics Express*, 20(16):17539–17544, Jul 2012.

[99] T. A. Birks, W. J. Wadsworth, and P. St. J. Russell. Supercontinuum Generation in Tapered Fibers. *Optics Letters*, 25(19):1415–1417, Oct 2000.

[100] W. J. Wadsworth, A. Ortigosa-Blanch, J. C. Knight, T. A. Birks, T. P. Martin Man, and P. St. J. Russell. Supercontinuum Generation in Photonic Crystal Fibers and Optical Fiber Tapers: A Novel Light Source. *Journal of the Optical Society of America B*, 19(9):2148–2155, Sep 2002.

[101] G. Pacchioni, L. Skuja, and D. L. Griscom. *Defects in SiO_2 and Related Dielectrics: Science and Technology*. Springer, 2nd edition, 2000.

[102] R. L. Mozzi and B. E. Warren. The Structure of Vitreous Silica. *Journal of Applied Crystallography*, 2:164–172, 1969.

[103] R. J. Bell and P. Dean. The Structure of Vitreous Silica: Validity of the Random Network Theory. *Philosophical Magazine*, 25:1381–1398, 1972.

[104] F.L. Galeener. Raman and Electron-Spin-Resonance Studies of the Thermal History of Amorphous SiO_2. *Journal of Non-Crystalline Solids*, 71:373, 1985.

[105] D. L. Griscom, M. E. Gingerich, E. J. Friebele, M. Putnam, and W. Unruh. Fast-Neutron Radiation Effects in a Silica-Core Optical Fiber Studied by a CCD-Camera Spectrometer. *Applied Optics*, 33:1022, 1994.

[106] K. Nagasawa, Y. Ohki, and Y. Hama. Gamma-Ray Induced 2 eV Optical Absorption Band in Pure-Silica Core Fibers. *Japanese Journal of Applied Physics*, 26:1009, 1987.

[107] O. Deparis, D. Griscom, P. Mgret, M. Decrton, and M. Blondel. Influence of the Cladding Thickness on the Evolution of the NBOHC Band in Optical Fibers Exposed to Gamma Radiations. *Journal of Non-Crystalline Solids*, 216:124, 1997.

[108] K. Kajihara, L. Skuja, M. Hirano, and H. Hosono. Formation and Decay of NBOHCs in SiO_2 Glasses Induced by F_2 Laser Irradiation: In-Situ Observation Using a Pump and Probe Technique. *Applied Physics Letters*, 79:1757, 2001.

[109] K. Kajihara, Y. Ikuta, M. Oto, M. Hirano, L. Skuja, and H. Hosono. UV VUV Laser Induced Phenomena in SiO_2 Glass. *Nuclear Inst. and Methods in Phys. Re. Sec. B: Beam Interactions with Materials and Atoms*, 218(0):323 – 331, 2004. Proceedings of the Twelfth International Conference on Radiation Effects in Insulators.

[110] J. M. Stone, W. J. Wadsworth, and J. C. Knight. 1064 nm Laser-Induced Defects in Pure SiO_2 Fibers. *Optics Letters*, 38(15):2717–2719, Aug 2013.

[111] E. J. Friebele, G. H. Sigel Jr., and D. L. Griscom. Drawing-Induced Defect Centers in a Fused Silica Core Fiber. *Applied Physics Letters*, 28:516 – 518, 1976,.

[112] H. Hanafusa, Y. Hibino, and F. Yamamoto. Formation Mechanism of Drawing-Induced Defects in Optical Fibers. *Journal of Non-Crystalline Solids*, 9596, Part 2(0):655 – 661, 1987.

[113] D. L. Griscom. Optical Properties and Structure of Defects in Silica Glass. *Journal of the Ceramic Society of Japan*, 99:923–942, 1991.

[114] L. Skuja, H. Hosono, and M. Hirano. Laser-Induced Color Centers in Silica. In *Proc. SPIE*, volume 4347, pages 155–168, 2001.

[115] L. Skuja. Optically Active Oxygen-Deficiency-Related Centers in Amorphous Silicon Dioxide. *Journal of Non-Crystalline Solids-Crystalline Solids*, 239:16–48, 1998.

[116] H. Hosono, Y. Ikuta, T. Kinoshita, K. Kajihara, and M. Hirano. Physical Disorder and Optical Properties in the Vacuum Ultraviolet Region of Amorphous SiO_2. *Phys. Rev. Lett.*, 87:175501, Oct 2001.

[117] H. Imai, K. Arai, J. Isoya, H. Hosono, Y. Abe, and H. Imagawa. Generation of E Centers and Oxygen Hole Centers in Synthetic Silica Glasses By Irradiation. *Physical Review B*, 48:3116–3123, 1993.

[118] H. Nishikawa, R. Nakamura, R. Tohmon, Y. Ohki, Y. Sakurai, K. Nagasawa, and Y. Hama. Generation Mechanism of Photoinduced Paramagnetic Centers from Pre-Existing Precursors in High-Purity Silicas. *Physical Review B*, 41:7828–7834, 1990.

[119] Y. Hibino and H. Hanafusa. Defect Structure and Formation Mechanism of Drawing Induced Absorption at 630 nm in Silica Optical Fibers. *Journal of Applied Physics*, 60:1797–1801, 1986.

[120] Y. Hibino H. Hanafusa and F. Yamamoto. Formation Mechanism of Drawing-Induced E Centers in Silica Optical Fibers. *Journal of Applied Physics*, 58:1356–1361, 1985.

[121] R. K. Iler. *The Chemistry of Silica.* John Wiley & Sons, 1979.

[122] I. Gris-Sanchez, B. J. Mangan, and J. C. Knight. Reducing Spectral Attenuation in Small-Core Photonic Crystal Fibers. *Optical Materials Express*, 1(2):179–184, Jun 2011.

[123] J. Stone, A. R. Chraplyvy, and C. A. Burrus. Gas-in-Glass, A New Raman-Gain Medium: Molecular Hydrogen in Solid-Silica Optical Fibers. *Optics Letters*, 7(6):297–299, Jun 1982.

[124] P. B. Lyons and L. D. Looney. Enhanced Radiation Resistance of High-OH Silica Optical Fibers. In *Proc. SPIE*, volume 1791, pages 286–296, 1993.

[125] P. Karlitschek, G. Hillrichs, and K.-F. Klein. Influence of Hydrogen on the Colour Center Formation in Optical Fibers Induced by Pulsed UV-Laser Radiation. Part 1: All Silica Fibers with High-OH Undoped Core. *Optics Communications*, 155(46):376 – 385, 1998.

[126] P. Karlitschek, G. Hillrichs, and K.-F. Klein. Influence of Hydrogen on the Colour Center Formation in Optical Fibers Induced by Pulsed UV-Laser Radiation. Part 2: All-Silica Fibers with Low-OH Undoped Core. *Optics Communications*, 155(46):386 – 397, 1998.

[127] A. L. Tomashuk, E. M. Dianov, K. M. Golant, and A. O. Rybaltovskii. γ-Radiation-Induced Absorption in Pure Silica Core Fibers in the Visible Spectral Region: The Effect of H_2-Loading. *IEEE Trans. Nuclear Science*, 45:1576 – 1579, 1998.

[128] H. Henschel, O. Kohn, and U. Weinand. Radiation Hardening of Pure Silica Optical Fibers by High-Pressure Hydrogen Treatment. *Nuclear Science, IEEE Transactions on*, 49(3):1401–1409, Jun 2002.

[129] Y. Colombe, D. H. Slichter, A. C. Wilson, D. Leibfried, and D. J. Wineland. Single-Mode Optical Fiber for High-Power, Low-Loss UV Transmission. *Optics Express*, 22(16):19783–19793, Aug 2014.

[130] J. Stone, A. R. Chraplyvy, J. M. Wiesenfeld, and C. A. Burrus. Overtone Absorption and Raman Spectra of H_2 and D_2 in Silica Optical Fibers. *AT&T Bell Laboratories Technical Journal*, 63(6):991–1000, 1984.

[131] J. Stone. Interactions of Hydrogen and Deuterium with Silica Optical Fibers: A Review. *Journal of Lightwave Technology*, 5(5):712–733, May 1987.

[132] L. Shang, I. Chou, W. Lu, R. C. Burruss, and Y. Zhang. Determination of Diffusion Coefficients of Hydrogen in Fused Silica Between 296 and 523 K by Raman Spectroscopy and Application of Fused Silica Capillaries in Studying Redox Reactions. *Geochimica et Cosmochimica Acta*, 73(18):5435 – 5443, 2009.

[133] B. Kumar, N. Fernelius, and J. A. Detrio. Deuterium Treatment and Infrared Transmission Spectra of Fused Silica. *Journal of the American Ceramic Society*, 64(12):C–178–C–180, 1981.

[134] D. L. Fry, P. V. Mohan, and R. W. Lee. Hydrogen-Deuterium Exchange in Fused Silica. *Journal Optical Society of America*, 50:1321–1322, 1960.

[135] J. E. Shelby, P. L. Mattern, and D. K. Ottesen. RadiationInduced Isotope Exchange in Vitreous Silica. *Journal of Applied Physics*, 50(8), 1979.

[136] R. W. Lee, R. C. Frank, and D. E. Swets. Diffusion of Hydrogen and Deuterium in Fused Quartz. *Journal of Chemical Physics*, 36:1062–1071, 1962.

[137] J. Stone and P. Lemaire. Reduction of OH Absorption in Silica Fibers By OH $\rightleftharpoons$ OD Exchange. *IEEE Journal of Quantum Electronics*, 17(12):2566–2566, December 1981.

[138] E. Modone and G. Roba. OH Reduction in Preforms By Isotope Exchange. *Electronics Letters*, 17(21):815–817, October 1981.

[139] L. Pei, T. G. Ning, Z. H. Xie, F. P. Yan, and S. S. Jian. The Anneal Research on H_2-Loaded Optical Fiber Grating. *Proc. SPIE*, 4579:282–285, 2001.

[140] L. Lin, X. Y. Ma, L. Zhong, and D. Yang. Effects of Rapid Thermal Processing on Oxygen Precipitation in Czochralski Silicon Wafer. *Semiconductor Science and Technology*, 19(5):630–633, 2004.

[141] N. Uchida and N. Uesugi. Infrared Optical Loss Increase in Silica Fibers Due to Hydrogen. *Journal of Lightwave Technology*, 4(8):1132–1138, Aug 1986.

[142] V. A. Fabrikant. PhD thesis, Lebedev Institiue Acad. of Science, U.S.S.R, 1939.

[143] A. Javan. Possibility of Production of Negative Temperature in Gas Discharges. *Phys. Rev. Lett.*, 3:87–89, Jul 1959.

[144] J. H. Sanders. Optical Maser Design. *Phys. Rev. Lett.*, 3:86–87, Jul 1959.

[145] A. Javan, W. R. Bennett, and D. R. Herriott. Population Inversion and Continuous Optical Maser Oscillation in a Gas Discharge Containing a He-Ne Mixture. *Physics Review Letters*, 6:106–110, Feb 1961.

[146] A. von Engel. *Ionized Gases*, volume 2nd Ed. Clarendon Press, Oxford, 1955.

[147] R. T. Young. Calculation of Average Electron Temperatures in Rare Gas Mixtures. *Unpublished*, 5, 1968.

[148] C. S. Willett. *Introduction to Gas Lasers: Population Inversion Mechanisms*, volume 67. Clarendon Press, Oxford, 1974.

[149] D. Schuocker, W. Reif, and H. Lagger. Theoretical Description of Discharge Plasma and Calculation of Maximum Output Intensity of He-Ne Waveguide Lasers as a Function of Discharge Tube Radius. *IEEE Journal of Quantum Electronics*, 15(4):232–239, Apr 1979.

[150] P. W. Smith. A Waveguide Gas Laser. *Applied Physics Letters*, 19(5):132–134, 1971.

[151] P. W. Smith and P. J. Maloney. A Self-Stabilized 3.5 μm Waveguide HeXe Laser. *Applied Physics Letters*, 22(12):667–669, Jun 1973.

[152] S. A. Gonchukov, S. T. Kornilov, V. N. Petrovskii, and E. D. Protsenko. Helium-Neon Waveguide Laser. *Soviet Journal Quantum Electronics*, 5:232–233, 1975.

[153] S. A. Gonchukov, S. T. Kornilov, and E. D. Protsenko. Oscillation Modes of a Gas Laser With Waveguide Resonator. *Soviet Journal Quantum Electronics*, 6:996–997, 1976.

[154] X. Shi, X. B. Wang, W. Jin, and M. S. Demokan. Characteristics of Gas Breakdown in Hollow-Core Fibers. *Technology*, 20(8):650–652, 2008.

[155] X. Shi, X. B. Wang, W. Jin, and M. S. Demokan. Investigation of Glow Discharge of Gas in Hollow-Core Fibers. *Applied Physics B*, 91(2):377–380, Apr 2008.

[156] A.A. Kruithof and F.M. Penning. Determination of the Townsend Ionization Coefficient α for Mixtures of Neon and Argon. *Physica*, 4(6):430 – 449, 1937.

[157] V. Cermk and Z. Herman. Penning Ionization Electron Spectroscopy: Ionization of Mercury. *Chemical Physics Letters*, 2(6):359 – 362, 1968.

[158] W. P. Sholette and E. E. Muschlitz. Ionizing Collisions of Metastable Helium Atoms in Gases. *The Journal of Chemical Physics*, 36(12), 1962.

[159] V. Bush and S. H. Caldwell. Thomas-Fermi Equation Solution by the Differential Analyzer. *Physical Review Letters*, 38:1898–1902, Nov 1931.

[160] J. B. Hasted. *Physics of Atomic Collisions*. Butterworth & Co, 1st edition, 1964.

[161] R. B. Brode. The Quantitive Study of the Collisions of Electrons with Atoms. *Rev. Mod. Phys.*, 5:257–279, 1933.

[162] B. E. Cherrington. *Gaseous Electronics and Gas Lasers*. Pergamon Press, 1st edition, 1979.

[163] I. H. Hutchinson. *Principles of Plasma Diagnostics*. Cambridge Univ. Press, 1st edition, 1990.

[164] E. F. Labuda and E. I. Gordon. Gas Pumping in Continuously Operated Ion Lasers. *Journal of Applied Physics*, 35:1647, 1964.

[165] R. T. Young, C. S. Willett, and R. T. Maupin. Effect of Helium on Population Inversion in the HeliumNeon Laser. *Journal of Applied Physics*, 41:2936, 1970.

[166] R. T. Young. Calculation of Average Electron Energies in HeNe Discharges. *Journal of Applied Physics*, 36:2324, 1965.

[167] P. O. Clark. Investigation of the Operating Characteristics of the 3.5 μm Xenon Laser. *Quantum Electronics, IEEE Journal of*, 1(3):109–113, Jun 1965.

[168] W. R. Bennett. Inversion Mechanisms in Gas Lasers. *Applied Optics*, 4(S1):3–22, Jan 1965.

[169] C. S. Willett and T. J. Gleason. Additional Excitation Transfer between Excited Helium Atoms and Neon in He-Ne Laser Discharges. *Laser Focus*, 8(32):30 – 33, June 1971.

[170] J. W. Gertwartowski and H. A. Watson. *Principles of Electron Tubes.* van Mostrand, 1965.

[171] G. Francis. *Ionisation Phenomena in Gases.* Academic Press, New York, 1960.

[172] A. I. Maksimov. Gas Discharges Driven at High Frequencies. *Optics and Spectroscopy*, 21:422, 1966.

[173] A. P. Motornenko. On Some Optical Properties of an UHF Gas Discharge. *Optics and Spectroscopy*, 18:603, 1965.

[174] C. K. N. Patel, W. L. Faust, and R. A. McFarlane. High Gain Gaseous (HeXe) Optical Masers. *Applied Physics Letters*, 1:84, 1962.

[175] A. D. White and J. D. Rigden. Continuous Gas Maser Operation in the Visible. *Proc IRE*, 50:1697, 1962.

[176] A. L. Bloom, W. E. Bell, and R. C. Rempel. Laser Operation at 3.39 μm in a Helium-Neon Mixture. *Applied Optics*, 2(3):317–318, Mar 1963.

[177] A. D. White and E. I. Gordon. Excitation Mechanisms and Current Dependence of Population Inversion in HeNe Lasers. *Applied Physics Letters*, 3(11):197–199, 1963.

[178] H. G. Heard and J. Peterson. Super-Radiant Yellow and Orange Laser Transitions in Pure Neon. *Proceedings of the IEEE*, 52(10):1258–1258, Oct 1964.

[179] W. B. Bridges. High Optical Gain At 3.5 μm in Pure Xenon. *Applied Physics Letters*, 3(3):45, 1963.

[180] D. Armstrong. A Method for the Control of Gas Pressure in the Xenon Laser. *IEEE Journal of Quantum Electronics*, 4(11):968–969, November 1968.

[181] C. C. Davis and T. A. King. Upper Level Lifetimes of High-Gain Laser Transitions in Neutral Xenon. *Physics Letters A*, 39(3):186 – 188, 1972.

[182] W. L. Faust, R. A. McFarlane, C. K. N. Patel, and C. G. B. Garrett. Gas Maser Spectroscopy in the Infrared. *Applied Physics Letters*, 1(4):85, 1962.

[183] R.A. Paananen and D.L. Bobroff. Very High Gain Gaseous (Xe-He) Optical Maser at 3.5 μm. *Applied Phyics Letters*, 2:99–100, 1963.

[184] A. A. Kuznetsov and D. I. Mash. Operating Conditions of an Optical Maser with a Helium-Xenon Mixture in the Middle Infra-Red Region of the Spectrum. *Radio Engineering and Electronic Physics*, 10:319, 1965.

[185] V. N. Smiley, A. L. Lewis, and D. K. Forbes. Gain and Bandwidth Narrowing in a Regenerative He-Xe Laser Amplifier. *Journal of the Optical Society of America*, 55(11):1552–1553, Nov 1965.

[186] K. D. Mielenz, K. F. Nefflen, K. E. Gillilland, R. B. Stephens, and R. B. Zipin. Gas Mixtures and Pressures for Optimum Output Power of RF-Excited Helium-Neon Gas Lasers at 632.8 nm. *Applied Physics Letters*, 7:277, 1965.

[187] F. Terman. *Radio Engineers' Handbook*. McGraw-Hill, 1943.

[188] P. R. Gray, P. J. Hurst, S. H. Lewis, and R. G. Meyer. *Analysis and Design of Analog Integrated Circuits*. New York: Wiley, 5th edition, 2009.

[189] S. Aisenberg. The Effect of Helium on Electron Temperature and Electron Density in Rare Gas Lasers. *Applied Physics Letters*, 2(10), 1963.

[190] A. Bogaerts, E. Neyts, R. Gijbels, and J. Van Der Mullen. Gas Discharge Plasmas and Their Applications. *Spectrochimica Acta Part B: Atomic Spectroscopy*, 57(4):609 – 658, 2002.

[191] X. L. Tong, Q. G. Zheng, S. L. Hu, Y. X. Qin, and Z. H. Ding. Structural Characterization and Optoelectronic Properties of GaN Thin Films on Si(111) Substrates Using Pulsed Laser Deposition Assisted by Gas Discharge. *Journal of Applied Physics A*, 79(8):1959 – 1963, 2004.

[192] I. R. Sinclair. *Sensors and Transducers*. Newnes, 3rd edition, 2001.

[193] R. A. McFarlane, W. L. Faust, C. K. N. Patel, and C. G. B. Garrett. Gas Maser Operation at Wavelengths Out to 28 μm. *Quantum Electronics*, 3:573–586, 1964.

[194] C. J. Humlphreys, E. Paul, R. D. Cowan, and K. L. Andrew. Spectra of the Noble Gases in the 4 μm Region. *Journal Optical Society Amercia*, 57(7):855–864, Jul 1967.

[195] C. J. Humlphreys. First Spectra of Neon, Argon, and Xenon 136 in the 1.2 4.0 μm Region. *Journal of Physical and Chemical Reference Data*, 2(3), 1973.

[196] A. Love, S. A. Bateman, W. Belardi, C. E. Webb, and W. J. Wadsworth. Double Pass Gain in Helium-Xenon Discharges in Hollow Optical Fibres at 3.5 μm. In *Conference on Lasers and Electro-Optics (CLEO) 2015*, May 2015.

[197] E. G. Aleksandrov, V.N. Kulyasov, and A. B. Mamyrin. Spectral Emissions in Xe Beyond 4 μm. *Optics and Spectroscopy*, 31:170, 1971.